INVESTIGATING THE POTENTIAL IMPACT OF WIND FARMS ON LAKE ERIE

SOUDEH AFSHARIAN

A DISSERTATION SUBMITTED TO THE FACULTY OF GRADUATE STUDIES

IN PARTIAL FULFILMENT OF THE REQUIREMENTS

FOR THE DEGREE OF

DOCTOR OF PHILOSOPHY

GRADUATE PROGRAMME IN EARTH AND SPACE SCIENCE

YORK UNIVERSITY

TORONTO, ONTARIO

May 2018

Abstract

Our traditional energy sources are mainly non-renewable resources like coal and oil. These fuels, when burned, have a negative impact on our environment due to release of greenhouse gases, and they are not replenishable. So, the world needs other sources of energy to prevent an environmental crisis. Green energy produced from sources like wind, solar, geothermal and hydro, etc., is renewable and has much less impact on our environment.

In our study, we focused on the potential impact of wind farms on Lake Erie's dynamic and thermal structure. We used COHERENS (a Coupled Hydrodynamical-Ecological model for Regional and Shelf Seas) numerical software for the simulations. They were applied in 1 and 3 dimensions. In both cases, we used real wind speed and other meteorological data including atmospheric pressure, air temperature, humidity and cloud cover to simulate possible temperature and current variations over the ice-free season in Lake Erie. We worked on Erie, since this lake has the highest potential for offshore wind turbine installation due to its proximity to population centres and its shallow depth.

In 1D mode, vertical profiles of temperature and water currents are driven by solar radiation and surface fluxes derived from observed three-hourly meteorological data, coupled with vertical mixing processes within the water column. Results are obtained for nine months of open (ice-free) water, March to November 2013, with different water depths of 10, 25 and 60 m. The model was run twice. In the second run, we used a reduced wind speed associated with the potential effect of wind turbines. For initial calculations, we used 25 percent reduction as a representative value.

In 3D mode, we investigated the circulation and thermocline pattern for the months of May to October, 2005. As in the 1D mode, the model was run twice. The model is forced by solar radiation plus momentum and heat fluxes (sensible and latent) at the surface derived from North American

Regional Reanalysis (NARR) and Canada Centre for Inland Waters (CCIW) data, plus initial conditions and with tributary flows represented as current vectors at river mouths. The Detroit River is the main inflow while outflow is via the Niagara River. With precipitation and evaporation balanced there was net zero accumulation of water in the basin. In the first run we explored water circulation patterns and the thermal structure (including the thermocline), of the lake and in the second run, we simulated the same parameters but added a large wind farm with 432 offshore turbines located in the shallow southern waters of the central basin.

We compared our first run COHERENS output with both the Princeton Ocean Model (POM), and the Estuary and Lake Computer Model (ELCOM) results, run by the National Oceanic and Atmospheric Administration (NOAA) and the Canada Centre for Inland Waters (CCIW- Environment Canada), respectively. Generally, good agreement was achieved with these runs, which in turn had compared satisfactorily with field measurements. Results from the second run are used to estimate the potential impact of a large wind farm on the circulation and thermal structure in the areas of the lake within and around the wind farm.

Acknowledgments

I would like to thank my supervisor Professor Peter A. Taylor for his valuable support and help. His wide knowledge about atmospheric science have been of great value to me. I also like to thank my Ph.D. committee Professors Robert McLaren, Yongsheng Chen and Jim Salmon for their continuous support and guidance.

I would like to thank Dr. Ladan Momayez from Royal Military College of Canada, Wensong Weng, Robert Milverton and Carol Weldon from York University and Katrijn Baetens from Royal Belgian Institute of Natural Sciences, Maryam Shie and Pooran Khedri for their continued help with COHERENS software and coding. I also would like to thank NSERC Discovery grant and IACPES program for financial support and Environment and Climate Change Canada's Research Support group Ram Yerubandi, Luis Leon, and Reza Valipour.

Table of Contents

List of Tables

LIST OF FIGURES

CHAPTER ONE

INTRODUCTION

1.1 Introduction

If we want to reduce our impact on the environment, using clean energy is a good action. One of the main sources of "Greenhouse" gases is electricity generation. Using clean energy is good for the planet and economy as well as reducing the human and industry dependency on oil and fossil fuels. Among the clean energy resources, wind power is a well-proven and cost-effective technology, which we can rely on in producing electricity. There are many reasons that people choose to use wind energy and the most important is that they "want to". Some other reasons are as follow, (UCS, 2017)

- Little to no global warming emissions
- Improved public health and environmental quality
- A vast and inexhaustible energy supply
- Jobs and other economic benefits

There are two ways in generating electricity by wind energy: onshore and offshore. There are some advantages associated with offshore wind energy and our study focused on this aspect. On the open water surface, the surface roughness is low as there are no physical barriers such as mountains or trees

so air flows more quickly and this leads to more energy production. However only a small fraction of the world's wind industry includes the offshore sector due to the additional costs and the risk of installing the huge wind turbines in water. Typically, offshore farms are located several kilometers away from the coast, in water that is up to 30 m deep, and turbines tend to be larger and must have a special design to withstand "stress loads" from high winds, tides, and ice accumulation. Further, the additional costs and difficulties of transmitting the power to the onshore grid make the offshore section less popular, (The Canadian Atlas, 2017).

Lake Erie would be a suitable location for offshore wind farms. It has a good wind resource, moderate depth and high electricity demand nearby. The combination of shallow depth of Lake Erie with its solid lake bottom and fresh water make it one of the friendliest locations to the offshore wind industry. The latter factor frees the project from dealing with corrosion or extra costs related to safeguarding the hardware. A first phase of a wind offshore project (Lake Erie Energy Development Corporation- LEEDCO) has started. This is a pilot project consisting of six wind turbines on the southern parts of the central basin.

1.2 World Wind Energy

"According to the Global Wind Energy Council (GWEC), by 2020, wind energy should provide 10 to 12 percent of the world's electricity, eliminating up to 1.5 billion tonnes of carbon emissions every year. The Earth's theoretical wind energy potential has been estimated to be about 72 terawatts, which is approximately five times the total global energy need", (The Canadian Atlas, 2017).

1.2.1 World Offshore Wind Energy

Over 10 GW of global offshore wind capacity were fully usable by the end of 2015. Northern Europe is the leader in this energy sector but despite significant potential especially in the Great Lakes

in North America, no commercial project is operated yet. There can be over 100 wind turbines in an offshore wind farm. The offshore wind turbines generating capacity has grown to over 6 MW and will reach 10 MW very soon, (Ontario.ca, 2017).

"While some offshore farms are being planned in the Great Lakes, the west coast of Canada and the Atlantic coast of the United States, the North Sea is where the most completed installations are found (off the coasts of Denmark, Germany, and the United Kingdom). As of 2008, there were just over 500 offshore turbines, representing about 1100 MW of generating capacity. 90 percent is produced by Denmark. Horns Rev 1 and 2 are considered to be the largest offshore wind farms, located between 14 and 20 km from the west coast of Denmark Jutland Peninsula", (The Canadian Atlas, 2017).

1.3 Canada Wind Energy

More than 12,000 MW of wind energy were installed by 2015 in Canada and the vision for 2025 is estimated to be 55,000 MW, which is projected to create 52,000 new "Green Collar Jobs", (The Canadian Atlas, 2017).

Wind power is going to be the second largest renewable power source in Canada in 2017 according to the government of Canada, (Figure 1.1). It produced 5 and 6 percent of the Canada's electricity in 2015 and 2017, respectively. The generating capacity of wind energy in 2017 is almost 18 times what it was in 2005.

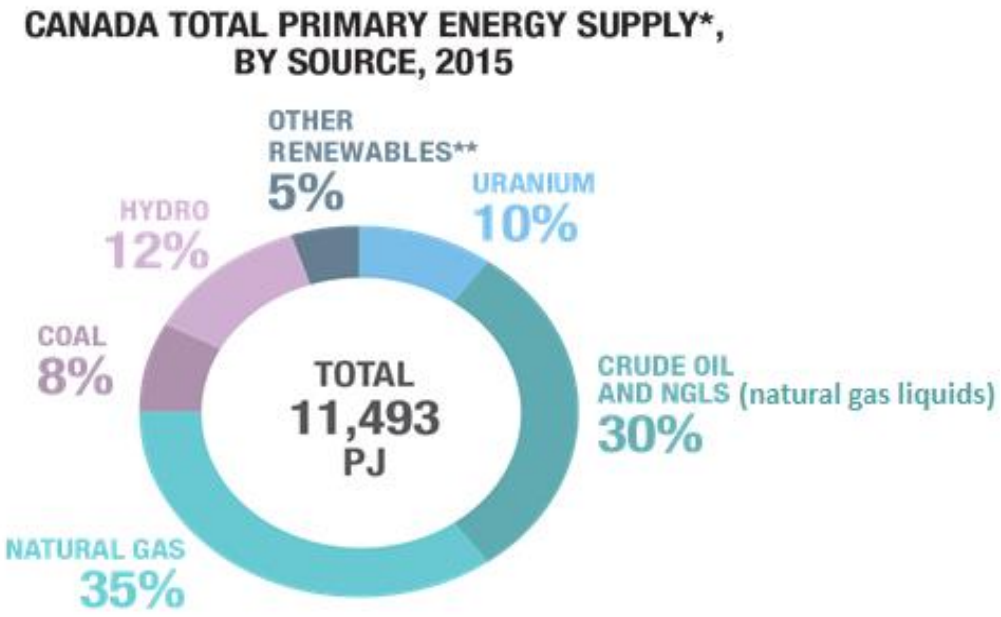

Figure 1.1: Energy Production in Canada by Resource in 2015. [Natural Resources Canada, 2017]

Continuing the growth of wind energy in the recent years, the capacity has reached to 12,239 MW in 2017 (Figure 1.2), which is 6 percent of the country's electricity demand and is enough to provide power for 3 million home. 341 MW of capacity (through 10 projects) with an investment of $800 million has been installed in 2017. Canada is in the world's ninth place in wind-generated electricity. When the winds are strong enough, there are 295 wind farms operating from coast to coast. Canada has continued its growing wind energy trend in 2017. Still there are many opportunities to strengthen the industrial-economic development in the Canadian wind energy section, (CANWEA, 2017a).

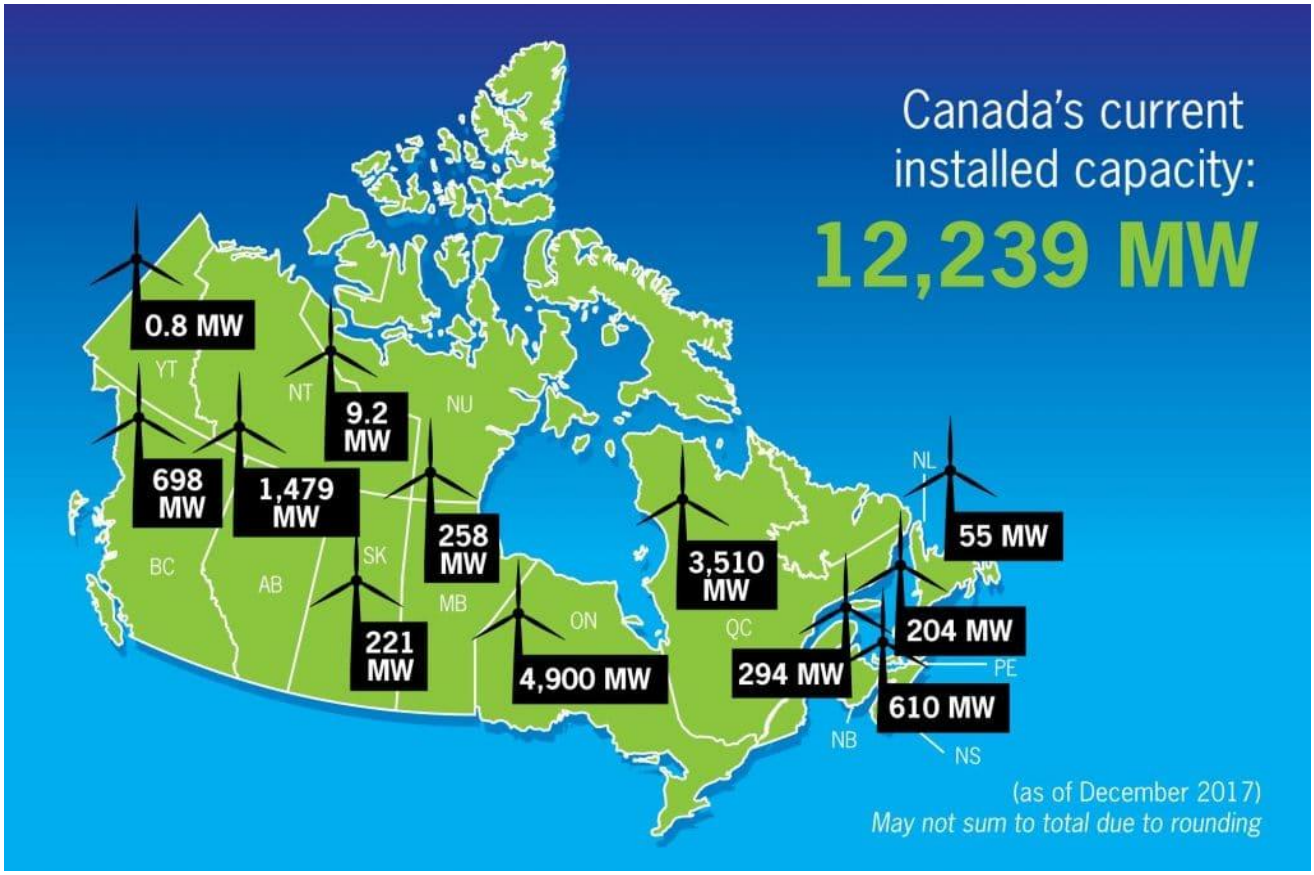

Figure 1.2: Canada's installed wind capacity as of 2017. [CANWEA, 2017a]

1.4 Ontario Electricity Demand Overview

Demand refers to the amount of electricity required in Ontario over a period of time. Table 1.1 shows an overview of Ontario electricity demand for year 1997 – 2016.

1.4.1 Total Annual Ontario Energy Demand

Table 1.1: Total Annual Ontario Energy Demand. [IESO, 2017]

Year	Total (TWh)	Increase Over Previous Year
2016	137	0percent
2015	137	-2percent

2014	139.8	-0.64percent
2013	140.7	-0.42percent
2012	141.3	-0.14percent
2011	141.5	-0.35percent
2010	142	2.2percent
2009	139	-6.1percent
2008	148	-2.3percent
2007	152	0.7percent
2006	151	-3.8percent
2005	157	2.3percent
2004	153	1.1percent
2003	152	-0.7percent
2002	153	4.1percent
2001	147	0percent
2000	147	2.1percent
1999	144	2.9percent
1998	140	1.4percent
1997	138	-

1.5 Wind Energy in Ontario

With 4,900 MW of installed capacity Ontario remains Canada leader in clean wind energy (Table 1.2), enough to supply about 40 percent of the national and approximately 7.5 percent of the province's electricity demand. In 2017, an additional 119 MW was added to the total capacity produced by

Ontario. Reducing the greenhouse gas emission by 80 percent below its level in 2005 is the Ontario's long-term plan by 2050, (CANWEA, 2017b).

Table 1.2: Wind by numbers in Ontario (December 2017). [CANWEA, 2017]

Number of installations	94
Number of wind turbines	2515
Total installed capacity (MW)	4900
Average turbine capacity (MW)	1.94

1.5.1 Ontario's Offshore Windfarm Moratorium

Ontario was planned to be a leader in renewable electricity in 2009 on behalf of the province's Green Energy Act. However, all offshore projects were canceled in 2011 and a moratorium proposed by the provincial government. It claimed more investigations on science and learning from the American projects need to be done. The investigations came into three reports. Two were about "protecting fish", one about "coastal engineering". However, the government did not find these reports enough and conducted two new studies in January 2015. The studies were:

- "The prediction of noise impacts in land-based reports from the operation of offshore wind turbines"
- "The decommissioning of offshore wind turbines and ancillary equipment at the end of their useful life without causing adverse effects to the surrounding environment".

The studies were expected to be completed in six to nine months but they are still in progress. "The only outcome of the moratorium was chasing the investors out of the province", (Reevely, 2016).

"The responsible choice is to keep the moratorium on offshore wind development in effect until all the potential impacts are fully understood", the ministry headed by Glen Murray wrote in a statement, (Ferguson, 2016).

So far, one study conducted that it was doable and the impacts were likely to be insignificant, however there are many unknowns about this section of wind projects, (Jones, 2017).

1.5.2 Offshore Wind Plan in Ontario

No matter if Ontario wants the offshore wind projects or not, they are coming to the Great Lakes to minimize the country's dependency on the coal. A comprehensive report on offshore wind from the U.S. Department of Energy and Department of the interior is calling for up to 86 GW of offshore projects to be developed by 2050. This amount of emission-free electricity will cover the Ontario's demand four times over – at least when the wind blows – which it does over open water more than a third of the time. However, it is not just a matter of developing wind capacity off the Atlantic or Pacific coasts. According to the reports, U.S. side of the Great Lakes can generate about 15 percent of the development, which is more than all the onshore wind installed in Canada today. It seems there is a love-hate behavior in this type of wind energy in Ontario, (Hamilton, 2016).

It is not too far from the days that Ontario wanted to become a leader in wind market in North America. In early 2008, after studying the environmental risks, then – Natural Resource Minister – Donna Canfield lifted a temporary ban on the Great Lakes offshore wind industry and declared Ontario is open for offshore wind business. At that time all the economists, businesspersons, highly skilled workforces and engineers imagined this could strengthen the economy growth and industrial opportunities in the province, so the projects started back to back on this side of the Great Lakes within a short time. Starting with Lake Erie it was imagined that as Ontario has the boundary with four of five Great Lakes, it can be the leader and the centre of the offshore wind industry and can grow so that the whole country can use its knowledge and products. This decision was so bold and the province government was so decisive that it launched the Feed-in Tariff initiative for renewable energy in the fall of 2009, and included the offshore program as well as onshore one. However, after only 18 months

of building and persuasion, it re-imposed a moratorium on the offshore part in February 2011. They asserted they need to do more environmental study. “Ontario will work with our U.S. neighbors on research to ensure that any future proposed projects protect the environment on both sides of the Great Lakes”, the environment ministry said at the time. “Today, the offshore wind file in Ontario is a mess”. The province has been taken to court by a developer who felt mistreated, while another is seeking damages through a trade tribunal. Still after 6 years of study, they kept the moratorium due to the lack of scientific information on the potential impact of the turbines on the Great Lakes. “Meanwhile, on the U.S. side, the offshore wind projects are growing and the five-turbine Block Island Wind Farm off the coast of Rhode Island is buoyed and is in progress. This project is the first built in North America waters and is expected to be followed in 2018 by the Great Lakes first: the Icebreaker Wind Farm in Lake Erie”, (Hamilton, 2016).

1.5.3 Offshore Wind Plan in Lake Erie

“Ohio – based Lake Erie Energy Development Corporation (LEEDCO) – is developing a pilot project, which will be composed of six 3.45 MW- turbines installed about 13 kilometers off the shores of Cleveland, (Figure 1.3). In May, the U.S. Energy Department identified it as one of three U.S. offshore projects to qualify for $40 million in federal funding support. LEEDCO is developing the $127 million Icebreaker project in a region with the potential to generate 1 GW of wind energy by 2020”, (Ryan, 2016).

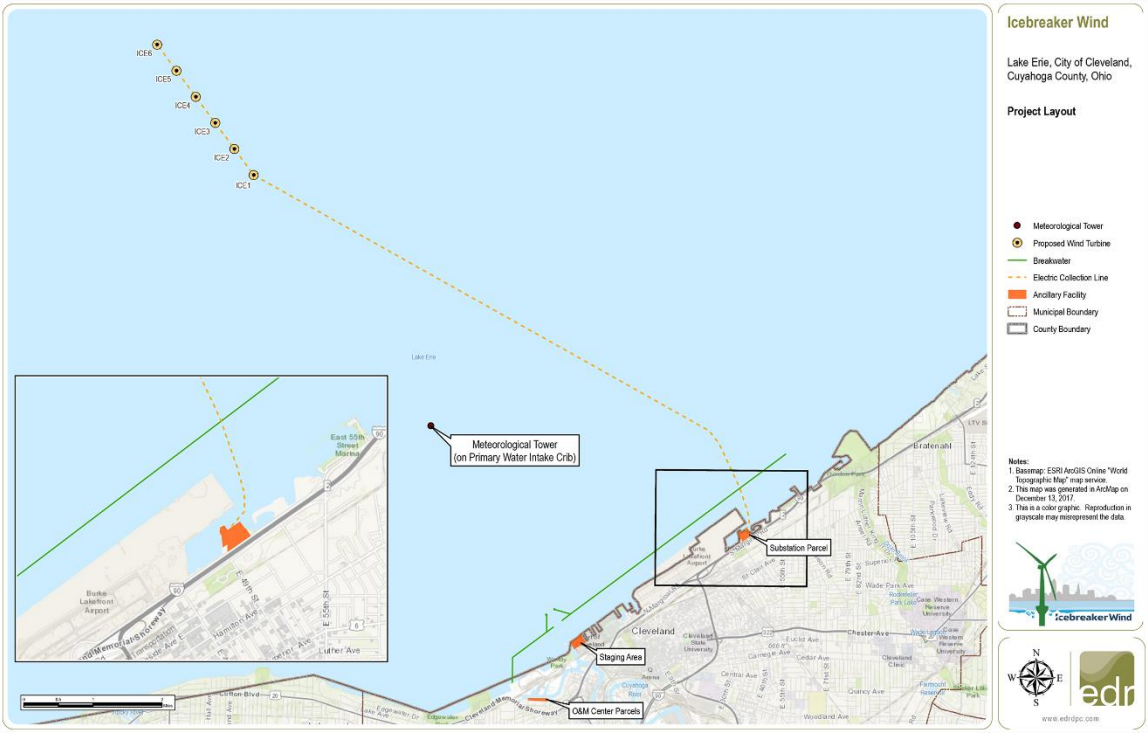

Figure 1.3: Proposed Project Icebreaker Layout [LEEDCO, 2017]

The potential of electric generation in the U.S. side of the Great Lakes is estimated to be 4,223 GW. Lake Erie counts for 50 GW of this capacity. The first six pilot wind turbines test the possibility of building larger wind farms in the lake. "It would generate 20.7 MW of electricity, enough to power about 7000 homes, and would be the first industrial wind farm in a freshwater lake in North America". The estimated potential of the Lake Erie wind turbines is more than 1000, that's why it is described as the Saudi Arabia of wind energy", (Ifpress, 2016).

It is concluded that the U.S. has not yet studied the environmental risk and is not aware of the past Ontario's concerns including the impact on the water quality and marine and birds /bats lives. Even the department of energy says that there are still lots of unknowns about the offshore. The first generation of the offshore projects in Lake Erie will reveal their impacts and the actual effects on biological communities and addresses the range of potential impacts that need to be monitored. By having those

data the “exclusion zones” where the offshore development has to be banned and prohibited will be determined. “The offshore wind market is booming globally. More than 15 GW were installed by the end of 2015, with 25 percent of that coming online by the end of year alone, according to Navigant Research, (Figure 1.4). Most of that development has taken place in the United Kingdom and Germany”, (Hill, 2016). It is suggested that Ontario takes the same learn-by-doing approach in collaboration with its southern neighbor. Therefore, that Ontario can install one or two small offshore projects. This for sure would not render the province “Open for business”. The outcome will be at least helping and improving the Ontario's understanding of offshore wind in the Great Lakes and may help Ontario to open its doors later on the offshore wind business and industrial opportunities, (Hamilton, 2016).

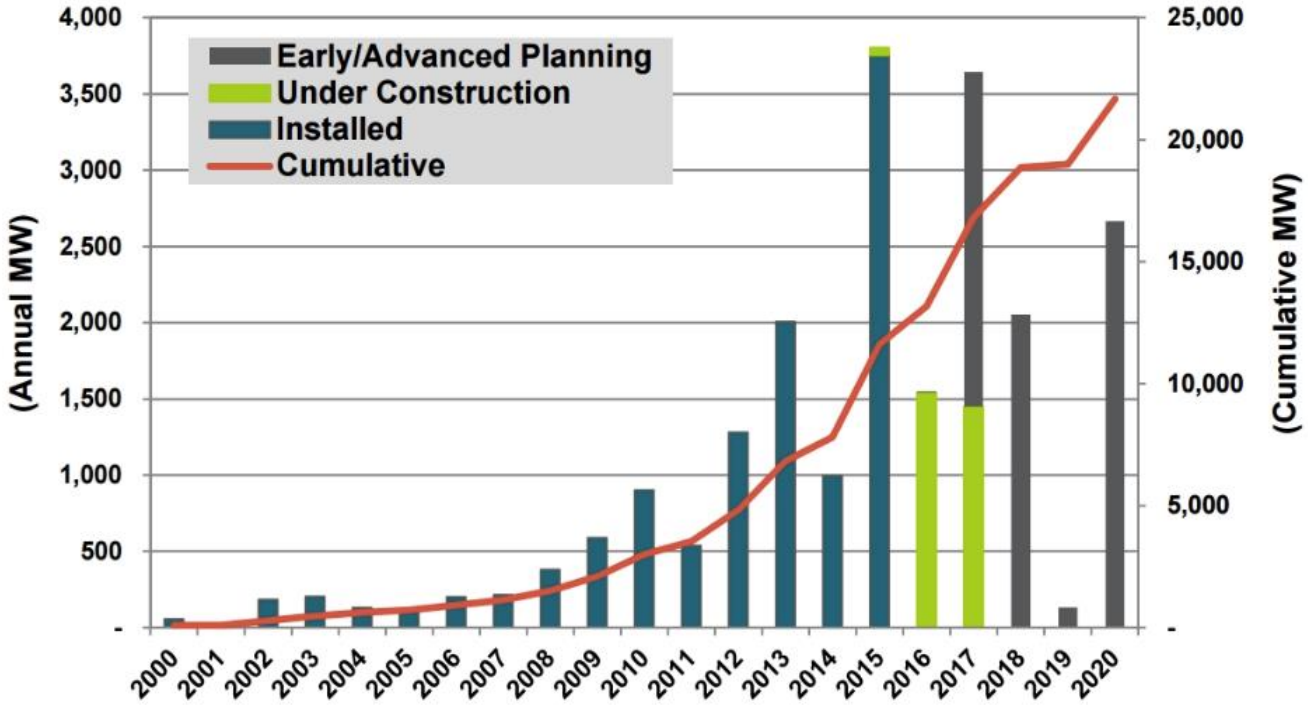

Figure 1.4: Capacity of wind projects online, under construction, and in planning by year, world markets: 2000-2020. [Hill, 2016]

1.5.4 Future of Offshore Wind Energy and Projects in Ontario

The wind energy fight domain now covers Lake Ontario and Erie. “Ontario’s Ministry of the Environment hasn’t created a permit application process, nor has it developed the guidelines for granting permits. The Ontario Minister of Natural Resources announce there will be clarification of the approval processes soon, and acknowledge there is some confusion under the current regime”, (May, 2017).

1.6 Lake Erie

Figure 1.5: Lake Erie [© Google, 2017]

“Lake Erie (Figure 1.5) is geologically the oldest of Saint Lawrence Great Lakes, (Bolsenga and Herdendorf, 1993). It is the smallest and shallowest among them. It lies between 41° 21´ N and 42° 50´ N latitude and 78° 50´ W to 80° 30´ W longitude. The mean and max depths are 19 m and 64 m, respectively and the area is 25,667 km^2. Lake Erie divides into three basins: western, central and

eastern. The western basin is the shallowest (Figure 1.6), and its mean depth is 7.4 m, while the eastern basin, with a mean depth of 24.4 m is the deepest", (Bolsenga and Herdendorf, 1993).

"Lake Erie is the eleventh largest lake in the world (by surface area), and the fourth largest of the Great Lakes in surface area and the smallest by the volume. 95 percent of Lake Erie's total inflow of water comes via the Detroit River water and is composed of water from all the "Upper Lakes" - Superior, Michigan and Huron – the Saint Clair River, Lake Saint Clair and numerous tributaries", (The Great Lakes Atlas, 1995).

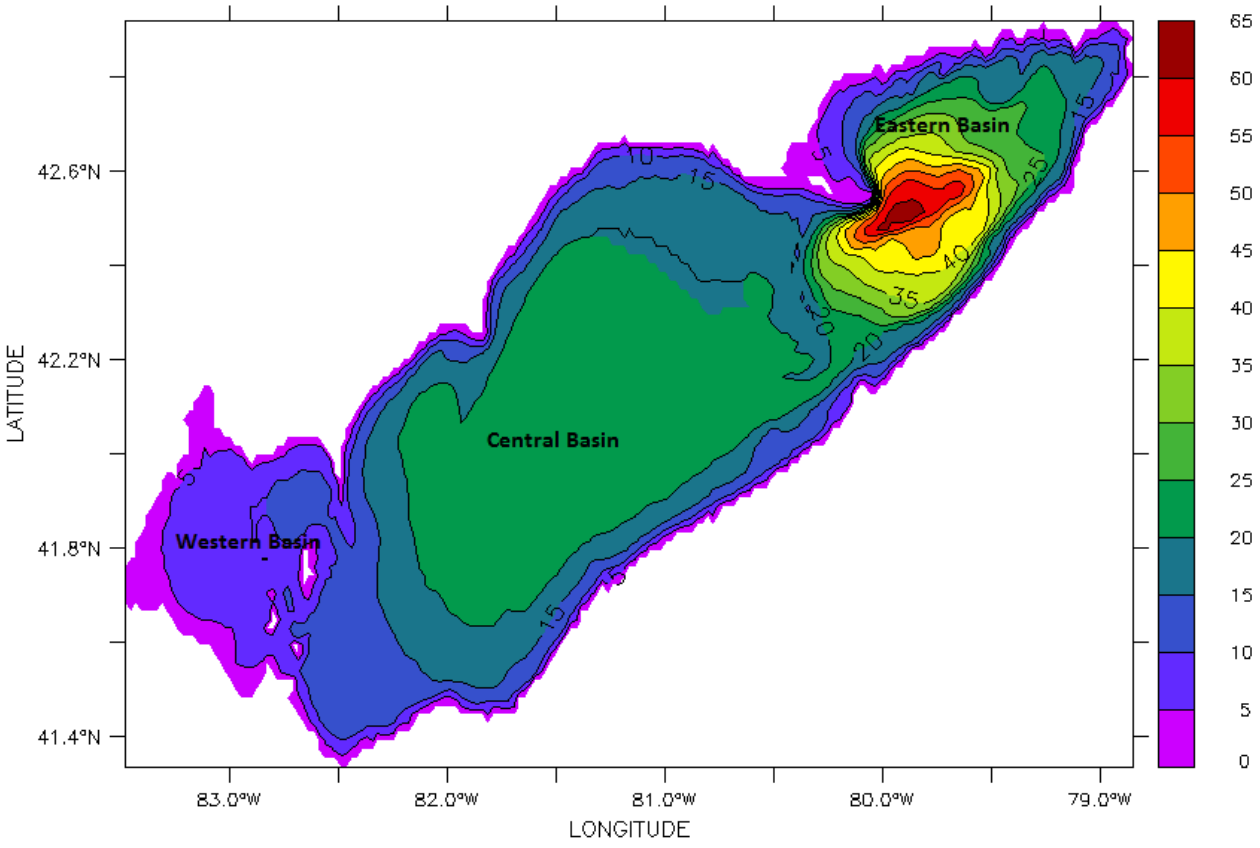

Figure 1.6: Lake Erie bathymetry. Isobaths shown every 5 m.

"Lake Erie is relatively narrow and approximately parallel to the prevailing Southwest winds", (Bolsenga and Herdendorf, 1993). The lake water is constantly in motion, so the lake has a high mixing

potential and as a result, the heating and cooling rate of water is very slow except for some diurnal variations in the near-surface layer. More than 90 percent of the Lake Erie is covered by ice most winters. Minimum surface temperature usually occurs in February (0.1 °C), but when water temperature cools to 4 °C or less in January a fully mixed condition can be observed. Based on the observations of Schertzer et al (1987) and presented in Bolsenga and Herdendorf (1993), isothermal conditions remain from mid-February to mid-April. Stratification, based on surface-bottom temperature, usually begins in May and reaches a maximum in mid-July (central basin) or mid-August (eastern basin). The water column generally becomes well mixed in October or a little later in the deepest sections. The shallow West basin is relatively well mixed most of the year.

In most thermally stratified lakes, the thermocline, a thin subsurface layer of rapid temperature change (See Appendix A), is deeper near the shoreline than near the centre of the lake. Lake Erie, however, has an inverted thermocline, which is deeper offshore than at the shoreline. Beletsky et al. (2013) first mapped this bowl-shaped thermocline during summer of 2005 with a large network of temperature sensors. In 2005, and again in 2007, moored instruments that collected temperature readings at 1-m depth intervals were spread 30 to 50 km apart around the central basin of the lake. Supporting these point measurements, higher-resolution temperature profiles were collected with a boat-towed sensor. It was found that the 2 or 3-m thick thermocline, which was the most pronounced in late summer, set up 8 m deeper offshore than at the coast. In addition to the anomalous thermocline behavior, it was found that the circulation of the central lake flows in a direction opposite of most Northern Hemisphere lakes. Using circulation sensors placed on the lake floor, a pronounced clockwise (anticyclonic) circulation was observed. The unusual circulation and thermocline patterns are attributed to anticyclonic winds that tend to blow over Lake Erie. Such anticyclonic winds would cause the warm surface waters to converge in the centre of the lake, driving down the depth of the thermocline and pushing up the free surface.

"It was suggested that the depressed thermocline squashed the cool region near the lake bed, where many species hide from summer heat. The depressed thermocline could also be responsible for amplifying deep-water summer hypoxia, reducing the oxygen available to lake-bottom plants and animals", (American Geophysical Union, 2012).

1.6.1 Lake Erie Mooring Locations and Bathymetry

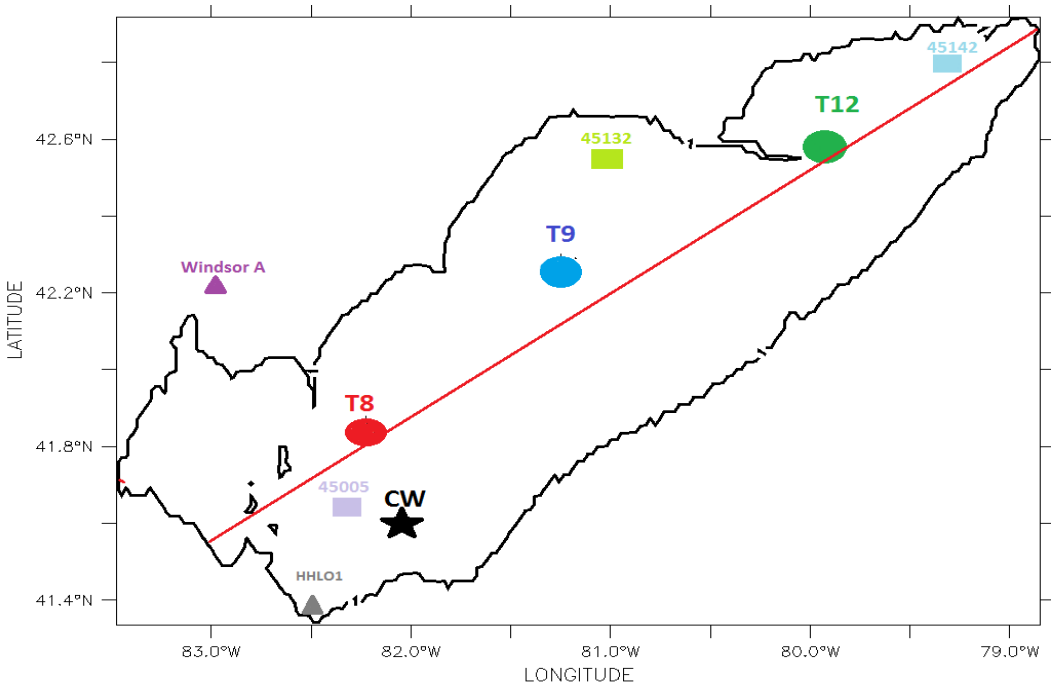

Figure 1.7: Lake Erie mooring locations. Filled circles: red (T08), blue (T09), and green (T12), made temperature observations in 2005. NOAA (45005) and Environment Canada (45132 and 45142) buoy locations are shown with rectangles. The solid red line shows our model transect. Transect is bounded by 5 m isobaths. A black star shows centre of wake (CW) – north side of the wind farm. The filled purple triangle shows the onshore Windsor Airport station and the filled grey triangle shows the HHLO1 station.

These locations, (Figure 1.7), are used later to provide examples of the difference between physical properties of the lake in the presence and absence of a large wind farm. Station T8, T9 and T12 are used in the comparison of case 1 (absence of a wind farm) with case 2 (presence of a wind farm) plots. Also, a point in the heart of the wake zone where the wind speed reduces by 60 percent of its original value is chosen and demonstrated by a black star as centre of wake on the north side of the wind farm (CW). This point is used as a representative of the centre of wake zone behavior. Stations 45005, 45132 and 45142 are buoys installed every summer and are selected to compare the modelled temperature with observations and to compare the NARR reanalyzed wind data used in the model with buoy wind data. The purple and grey triangles show the location of Windsor A and HHLO1 meteorological stations. We used those data in our model when buoy 45005 data were not available. The solid red line along the lake shows the cross-section transect of length of 423.5 km, however in result presentations, plots are restricted to 100 km to 400 km, as the main focus is on the location where the wind turbines are deployed – in the central basin, and where the thermocline is significant – in the eastern basin. Locations and water depths are given in Table 1.3.

Table 1.3: Summary of Station coordinates and depths.

Station	Latitude (°N)	Longitude (°W)	Depth of Water (m)
45005	41.677	82.398	12.6
45132	42.460	81.220	20.0
45142	42.740	79.920	23.9
T08	41.833	82.199	19.5
T09	42.252	81.248	21.8
T12	42.581	79.914	53.9

CW	41.600	82.040	16.9
Windsor A	42.280	82.960	-
HHLO1	41.400	82.540	-

1.7 Previous Work on Lake Erie Dynamics

Beletsky et al. (2013) investigated the summer thermal structure and anticyclonic circulation of Lake Erie, A three-dimensional primitive equation numerical model was applied to Lake Erie on a 2-km grid to study its summer circulation and thermal structure. Model results were compared to long-term observations of currents and temperature made in 2005 at several locations, mostly in its central basin. They investigated the effect of wind stress and bathymetry on the thermal structure and circulation of Lake Erie.

Dupont et al. (2012) investigated the hydrodynamic forecasting. Environment Canada developed a coupled lake-atmosphere-hydrological modelling system for the Laurentian Great Lakes. This model consists of the Canadian Regional Deterministic Prediction System (RDPS), which is based on the Global Environmental Multiscale model (GEM), the MESH (Modelisation Environmental Surface et Hydrology) surface and river routing model, and a hydrodynamic model based on the three-dimensional global ocean model Nucleus for European Modelling of the Ocean (NEMO). The model was run from 2004 to 2009 with atmospheric forcing from GEM and river forcing from the MESH modelling system for the Great Lakes region and compared with available observations in selected lakes.

Fujisaki et al. (2012), focused on the ice process. A hydrodynamic model that includes ice processes and is optimized for parallel processing was configured for Lake Erie in order to study the ice-water coupling processes in the lake. A hind cast from April 2003 to December 2004 with hourly atmospheric forcing was conducted. The model reproduced the seasonal variation of ice cover, but the

development of ice extent in January and its decay in March somewhat preceded the observations. Thermal structure of the lake was compared to both satellite-derived observations and in-situ measurements. The impacts of ice-water stress coupling and basal melting of ice were examined based on numerical experiments. The demonstrated model validity could lead to further studies of ice-water processes in the lake, including inter-annual variation and impacts on ecosystems.

In 2010, Boyce et al. (2010) investigated thermal structure and circulation in the Great Lakes. They reviewed more than a century of physical study of the Great Lakes.

Wang et al. (2010), simulated ice and water circulation in Lake Erie over a yearly cycle, a Great Lakes Ice-circulation Model (GLIM) was developed by applying a Coupled Ice-Ocean Model (CIOM). The hourly surface wind stress and thermodynamic forcing for input into the GLIM are derived from meteorological measurements interpolated onto the 2-km model grid points. The seasonal cycles for ice concentration, thickness, velocity, and other variables are well reproduced in the 2003/04 ice season. Satellite measurements of ice cover were used to validate GLIM. The seasonal cycle for lake surface temperature was well reproduced in comparison to the satellite measurements. Additional sensitivity experiments further confirmed the important impacts of ice cover on lake water temperature and water level variations. Furthermore, a period including an extreme cooling (due to a cold air outbreak) and an extreme warming event in February 2004 was examined to test GLIM's response to rapidly-changing synoptic forcing.

Schwab et al. (2009), worked on the ecological aspects and investigated particle transport The purpose of their work was to show how a high-resolution numerical circulation model of Lake Erie can be used to gain insight into the spatial and temporal variability of phosphorus (and by inference, other components of the lower food web) in the lake. The computer model simulated the detailed spatial and temporal distribution of total phosphorus in Lake Erie during 1994 based on tributary and atmospheric loading, hydrodynamic transport, and basin-dependent net apparent settling. Results of

the model simulations were presented in terms of maps of 1) annually averaged phosphorus concentration, 2) temporal variability of phosphorus concentration, and 3) relative contribution of annual phosphorus load from specific tributaries. The model was also used to estimate the spatial distribution of phosphorus variability and to produce maps of the relative contribution of individual tributaries to the annual average concentration at each point in the lake.

The most significant effort was made as part of the NOAA ECOFORE (Ecological Forecasting) program, studying the dynamics and inter-annual variability of hypoxia in Lake Erie. The data for the hydrodynamic model validation were collected as part of the US – Canada IFYLE (International Field Years on Lake Erie) program, (Hawley et al., 2006).

Leon et al. (2005) found that coupled physical-biological numerical models were useful tools for understanding the relevant processes and the influence of biota and human activity on the ecological conditions in the lake. Such a suite of models has been used to assess the impact of zebra mussels on the nutrient cycling in the lake. They presented the hydrodynamic part of a Lake Erie modelling exercise using the 3D ELCOM model. Validation runs were performed with 1994, 2001, 2002, and 2003 data. The validated model was then used to understand the flushing of the deep water, the internal wave dynamics, and the residual circulation. The hydrodynamic results can be used as the drivers for future simulations aimed at studying the fate and transport of nutrients.

O'Connor et al. (1999), have applied various hydrodynamic models to Lake Erie. They worked on two factors. The first was to describe how the Great Lakes Coastal Forecasting System (GLCFS) could be used to validate wind forecasts for the Great Lakes using observed and forecast water levels. The second was to evaluate how well two versions (40 km and 29 km) of the numerical weather prediction, step-coordinate Eta Model are able to forecast winds for the Great Lakes region, using the GLCFS as a verification technique. A description was given of the GLCFS for Lake Erie. The numerical Princeton Ocean Model (POM) was used for lake circulations. The observed winds were

used to force the POM for Lake Erie for several periods in 1993 when water level surges were recorded. Twin experiments were made with the GLCFS to determine: 1) how well it can predict (hind cast) water levels using observed winds as forcing, and 2) how well it can predict water levels using both the 40- and 29-km Eta Model forecast winds as forcing. Then they discussed the use of this forecast validation technique for other coastal forecasting systems.

Bolsenga and Herdendorf (1993) published the "Lake Erie and Lake St Clair Handbook". The Handbook is actually a good reference, intended for anyone who lives near the lakes or visits them for recreation, and who has beyond average curiosity about their geological and natural history, shoreline topography, weather patterns, water characteristics, reef features, fish and bird life, wetlands, and pollution status.

In the Schwab and Bennett (1987) investigation, currents measured at 28 moorings in Lake Erie during May through October 1979, were low-pass filtered to remove energy at diurnal, inertial, and higher frequencies. The current meter observations were interpolated to a regular grid over the lake. In addition, a numerical, time-dependent, barotropic, rigid-lid circulation model was run using winds from six meteorological buoys on the lake as the forcing function. Twelve 5-day storm cases were selected for detailed Lagrangian analysis. They also showed how numerical models and the objective analysis technique could be used to design more effective instrument deployment schemes for measuring lake and ocean circulation patterns.

In Simon's (1976) paper, "A numerical model of Lake Erie used to compute water transports throughout the 1970 shipping season on the basis of continuous wind observations from six shore stations", a vertically integrated model was used for quasi-homogeneous conditions, and a two-layer model was employed to simulate summer stratification. The computed water circulations were retained for a study of the horizontal distribution of various chemical parameters measured by regular ship cruises on the lake during this period. Computed surface elevations were compared with observed

water level data to verify the model calculations and to adjust the wind stress coefficient from month to month. The results showed the feasibility of quasi-operational applications of a model of the present type for computing the necessary water transport information for ecosystem modelling and water resources planning.

Because of its size and geometry, the central basin of Lake Erie is subject to periods in the late summer when dissolved oxygen concentrations are low (hypoxia). The International Field Years for Lake Erie (IFYLE) project of the Great Lakes Environmental Research Laboratory (GLERL, a U.S. National Oceanic, and Atmospheric Administration (NOAA) laboratory), was established in 2005 in response to this increase. This project was investigating the causes and consequences of hypoxia in the lake. As part of the effort, scientists from the United States and Canada conducted an extensive field study in 2005 to gather more information on the duration and extent of the hypoxic zone and its effects on the biota in the lake, (Beletsky et al., 2013).

The Michigan Great Lakes Wind Council developed a set of criteria to identify areas of Michigan Great Lakes that are "most" and "least" favorable for offshore wind energy development, in June 2010. They were looking for areas with water depth of 45 m or less. They identified five wind resource areas that are most appropriate for offshore wind energy: Southern Lake Michigan, Northern Lake Michigan, central Lake Superior, central Lake Huron and Southern Lake Huron, (Michigan Great Lakes Wind Council, 2010).

In 2010, AWS Truewind on behalf of the New York State Energy Research and Development Authority, (NYSERDA) prepared a study. The project assessed the feasibility of offshore wind development in New York's Great Lake Waters and identified the major areas of study associated with development. The project approach consisted of a desktop investigation of parameters affecting the feasibility of offshore wind development in New York's Great Lakes waters. The investigation relied on existing data sources describing the states coastal and offshore resources, the documented

experiences of others with offshore development, and the characteristics of offshore wind energy technology. The study was intended to assess the general feasibility of offshore wind energy development in the vicinity of the Great Lakes coastline, addressing various physical, technical, environmental, regulatory and commercial considerations. The assessment acknowledges some of the Great Lakes' unique characteristics relative to offshore experience elsewhere, such as lake ice development in winter and construction vessel size limitations, (AWS Truewind, 2010).

In April 2005, Pryor et al. worked on the Michigan Renewable Energy Program (MREP) project titled "offshore wind energy development in the Great Lakes", they did the primarily assessment of the potential for offshore wind energy in Great Lakes.

Our study adds another model and investigates a specific topic – wind farm impacts. COHERENS also has potential for chemical and biological modelling and this will be investigated further in the future.

CHAPTER TWO

DESCRIPTION OF THE NUMERICAL MODEL

Full details of the COHERENS "modelling system for shallow waters" V 2.11 are available from the ROYAL BELGIAN INSTITUTE OF NATURAL SCIENCES web site, including the manual (http://odnature.naturalsciences.be/coherens/manual). The COHERENS model is freely available and is released under the "European Union Public Licence" (EUPL). Specifically, "The model is available as a free source code for the scientific community following the GNU General Public License principles and can be considered as a tool for a better understanding of the physical and ecological processes and for the prediction and monitoring of waste material in shelf seas, the coastal zone and estuaries."

In this chapter, we provide some of the model details, based mostly on the material in the COHERENS manual. The material in this chapter is not our own, original work, but is included here, in a selected and condensed form, for the convenience of the reader.

The reason for using COHERENS in our simulation is that it is reliable software, producing interesting results. It has been used in the North Sea simulation by European researchers. From a personal, practical viewpoint, an earlier version of COHERENS was used previously in my master project and thesis (3D simulation of the thermal structure and hydrodynamics of Chabahar Bay, 2008). Furthermore, our simulation results can be compared with other simulated results done by different people such as Canadian Centre for Inland Waters (using ELCOM model) and/or Beletsky et al., (using POM model) as support for the performance of all three models.

2.1 COHERENS (Coupled Hydrodynamical-Ecological model for Regional and Shelf sea)

This work focuses on quantifying the impact of wakes within and downwind of wind farms on mixing, circulation and the thermal structure of Lake Erie. To run this simulation we used COHERENS numerical software. COHERENS (Coupled Hydrodynamical-Ecological model for Regional and Shelf sea) is a three-dimensional hydrodynamic multi-purpose model for coastal and shelf seas, which resolves mesoscale to seasonal scale processes. The program has been developed by a multinational European group over the period of 1990-1998. The first version was released in April 2000 and the second version in 2006. Important advantages of the model are its modular structure and flexibility because of the possibility to select different processes, specific scheme or different types of forcing for a particular application. The code has been written in FORTRAN 90 and uses σ-coordinate in the vertical direction. The model equations are discretized on an Arakawa C-grid, (Luyten, 2012).

2.2 Model Description

Physical Model:

The coordinate units can be either Cartesian (x, y, z) or spherical (λ, φ, z), with the z-axis directed upwards along the vertical. Our application used the vertical coordinate such that the surface z = 0 corresponds to the mean lake water level. This gives

$z = \zeta(x, y, t)$ or $z = \zeta(\lambda, \varphi, t)$ at the free surface (2.1)

$z = -h(x, y)$ or $z = -h(\lambda, \varphi)$ at the bottom (2.2)

Where ζ is the lake surface elevation and h the mean water depth so that the total water depth H is given by $H = h + \zeta$. For our size-limited area, the Earth's curvature is negligible and the Coriolis frequency can be considered as uniform in space. The σ-coordinate is defined by (Phillips, 1957)

$$\sigma = (z + h) / H \quad = (z + h) / (h + \zeta) \tag{2.3}$$

Where σ varies between 0 at the bottom and 1 at the surface. The grid spacing in the vertical becomes

$$\Delta z = H \, \Delta\sigma \tag{2.4}$$

The spacing of vertical σ-points Δσ are horizontally uniform but can be taken as either uniform or non-uniform in the vertical. Advantages are:

• Much simpler boundary conditions at the surface and bottom

• A better resolution of surface and bottom layers

Different types of horizontal grid are available,

1: uniform rectangular (i.e. non-curvilinear) grid. In the Cartesian case, the grid lines are equidistant in the X- and Y-direction, but Δx (distance in the X-direction) may differ from Δy. In the spherical case, the coordinate lines are latitude and longitude circles, but $\Delta\lambda \neq \Delta\varphi$ in general.

2: non-uniform rectangular grid, with Δx (x) and Δy (y), or Δλ (λ) and Δφ (φ).

3: curvilinear (i.e. non-rectangular) grid. In that case, the grid spacing depends on both horizontal coordinates. Without loss of generality, the distance between two grid lines in curvilinear coordinates can be set to 1.

2.3 Basic Model Equations

There are three main assumptions used in the model:

1. The Boussinesq approximation which means that the density is constant except when coupled with the Earth's gravitational force.

2. Hydrostatic balance

3. The horizontal component of the Earth's rotation vector is set to zero. (Except for non-hydrostatic water masses or near equator zones).

The equations for the "3D" mode in Cartesian coordinates consist of the continuity equation, the momentum equations and the equations of temperature. It worth noting that many of the COHERENS equations involve salinity but because the salinity of Lake Erie is set to zero in our application so the salinity equations are not included here.

$$\partial u/\partial x + \partial v/\partial y + \partial w/\partial z = 0 \quad (2.5)$$

$$\partial u/\partial t + u\,\partial u/\partial x + v\,\partial u/\partial y + w\,\partial u/\partial z - fv = -(1/\rho_0)(\partial p/\partial x) + F^t_x + (\partial/\partial z)(\nu_T\,\partial u/\partial z) + (\partial/\partial x)\,\tau_{xx} + (\partial/\partial y)\,\tau_{xy} \quad (2.6)$$

$$\partial v/\partial t + u\,\partial v/\partial x + v\,\partial v/\partial y + w\,\partial v/\partial z + fu = -(1/\rho_0)(\partial p/\partial y) + F^t_y + (\partial/\partial z)(\nu_T\,\partial v/\partial z) + (\partial/\partial x)\,\tau_{yx} + (\partial/\partial y)\,\tau_{yy} \quad (2.7)$$

$$\partial p/\partial z = -\rho g \quad (2.8)$$

$$\partial T/\partial t + u(\partial T/\partial x) + v(\partial T/\partial y) + w(\partial T/\partial z) = (1/\rho_0\, c_p)(\partial I/\partial z) + (\partial/\partial z)(\lambda_T\,\partial T/\partial z) + (\partial/\partial x)(\lambda_H\,\partial T/\partial x) + (\partial/\partial y)(\lambda_H\,\partial T/\partial y) \quad (2.9)$$

where (u, v) are the horizontal components of the current, w the vertical current, f the Coriolis frequency given by $2\Omega\sin\varphi$ where $\Omega = \pi/43082$ radians/s, is the Earth's rotation frequency, p the pressure (pressure is defined as the pressure minus its homogeneous hydrostatic part, i.e. $P = p + \rho_0 g(z - \zeta) - P_a$.), reference atmospheric pressure P_{ref} (P_a) is 101325.0 pa. ρ the density, ρ_0 a uniform reference density, g the acceleration of gravity, (F^t_x,F^t_y) the components of the astronomical tidal force, ν_T and λ_T the vertical turbulent diffusion coefficients, τ_{ij} the horizontal friction tensor, T potential temperature, I the solar irradiance within the water column and c_p the specific heat capacity of lake water at constant pressure. To remove the compressibility term in the temperature equation T is the potential temperature, defined as the temperature of a fluid parcel, moved adiabatically to a certain level (usually near the surface).

Since the model does not allow for the formation of ice at the surface, the temperature must stay above the freezing point of lakewater, i.e. $T > \alpha_f S$ (2.10)

Where $\alpha_f = -0.0575$ °C/PSU and S is salinity (which is zero in our application). The horizontal diffusion coefficient $\nu_H = C_m \Delta x \Delta y (D_T^2 + D_S^2)^{1/2}$ (2.11)

And the scalar coefficient $\lambda_H = C_s \Delta x \Delta y (D_T^2 + D_S^2)^{1/2}$ (2.12)

Which D_T and D_S are the horizontal tension and shearing strain

$D_T = \partial u/\partial x - \partial v/\partial y$ (2.13)

$D_S = \partial u/\partial y + \partial v/\partial x$ (2.14)

The coefficients C_m and C_s usually have the same value of the order of 0.1-0.2. The model assumes that "horizontal" diffusion of momentum and scalars takes place along horizontal planes. ν_T and λ_T are considered as vertical diffusion coefficients. Since $\nu_T \ll \nu_H$ and $\lambda_T \ll \lambda_H$, then horizontal mixing scheme may produce an excessive diapycnal diffusion in the presence of lateral fronts. Complex schemes for isopycnal mixing have been developed and applied to global ocean models, but as COHERENS is primarily developed for coastal and regional seas, these schemes are not implemented in this model. The absorption of solar irradiance within the water column is generally a function of solar wavelength and the penetration depth of solar light. According to Paulson & Simpson (1977),

$I(x_1, x_2, z) = Q_{rad} (R\, e^{-z/\lambda 1} + (1 - R)\, e^{-z/\lambda 2})$ (2.15)

Where R represents the fraction in the red end of the solar spectrum where is absorbed primarily in the upper (1–2) meters of the water column, the fraction 1−R of blue-green light penetrates to larger depths. The solar radiance incident on the surface is Q_{rad}. Since turbidity effects are not explicitly taken into account by the physical model, values of R, λ_1, $\lambda_2 \gg \lambda_1$ depend on the optical properties of the water masses, (Luyten, 2012).

Solar radiation is absorbed within a column using a $\lambda_1^{-1} = 10.0$ m and $\lambda_2^{-1} = 0.067$ m which are inverse optical attenuation depths for absorption of long-wave and short-wave solar radiation, respectively. The infrared fraction of irradiance absorbed at the lake surface is 0.54.

2.3.1 2D Mode Equations

In depth-averaged mode it is assumed that the 3D current and all 3D scalar quantities are depth-independent, so w=0. There are additional 2D equations for the depth-integrated current and surface elevation. The reason is that the surface elevation appearing in the momentum equations cannot be determined from 3D equations only and also the numerical solution of the 3D equations are constrained by the CFL limit which poses a severe limit on the time step used in the numerical discretization. Mode splitting techniques, which use smaller 2D time step, can resolve this problem, (Luyten, 2012).

2.3.2 1D Mode Equations

In case of a water column application, the horizontal grid reduces to one point so advection, horizontal diffusion, and horizontal pressure gradient are neglected and the vertical current is no longer calculated, (Luyten, 2012).

2.4 Turbulence Schemes

The objective of a turbulence scheme is to parameterize the effects of turbulent motions. It is assumed that turbulence is fully developed and in a quasi-equilibrium state. The main characteristics can be described as follows (Ferziger, 2005; Kantha & Clayson, 2000a):

• Three-dimensional. In contrast to the mean flow, which may be two-dimensional, turbulent motions are fully three-dimensional. This definition excludes the two-dimensional turbulence of geophysical flows on the mesoscale, which is parameterized by a horizontal mixing scheme.

• Randomness. Turbulence has a “short-time” memory. This means that turbulent states arising from slight changes in initial, boundary or forcing conditions become uncorrelated in time within short time intervals. Therefore, the only meaningful way to analyze turbulence is through its statistical properties.

• Broad spectrum. Turbulent motions span a large spectrum of scales in space and time.

• Vorticity. In contrast to waves, turbulent motions are characterized by random vorticity fluctuations. This explains why turbulence can be visualized in laboratory experiments as a spectrum of eddies on different spatial scales. On the largest scales, eddies extract energy from the mean flow, whereas on the shortest (so-called Kolmogorov) scales this energy is converted into heat by molecular dissipation.

The spatial scales of turbulence, which need to take into account in models for the ocean, shelf seas or coastal areas, range from 10^{-3} to 10^{2} m and are not resolved by the model except eventually for the largest ones. Turbulence schemes need to be developed based upon the statistical properties of the turbulence spectrum. Starting point are the Navier-Stokes equations and the equations of continuity and temperature. Despite the similarity with laminar flows, there are fundamental differences between turbulent and laminar diffusion:

• For fully developed turbulence, ν_T and λ_T are larger than their laminar counterparts by several orders of magnitude.

• The turbulent diffusion coefficients are of the same order of magnitude whereas the molecular coefficients for momentum, T is of the order of $(\nu, k_T, k_S) \sim (10^{-6}, 10^{-7}, 10^{-9})$ m^2/s.

• Turbulence is initiated by instabilities of the mean flow. This means in practice that ν_T and λ_T are not constant but depend on the mean flow properties generating and controlling those instabilities, i.e. the current shear $\partial U_i/\partial x_j$ and the density gradient $\partial \rho/\partial x_i$.

The turbulence models, implemented in COHERENS, fall in three categories of increasing complexity:

1. The simplest formulation is to set the diffusion coefficients to constant values ν_T and λ_T = constant, where ν_c and λ_c are set by the user. Despite its simplicity, it is recommended not to use this form. Turbulence usually occurs in the surface and bottom boundary layers, which requires spatially varying coefficients.

2. Empirical Algebraic Scheme: Models using simplified empirical or semi-empirical (algebraic) relations not derived from a turbulence closure theory.

3. RANS Scheme: Models obtained from the Reynolds averaged Navier-Stokes (RANS) equations. These models are physically more robust but have a larger computational overhead.

The first option is not recommended, and for the algebraic schemes, there are two schemes of either a Richardson number dependent or flow dependent. Finally, by choosing RANS scheme the user can choose the k-ε and k-l scheme. In the k-l theory, all equations are written explicitly as a function of k and l, where l is the mixing length and can be calculated from either parabolic or quasi-parabolic law or Xing and Davis or Blakadar formulation. k is the turbulence kinematic energy (J/kg) obtained from k = 1/2 ($\bar{u}^2 + \bar{v}^2 + \bar{w}^2$) and ε is the dissipation rate in W/kg, (Luyten, 2012).

2.5 Solar Radiation

The radiation entering at the top of the atmosphere is given by

$$Q_s = Q_0\, p_{cor}\, H\, (\sin \gamma_\odot) \tag{2.16}$$

Where Q_0 = 1367.0 W/m^2, is the solar constant, $\gamma_\odot$ the altitude of the sun (elevation angle), H the Heaviside function (H(x) = 0 for x < 0 and = 1 otherwise), and p_{cor} a correction term due to the elliptical orbit of the earth. Taking account of absorption by the atmosphere, the direct solar radiation incident on the lake surface is given by

$$Q_{dir} = Q_s\, e^{-\tau} \tag{2.17}$$

Where optical depth τ is the function of solar altitude $\gamma_\odot$ in degrees.

$$Q_{dif} = ((1 - A_\alpha)\, Q_s - Q_{dir}) / 2 \tag{2.18}$$

Where the value of 0.09 for the water vapor and ozone absorption coefficient A_α is considered. Q_{dif} is the diffuse sky radiation, which assumes that one-half of the scattered radiation reaches the lake

surface, and the total radiation flux (Q_{cs}) at the lake surface under clear sky condition is the sum of Q_{dif} and Q_{dir}. The short wave radiation flux at the lake surface then finally takes the form

$$Q_{rad} = Q_{cs}\,(1 - 0.62\,f_c + 0.0019\,\gamma_{\odot,\,max})\,(1 - A_s) \qquad (2.19)$$

Where $\gamma_{\odot max}$ is the solar altitude at noon. A constant value of 0.06 is assumed for the lake surface albedo (A_s), and f_c is the fractional cloud cover that needs to be supplied externally, (Luyten, 2012).

2.6 Water Surface Boundary Condition

Can be either Neumann or Dirichlet type.

2.6.1 Currents:

The surface condition for horizontal current (u, v), is obtained by specifying the surface stress as a function of the wind components

$$(\rho_0\,\nu_T/h_3)\,(\partial u/\partial s\,,\,\partial v/\partial s) = (\tau_{s1},\,\tau_{s2}) = \rho_a\,C_{ds}\,W_{10}\,(U_{10},\,V_{10}) \qquad (2.20)$$

Where (U_{10}, V_{10}) are the components of the wind vector at a reference height of 10 m, $W_{10} = (U_{10}^2 + V_{10}^2)^{1/2}$ is the wind speed, ρ_a = 1.2 kg/m^3 the air density and C_{ds} the surface drag coefficient. The boundary condition for the transformed vertical velocity takes the simple form $\omega = 0$, (Luyten, 2012).

2.6.2 Temperature

The surface boundary condition for temperature can either be taken as a Dirichlet condition in which case T_s is specified directly at (or near) the surface or a Neumann condition in which case the surface flux of temperature is given as

$$(\rho_0\,c_p\,/\,h_3)\,(\lambda_T\,\partial T/\partial s) = Q_s \qquad (2.21)$$

Where Q_s is the downwards directed heat flux at the surface and c_p the specific heat of lake water at constant pressure. The net total heat flux into the water column is composed of a term $-Q_{nsol}$ of all non-solar contributions plus the radiative flux Q_{rad}.

$$Q_{nsol} = Q_{la} + Q_{se} + Q_{lw} \qquad (2.22)$$

Where Q_{la} is the latent heat flux released by evaporation, Q_{se} the sensible heat flux due to the turbulent transport of temperature across the air/lake interface and Q_{lw} the net long-wave radiation emitted at the lake surface. Both Q_{la} and Q_{se} are functions of air density and wind. Also, are function of specific humidity and air temperature, respectively. The long-wave radiation flux term is parameterised as

$$Q_{lw} = \epsilon_s \, \sigma_{rad} \, (T_s + 273.15)^4 \, (0.39 - 0.05 \, e_a^{1/2}) \, (1 - 0.6 \, f_c^2) \quad (2.23)$$

where $\epsilon_s = 0.985$ is the emissivity at the lake surface, $\sigma_{rad} = 5.67 \times 10^{-8}$ W m^{-2} K^{-4} is Stefan's constant, f_c the fractional cloud cover (between 0 and 1) and e_a the vapour pressure in hecto Pascal.

Heat flux is composed of two components, sensible and latent. Sensible heat flux is controlled by temperature fluctuation correlations with velocity, and the near-surface is in part governed by molecular thermal diffusion across a thin layer. The thickness of the viscous layer is inversely dependent on u_* over a long average, but locally it depends on the local velocity shear along the phase of propagating surface waves. When waves break, the viscous layer destroys, thus accelerating the heat exchange. The heat exchange caused by the difference of temperature between sea spray and the ambient air provides an additional small contribution to the heat exchange, in particular during high wind speed. The latent heat exchange governs by the rate of surface evaporation or condensation, which in turn is dependent upon the humidity gradient. Similar to the sensible heat flux, there is substantial heat exchange due to evaporation of sea spray during high wind events. Short wave solar radiation substantially depends on the latitude of the lake and on the cloudiness, with the former presenting a rather regular annual trend and the latter being important mainly at short time scales (from hourly to weekly), (Piccolroaz et al., 2013).

2.7 Generalized σ-coordinates

Instead of using the traditional σ-coordinate a generalized vertical "s" coordinate can be defined by $z = F(x_1, x_2, s, t)$ (2.24)

With $(x_1, x_2) = (x, y)$, (λ, φ) or $(\xi_1, \xi 2)$ which are called orthogonal curvilinear coordinates. This means geometrically that the coordinate curve along which ξ_1 is a constant intersects the curve along which ξ_2 is constant orthogonally. And s = 0 at the bottom and s = 1 at the surface, (Figures 2.1 and 2.2), so that $F(x_1, x_2, 0, t) = -h$, $F(x_1, x_2, 1, t) = \zeta$ (2.25)

Which means h and ζ depend on x (x_1), y (x_2) and t.

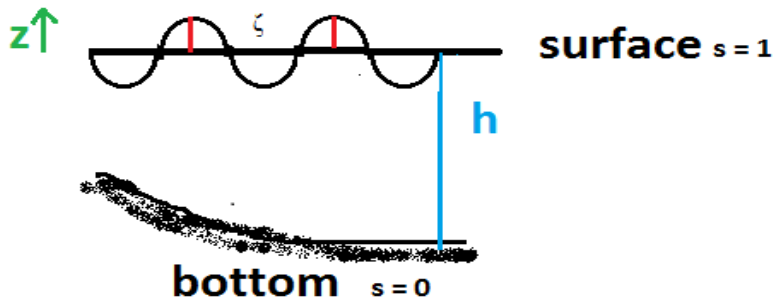

Figure 2.1: generalized vertical "s" coordinate.

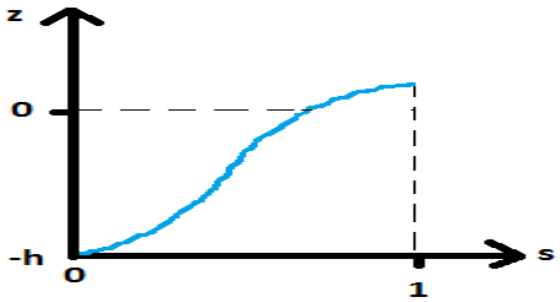

Figure 2.2: "z" versus vertical "s" coordinate.

The vertical grid spacing now becomes $\Delta z = (\partial F/\partial s)\, \Delta s = h_3 \Delta s$ (2.26)

Song and Haidvogel (1994) related the s-coordinate to the σ-coordinate by letting

$F = sH - h + hF_*(x_1, x_2, s)$, $F_*(x_1, x_2, 0) = F_*(x_1, x_2, 1) = 0$ (2.27)

Equation (2.26) is re-written as $h_3 = H + h\, (\partial F_*/\partial s) = H\, (1 + (h/H)\, \partial F_*/\, \partial s) \simeq H\, (1 + \partial F_*/\partial s)$ (2.28)

Where the approximation is made that h ≃ H. The assumption is reasonable since the s-coordinate is designed for non-shallow areas with large bathymetric gradients, such as shelf breaks. The s-coordinate, defined by (2.27) is related to the σ-coordinate by

$$\sigma = s + (h/H)\, F_*(x_1, x_2, s) \simeq s + F_*(x_1, x_2, s) \quad (2.29)$$

And $$\Delta\sigma = \Delta z/H \simeq (1 + \partial F_*/\partial s)\, \Delta s \quad (2.30)$$

Which means that the Sung-Haidvogel s-coordinate can be seen as a generalized σ-coordinate with non-uniform spacing in the horizontal if $F_* \neq 0$. The new coordinate should be defined so that it can represent surface and bottom layers in shallow as well as deep waters and can deal with areas with a steep topography. Song & Haidvogel (1994) proposed the following expression for F∗(s):

$$F*(x_1, x_2, s, t) = \max [0, ((h - h_c) / h)\, (C(s) + 1 - s)] \quad (2.31)$$

$$C(s) = [(1 - b) \sinh [\theta(s - 1)] / \sinh \theta] + (b/2)\, [(\tanh [\theta(s - 0.5)] / \tanh (0.5\theta)) - 1]$$

(2.32) where h_c is a critical water depth below which the s-coordinate reduces to the σ-coordinate and b and θ are tunable parameters. The vertical grid is defined by taking uniformly spaced s-levels, i.e. $s_k = (k - 1)/N$, k = 1,N + 1 and calculating the corresponding generalised σ-levels using (2.27).

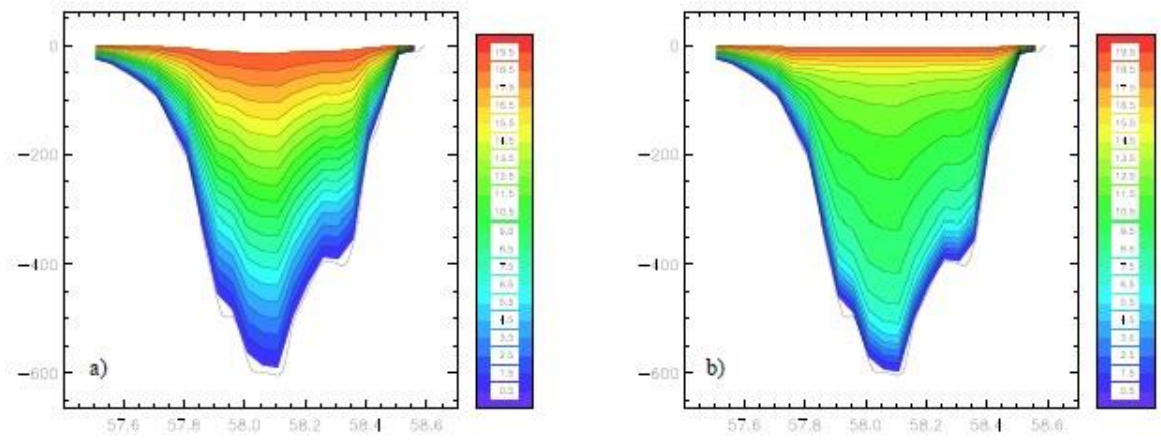

Figure 2.3: Distribution of vertical levels along transect from Denmark to Norway: (a) uniform σ-coordinates, (b) non-uniform σ-coordinates (s-coordinate). [Luyten, 2012]

Figure 2.3 compares the distribution of vertical levels for a uniform σ-spacing with the s-coordinate. While the σ-coordinate provides an accurate resolution in the shallow waters near the Danish coast (left side of the Figure 2.3), the layer thickness is ~30 m in the deepest part that is clearly insufficient. A (vertically) non-uniform σ-grid will not resolve the problem since any improvement for the deepest parts will deteriorate the solution in the coastal areas, which have very shallow depths. The s-coordinate has a much more accurate resolution near top and bottom in deep water as seen in the Figure 2.3 on the right and reduces to the σ-coordinate when $h < h_c$ near the coasts, where h_c is a critical water depth (0.1 m), below which the s-coordinate reduces to the σ-coordinate.

Note that spherical coordinates can be considered as "pseudo"-curvilinear coordinates with respect to Cartesian coordinates with $h_1 = R\cos\varphi$ and $h_2 = R$, where R is the mean radius of the Earth, defined as the radius of a sphere having the same volume as the Earth or 6371 km. In practice $\Delta\xi_1$, $\Delta\xi_2$ are both normalized to 1, so that the metric coefficients h_1, h_2 now become the grid spacing along the curvilinear coordinate lines, (Luyten, 2012).

2.8 Water Bottom Boundary Condition

A slip boundary condition is applied at the grid point nearest to the bottom for the current, which takes the form

$$(\nu_T/h_3)\,(\partial u/\partial s\,,\ \partial v/\partial s) = (\tau_{b1}, \tau_{b2}) \tag{2.33}$$

Where

$$(\tau_{b1}, \tau_{b2}) = C_{db}\,(u_b^2 + v_b^2)^{1/2}\,(u_b, v_b) \tag{2.34}$$

Where the bottom currents (u_b, v_b) are evaluated at the grid point nearest to the bottom.

$$C_{db} = (\kappa/\ln(z_r/z_0))^2 \tag{2.35}$$

Where z_r is a reference height taken at the grid centre of the bottom cell. The value of z_0, which may vary in the horizontal directions, depends on the geometry and composition of the lakebed. In analogy with the surface condition, the bottom value of the vertical velocity equals zero, i.e. $\omega = 0$. The bottom boundary conditions for temperature is obtained by considering a zero flux normal to the lakebed:

$\lambda_T / h_3 (\partial T/\partial s) = 0$ (2.36)

It is remarked that the non-allowance of any heat exchange at the bottom interface may not be realistic but is only imposed in the absence of a useful parameterization which takes account of a bottom exchange (e.g. release of geothermal energy), (Luyten, 2012).

2.9 Numerical Model

Conservative finite differences (equivalent to finite volume techniques for the Cartesian mesh) are used to discretize the mathematical model in space. The grid chosen for horizontal discretization is the well-known Arakawa "C" grid (Mesinger & Arakawa, 1976) which staggers the currents and pressure /elevation nodes to give a good representation of the crucial gravity waves and provides simple representations of open and coastal boundaries. As discussed in previous sections the model equations are solved on a rectangular or a curvilinear grid in the horizontal and σ- or an extended σ-coordinate grid in the vertical, whereby varying surface and bottom boundaries are transformed into constant surfaces. The σ-coordinate provides for accurate representation of surface and bottom boundary processes. It also results in an equal number of cells in each vertical water column.

Two options are available to solve the hydrodynamic equations. The original implementation in COHERENS used the mode-splitting technique as in the model of Blumberg & Mellor (1987) to solve the momentum equations. This method consists in solving the depth-integrated momentum and continuity equations for the "external" or barotropic mode with a small time step to satisfy the stringent Courant-Friedrichs-Lewy (CFL) stability criterion for surface gravity waves, and the 3D momentum and scalar transport equations for the "internal" or "baroclinic" mode with a larger time step.

Total Variation Diminishing (TVD) (Roe, 1986; Sweby, 1984), and upwind schemes are available for the advection of momentum and scalars, to reduce the programming and computational overhead. A TVD scheme (which is used in our simulation), is implemented with the symmetrical operator

splitting method for time integration and can be considered as a useful tool for the simulation of frontal structures and areas with strong current gradients. The upwind scheme, on the other hand, is only first order accurate and therefore more diffusive, and should be used only if CPU time is considered of more importance than accuracy, (Luyten, 2012).

2.10 Grid Nodes and Indexing System

Figures 2.4 and 2.5 show the horizontal layout of the C-grid domain as it appears in curvilinear coordinates (ξ_1, ξ_2). A normalization is applied so that $\Delta\xi_1=\Delta\xi_2=1$. For convenience, the notations X and Y will be used for ξ_1 and ξ_2.

• C-nodes (empty circles): located at the centres of the grid cells, used for 2D and 3D scalar quantities (elevations, water depths) and wind components.

• U-nodes (horizontal bars): at the centres of the left (West) and right (East) cell faces, used for the X-components of vectors except the surface wind (transports, depth-mean currents, bottom stress).

• V-nodes (vertical bars): at the centres of the lower (South) and upper (North) cell faces, used for the Y-components of vectors except the surface wind (transports, depth-mean currents, bottom stress).

• UV-nodes (solid circles): at the corners of the grid cells, used for the horizontal coordinate arrays which determine the geographical location of the grid.

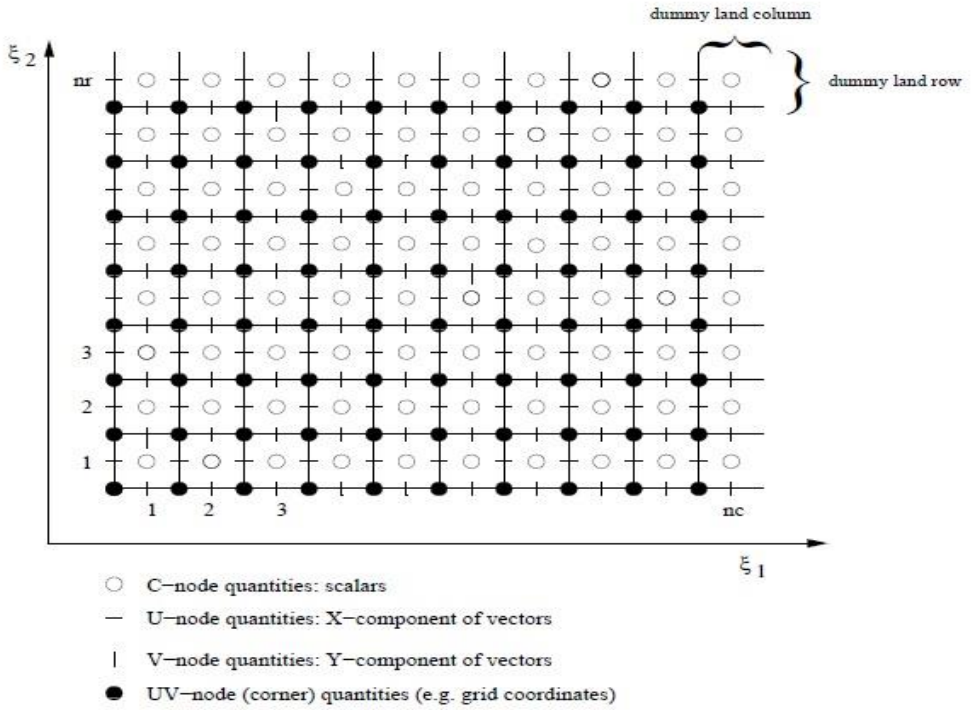

Figure 2.4: Layout of the (global) computational grid in the horizontal. [Luyten, 2012]

Each horizontal grid cell has an index, generally denoted by 'i', in the x-direction between 1 and nc (number of grid cells in the x-direction) and an index ('j') in the y-direction between 1 and nr (number of grid cells in the y-direction).

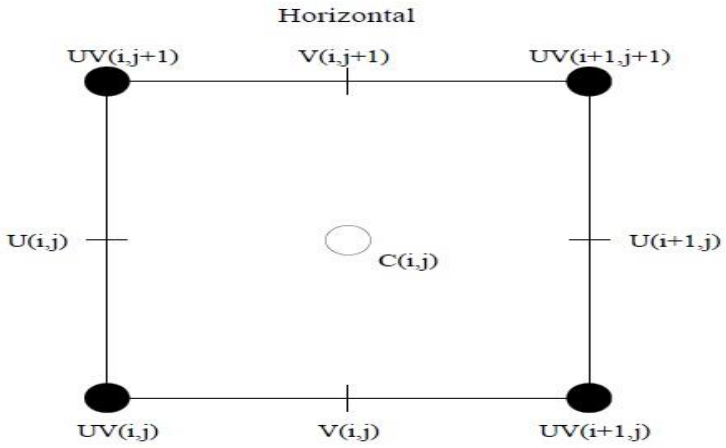

Figure 2.5: Grid indexing in the horizontal plane. [Luyten, 2012]

In the C-node, grid points with x-index nc or y-index nr have to be declared as spurious dry cells. This means in practice that, whereas the computational size of the domain is nc × nr, the physical size is (nc-1) × (nr-1). In analogy with the horizontal directions, a staggered grid is used in the vertical as well. The water column is divided into nz layers. The layers, which in transformed vertical coordinates have equal sizes, are illustrated in Figure (2.6). C-nodes are vertically located at the midst of each layer.

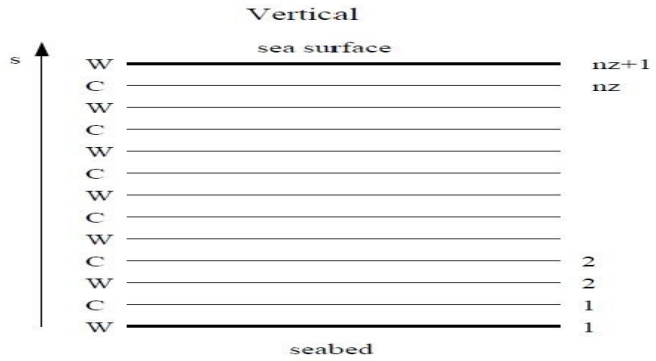

Figure 2.6: Layout of the computational grid in the vertical. [Luyten, 2012]

The vertical position of a 3D model variable is determined by the vertical (z-) index ("k") which varies between 1 and nz for C-node. The grid indexing system for the full 3D mode is shown in Figure (2.7). The lower bound of all grid indices is 1; the upper boundary depends on the nodal type and on whether it is taken along the computational or physical domain, (Luyten, 2012).

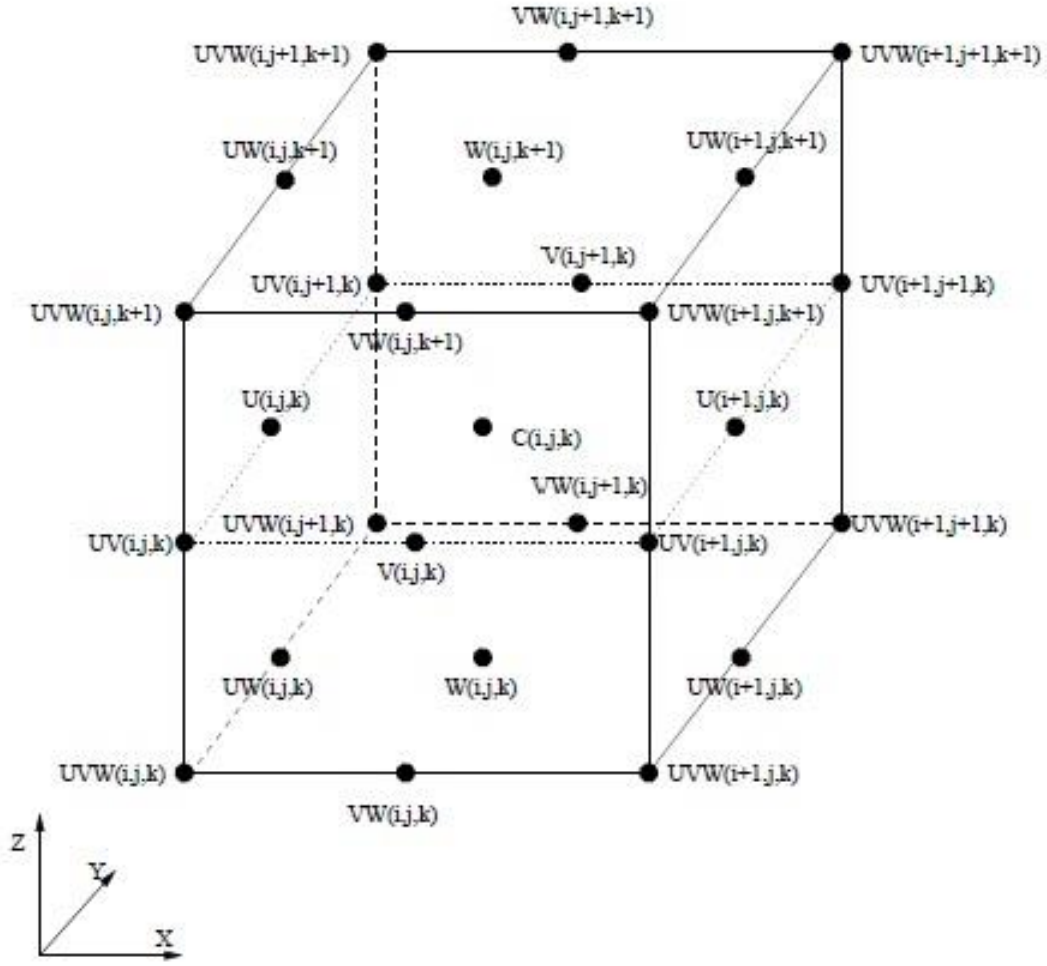

Figure 2.7: Grid indexing in three-dimensional space. [Luyten, 2012]

2.11 Time Discretization

In case a mode-splitting technique is used (Blumberg & Mellor, 1987), separate time steps are taken for the 2D "external" barotropic equations ($\Delta\tau$) and the "internal" baroclinic equations (Δt). The 2D time step ($\Delta\tau$) has to be small enough to satisfy the Courant-Friedrichs-Lewy (CFL) criterion. The 3D time step is a multiple, M_t, of $\Delta\tau$ (typically of the order of 10-20) and the model is integrated forward in time for N_t baroclinic time steps (equal to $N_t M_t = M_{tot}$ barotropic time steps). From stability analysis for linear-surface gravity waves

$$\Delta\tau \leq \Delta h_{min} / 2\sqrt{(g\, h_{max})} \quad (2.39)$$

$$\Delta t \leq \Delta h_{min} / 2\sqrt{(g'\, h_{max})} \quad (2.40)$$

Where $\Delta h_{min} = \min(h_1, h_2)$ is the minimum horizontal grid spacing, $g' = g\,\Delta\rho/\rho_0$ the reduced gravity, h_{max} the maximum water depth and $\Delta\rho$ a typical value for the vertical density difference. Since $g' \ll g$ the second condition is less constraining than the first one. A more stringent condition for the 3-D mode, imposed by the explicit schemes for horizontal advection, is that the horizontal distance traveled by a fluid element during the internal time step Δt must be smaller than the grid spacing, or

$$(u\,\Delta t / h_1, v\,\Delta t / h_2) \leq 1 \quad (2.41)$$

All horizontal derivatives are evaluated explicitly while vertical diffusion is computed fully implicitly and vertical advection quasi-implicitly, (Luyten, 2012).

2.12 1D model Set up

A simulation is done which describes the evolution of a wind-driven surface mixed-layer. This simulation takes account the effects of wind and seasonal stratification. We have investigated the formation of the thermocline during the summer in three different depths of water. The model is forced using realistic meteorological data. To limit CPU time on the first round of computer run, the annual cycle of thermal stratification simulation is performed with the 1D (water column) version of the program so that advection effects are ignored. The initial state consists of a water column at rest with a stable stratification in the vertical using a constant density gradient. The density equation is derived from the McDougall et al. (2003), general equation of state (2.42-2.44) without considering the pressure effects.

$$\rho(S, T, p) = P_1(S, T, p) / P_2(S, T, p) \quad (2.42)$$

$$P_1 = a_0 + a_1T + a_2T^2 + a_3T^3 + a_4S + a_5ST + a_6S^2 + a_7p + a_8pT^2 + a_9pS + a_{10}p^2 + a_{11}p^2T^2 \quad (2.43)$$

$$P_2 = 1 + b_1T + b_2T^2 + b_3T^3 + b_4T^4 + b_5S + b_6ST + b_7ST^3 + b_8S^{3/2} + b_9S^{3/2}T^2 + b_{10}p + b_{11}p^2T^3 + b_{12}p^3T \quad (2.44)$$

Contrary to potential temperature (T) and salinity (S), the density is not obtained by an additional transport equation but by means of an equation of state (EOS). The international EOS (Millero et al, 1980) relates the density to the three state variables T, S and P, where S is considered 0 in fresh water, (Jacket & McDougall, 1998). With a precision of 0.003 kg/m^3 the density is given by (2.42) where P_1 and P_2 depend on T, S, ρ, a and b which the two latter are empirical parameters. Neglecting density variations in the water column and atmospheric pressure, P can be approximated by

$$p \simeq -\rho\, g\, (z - \zeta) \quad (2.45)$$

The expansion coefficient for temperature is

$$\beta_T = (-1/\rho)\,(\partial\rho/\partial T) = (1/P_2)\,(\partial P_2/\partial T) - (1/P_1)\,(\partial P_1/\partial T) \quad (2.46)$$

The RANS model with limiting conditions – critical Richardson number – is used in our simulation and advection is disabled. The RANS model does not take the eddy viscosity – diffusivity concept as a prior assumption. It contains unknown second and third order correlations, which need to be parameterized. The following parameterizations are adopted:

- Pressure-strain correlation.
- Pressure-buoyancy gradient correlation.
- Dissipation terms, the turbulence energy is dissipated isotopically: since the laminar diffusion scales are much smaller than the scales of the largest eddies, the laminar terms can be neglected.
- Pressure transport is neglected.

The expressions for the pressure-strain and pressure-buoyancy gradient are compiled from different sources and presented in their most general form. In our run, we use the Hossein & Radi, 1982 (HR82) source. Different schemes are available for the modelling of the third-order correlations.

They are based on the classification scheme introduced by Mellor & Yamanda (1974, 1982) and Galperin et al. (1988).

1. Non-equilibrium or "level 3" method.

2. Quasi-equilibrium or "level 2.5" method after Galperin et al. (1988). This is the same as the previous schemes except that P+G is set to ε in all equations except in the one for turbulent energy.

3. Equilibrium or "level 2" method. A full equilibrium, i.e. P + G = ε in all equations including the k-equation.

• P is a source term and equals the energy withdrawn by the "energy containing eddies" at the largest spatial scales of the turbulence spectrum

• G is a buoyancy term, which can be a sink term for stable stratification (Ri > 0) and a source term for an unstable stratification (Ri < 0).

• ε represents the rate of viscous dissipation of turbulent energy, which occurs at the smallest scales of turbulence.

For the neutral surface drag coefficient, the Charnock (1955) relation is used $z_{0s}\, g/u^2_{*s} = a$

$$C_{ds} = (\kappa / \ln (z_{0s}/10))^2 \quad (2.47)$$

Where z_{0s} is the surface roughness length, u_* the surface friction velocity and a = 0.014 Charnock's constant. Dirichlet conditions $k = u^2_{*b} / S_{u0}^{\frac{1}{2}}$, $\varepsilon = u^3_{*b} / \kappa d_b$, $l = \kappa d_b$ (2.48)

S_{u0} (0.108), is the neutral value of the momentum stability coefficient S_u.

Where $u^2_{*b} = (\tau^2_{b1} + \tau^2_{b2})^{1/2} = (S_{u0}\, k^2/ \varepsilon)\, (\partial U / \partial z) = \text{constant}$ (2.49)

Where l the mixing length is proportional to the distance d_b from the "wall" boundary.

$$l = l_1 = \kappa d_b = \kappa\, (h + z + z_{0b}) = \kappa\, (H\sigma + z_{0b}) \quad (2.50)$$

And z_{0b} a bottom roughness length is used for bottom boundary condition, and quasi-equilibrium, k-ε scheme is used in turbulence. Reference height is 10 m, reference density is 1000 kg/m^3, reference salinity is 0 PSU, and reference temperature is 4 °C. The mean depth of water is set to be either 10 m,

25 m or 60 m, and the uniform bottom roughness length is 0.01 m. The temperature field is initiated by field data gathered by Canadian Centre for Inland Waters and is updated in time. COHERENS defines the mixed-layer depth as the surface distance of the first grid point below the surface where the current is lower than one percent of its surface value. Uniform surface drag coefficient, uniform exchange coefficient for latent and sensible heat are set to 0.0013.

2.13 1D Mode Equations

The basic equations in the absence of advection and horizontal diffusion are given by

$$\partial u / \partial t - fv = (\partial / \partial z)(\nu_T . \partial u / \partial z) \quad (2.51)$$

$$\partial \rho / \partial t + fu = (\partial / \partial z)(\lambda_T . \partial \rho / \partial z) \quad (2.52)$$

$$\partial T / \partial t = (1/\rho_0 c_p)\, \partial I/\partial z + (\partial / \partial z)(\lambda_T \partial T / \partial z)$$

where z is the vertical coordinate (increasing upwards and zero at the surface), u the current, ρ the density and ν_T, λ_T the vertical eddy coefficients $f = 2 \Omega \sin \varphi$ is the Coriolis frequency, φ the latitude, T the temperature, c_p the specific heat of lake water at constant pressure and I(z, t) solar irradiance. The eddy coefficients reduce to their molecular values in the absence of turbulence.

The initial and boundary conditions are given by

$$u = 0, -(g / \rho)(\partial \rho / \partial z) = N_0^2 \quad \text{at} \quad t = 0 \quad (2.53)$$

$$\nu_T (\partial u / \partial z) = u_{*s}^2, \quad \lambda_T (\partial \rho / \partial z) = 0 \quad \text{at} \quad z = 0 \quad (2.54)$$

Where N_0 is the uniform, initial buoyancy frequency and ρ_0 a reference density. Additional assumptions are made:

- $u = 0$
- The eddy coefficients can be cast into the form

$$\nu_T = f_\nu (\xi)\, h^2 / t, \lambda_T = f_\lambda (\xi)\, h^2 / t \quad (2.55)$$

Where $\xi = -z / h_t$ (t), h_t (t) is the depth of the turbulent layer. Equations (2.51-2.54) are solved numerically with the following parameters $u_{*s} = 0.01$ m/s, $N_0 = 0.01\ s^{-1}$ (2.56)

To remove the influence of initial conditions and adjustments, the analysis is restricted to the running period so that the first few days results as a spin-up time for the model are ignored in both 1D and 3D cases. However, most of our interest is in terms of summer water temperature so spin-up time is not a major concern. A number of output parameters are defined. Their intention is primarily to compare the results with the results made by (Estuary and Lake Computer Model) ELCOM numerical model used in CCIW, the Princeton Ocean Model (POM) numerical model used by Beletsky et al. 2013 – who validated their results with the observed data sets –, and the observation and field measurements made by Environment Canada and NOAA. 1D mode enables us to compare the influence of different formulations available in the program (turbulence, boundary conditions, optic, equation of state, etc.)

CHAPTER THREE

WIND TURBINE WAKES

3.1 One-dimensional Momentum Theory and the Betz Limit

Determining the power from an ideal turbine rotor, and the effect of the rotor operation on the local wind field can be calculated and estimated by the simple Betz (1926) model. The linear momentum theory is the basis of this model. A control volume is assumed in the analysis so that the control volume boundaries are the surface of a stream tube and two cross-sections of the stream tube, (Figure 3.1). The flow is considered only across the ends of the stream tube. A uniform "actuator disc" represents a turbine and creates a discontinuity in the pressure in the stream tube of air flowing through it. The following assumptions are considered in this analysis: (Manwell, 2009)

- homogenous, incompressible, steady-state fluid flow
- no frictional drag
- an infinite number of blades
- uniform thrust over the disc or rotor area
- a non–rotating wake
- the static pressure far upstream and far downstream of the rotor is equal to the undisturbed ambient static pressure

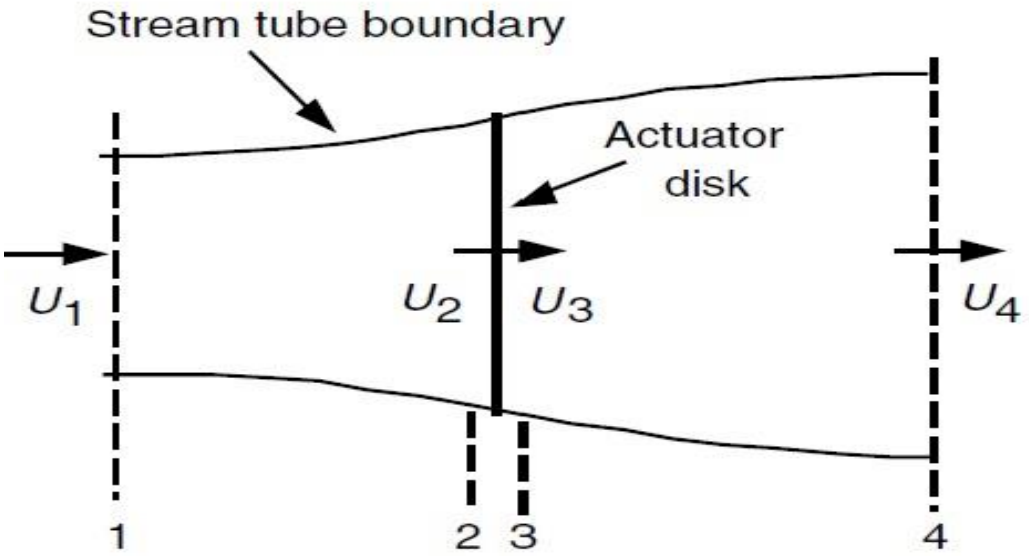

Figure 3.1: Actuator disc model of a wind turbine; U, mean air velocity; 1, 2, 3, and 4 indicate locations. [Manwell, 2009]

If the conservation of linear momentum is applied to the control volume, the net force on the contents of the control volume can be found. That force is equal and opposite to the thrust, T, which is the force of the wind on the wind turbine. From the conservation of linear momentum for a one-dimensional, incompressible, time-invariant flow, the thrust is equal and opposite to the rate of change of momentum flux of the air stream.

$$T = U_1 (\rho AU)_1 - U_4 (\rho AU)_4 \quad (3.1)$$

Where ρ is the air density, A is the cross-sectional area, U is the air velocity, and the subscripts indicate values at numbered cross-sections in Figure 3.1. For steady state flow, $(\rho AU)_1 = (\rho AU)_4 = \dot{m}$, where $\dot{m}$ is the mass flow rate. Therefore, $T = \dot{m} (U_1 - U_4)$ (3.2)

Because the thrust is considered positive the velocity behind the rotor, U_4, is less than the free stream velocity, U_1. No work is done on either side of the turbine rotor. By applying the Bernoulli function in the control volume on either side and in the stream tube downstream of the disc

$$p_1 + 1/2\ \rho U_1^2 = p_2 + 1/2\ \rho U_2^2 \quad (3.3)$$

$P_3 + 1/2\ \rho U_3^2 = p_4 + 1/2\ \rho U_4^2$ (3.4)

It is also assumed that the far upstream and far downstream pressures are equal ($p_1 = p_4$) and that the velocity across the disc remains the same ($U_2 = U_3$). The thrust can also be expressed as the net sum of the forces on each side of the actuator disc. $T = A_2 (p_2 - p_3)$ (3.5)

If one solves for $(p_2 - p_3)$ using Equations (3.3) and (3.4) and substitutes that into Equation (3.5), one obtains $T = 1/2\ \rho\ A_2 (U_1^2 - U_4^2)$ (3.6)

Equating the thrust values from Equations (3.2) and (3.6) and recognizing that the mass flow rate is also $\rho A_2 U_2$, one obtains $U_2 = (U_1 + U_4) / 2$ (3.7)

Thus, the wind velocity at the rotor plane is the average of the upstream and downstream wind speeds. If one defines the axial induction factor, *a*, as the fractional decrease in wind velocity. Between the free stream and the rotor plane, then

$a = (U_1 - U_2) / U_1$ (3.8)

$U_2 = U_1 (1 - a)$ (3.9)

$U_4 = U_1 (1 - 2a)$ (3.10)

$U_1 a$ is described as the induced velocity at the rotor, in which the velocity of the wind at the rotor is a combination of the free stream velocity and the induced wind velocity. The wind speed behind the rotor and the actual induction factor are inversely related, as the axial induction factor increases the wind speed decreases. If a=1/2, the wind has slowed to zero velocity behind the rotor and the simple theory is no longer applicable. The power out, P, is the product of the thrust and the velocity at the disc.

$P = 1/2\ \rho\ A_2 (U_1^2 - U_4^2)\ U_2$ (3.11)

Substituting for U_2 and U_4 from Equations (3.9) and (3.10) gives

$P = 1/2\ \rho\ A\ U^3\ 4a\ (1 - a)^2$ (3.12)

where the control volume area at the rotor, A_2, is replaced by A, the rotor area, and the free stream velocity U_1 is replaced by U. Wind turbine rotor performance is usually characterized by its power coefficient, C_P. $C_P = P / [(1/2) \rho A U^3]$ = Rotor power /Power in the wind (3.13)

The non-dimensional power coefficient represents the fraction of the power in the wind that is extracted by the rotor. From Equation (3.12), the power coefficient is. $C_P = 4a (1 - a)^2$ (3.14)

The maximum C_P is determined by taking the derivative of the power coefficient (Equation 3.14) with respect to *a*, and setting it equal to zero, yielding $a = 1/3$. Thus $C_{P;\,max} = 16/27 = 0.5926$ (3.15)

When $a = 1/3$. For this case, the flow through the disc corresponds to a stream tube with an upstream cross-sectional area of 2/3 the disc area that expands to twice the disc area downstream. This result indicates that if the wind speed at the rotor were 2/3 of the free stream wind speed in an ideal designed rotor then it would produce the maximum power according to the basic laws of physics. From Equations (3.6), (3.9) and (3.10), the axial thrust on the disc is. $T = (1/2) \rho A U^2 [4a (1 - a)]$ (3.16)

Similar to the power, the thrust on a wind turbine can be characterized by a non-dimensional thrust coefficient. $C_T = T / [(1/2) \rho A U^2]$ = Thrust force / Dynamic force (3.17)

From Equation (3.16), the thrust coefficient for an ideal wind turbine is equal to $4a (1 - a)$. C_T has a maximum of 1.0 when $a = 0.5$ and the downstream velocity is zero. At maximum power output ($a = 1/3$), C_T has a value of 8/9. A graph of the power and thrust coefficients for an ideal Betz turbine and the non-dimensionalized downstream wind speed are illustrated in Figure 3.2. The Betz limit, $C_{P;max} = 16/27$, is the maximum theoretically possible rotor power coefficient. In practice, three effects lead to a decrease in the maximum achievable power coefficient, (Manwell, 2009).

- rotation of the wake behind the rotor
- finite number of blades and associated tip losses
- non-zero aerodynamic drag

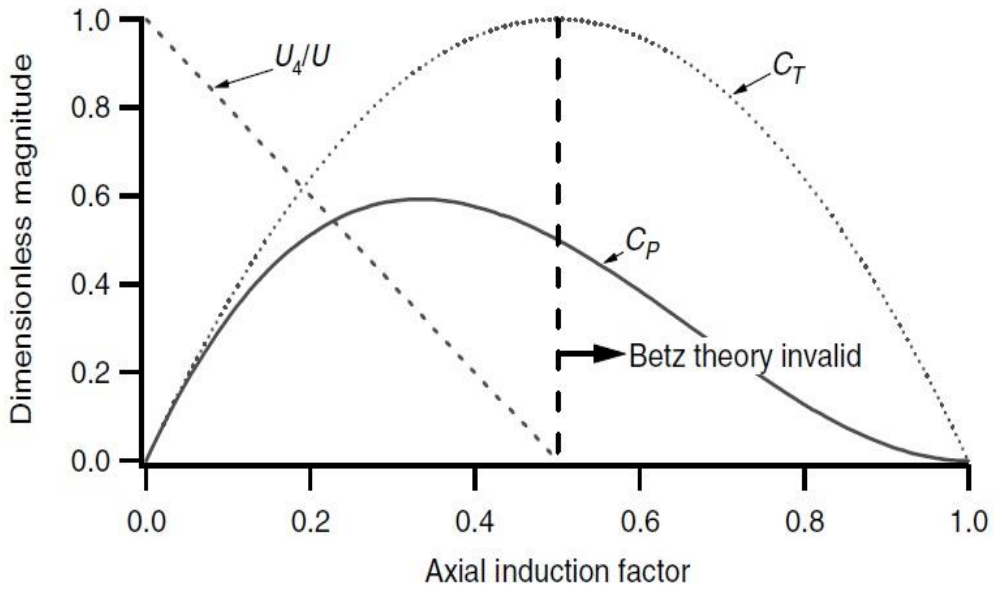

Figure 3.2: Operating parameters for a Betz turbine; U, velocity of undisturbed air; U_4, air velocity behind the rotor; C_P, power coefficient; C_T, thrust coefficient. [Manwell, 2009]

3.2 Wind Turbine Wakes

As the wind energy industry grows, the wind turbine wake topic becomes important as well. Wind turbine wakes affect those wind turbines that are in the shadows of the upstream wind turbine wakes and the consequent reduced wind speed. This leads to less power production. Various investigations have been done on wind turbine wakes. Some of the models include Jensen, Ainslie, Frandsen and the Mosaic Tile models, (Gonzalez and Longatt, 2011).

All of these models have one common purpose: "accurate assessment of wake". Although these analytical models are generally simple, their results are in reasonable agreement with available observation data although stability effects have not been considered explicitly so far. The Jensen model (Figure 3.3), is the one we have initially used in our 3D mode. The Jensen model is widely used due to its simplicity and low computational cost (Crespo et al., 1999), and is based on the assumption of a

wake with linearly expanding diameter and assumes a top – hat shape for the velocity deficit in the wake.

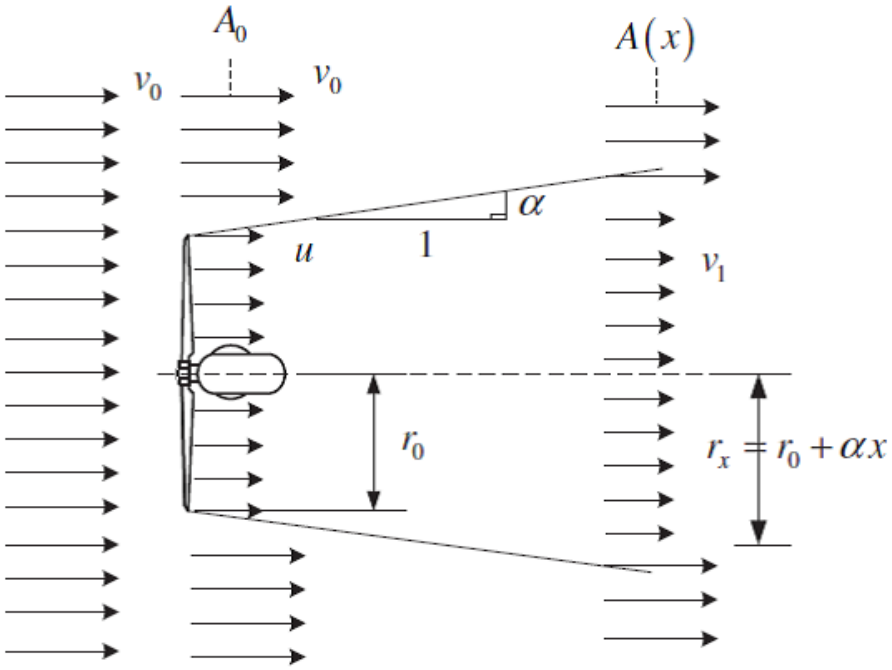

Figure 3.3: Wake behind a turbine, Jensen model [Offwind, 2016]

The wake diameter is given by $D_w = D\ (1 + 2ks)$ (3.18)

D is the diameter of the wind turbine. And the velocity in the (fully developed) wake by

$u = U_\infty\ [1 - ((1 - (1 - C_T)^{1/2}) / (1 + 2ks)^2]$ (3.19)

both depend on the relative distance behind the rotor, s = x/D and the Wake Decay Constant (WDC) k. As the velocity in the wake is considered constant for a given downstream distance, the velocity profile is called 'hat-shaped'. Jensen considered a constant value for the rate of wake expansion (k = 0.1). However, the suggested values for k is generally taken to be 0.075 (Barthelmie et al., 2005), which is adequate for land cases, but for offshore use, a value of 0.04 (Barthelmie et al., 2010; Cleve et al., 2009) or 0.05 (Barthelmie et al., 2007), is recommended. It can easily be seen from Equation. (3.19) that just behind the rotor (s = 0) the velocity in the wake is

$u|_{s=0} = U_\infty (1 - C_T)^{1/2}$ (3.20)

Where, C_T is the thrust coefficient of the turbine, x the downwind distance and U_∞ is the incoming wind velocity. Hence, due to its simplifications, the Jensen model requires that the thrust coefficient of the rotor is smaller than one, (Douwe, 2007). The Jensen equation has been used in commercial software such as WASP, WindPRO, WindSim, WindFarmer, and Openwind. Later, we noticed some limitation in this model through more research, which forced us to switch to a more developed and optimized wake model, (Chamorro and Porté-Agel, 2010). The limitations are:

1. Non-realistic assumption of the top-hat distribution of the velocity deficit.
2. Despite model claim, the model can be derived by considering mass conservation alone without any consideration of the balance of momentum, (Bastankhah and Porté-Agel, 2014).

A new analytical model for wind turbine wakes is able to capture a better estimation for wake. In this model conservation of mass and momentum is applied and a Gaussian distribution for the wind velocity reduction in the wake zone is assumed. Bastankhah et al. (2014) compared their results to the wind-tunnel measurements and large-eddy (LES) simulation data of wind turbine wakes. They found good agreement with the experimental and LES data. This model predicts the extracted power more accurately. $\Delta U/U_\infty$ is the normalized velocity deficit where ΔU is the difference between the incoming wind velocity (U_∞) and the wake velocity (U_w). By neglecting viscous and pressure terms in the momentum equations and applying mass and momentum conservation, the total force over the wind turbine is determined. As $T = (1/2)\, C_T \rho\, A_0\, U_\infty^2$ (3.21)

the normalized velocity deficit becomes as $\Delta U/U_\infty = C(x)\, f(r/\delta(x))$ (3.22)

where C(x) represents the maximum normalized velocity deficit at downwind centre of the wake, r is the radial distance from centre of wake and $\delta(x)$ the characteristics wake width at each x. Regardless of incoming conditions, the velocity deficit in the turbine wake is assumed to have a Gaussian shape and thus $\Delta U/U_\infty = C(x) \exp(-r^2/2\sigma^2)$ (3.23)

where σ is the standard deviation of the Gaussian-like velocity deficit profile at each x. After some substitutions and integrations, two values for C(x) can be obtained and only the one, which predicts the smaller value for the velocity deficit at larger downwind distances, is physically acceptable:

$$C(x) = 1 - \text{sqrt}\,(1 - C_T/8(\sigma/d_0)^2) \quad (3.24)$$

By assuming the linear expansion of the wake and some rearranging, we end up with: (Bastankhah and Porté-Agel, 2014)

$$\Delta U/U_\infty = [1 - (1 - C_T/\,8(k^*x/D + \varepsilon)^2)^{1/2}] \times \exp[(-1/\,2(k^*x/D + \varepsilon)^2) \times \{((z - z_h)/D)^2 + (y/D)^2\}] \quad (3.25)$$

Where y and z are span wise and vertical coordinates, respectively, and z_h is the hub height. k^* is a growth rate and measures lies 0.023 and 0.055. From different offshore experimental values, a value of 0.03 is used in our study. ε is equivalent to the value of σ/D as x approaches zero. According to the Large-Eddy Simulation (LES) data for wind turbine wakes: $\varepsilon = 0.2\,(\beta)^{1/2}$, where β is a function of C_T and can be expressed as: $\beta = (1 + (1 - C_T)^{1/2}) / 2\,(1 - C_T)^{1/2}$ (3.26)

By applying $C_T = 8/9$ (at maximum power output), in equation (3.25), ε has the value 0.27.

The Jensen model's limitation is summarized as follows:

1. Generally, the Jensen model predicts the wake reasonably well, but it underestimates the maximum wake in some regions with respect to LES (Beletsky et al., 2013) and experiments data. (Wu and Porté-Agel, 2011 and 2012) The reason for this problem can be attributed to the sole use of mass conservation and assumption of a uniform velocity distribution in the wake.

2. It underestimates the velocity deficit at hub height and overestimates it near the edge of the wake.

3. The effect of assuming a top – hat shape for the velocity deficit leads to an inherent error in power prediction.

It worth noting that, wakes recover faster when increasing the ambient turbulence enhances mixing processes, which result in faster wake recovery, (Bastankhah and Porté-Agel, 2014).

3.3 Selection of the Wind Project Location

In 2009, a feasibility study was completed for the Great Lakes Wind Energy Task Force (JuwiGmbH, 2009). The Feasibility study compared nine potential project areas with respect to important siting criteria including shipping channels, water depth, distance to possible onshore interconnection, wind resources, environmental condition, interconnection and offshore cabling etc. One of these locations was been selected for the first phase of the Icebreaker project, (LEEDCO, 2017).

3.4 Selection of the Proposed Turbine Layout

The National Renewable Energy Lab (NREL) conducted a wind turbine layout optimization study to evaluate the energy output and performance on the variety of layouts. Important factors which played a crucial role in determining the layout were net energy production, turbine net capacity factor and wake losses, (LEEDCO, 2017).

By considering the potential turbine layout and the location of the Icebreaker project we have decided to put our very large wind farm turbines in 24 rows and 18 columns with the wind turbines positioned so that the north-south (y-direction) and east-west (x-direction) spacing between wind turbines are 500 m (≃3 D) and 3000 m (≃18 D), respectively, where D is the wind turbine's rotor diameter of 164 m as shown in Figure 3.4. The first turbine, in the southwest corner, is located at 41.51 N and 82.279 W. Turbines are laid out within an area of 586 km^2. The depth of the water within the wind farm zone ranges between 9.9 m and 19.2 m and averages 15.8 m.

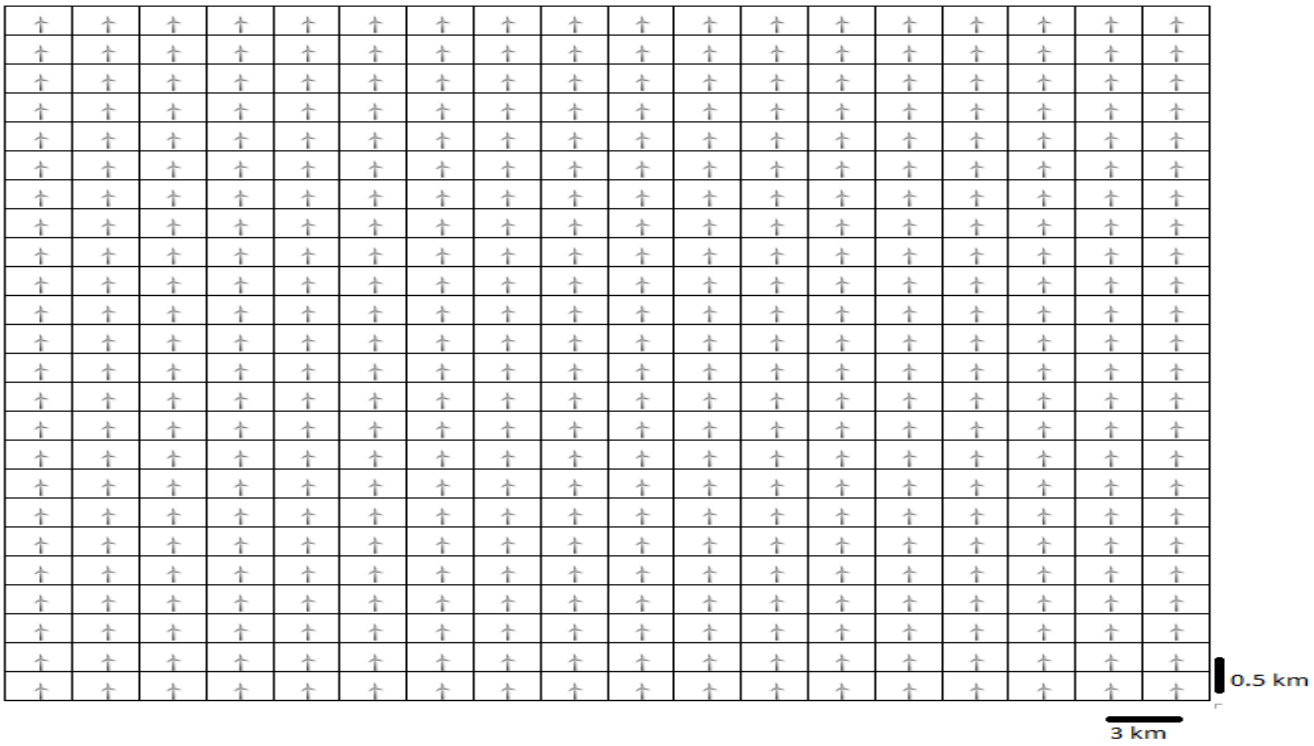

Figure 3.4: 432 wind turbine layout

For optimal performance, a distance of no less than two rotor diameter will generally be expected and the distance between three to ten rotor diameters is recommended depending on the individual circumstance of the site. The required spacing will often be dependent on the prevailing wind direction, (Planning.gov, 2017).

The V164-9.5 MW model wind turbine that is used in our simulation is the most powerful serially produced wind turbine in the world at the time of writing. The V164 platform with a massive 80-m blade (Vestasoffshore, 2017), has a rotor diameter of 164 m and hub height of 140 m. The prevailing wind direction on Lake Erie is from the SW to NE, and the turbines are deployed near the shallow southern shore of the central basin. The wind turbine layout and spacing are set according to this optimizing standard factors, so that the horizontal spacing (parallel to the direction of SW-NE winds), is six times greater than lateral distance (perpendicular to the direction of wind), to minimize the wake effect.

CHAPTER FOUR

ONE-DIMENSION LAKE ERIE 2013 SIMULATION

4.1 1D Set up

4.1.1 1D Input Data

NOAA hourly meteorological input, wind speed and direction, air temperature, relative humidity and cloud coverage and daily-averaged solar radiation are shown in Fig 4.1 a-f. When buoy data (45005-buoy station) were not available, we used the nearby HHLO1 and Windsor A meteorological station data, (see Figure 1.7). Hourly cloud coverage is highly variable and a nine-month time series plot quickly becomes a jumbled mess with too many lines, so, alternatively, we used the cloud coverage histogram to illustrate the data used (Figure 4.1e). On the vertical axis, the frequency is presented and on the horizontal axis the lower value of each interval to the lower value of the next interval is displayed – interval values are between 0 and 1 – where 0 corresponds to a sunny clear sky and 1 to a fully cloudy sky. Bars are extending from the lower value of each interval to the lower value of the next interval. The cloud cover is important in computing solar radiation flux (Equation 2.19).

Our program simulates DOY (Day Of Year) 92 to 365 in 2013. As illustrated in Figure 4.1a, wind speed (in m/s) is highly variable but does not exceed 17 m/s. Generally, in cold seasons stronger winds are dominate while slower winds are observed in spring and summer. The observed wind data yield an average wind speed of 6 to 7 m/s in 2013 at those particular locations. Air temperature increased from April to July when it reaches a maximum of 30 °C, after this point, a decreasing trend starts and continues to mid-December. As historical data and previous investigations highlight, the dominant wind direction is southwest. This fact is confirmed by the 2013 (DOY 92 to 365), wind rose. However,

this is not representative of the whole dataset and just confirms the previous studies and observations on dominant wind direction apply to the simulated period in our model. Observations show that our region of study is a relatively humid area with a mean humidity of 50 percent, which is within the expected range for near water and coastal zones. The incoming solar radiation is depicted in a daily total format for the sake of producing a cleaner graph and the fact that absence of the solar radiation during night makes the graph illegible. Air temperature corresponds generally to the solar radiation so their plots behave similarly. The daily solar radiation maximum is in July when it reaches to 30000 kJ/m^2. Solar radiation reduces afterward and has a minimum value of 5000 kJ/m^2, in December. A well-mixed, uniform water temperature of 4 °C is set for the water column on the first day of the run, (DOY 90).

4.1.2 1D Model Water Depth Selection

Based on the bathymetry and mooring data, Lake Erie's western, central and eastern basins maximum depths are about 10, 25 and 64 meters, respectively. Accordingly, typical depths of 10, 25, and 60 m are used in our 1D model simulation. To better interpret and compare output profiles, COHERENS applies σ-coordinate rather than a z-coordinate. A fixed number of layers applies to different water columns with different depths. In order to capture a good vertical distribution 50 vertical layers are set. This gives a vertical spatial resolution of 0.2, 0.5, and 1.2 m, in 10, 25, and 60 m water columns, respectively. Profile results are shown by layer number rather than depth in meters. The advantage is for comparing the results related to various water column depths.

4.1.3 1D Initial Condition (Numeric)

Initial conditions assumed no current $u_0 = 0$, $v_0 = 0$ (horizontal components of water current in x and y-direction, respectively), a well-mixed water column at 4 °C after ice break up at midnight April 1^{st}. 10^{-6} J/kg is the background limit for k (kinetic energy), although this value is not realistic for

turbulence since turbulence is assumed to be in quasi-equilibrium and will adjust itself rapidly to changes in the forcing conditions caused by the current shear and stratification. The reason for adopting this lower limit for k is to avoid unrealistically large eddy coefficients that could be created by rounding errors. The model is forced using nine months of typical ice-free season meteorological hourly data for 2013 taken from National Oceanic and Atmospheric Administration (NOAA) stations 45005 (a three-meter offshore buoy deployed in 12.6 m of water by the National Data Buoy Centre weather station (NDBC), located far offshore and from the Environment Canada, Windsor A, ON (Figure 1.7), since the buoy is removed during winter to prevent damage from ice, no buoy measurements are available during winter months. The cloud coverage (f_c) data from the Windsor A station are reported in categorical form, so we converted them into values in a range of 0 to 1.

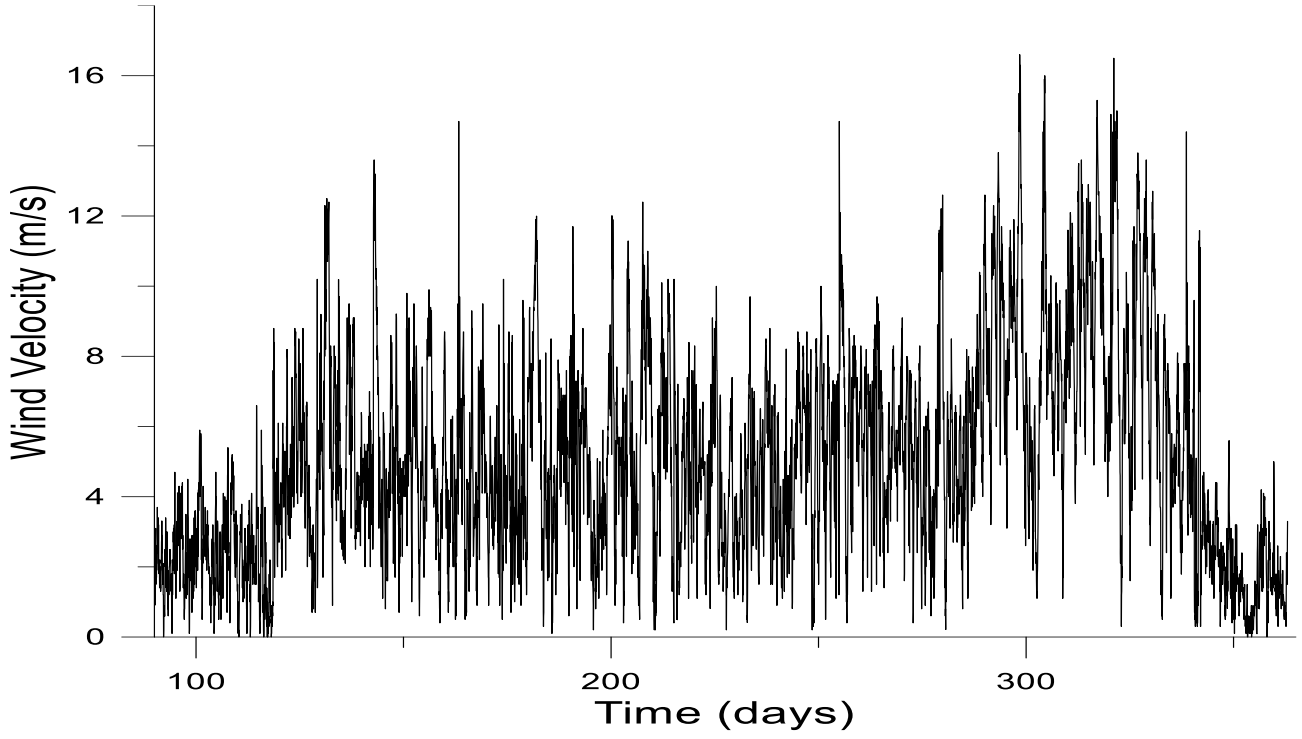

a

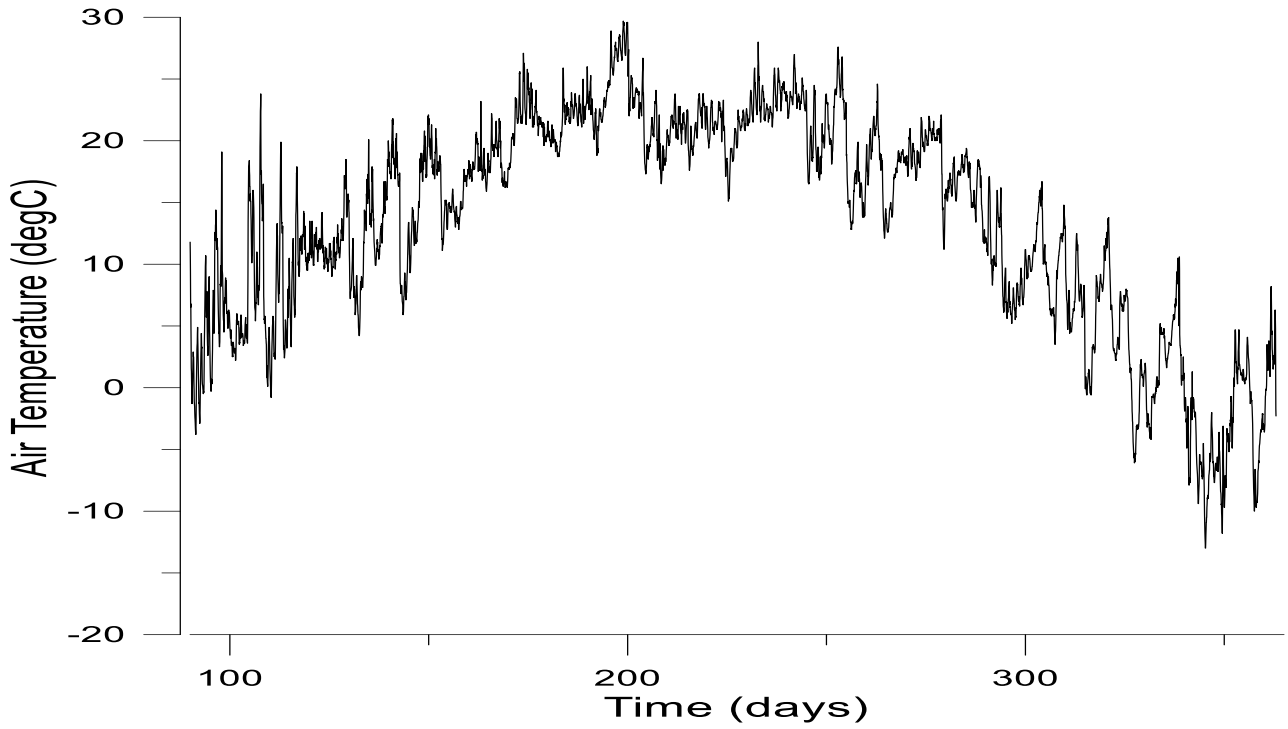
Air Temperature (degC)
30
20
10
0
-10
-20
100
200
300
Time (days)

b

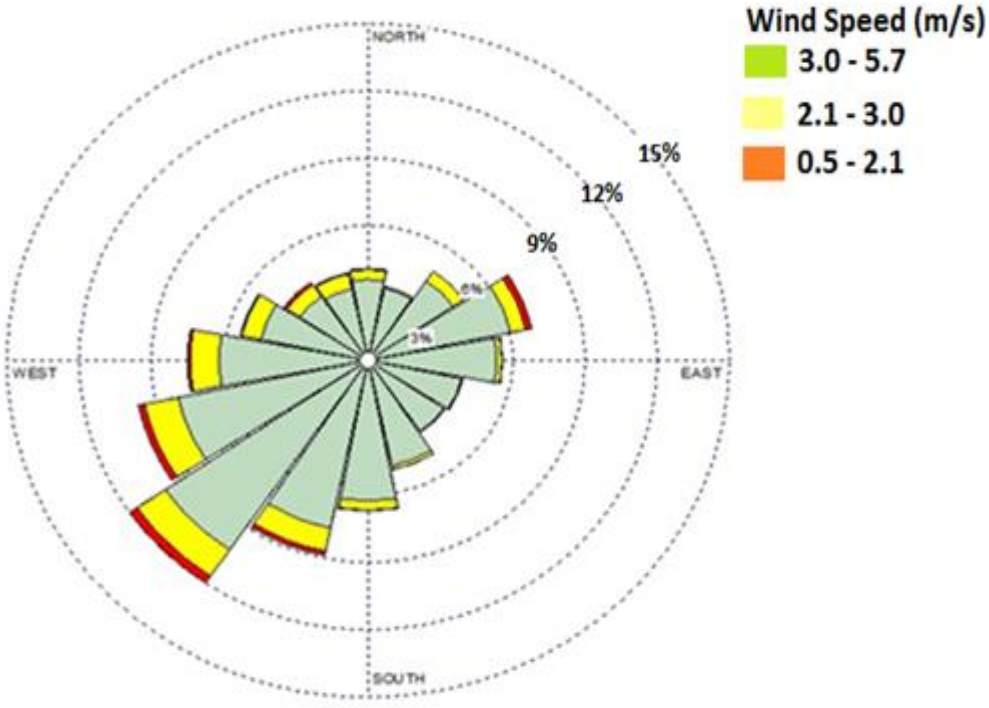
Wind Speed (m/s)
3.0 - 5.7
2.1 - 3.0
0.5 - 2.1
NORTH
EAST
SOUTH
WEST
15%
12%
9%
6%
3%

c

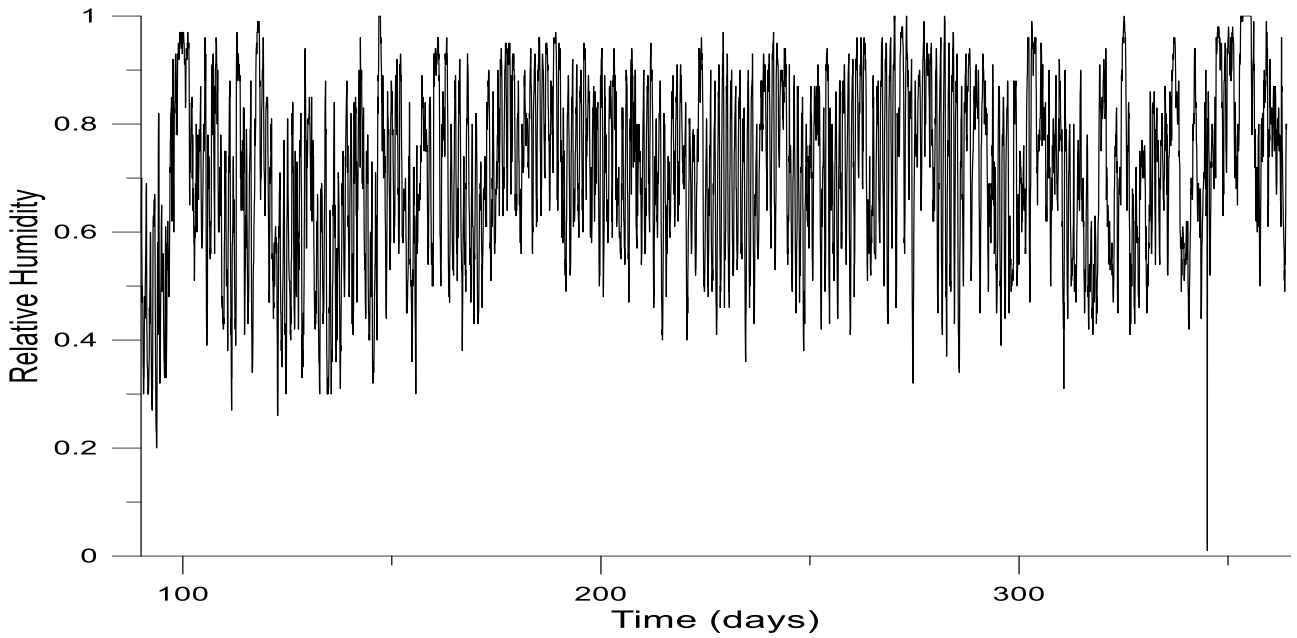
Relative Humidity
1
0.8
0.6
0.4
0.2
0
100
200
300
Time (days)

d

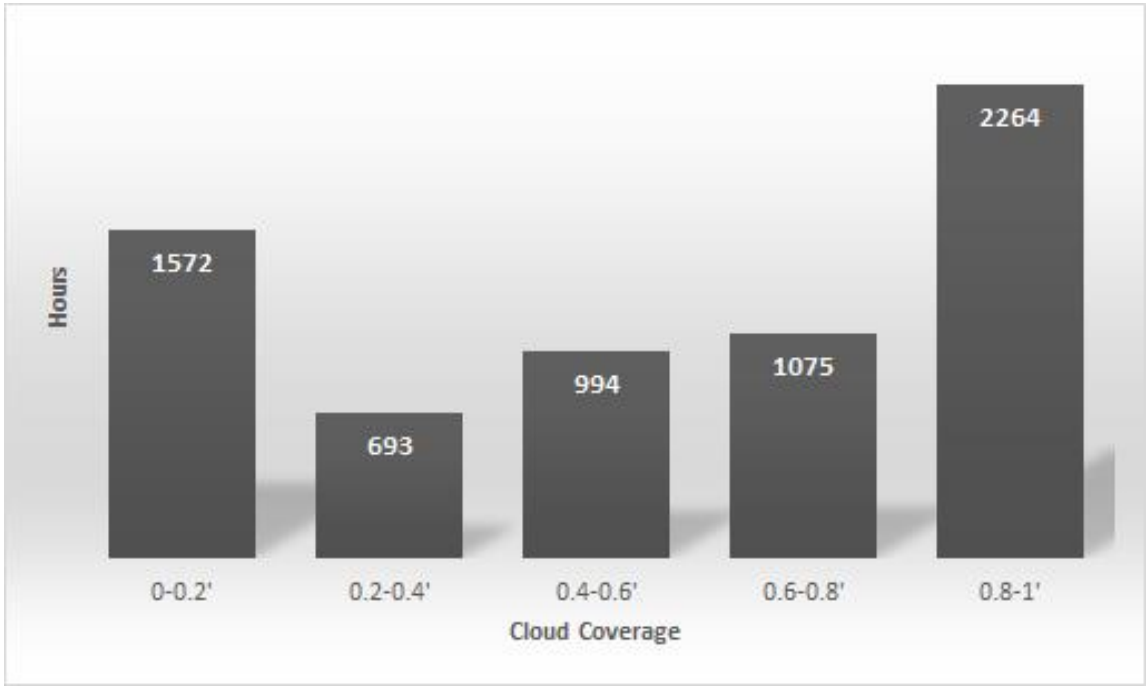
Hours
1572
693
994
1075
2264
0-0.2'
0.2-0.4'
0.4-0.6'
0.6-0.8'
0.8-1'
Cloud Coverage

e

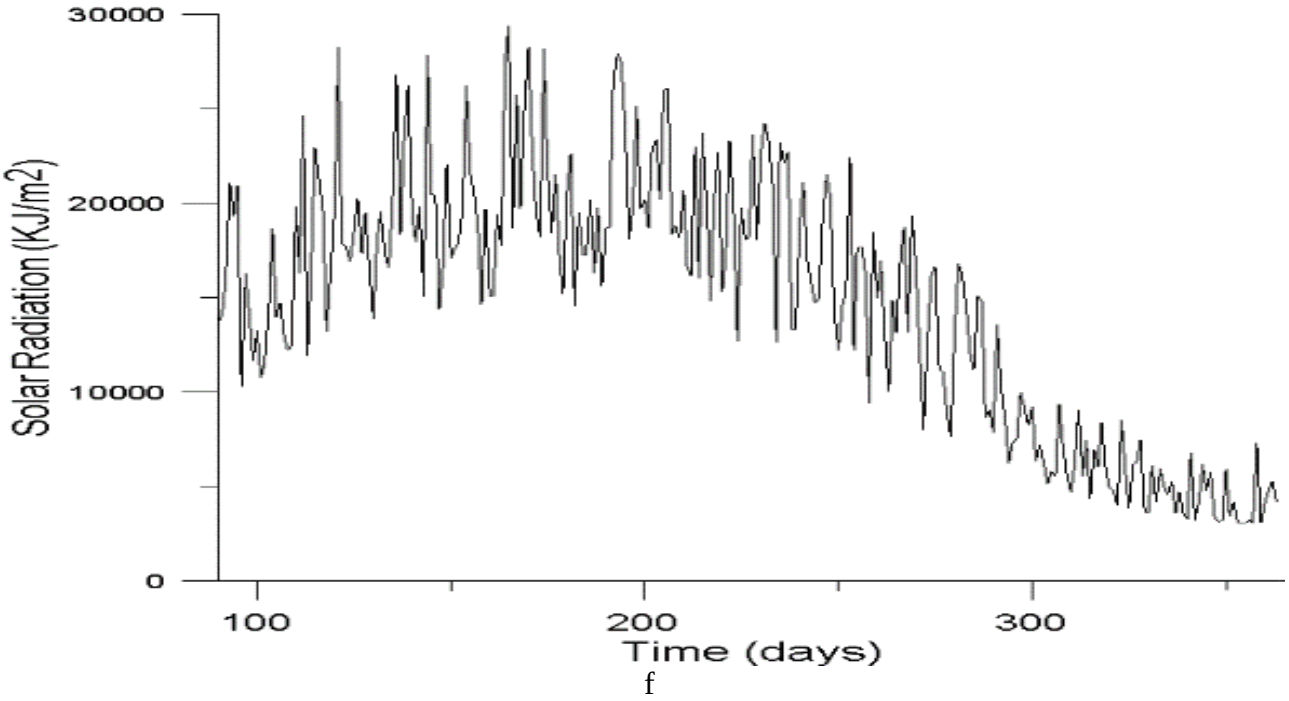

f

Figure 4.1: Meteorological data used as input from day of the year DOY 90-365. a) Hourly wind speed (adjusted to 10 m height), b) Hourly air temperature, c) Hourly wind direction, d) Hourly relative humidity, e) Hourly cloud coverage, f) Daily-total incoming solar radiation. Data are from NOAA stations 45005 located at 41.677 N and 82.398 W and HHLO1 located at 41.400 N, 82.540 W and from Windsor A Ontario station at 42.280 N and 82.960 W. See text for details.

4.2 1D Model Results

4.2.1 Thermal Structure

Characteristics of the thermal cycle of the 1D model are illustrated in Figure 4.2. The graphs show near-surface and near-bottom temperatures for water columns of 10, 25 and 60 m depths, developing in the presence and absence of wind turbine wake (wind speed reduction) of 25%. The results shown start on DOY 90 (March 31) with well-mixed, uniform temperature water columns at 4 ºC. From April

onwards we can see distinct differences depending on water depth. In all three cases, the water surface temperature reaches its maximum in July and August (DOY 200-250). Average water surface temperatures over this period with no wind farm wake reductions in wind speed are approximately 25 and 21 °C for the 10 and 60 m water depths. With reduced mixing and heat transfer to the air in the presence of wake reduction of wind speed, they increase by about 1.2 ºC. This highlights the role of bathymetry in heat storage. The 10 m water column is the shallowest, so has the smallest volume and by considering the equal amount of solar radiation falling on the water surface it accounts for the highest summer temperature. It cools down and heats up at a faster rate while deeper water columns retain their heat storage for a longer time. When our calculations end, on Dec 31, the water columns are well mixed. Temperatures are higher (7.5 ºC) in the 60 m water column than in the 10 m water where surface and bottom temperatures are about 0.5 ºC and 2 ºC, respectively. The 25 m depth calculation has approximately the same Dec 31 temperature (6.7 ºC) as for the 60 m water column. We can see from Figure 4.2a that in the 10 m column, the bottom has approximately the same temperature as the surface throughout the year while this well-mixed character only occurs during the colder months in the deeper cases. Although the surface temperature pattern is approximately compatible in all cases, there is a clear difference in the annual cycle in bottom temperature between the three cases. While surface temperatures fall quickly after day 275 the bottom temperatures are still increasing until December for the 60 m case when the surface temperatures have cooled sufficiently to overturn the layers. The gradual heating of the bottom waters over the summer is partially turbulent transfer of heat from above and partly heating by deeply penetrating solar radiation.

The general pattern of seasonal variations in surface and bottom waters show a similar pattern to the 1979 survey measurements of Schertzer et al. (1987), which are reported also in Bolsenga and Herdendorf (1993). In the 1979 data, temperature maxima, monthly-averaged surface temperatures of about 21-23 ºC were observed in July and August. Our modelled, 2013, situation is similar for 25 and

60 m water depths, while in 10 m water our temperatures appear somewhat warmer. In the shallow western basin Schertzer et al. report, surface and bottom temperatures are approximately the same. Our model gives the same result. The observed bottom temperatures in the central and eastern basins show maxima in October and November respectively, but no observations are reported in December. Our modelled maxima occurs over the DOY 250-300 (September-October) in 25 m water but in early December in the 60 m water column simulation. Maximum observed bottom temperatures are 16 and 10 ºC in the central and eastern basins while our modelled 25 and 60 m values are somewhat different (22 and 8 ºC, respectively) but there is considerable depth variation in the basins and also year to year variation.

Beletsky et al. (2013) compared their 3D POM model results for surface water temperature with 2005 water temperatures from three buoys, one in each basin. Their modelled summer temperatures show less variation with water depth than ours and are higher than our values in 25 and 60 m water columns. The 2005 measurements show lower temperature maxima than the Beletsky et al. model but are significantly warmer than the values reported for 1979 and warmer than our 1D model values. One notable difference is in the year-end temperatures. Our 10 m model is close to the Beletsky et al. model results but their simulations for buoys 45132 (central basin, 22 m water depth) and 45142 (eastern basin, 27 m water depth) have colder temperatures (near 3.5 ºC) than our simulations (near 8 ºC). Both simulations have temperatures near 4 ºC on March 31.

Overall we are satisfied that our 1D simulations produce realistic seasonal variations in water temperatures and can be used to give an approximate indication of the impact of reduced wind speeds. The computations with reduced surface wind speeds show essentially the same seasonal pattern except that water temperatures reach higher values in spring and summer, especially in the deeper water column calculations, where mid-summer temperatures can be 5 ºC higher. For the 25 and 60 m cases,

they also affect the bottom temperatures in the opposite way. More heat remains in the upper layers with less mixing and summer and fall temperatures at the bottom are colder as a result.

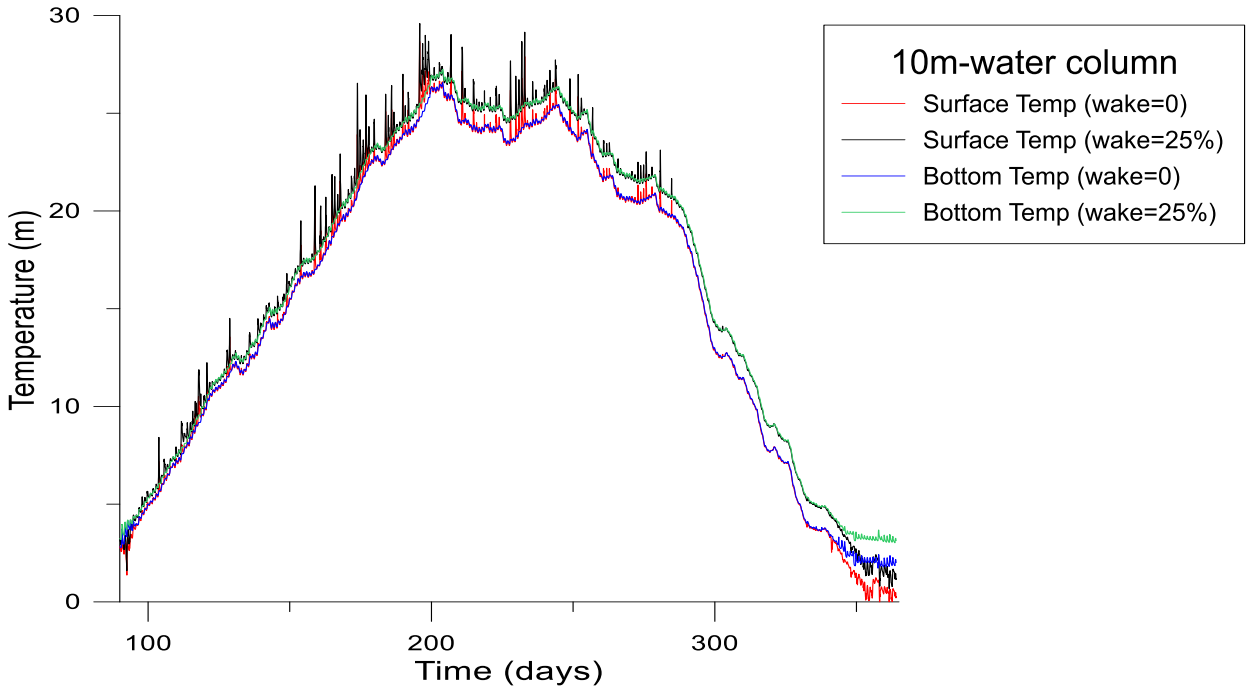

a

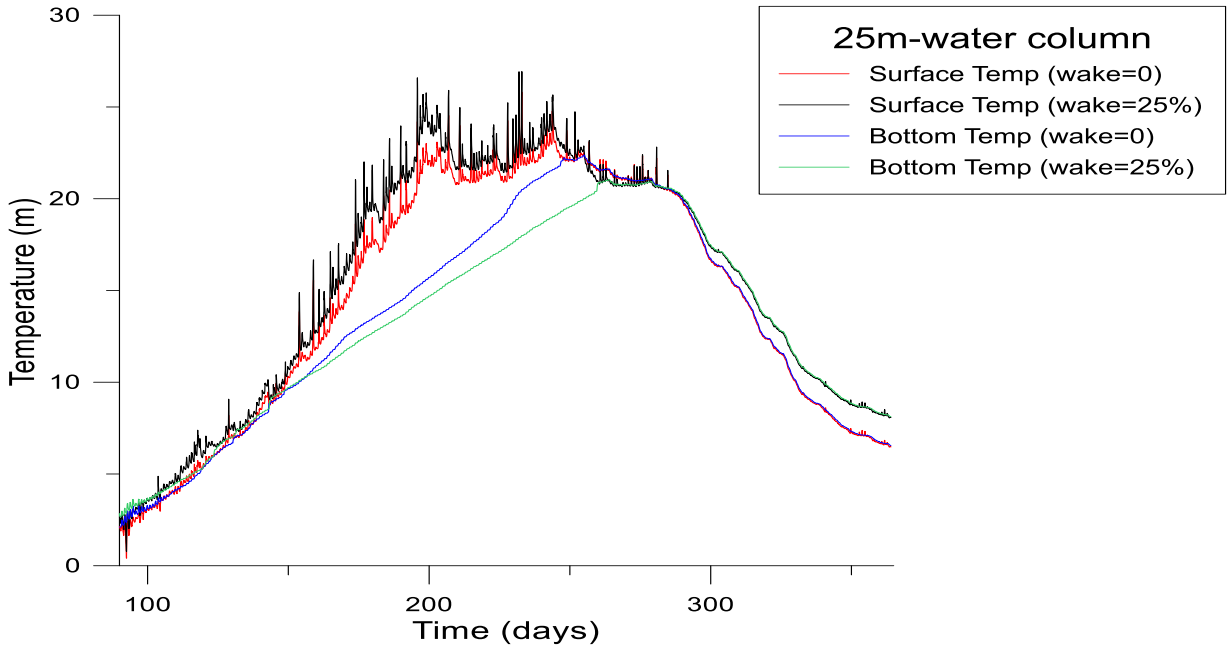

b

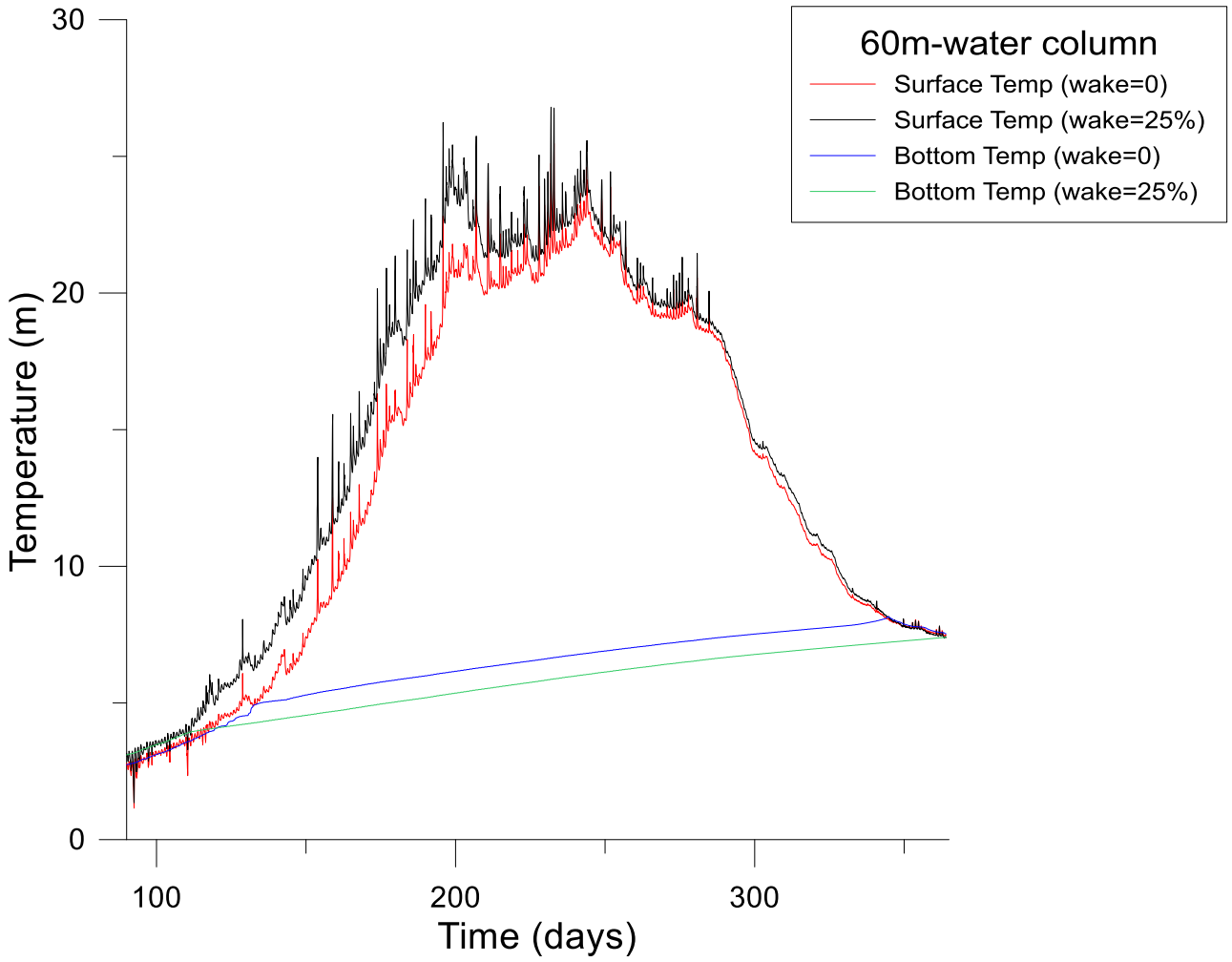

c

Figure 4.2: Near-surface and near-bottom temperatures throughout the open water season. 1D model results for water depths of 10, 25 and 60 m, with measured meteorological input and with a 25 percent wake reduction in wind speed.

4.2.2 Pycnocline and mixed-layer depth (MLD)

Although many limnology studies focus on the thermocline while oceanographers consider pycnoclines because of the role of salinity, we use pycnoclines and density profiles in the determination of the mixed-layer depth as density produces more stable results. This is necessary since in parts of the year the water temperature may lie in the 0-4 ºC range where density increases while temperature

increases. Note also that COHERENS uses density in determining the stratification of fluid layers for eddy mixing purposes. We do however show temperature profiles in preference to density since these are more familiar to most readers.

Bathymetry and meteorological influences on the vertical temperature distribution have been identified as contributing factors in the development of pycnocline and mixed-layer depth variations. It is assumed that physical parameters like temperature or density are mixed and homogeneous to a certain level from the surface down, which is called the mixed-layer. In the modelled profiles (Figure 4.3b, c) the variation of T with depth below the well mixed-layer is often relatively smooth and the pycnocline depth, defined as the depth of the maximum in $-d\rho/dz$, can be somewhat deeper than the depth over which the temperature and density are relatively uniform, although it will generally occur just below the bottom of the mixed-layer. In our determination of the mixed-layer depth, we seek to eliminate diurnal thermocline effects in the top meter of the water column and to put a threshold density difference within which we would still regard the column as well mixed. A linear interpolation between levels is then used to estimate the exact depth at which the difference criterion is reached. We initially took that difference as 0.02 kgm^{-3}, roughly corresponding to a 0.2 ºC temperature difference for temperatures near 11 ºC, as suggested by Boyer Montégut (2004) but it produced multiple variations in mixed-layer depth associated with diurnal or other short-term variations. As a result, we choose 0.1 kgm^{-3} (typically 1 ºC) as our threshold. Mixed-layer depths (Figure 4.4) are still noisy but partially avoid the determination of mixed-layers above weak diurnal thermoclines when we are primarily interested in the seasonal thermocline evolution. Figure 4.5 illustrates this with computed, relatively shallow, mixed-layer depths over a short, five-day period starting on DOY 195. Figure 4.3 shows temperature profiles at days 138, 230 and 290 for the three water depth cases, with and without the wake effect wind speed reductions. From Figure 4.3a, it is clear that on these three days, the 10 m water column is well mixed and no thermocline exists. The same inference can be drawn from Figure

4.2a where temperature differences between top and bottom of the column remain small throughout the nine-month calculation. On other days, typically with weak winds, we do see a weak thermocline below a shallow, 1-2 m mixed-layer. Looking back at Figures 4.2b and c, we can see that the temperature difference between top and bottom of the water column is much larger in deeper water, develops earlier, and persists longer. This is reflected in the profiles of Figures 4.3b and c, with strong thermoclines at about 10 m depth in the 60 m column on day 230 compared to a weaker thermocline at about the same depth in the 25 m deep water. By day 290, the 25 m water column is well mixed while the thermocline remains in the 60 m water. In the cases with reduced wind speeds, the surface temperatures are higher and the mixed-layers are shallower. As noted above we can use the predicted potential temperatures to compute water density (from a high order polynomial fit excluding pressure effects to better represent stability) and estimate the mixed-layer depth. If the surface and bottom densities differ by less than 0.1 kgm^{-3} we classify the whole column as well mixed in the plots shown in Figure 4.4. In the shallow 10 m water depth case, weak thermoclines do develop and there are shallow mixed-layers of depth 1-2 m until the surface layer starts to cool steadily around day 250. In the 25 m case, the main mixed-layer starts to develop around day 150 and has a depth of around 10 m through much of the summer. After DOY 250, the mixing extends through the whole column much of the time. Summer mixed-layers in the 60 m depth water case are similar but the existence of a mixed-layer continues much longer (to DOY 330).

Differences between the mixed-layer depths between the 100 percent and 75 percent wind speed simulations generally show shallower mixed-layer and longer persistence into the fall in the 25 and 60 m depth cases with lower winds.

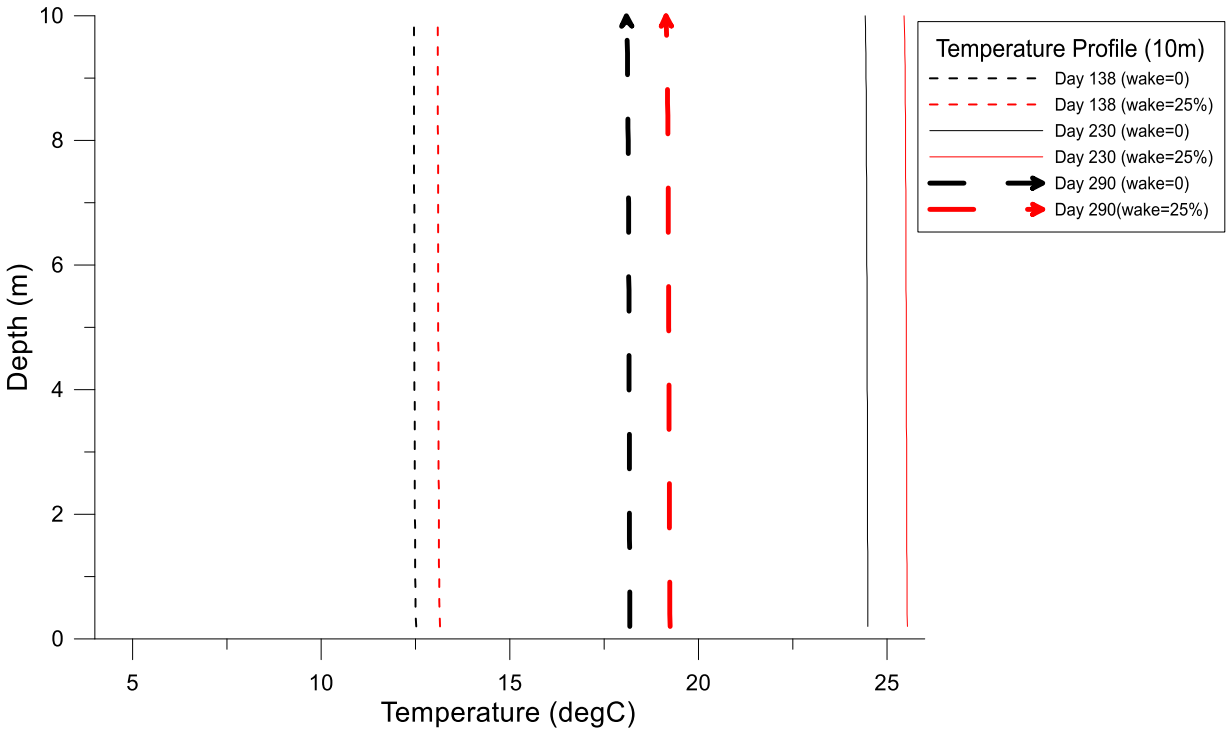
Temperature Profile (10m)
Day 138 (wake=0)
Day 138 (wake=25%)
Day 230 (wake=0)
Day 230 (wake=25%)
Day 290 (wake=0)
Day 290(wake=25%)
Depth (m)
Temperature (degC)
0
2
4
6
8
10
5
10
15
20
25

a

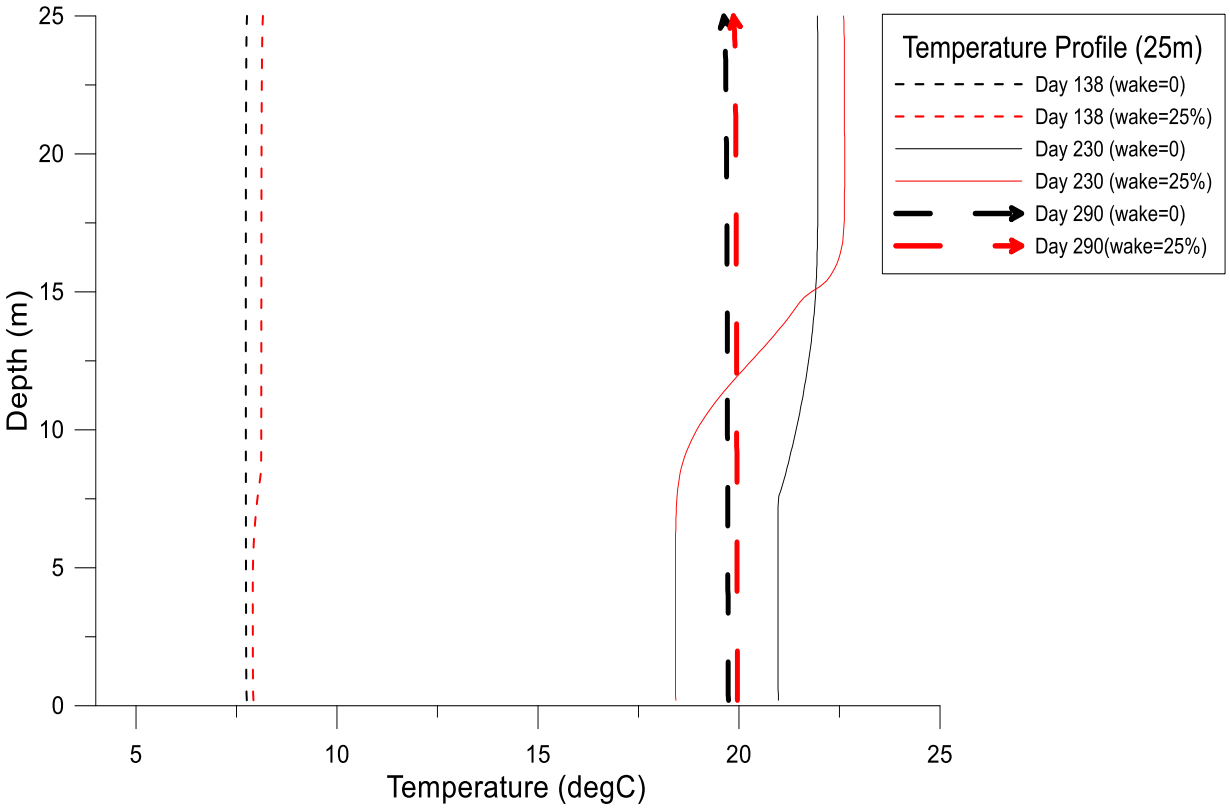
Temperature Profile (25m)
Day 138 (wake=0)
Day 138 (wake=25%)
Day 230 (wake=0)
Day 230 (wake=25%)
Day 290 (wake=0)
Day 290(wake=25%)
Depth (m)
Temperature (degC)
0
5
10
15
20
25
5
10
15
20
25

b

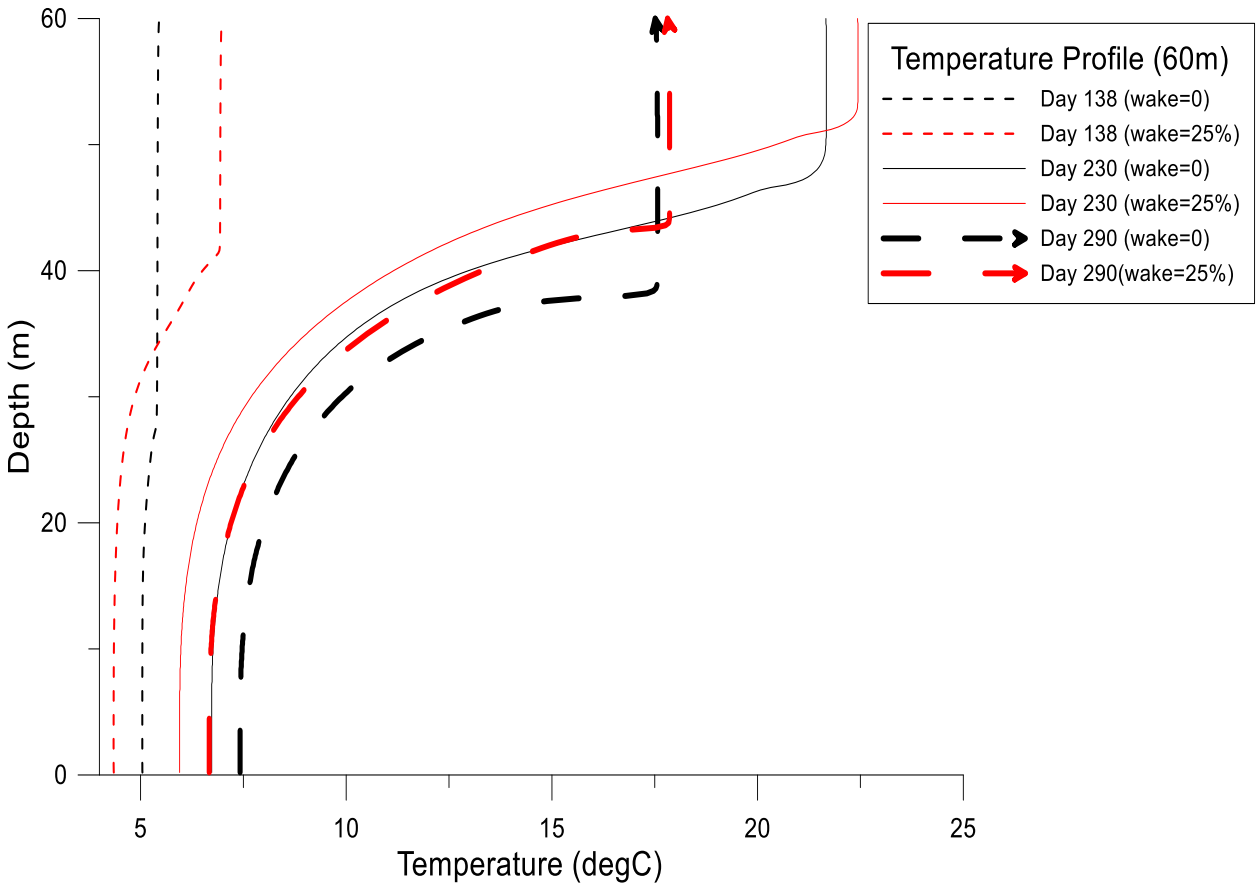

c

Figure 4.3: Sample temperature profiles for three water depths with and without wake effect wind speed reductions. “Depth” is to be interpreted as the height above the bed.

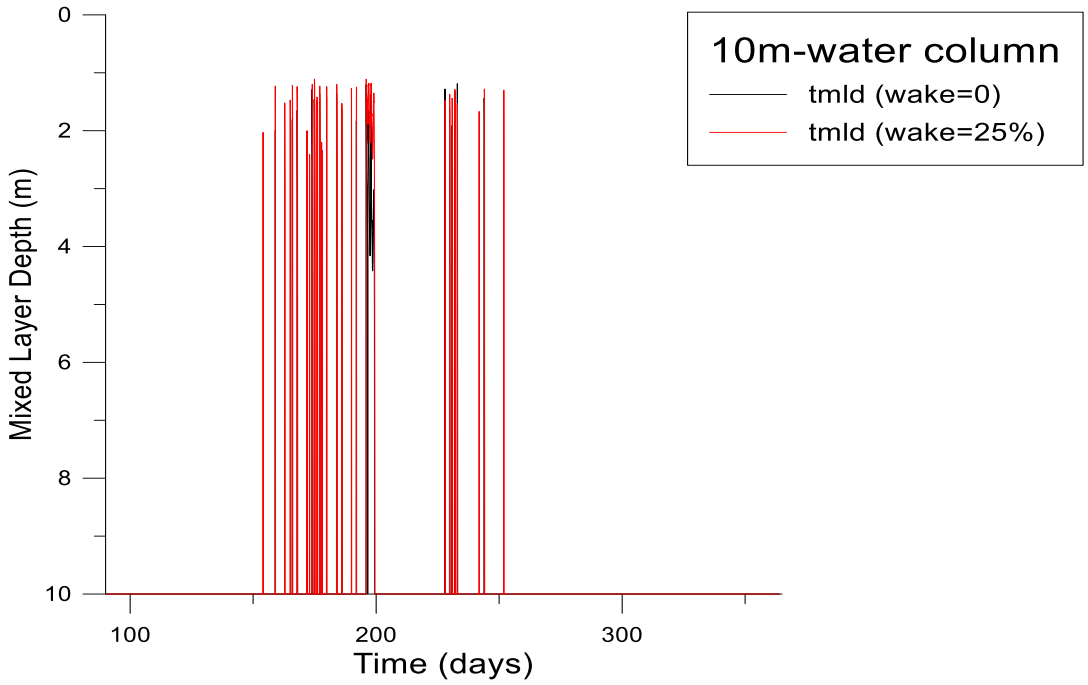
10m-water column
tmld (wake=0)
tmld (wake=25%)
Mixed Layer Depth (m)
0
2
4
6
8
10
100
200
300
Time (days)

a

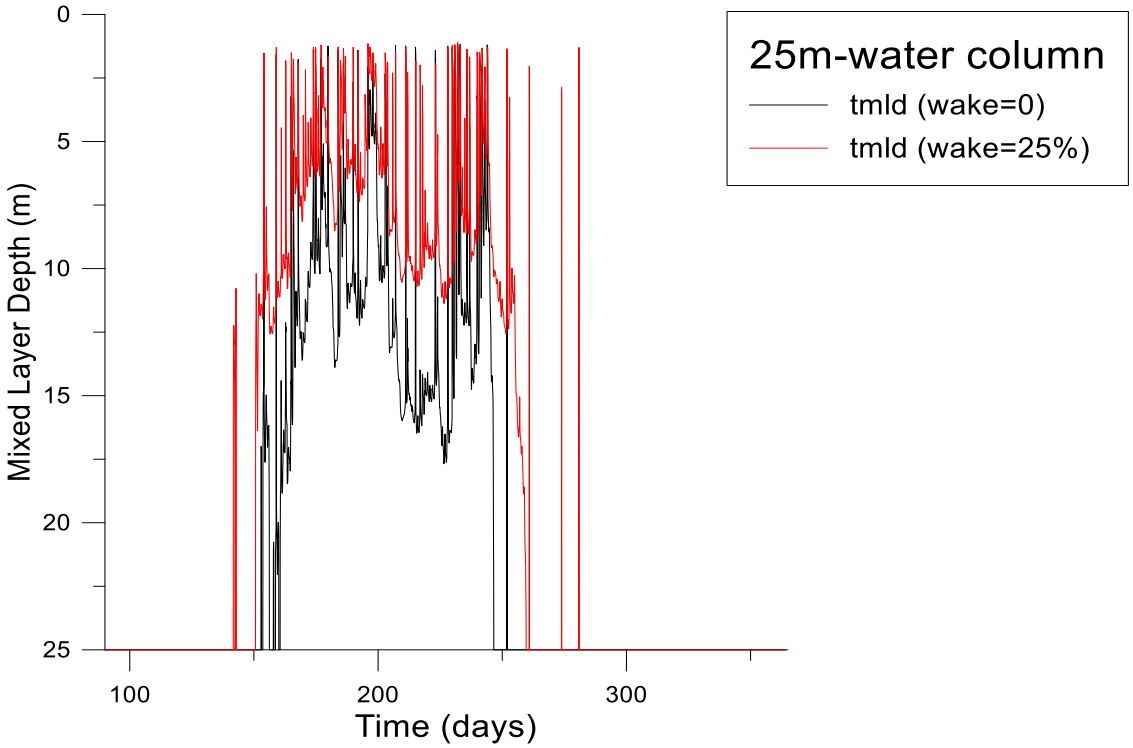
25m-water column
tmld (wake=0)
tmld (wake=25%)
Mixed Layer Depth (m)
0
5
10
15
20
25
100
200
300
Time (days)

b

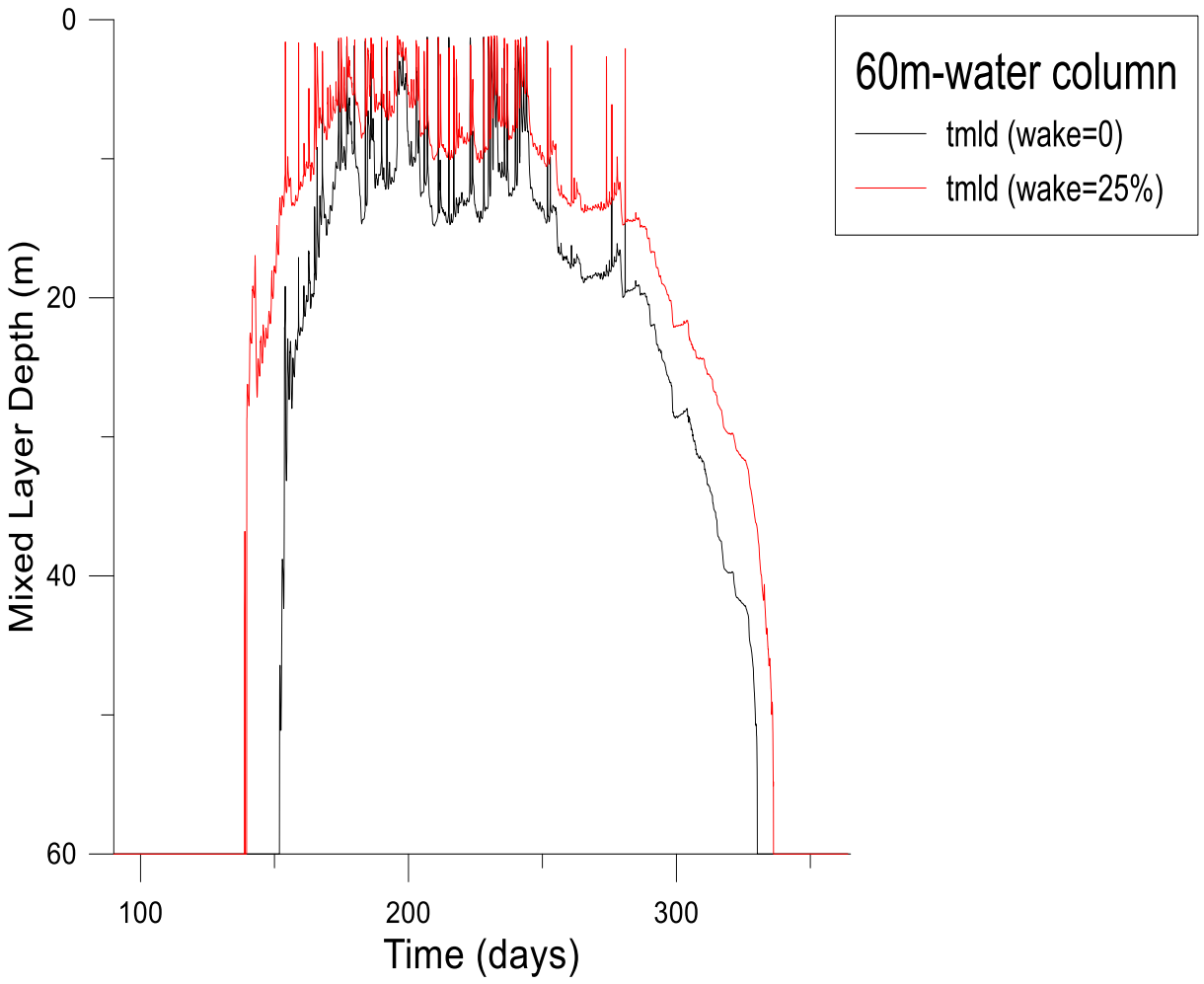

c

Figure 4.4: Computed mixed-layer depths, based on water density for water depths of 10, 25 and 60 m, with measured meteorological input and with a 25 percent wake reduction in wind speed.

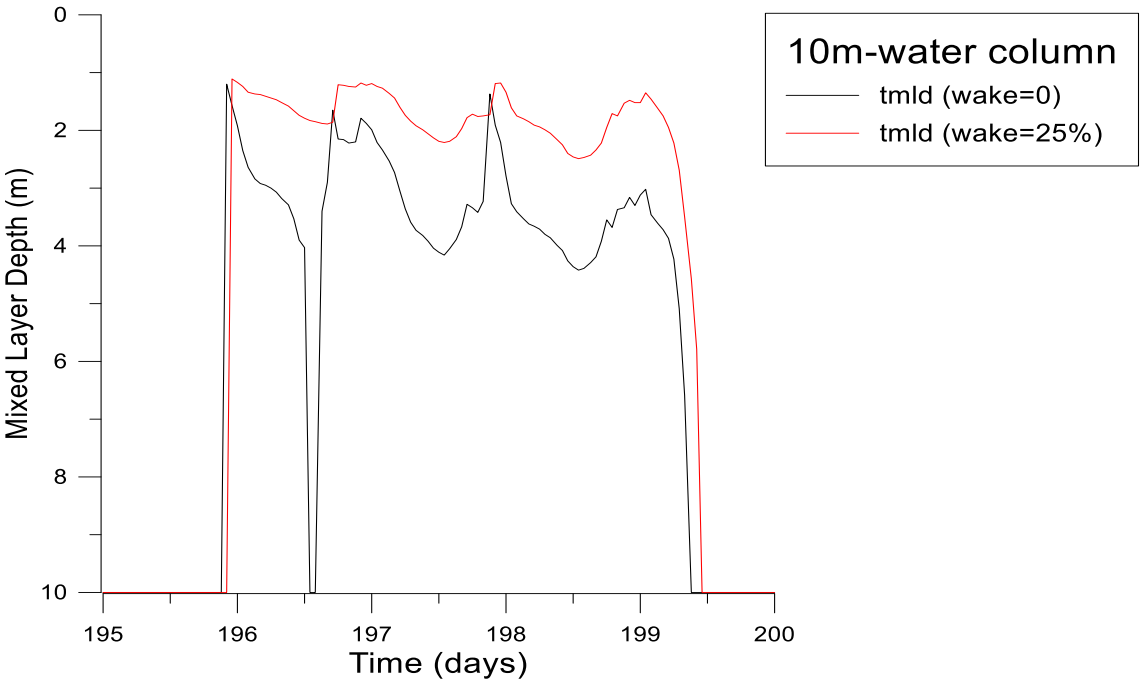
10m-water column
tmld (wake=0)
tmld (wake=25%)
Mixed Layer Depth (m)
0
2
4
6
8
10
195
196
197
198
199
200
Time (days)

a

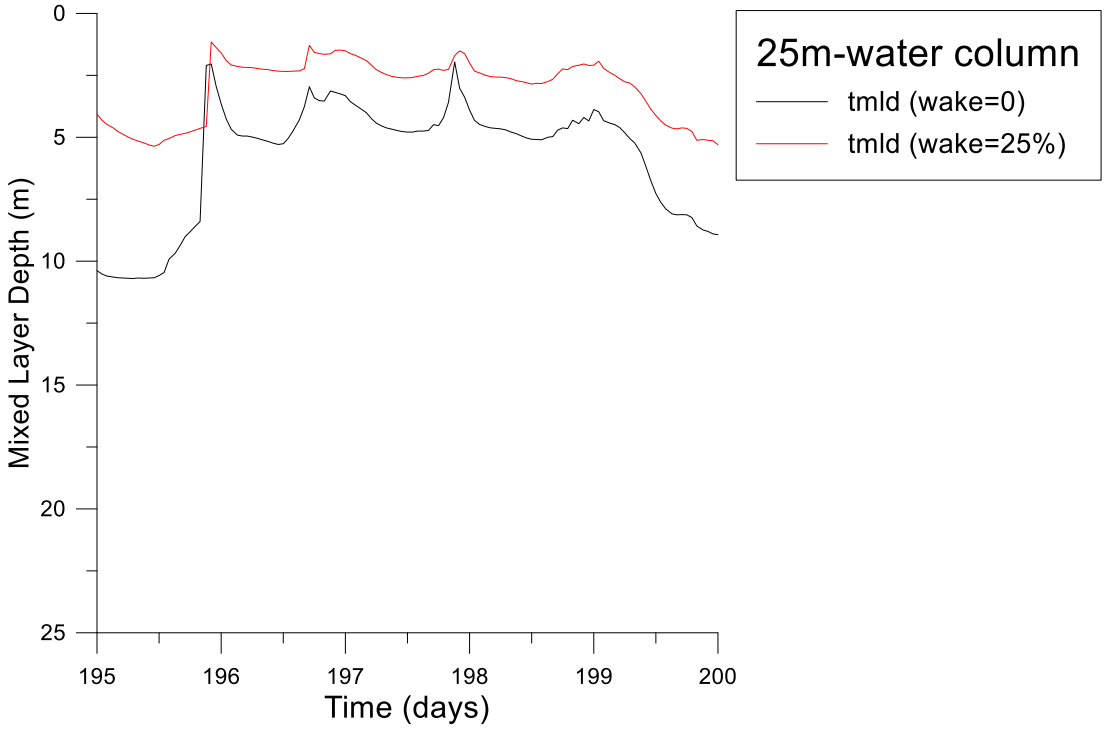
25m-water column
tmld (wake=0)
tmld (wake=25%)
Mixed Layer Depth (m)
0
5
10
15
20
25
195
196
197
198
199
200
Time (days)

b

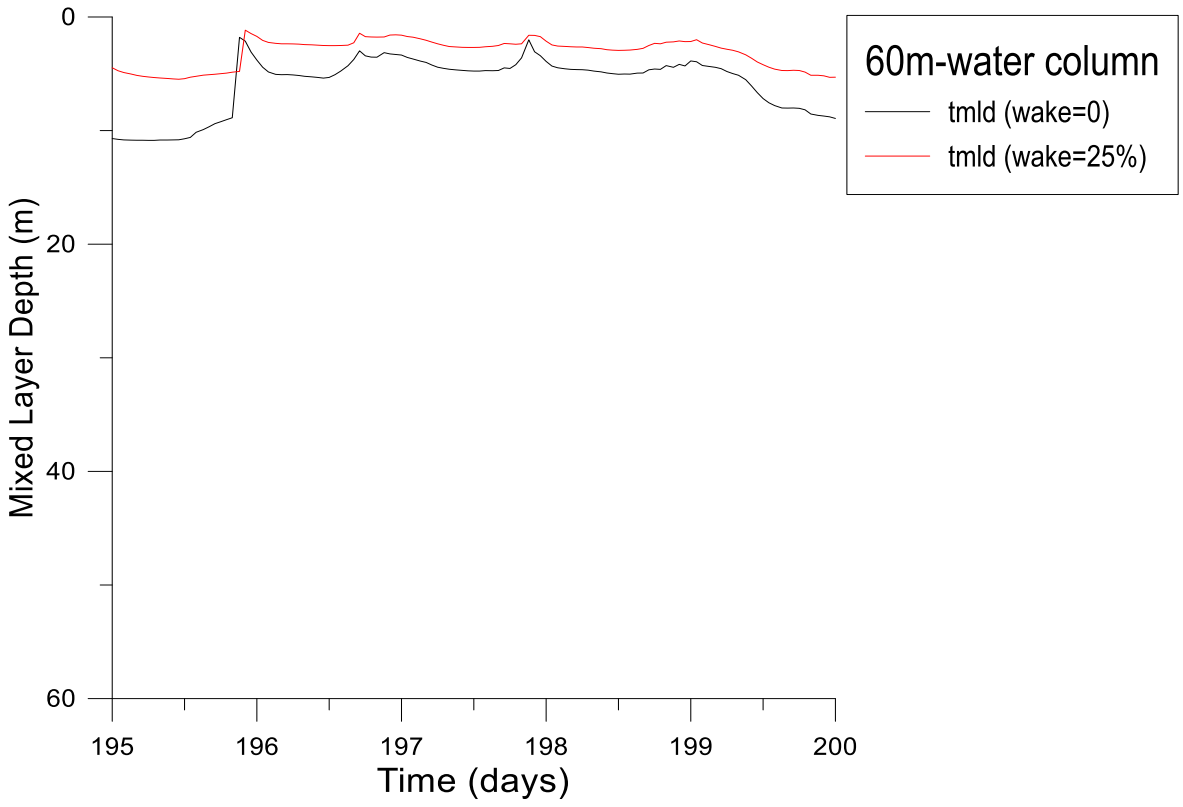

c

Figure 4.5: Computed mixed-layer depths during DOY 195-200.

4.2.3 Water Currents

The overall, primarily wind-driven, circulation of Lake Erie's central basin is anti-cyclonic as noted in the discussion above. While we are only using a 1D model at present it is still of interest to see what the model predicts in terms of near-surface and near-bottom (hereafter surface and bottom) currents and how these might vary as a result of reduced winds in wind farm wake areas.

Figure 4.6a shows hourly plots of surface and bottom currents for water depths of 10, 25 and 60 m for two ten-day blocks. Days 200-210 are selected for summer and 330-340 for early winter. The plots show that, for 25 and 60 m depth cases, summer surface currents are greater than winter ones. For the 10 m depth case, where the water column is well mixed the summer and winter currents are comparable, just depending on the wind stress. The bottom currents are generally weak and the bottom

water is virtually stagnant in the summer days shown for 25 and 60 m depth water. In the early winter case, there are weak bottom currents in 25 m water but none in 60 m water. As expected, all currents are reduced when wind speeds are reduced by 25 percent. Figure 4.6b illustrates the case when wake is included, and because of slower winds, water currents are smaller. Currents are of order 0.5 to 1 ms^{-1} on the surface and only 0 to 0.01 ms^{-1} near the bottom.

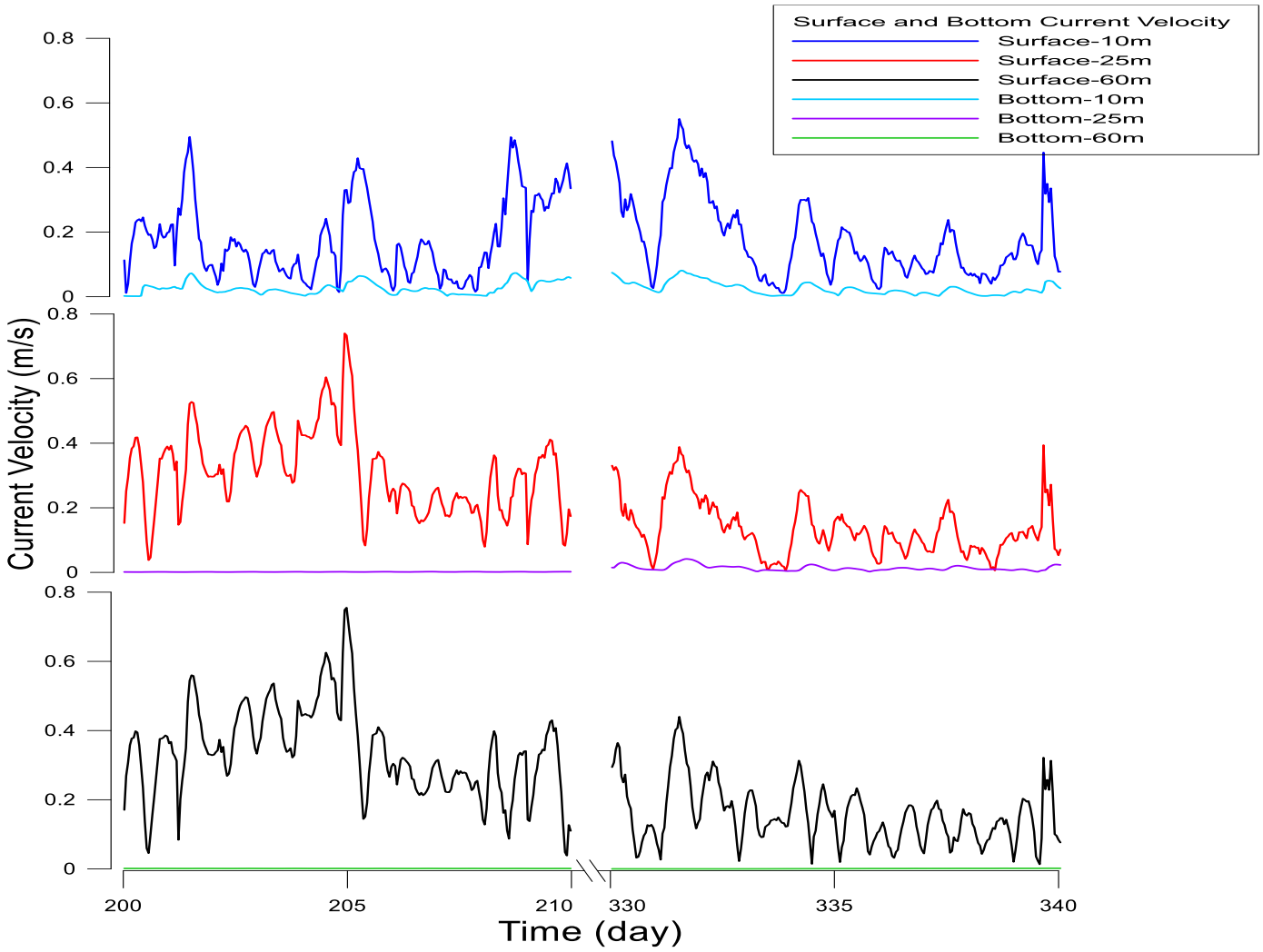

a

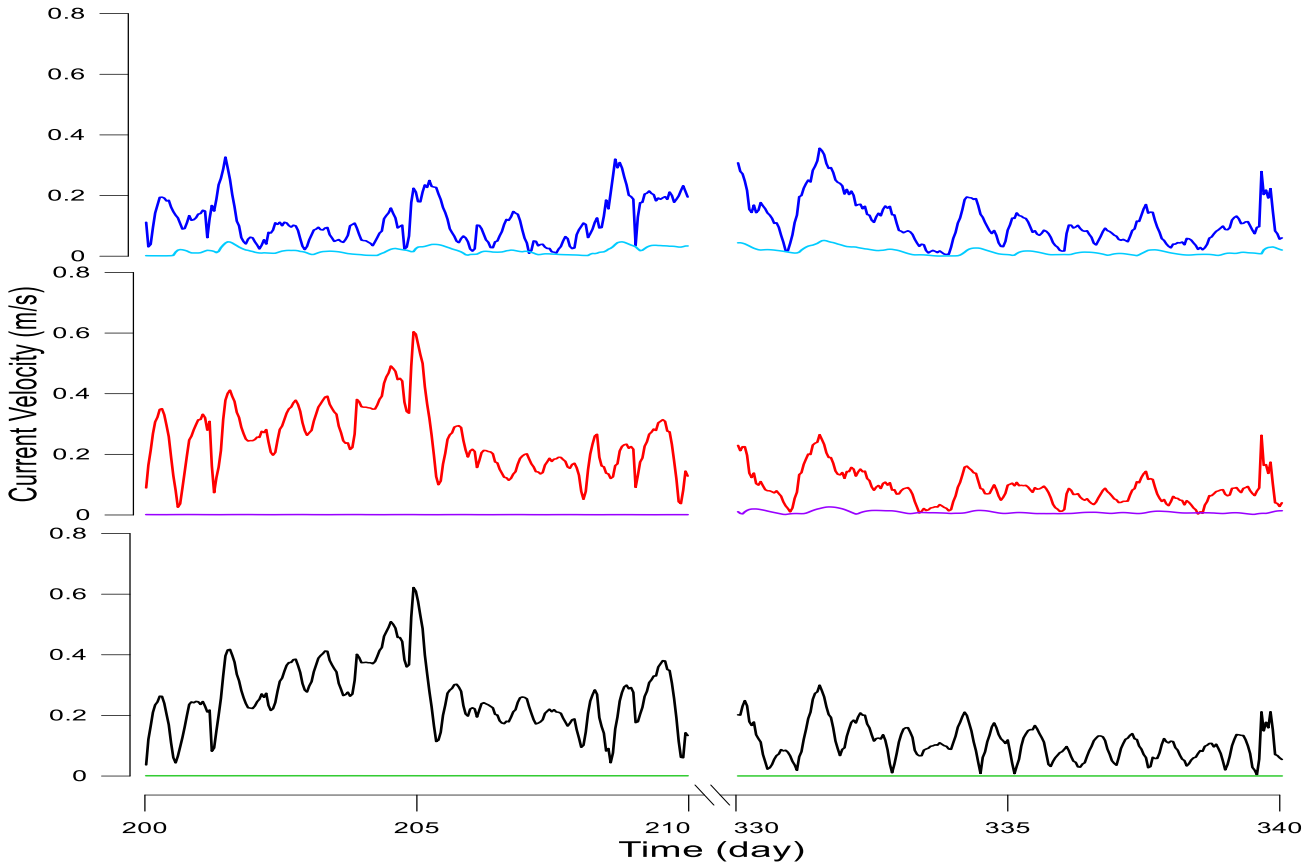

b

Figure 4.6. Near-surface and near-bottom hourly currents for sample 10 day blocks. 1D model results for water depths of 10, 25 and 60 m. a) with measured meteorological input and b) with a 25percent wake reduction in wind speed.

CHAPTER FIVE

THREE DIMENSION LAKE ERIE 2005 SIMULATION

5.1 3D Model Set up

5.1.1 Forcing Functions and Model Initialization

We ran 3D simulation for years 2013 and 2005, with generally similar results. Only the results for year 2005 are shown because of accessibility to the observations and other numerical model results. Despite our best efforts, we could not get access to the original Great Lakes Environmental Research Laboratory water current and temperature observations for either year. Alternatively, we decided to compare our results with the results printed in a reliable paper presenting the work done by Beletsky et al. in 2013. They compared their work with observations and it was a good source for us. Beletsky et al. ran the 2005 simulation so we did the same. In addition, our 2013 simulation results were compared to ELCOM model ones used by CCIW group and, apart from some limitations in obtaining initial condition data such as initial water temperature profile and grid point meteorological data, there was satisfactory agreement.

The model is set to run from midnight April 31st, 2005 to midnight October 31st of the same year. The barotropic time step is set to 15 seconds while the baroclinic one is considered twenty times greater. The Lake Erie water is forced by momentum, heat fluxes at the surface, and tributary flows are represented as current vectors at river mouths. The Detroit River is the main tributary while the Niagara River is the main outflow path. The Detroit River inflow was balanced by the Niagara River

outflow on a daily timescale. So that the lake has zero (net) accumulation of water in the basin since the seasonal cycle of the lake level is not modelled, (evaporation and precipitation are assumed to balance each other in our study). The Detroit River discharge provides the major input of fresh water, nutrients, and sediments. The drainage mouth is about 8 km wide where it joins Lake Erie. The mean river discharge is 5346 m^3/s with a relatively low seasonal variation of 600 m^3/s. The Niagara River is about 1 km wide at the point where Lake Erie joins it, located at the north shore of the eastern basin and has a mean river discharge of 5610 m^3/s. Seasonal variation in the Niagara River is more pronounced and the difference between maximum and minimum water flux reaches approximately 1800 m^3/s, during May-November 2005. River daily discharge obtained from Environment Canada, Canada Centre for Inland Waters, (CCIW). Three-hourly horizontal components of wind velocity, atmospheric pressure (at 1000 hPa- geopotential height), air temperature, relative humidity and cloud cover are available from the National Oceanic and Atmosphere Administration (NOAA). Wind speeds are adjusted to the reference height of 10 meters. The lake is initially at rest and the initial temperature profile data are obtained from CCIW and from the Great Lakes Environmental Research Laboratory (GLERL), which is part of NOAA. There are twenty stations that are distributed on Lake Erie and most of them are located in the central basin. The number of observations is fairly limited in the eastern and western basins. In this study, it is not a constraint as more focus is on the central basin. Some temperature moorings have a string of thermistors spaced vertically every one to two meters from one meter below the surface to the bottom. While in some stations, the available data was from late April to mid-October, in the others it started in early summer. This constraint left us only ten stations out of twenty. Figure 5.1 shows the location of those stations. May 1st, 2005 was chosen as the first day of the simulation period based on the available data. Year 2005 is chosen for the model validation efforts as extensive temperature and current measurements were made in the lake that year. The data from the selected stations were used to interpolate the temperature profile for each grid point in our model

domain. The main constraint in temperature profile interpolation was using the sigma coordinate in the vertical direction. This prevents us from simple interpolation of the water temperature at specific vertical depth along the whole lake domain. Alternatively, we had to interpolate the temperature in each layer number located in the different water level with non-uniform depth varying from one grid to another one. This problem was eliminated by adding new FORTRAN code to the model, which interpolates in both vertical and horizontal directions.

For the interpolation/extrapolation, a bilinear method has been applied. Bilinear interpolation is an extension of linear interpolation. It is assumed that we know the value of the unknown function F at four points $Q_{11}= (x_1,y_1)$, $Q_{12}= (x_1,y_2)$, $Q_{21}= (x_2,y_1)$, and $Q_{22}= (x_2,y_2)$ and to find the value of F at the point (x,y).

$$F(x, y) = ((y_2-y)/ (y_2-y_1)) F(x,y_1) + ((y-y_1)/ (y_2-y_1)) F(x,y_2) \quad (5.1)$$

where:

$$F(x,y_1)= ((x_2-x)/(x_2-x_1)) F(Q_{11}) + ((x-x_1)/(x_2-x_1)) F(Q_{21}) \quad (5.2)$$

$$F(x,y_2)= ((x_2-x)/(x_2-x_1)) F(Q_{12}) + ((x-x_1)/(x_2-x_1)) F(Q_{22}) \quad (5.3)$$

This method is applied to interpolate the water temperature for each grid point of the lake domain in the horizontal direction from the observations at multiple depths. Then we need to calculate the water temperature data for the vertical grids in each layer (here 25 sigma-layers). By dividing the water depth of each grid point (column) by 25 and calculating the depth of each vertical layer and applying the bilinear method once again, we were able to interpolate/extrapolate the water temperature of all grid points in each sigma layer.

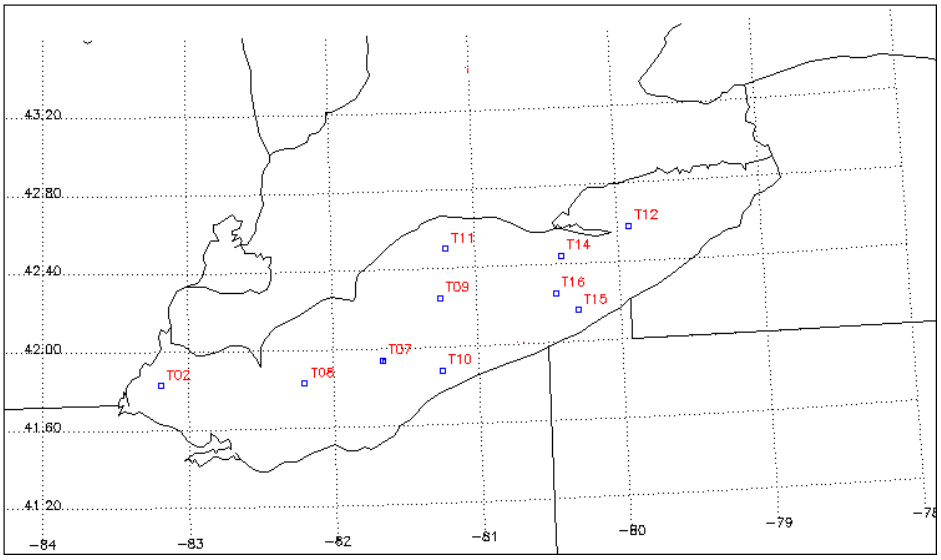

Figure 5.1: Lake Erie mooring stations, 2005. [GLERL, 2005]

Initial water temperature is provided to the model at the very first time step to start the simulation (run) with. This means, to start the run at midnight of April 31st we need to know the water temperature both horizontally and vertically. After this very first time step, an external continuous atmospheric forcing data file updates the run in each time step.

From the data set, initial water column temperatures in eastern, central and western basins vary from 2.5 °C to 6.7 °C, 4.7 °C to 5.5 °C and 4.79 °C to 4.75 °C, respectively from bottom to the surface. These measurements illustrate that the eastern basin (the deepest), has a stable stratification condition on the first day of run so that colder water lasting from winter remains near the bottom while surface waters are warmer due to the more intense solar radiation. This trend weakens by moving westwards and entering into the shallower waters so that in the shallowest basin (western) water is well mixed.

The simulation in the case of no wake is initiated with the uwind (wind velocity component in x-direction), vwind (wind velocity component in y-direction), atmospheric pressure, air temperature, relative humidity and cloud cover values of 2.9 m/s, 0.17 m/s, 98914.09 N/m^2, 9.9268 °C, 0.6175 and 0.36, respectively. Apart from wind, solar radiation (Q_{rad}) is another significant input.

To show the model validation, stations 4500, 45132, 45142 and Windsor Airport stations are selected to present the observed and input metrological data and compare the modeled surface water temperature with observation. As the simulated domain covers an area of 384 km by 172 km (along the horizontal X and Y directions, respectively) and weather condition may vary within a relatively wide domain so the observed and input values only belong to these specific points (stations) and vary in other grid points of the domain.

Figures 5.2 and 5.3 compare the monthly-averaged 10-m winds over Lake Erie from May to October 2005 driven from GEM (scale of 5 m/s) and NARR (scale of 2 m/s), respectively. GEM wind velocities are generally stronger than NAAR by a factor of 2 approximately. Comparison of 2005 NARR data with buoy and Windsor airport observations are discussed later in chapter 5. On average NARR wind, analyses are slightly high relative to Windsor airport and slightly low relative to buoy data but not by a factor 2, (Figures 5.32 – 5.35).

Monthly-averaged wind velocity does not provide a clear idea about the wind speed in Lake Erie, so instantaneous wind velocity plots of a few random days from May to October 2005 at 5 a.m. UTC are displayed in Figures 5.4 to 5.9. As the plots show, the instantaneous winds (plots of scale 10 m/s) are stronger compared to the monthly-averaged ones (plots of scale 2 m/s). October 15th, has the strongest winds of the order of 10 m/s and higher, while May 5th, has the slowest winds of the order of a few m/s. However as mentioned above these days are selected randomly and there was no preference in selecting these days and the only purpose is to highlight the difference between the instantaneous and the monthly-averaged wind velocity.

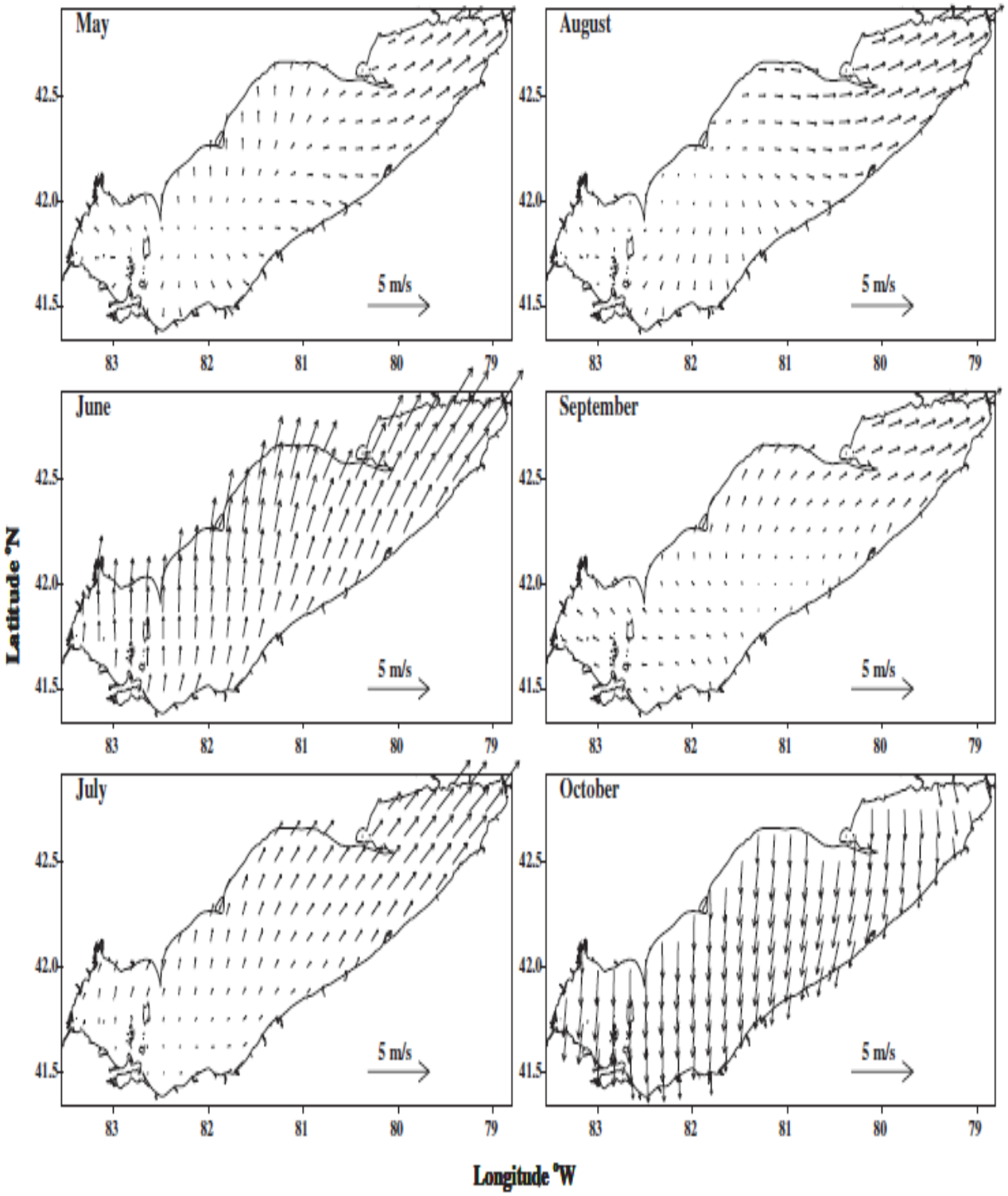

Figure 5.2: Spatial plots of monthly-averaged winds (GEM) in 2005. (Beletsky et al., 2013)

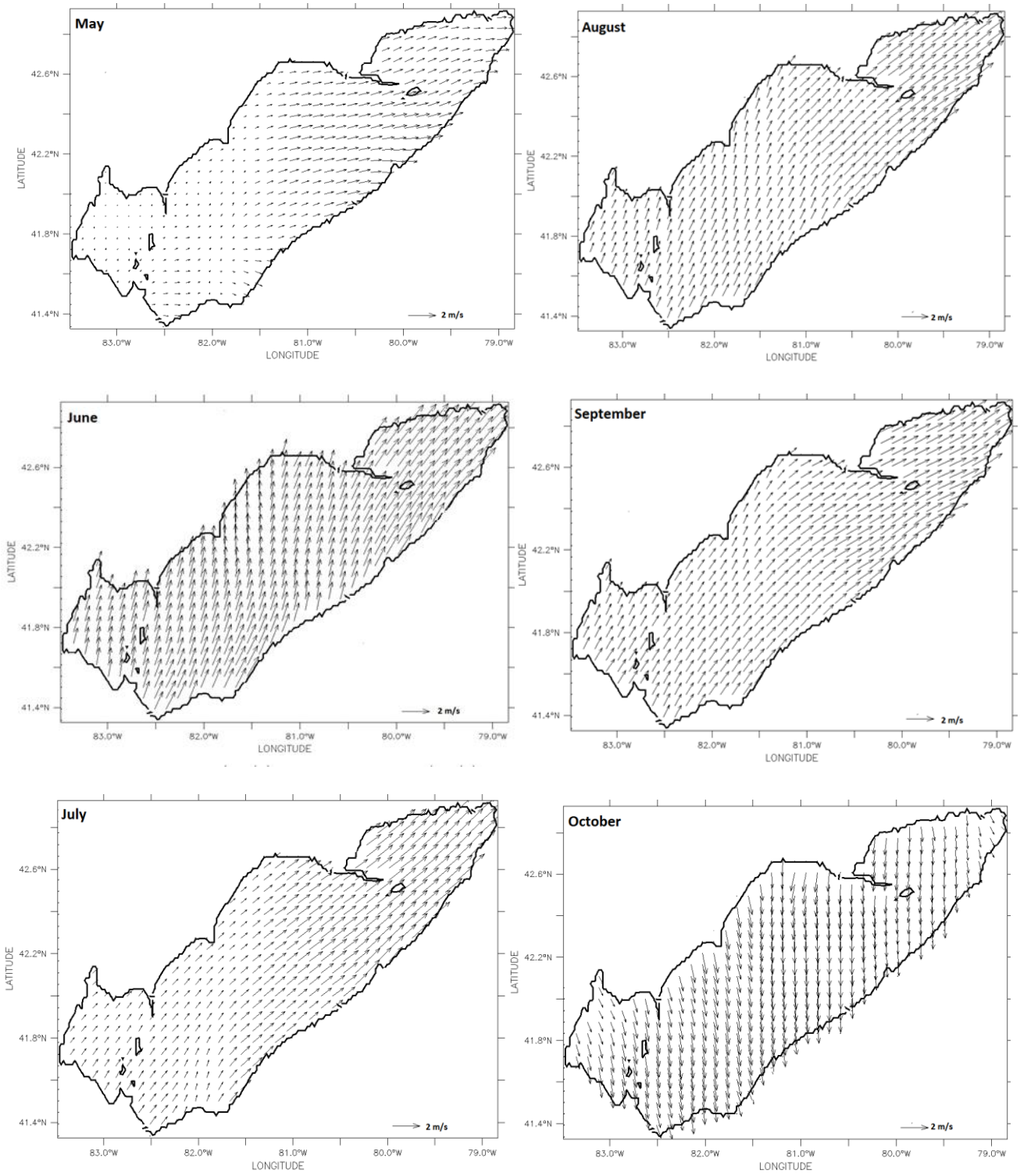

Figure 5.3: Spatial plots of monthly-averaged winds (NARR) in 2005, (May-October).

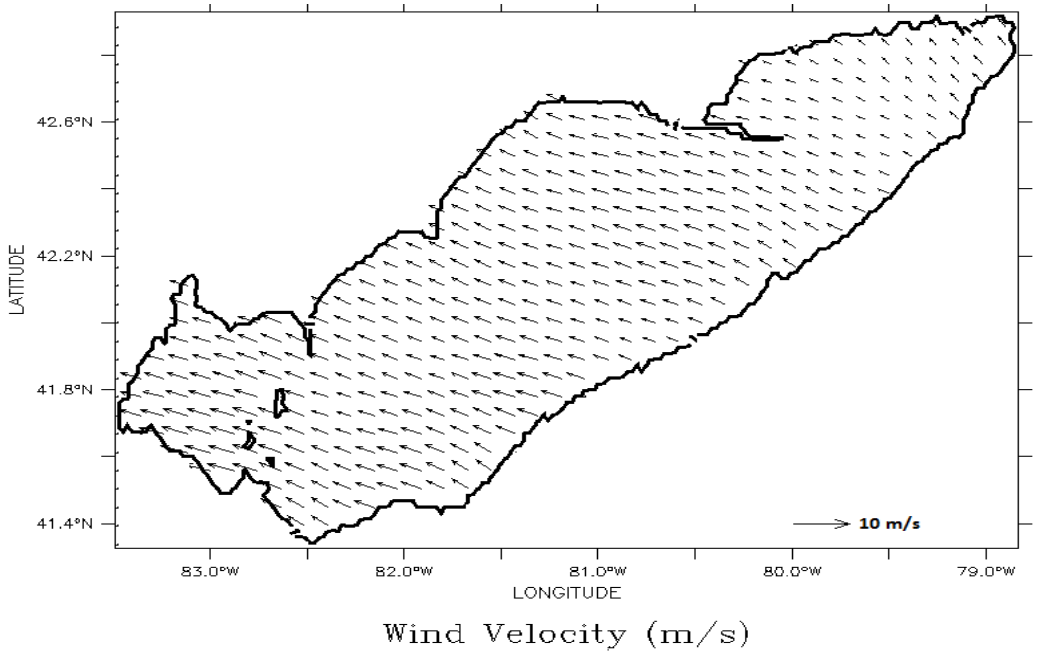

Figure 5.4: Spatial plots of NARR winds - UTC 5 A.M. May 5, 2005.

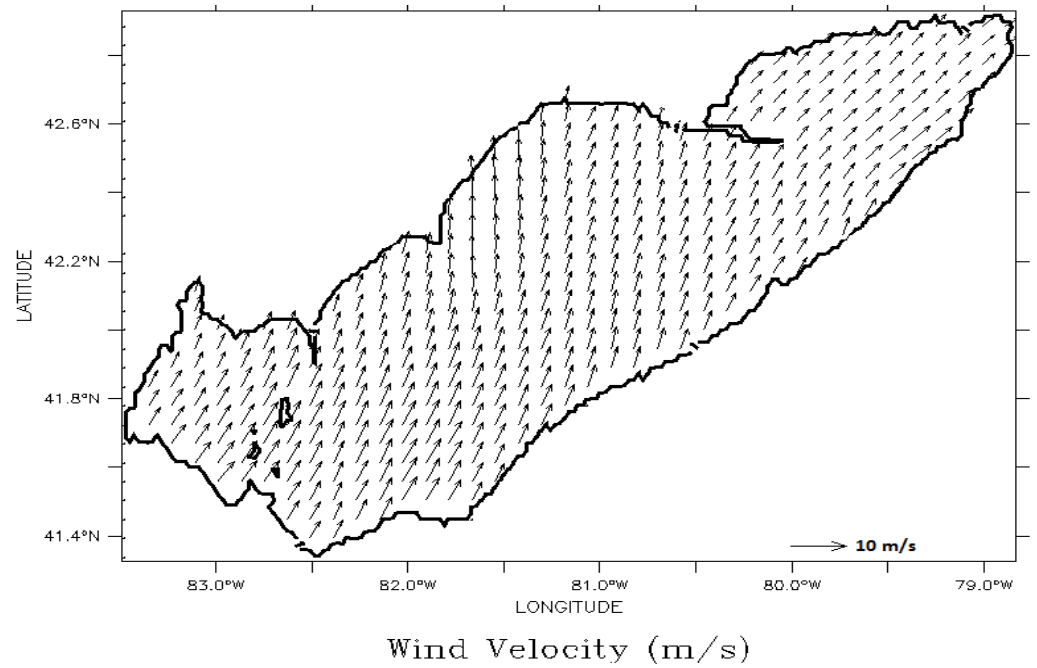

Figure 5.5: Spatial plots of NARR winds - UTC 5 A.M. June 8, 2005.

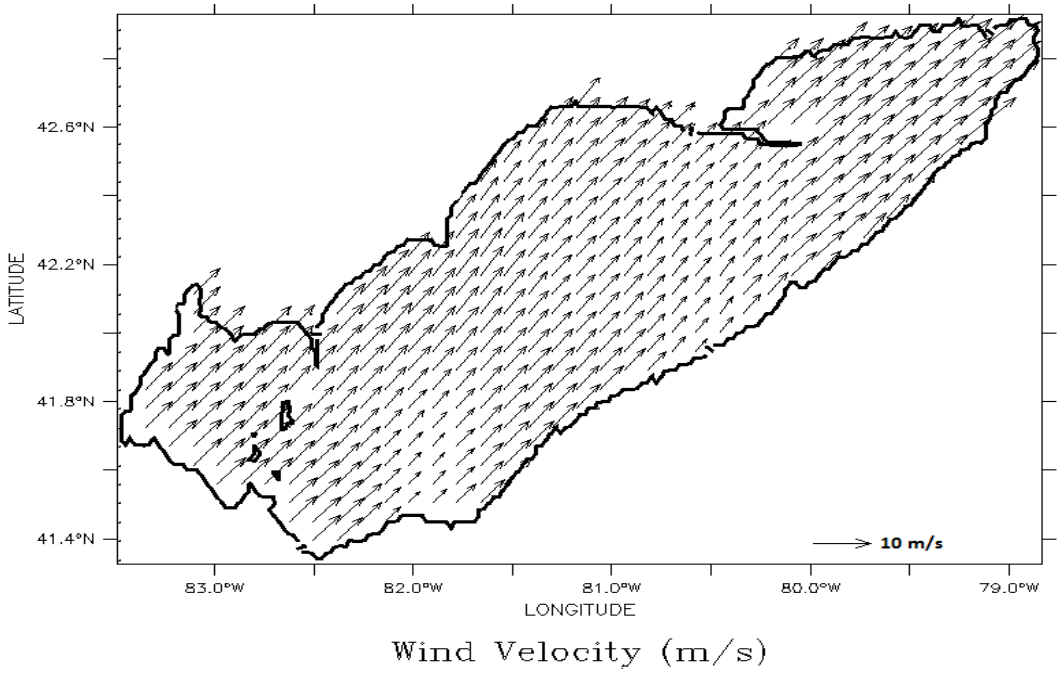

Figure 5.6: Spatial plots of NARR winds - UTC 5 A.M. July 18, 2005.

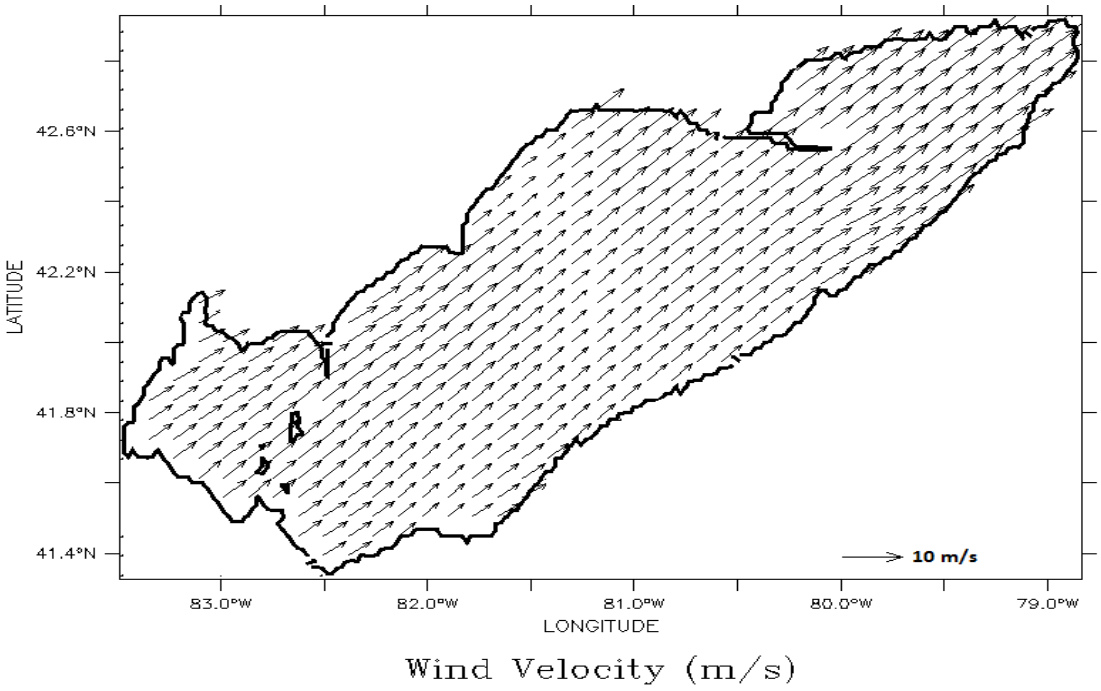

Figure 5.7: Spatial plots of NARR winds - UTC 5 A.M. August 10, 2005.

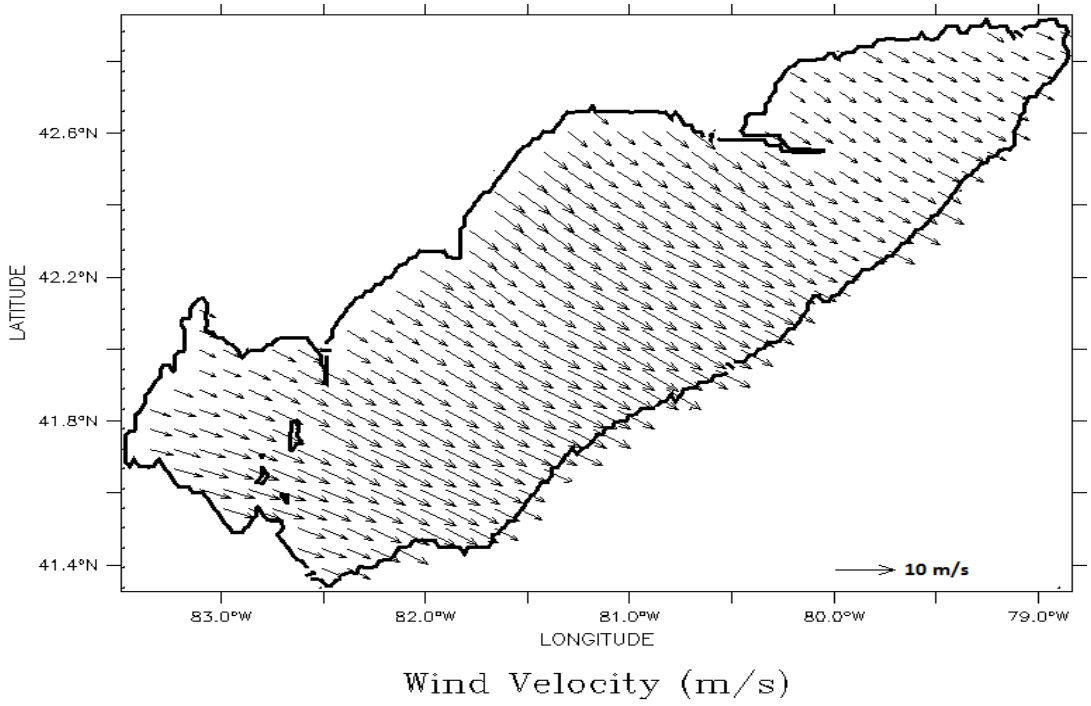

Figure 5.8: Spatial plots of NARR winds - UTC 5 A.M. September 16, 2005.

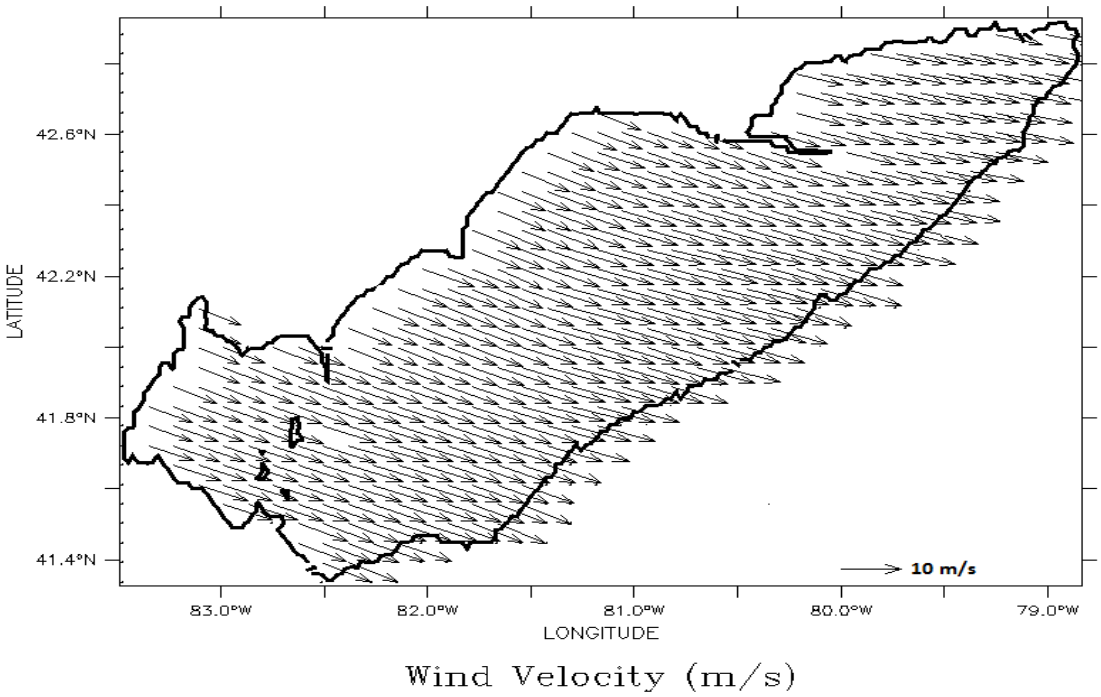

Figure 5.9: Spatial plots of NARR winds - UTC 5 A.M. October 15, 2005.

5.1.2 Model Horizontal Domain and Bathymetry

The bathymetry of Lake Erie has been compiled as a component of a NOAA project to rescue Great Lakes lake floor geological and geophysical data and make it more accessible, (NOAA, 2017). The bathymetry data file was obtained from CCIW and NOAA. A horizontal spatial resolution of 2 km by 2 km has been chosen for this run and the domain has 194 by 88 grid points in the x and y-directions, respectively. A spherical coordinate system is used so the latitude and longitude resolutions are 0.0184069° and 0.0240958°, respectively, and correspond to the 2 km – Cartesian resolution. The domain starts southwest at 41.336 N and 83.4741 W and ends northeast at 42.919 N and 78.8477 W.

As mentioned before, meteorological data are obtained from NARR. North American Regional Reanalysis grid uses the Northern Lambert Conformal Conic grid. The NARR model data is output onto a 349 by 277 Lambert Conformal Conic grid. This has a resolution that is approximately 32 km. The coverage area is shown in Appendix C and Lake Erie in Figure 5.10. By interpolation the 32 km – Lambert Conformal Conic grid data is converted to a 2 km – UTM (Universal Transverse Mercator) latitude and longitude data format.

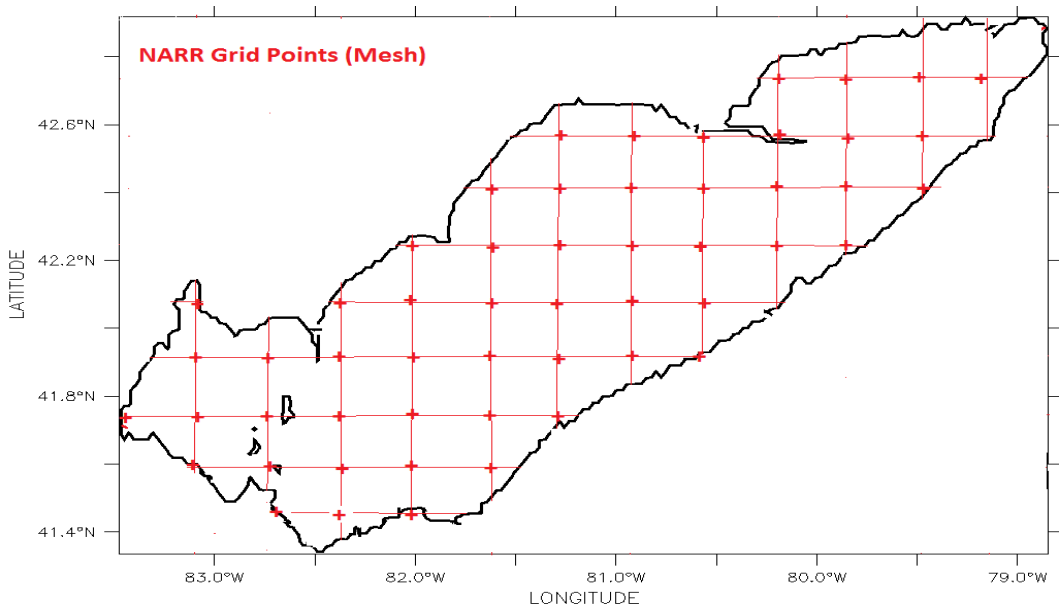

Figure 5.10: NARR model data Lambert Conformal Conic grid points in Lake Erie.

In the vertical direction, the water column is divided into 25 uniform sigma layers. Based on this division, west, central, and east basins have a maximum vertical resolution of 10.4/25, 24/25 and 64/25, or about 0.41, 0.96, and 2.56 m, respectively. This distribution with depth translates into about 1 m vertical resolution in most of the central basin (where the turbines are deployed), and about 3 m in the deepest part of the eastern basin. These vertical and horizontal resolutions are selected based on previous model applications and the computational demands of the ecological models in the lake.

Because a C-grid is used in the vertical direction, the calculations are done in the centre of each cell, so the surface and bottom layers are not located exactly on the surface and bottom of the lake. They are essentially near-surface and near-bottom layers, which are not at fixed depths as the model uses sigma-coordinates. Therefore, the top grid depth varies slightly corresponding to the water depth in each cell but wind mixing near the surface and zero heat flux at the bed will minimise the impacts.

5.2 3D Model Result

5.2.1 Wind Patterns and Water Hydrodynamics - Current Velocity and Circulation

Investigating the local three-dimensional velocities for Lake Erie as a shallow lake is important since the velocities in the lake vary greatly with horizontal position and depth. The length scale of Lake Erie is such that Coriolis force is important but the variation of Coriolis parameter with latitude is not significant. Considering the wind-driven currents far away from the shoreline in large lakes, it is assumed that there is a layer at the top and bottom, which is not in geostrophic balance. Usually, it is assumed that the thickness of this Ekman layer is small compared to the depth of the lake (see Appendix B). However, in shallow lakes or shallow parts of a lake, geostrophic dynamics are not applicable, as significant portions of the lake have a depth on the order or smaller than the Ekman layer. Lake Erie falls into the latter category, (Gendney, 1972).

Lake Erie monthly-averaged (May to October 2005) current velocity plots are shown in Figures 5.11 to 5.16. Plots a and b illustrate depth-averaged horizontal velocities from the POM numerical model using GEM modelled winds and spatially uniform winds, respectively, ran by Beletskey et al., 2013. They ran two experiments. One by using the GEM winds and another by running the model with spatially uniform (lake average) winds while all other input fields and model parameters were kept unchanged to eliminate the wind vorticity. The velocity length scale for POM current plots is 10 cm/s. Plots c show the corresponding COHERENS model results using NARR modelled winds with a velocity length scale of 5 cm/s. POM model results are reported to be in good agreement with the observed hydrodynamic and temperature of Lake Erie. Because we did not have access to the observed current and temperature data, COHERENS current and temperature plots are compared with POM outputs.

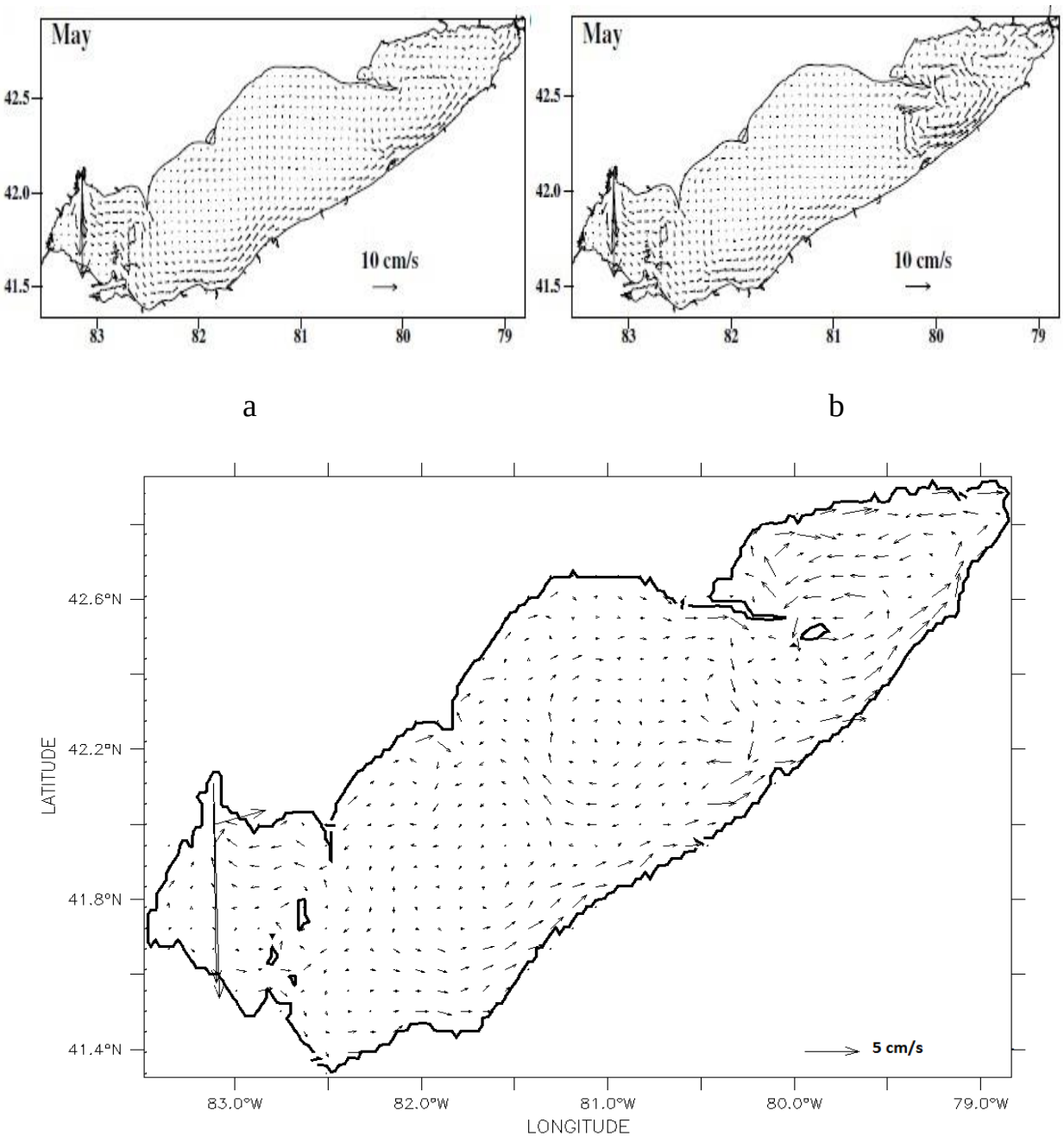

Figure 5.11: May depth-averaged currents (a) POM model using GEM modelled winds, (b) POM model using spatially uniform winds (Beletsky et al., 2013) and (c) COHERENS model, 2005.

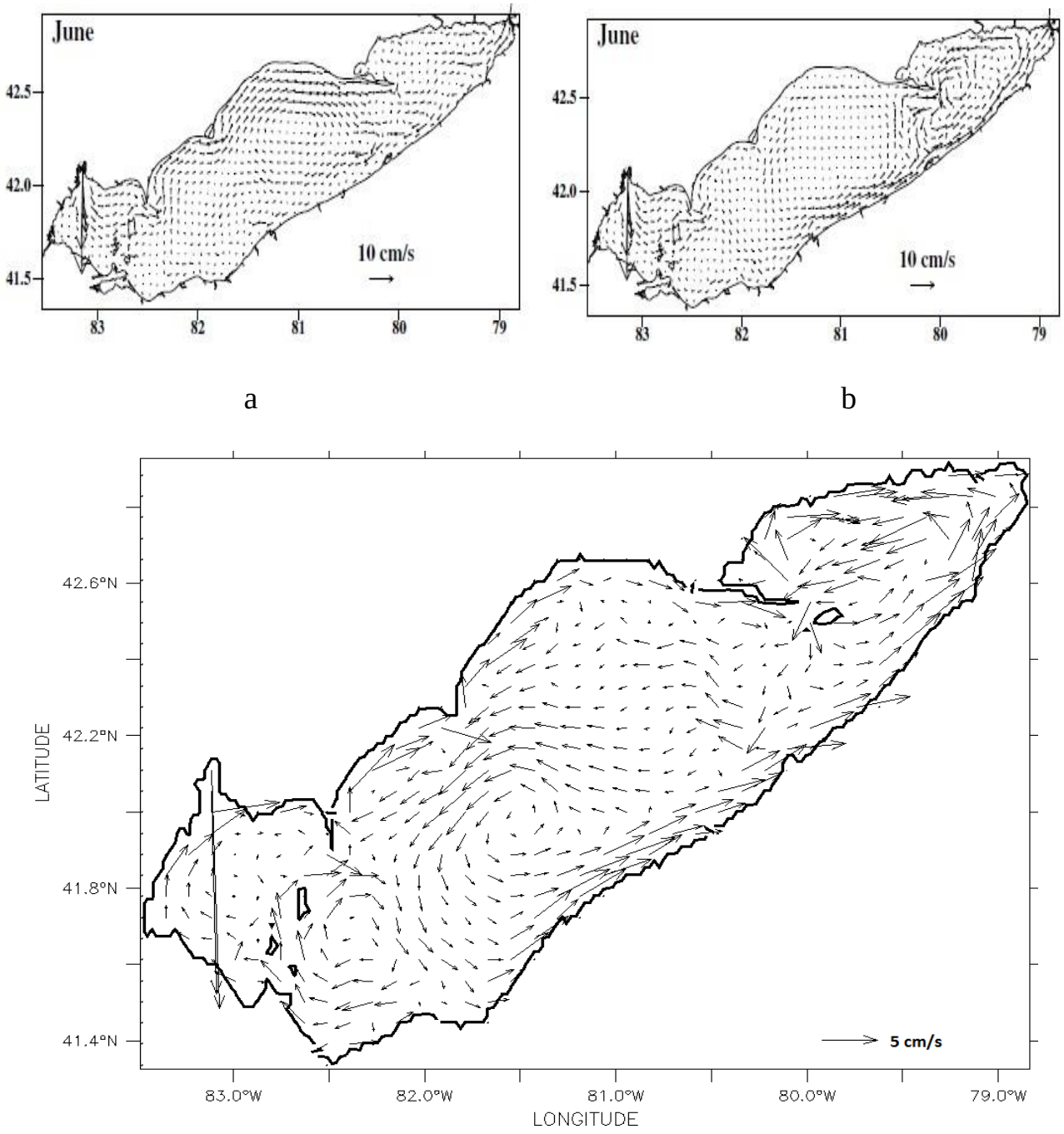

Figure 5.12: June depth-averaged currents (a) POM model using GEM modelled winds, (b) POM model using spatially uniform winds (Beletsky et al., 2013) and (c) COHERENS model, 2005.

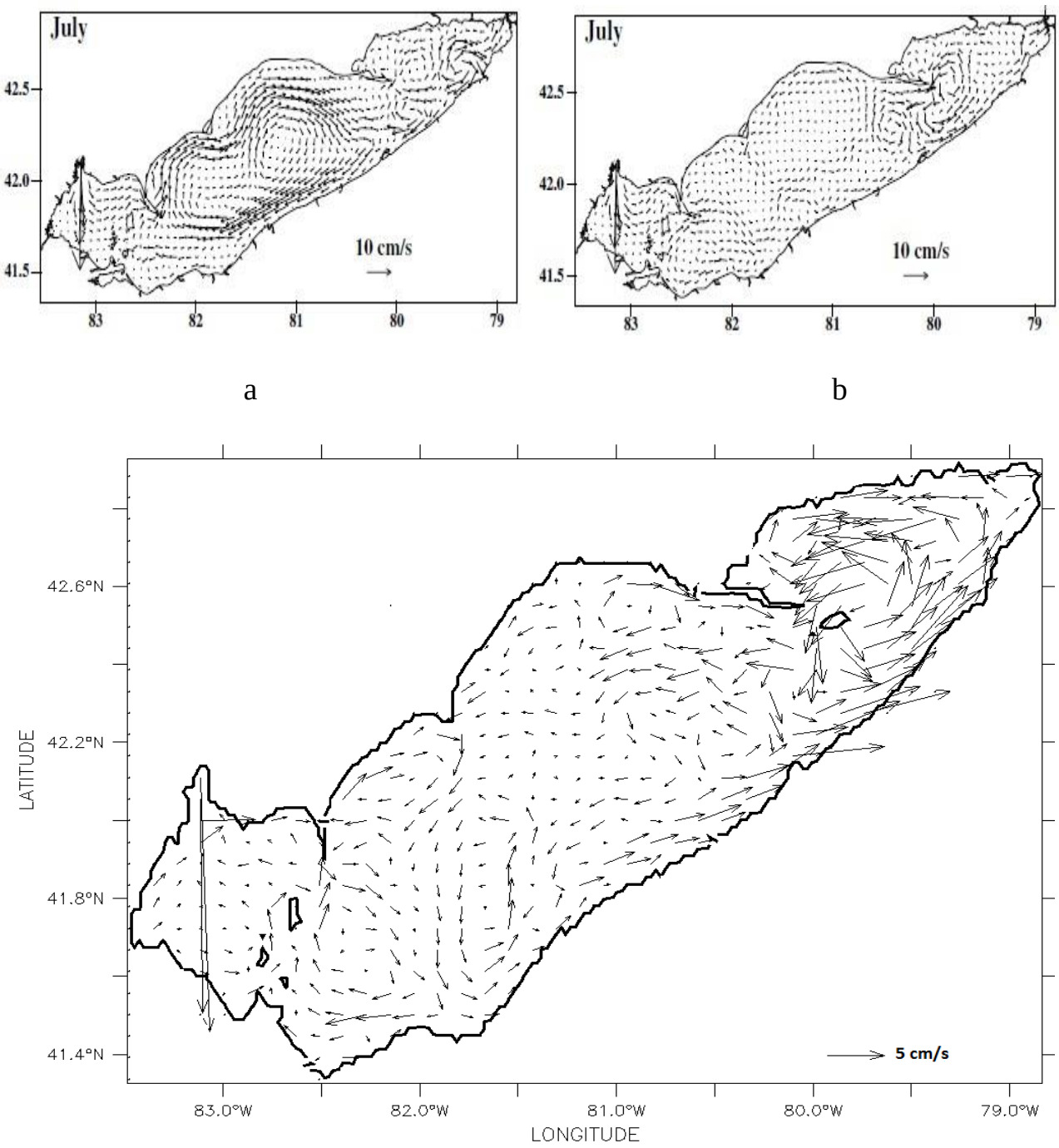

Figure 5.13: July depth-averaged currents (a) POM model using GEM modelled winds, (b) POM model using spatially uniform winds (Beletsky et al., 2013) and (c) COHERENS model, 2005.

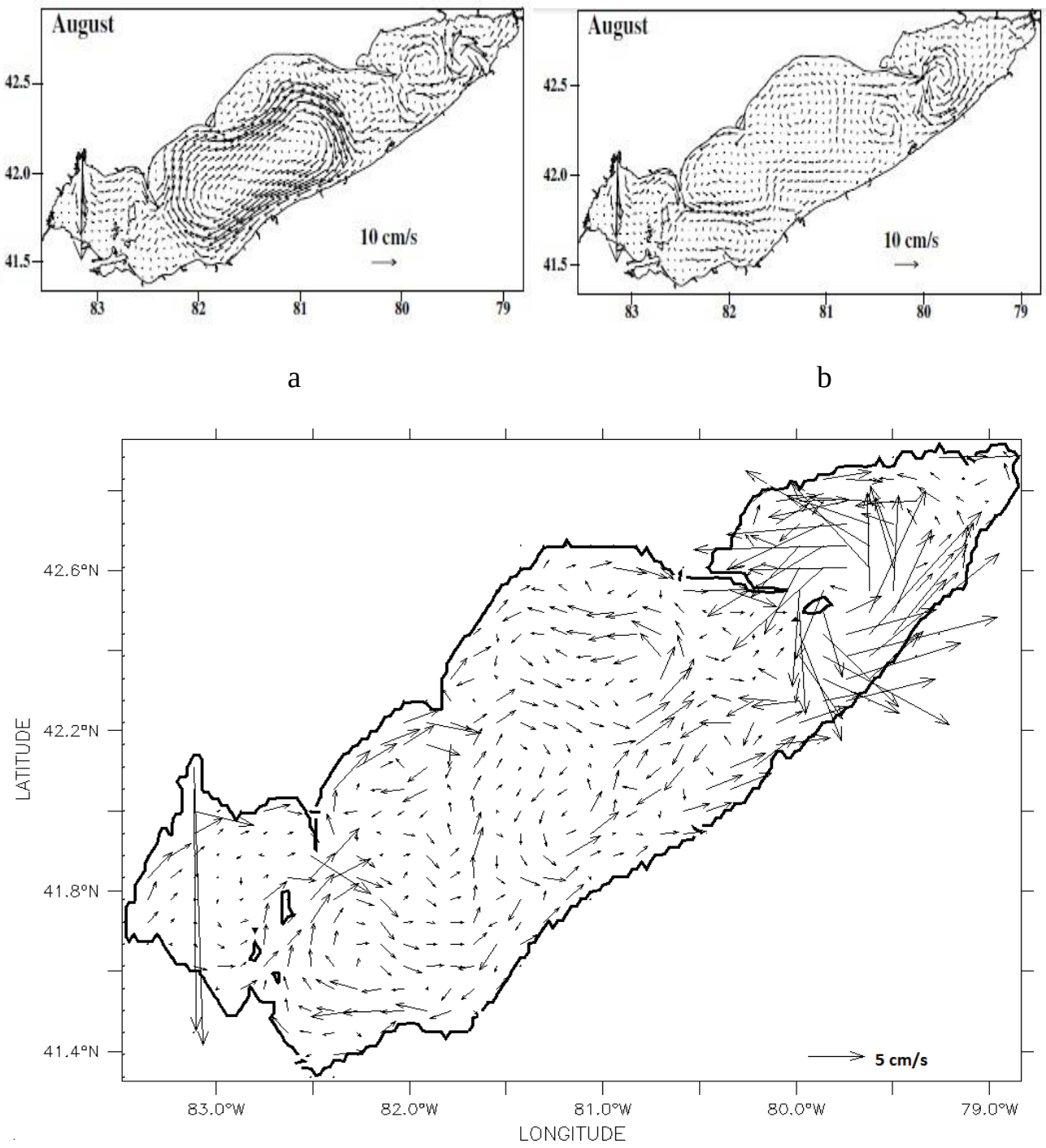

Figure 5.14: August depth-averaged currents (a) POM model using GEM modelled winds, (b) POM model using spatially uniform winds (Beletsky et al., 2013) and (c) COHERENS model, 2005.

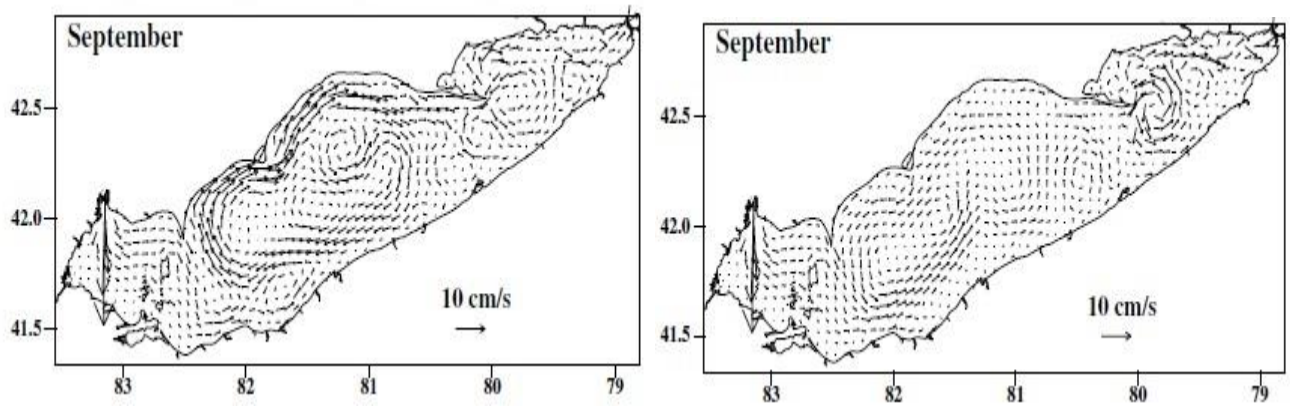

a

b

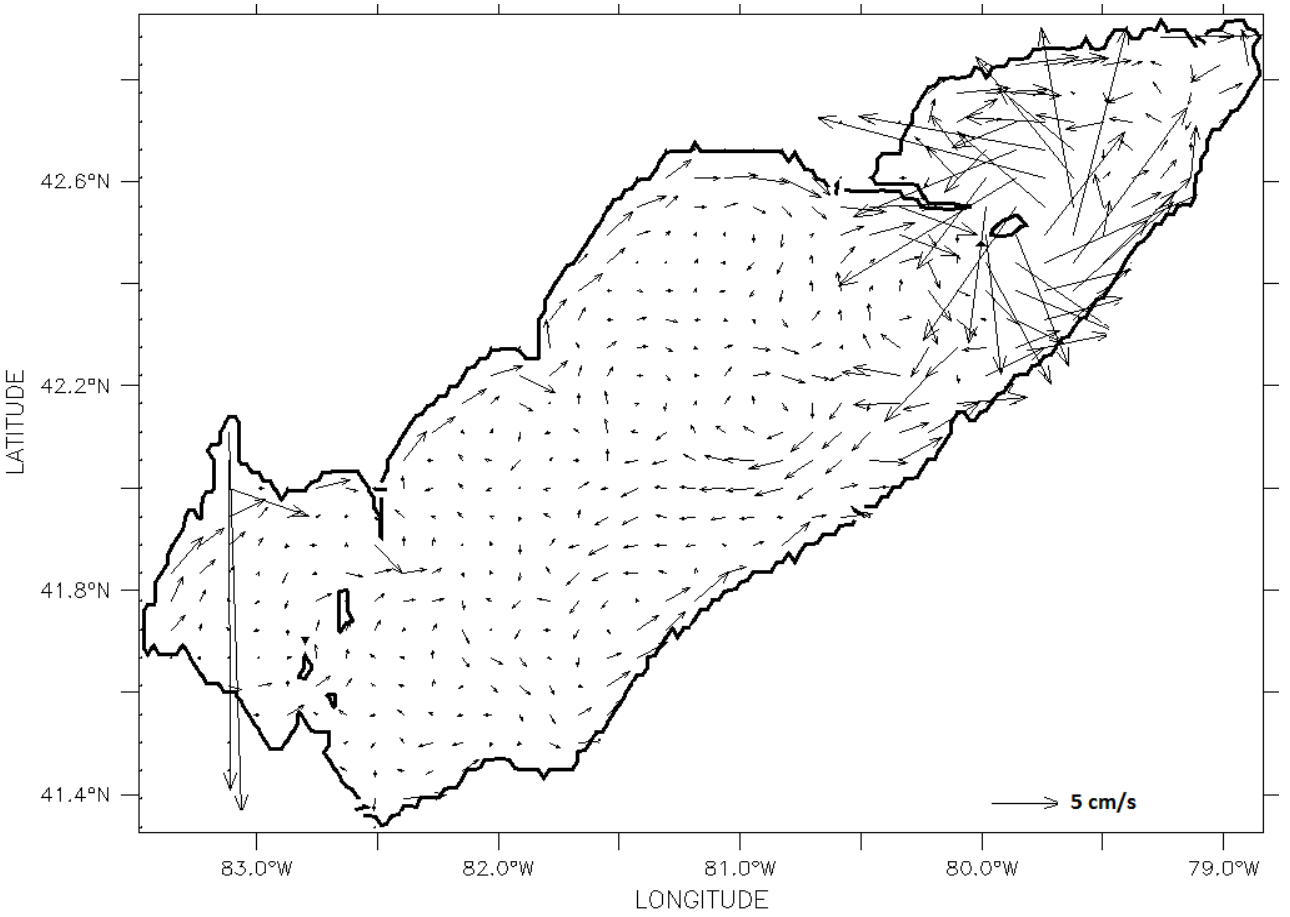

c

Figure 5.15: September depth-averaged currents (a) POM model using GEM modelled winds, (b) POM model using spatially uniform winds (Beletsky et al., 2013) and (c) COHERENS model, 2005.

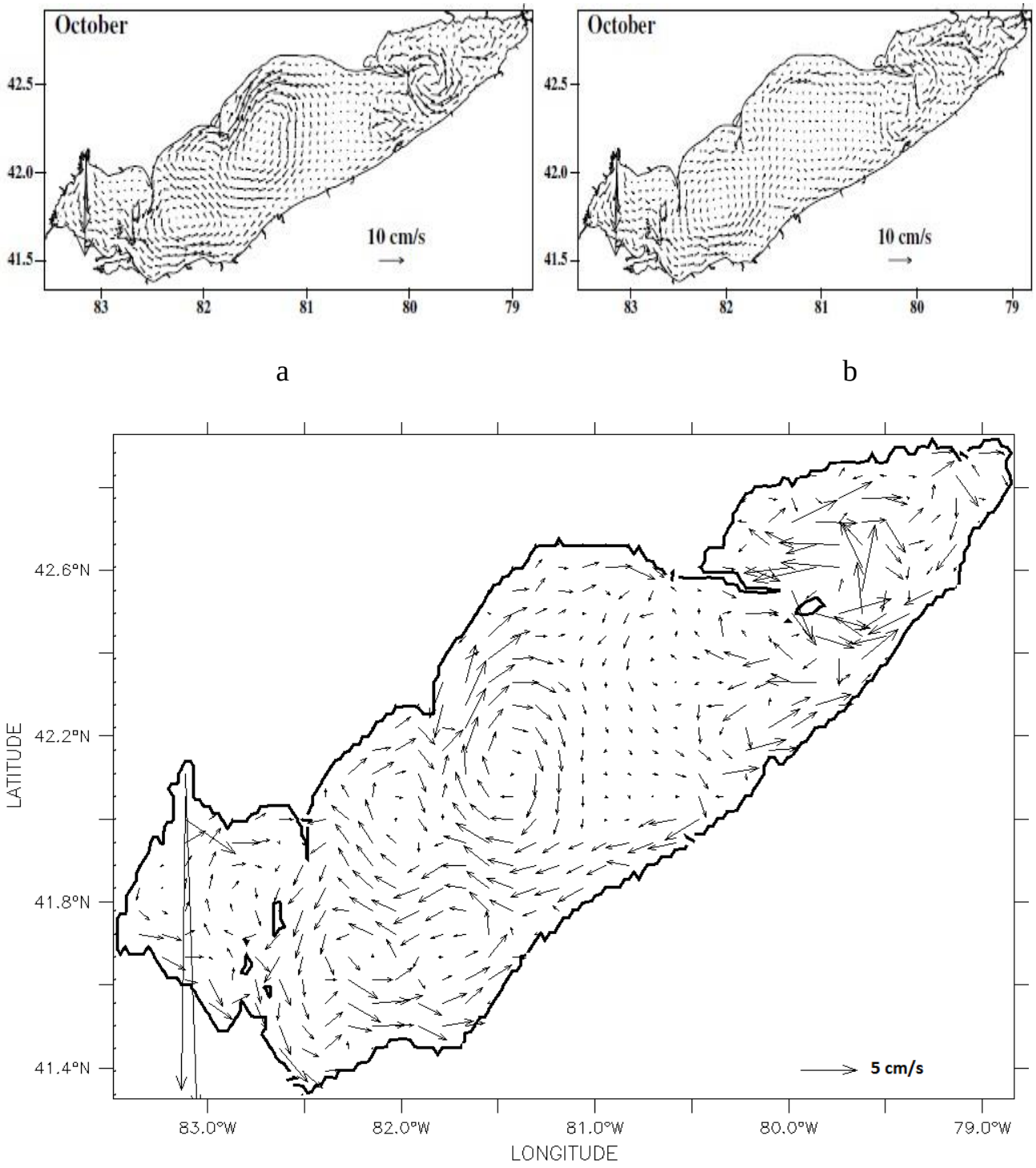

Figure 5.16: October depth-averaged currents (a) POM model using GEM modelled winds, (b) POM model using spatially uniform winds (Beletsky et al., 2013) and (c) COHERENS model, 2005.

The large-scale monthly and depth-averaged circulation shows significant variability during the simulated period (May to October 2005). In May (Figure 5.11c), depth-averaged currents are weak and of the order of only a few cm/s. However, there are west-east currents on the north and south shores of the western basin, which are driven by the water discharge of the Detroit River. There are two weak anticyclonic and cyclonic asymmetric gyres in the northeast and southwest of the central basin and a stronger (about 2 cm/s) cyclonic gyre in the eastern basin. The differences in the main gyres are a direct result of the differences in the bottom topography, (Beletsky et al., 2013).

In June (Figure 5.12c), the water picks up speed and particularly in the shoreline region current speeds reach 5 cm/s or more. The southern half of the lake is strongly affected by the southwest winds, which drive currents to the northeast. A cyclonic gyre takes the place of the two smaller gyres in the central basin while a small anticyclonic gyre forms on the boundary of the western and central basins near Peele Island. In July (Figure 5.13c), the cyclonic gyre in the central basin weakens and splits while the anticyclonic gyre on the boundary of the western and central basins retains its strength. During August (Figure 5.14c), a small anticyclonic gyre forms in the middle of the central basin and the anticyclonic gyre in the central basin gets stronger. A large anti-cyclonic gyre forms in the central basin during September (Figure 5.15c), and reaches its maximum value during October (Figure 5.16c).

In the eastern basin, a cyclonic circulation develops and speeds up during June to October so that in October current speeds reach 20 cm/s. This cyclonic direction is in geostrophic balance with a dome-shaped thermocline. Generally, an anticyclonic circulation occupies the northern part of the central basin while a small cyclonic gyre exists on the southwestern parts. The anticyclonic gyre is largely due to a narrow underwater ridge that extends southeast, (Beletsky et al., 2013).

In the middle of the central basin, currents are in general smaller than the shoreline currents. This can be explained by the large subsurface return water currents, which are in the opposite direction to the surface current, (not shown). Also, the main transport of water is via both shoreline regions

(northeastwards) while there is a return flow in the central region. The southern shoreline flows are essentially parallel to the shore in an easterly direction until October. But, overall north shore currents differ markedly from those in the central region of the lake. The flow is mainly along shore and of higher velocity near the shorelines. Stratification, bottom topography, inertial acceleration, and friction are among the important factors in the boundary regions. The north part of the western basin is responsible for carrying more water into the central basin. Water exits away through the Niagara River on the northeast part of the lake.

Comparing the COHERENS results (Figures 5.11 to 5.16, c), (and ELCOM model, used at CCIW -Luis et al., 2013 – not shown) with POM numerical model results (Figures 5.11 to 5.16, a), (Beletsky et al., 2013) - which are in turn compared with observations and field measurements - there is generally fairly good agreement between COHERENS (and ELCOM) model results with the POM model. However, in some cases, some discrepancies between models were observed.

The central basin water circulation patterns produced by POM were compared with observations and the results showed the overall anticyclonic circulation. While a cyclonic gyre in the eastern basin, which is driven by the density gradient, is seen, the central basin is almost shallow (less than 25 meters), so is under the effect of the prevailing wind vorticity. The eastern basin observed currents in the deep parts were weaker than the numerical model results (POM, COHERENS, and ELCOM), a possible explanation might be stronger actual anticyclonic wind vorticity than in GEM and NARR reanalyzed winds. Another factor can be the need for finer spatial resolution in the models (smaller than 2 km), (Beletsky et al., 2013).

An important difference between COHERENS and POM results is the wind data used in the models. Beletsky et al. (2013), used a 15-km resolution winds obtained from the original version of the Global Environmental Multi-scale (GEM) forecast model, which is run for operational forecasts in

Canada. COHERENS and ELCOM models' wind data are primarily based on NARR reanalyzed data with 32-km resolution.

Beletsky et al. (2013) had also used observed winds to drive the model but they found that for Lake Erie the winds produced by a mesoscale atmospheric model were superior to observed winds in reproducing both the observed thermocline shape and type of circulation pattern in the central basin.

Comparison of monthly-averaged GEM and NARR modelled winds (Figures 5.2 and 5.3) shows that during the May to October period they were largely from west to east. But GEM winds were stronger than NARR winds and also had a clearer and visible anticyclonic vorticity over the central basin. This can be caused by monthly averaging. This is probably the most important factor explaining why there are two cyclonic and anticyclonic gyres in the central basin in COHERENS, while there is a dominant giant anticyclonic pattern in POM circulation results. As GEM winds are stronger and have an anticyclonic vorticity, they impact water currents more strongly and are the dominant mechanism governing the central basin. With weaker and more cyclonic southwest to northeast NARR wind stress vorticity decreases, while baroclinic effects dominate and this explains why there are two weaker and smaller gyres.

On the other hand, Beletsky et al. (2013), confirms that anticyclonic circulation is not the sole and dominant pattern in the central basin and in some years two cyclonic and anticyclonic gyres are seen. Also, he mentions "recent hydrodynamic models of Lake Erie that used either observed winds (Schwab et al., 2009; Fujisaki et al., 2012 and 2013) or relatively coarse-resolution (36 km) atmospheric model winds (Bai et al., 2013) produced quite different thermocline and circulation patterns in the central basin. Schwab et al. (2009) and Fujisaki et al. (2013) presented a two-gyre circulation pattern, with an anticyclonic gyre occupying roughly the north and eastern parts of the central basin while a cyclonic gyre occupied the south and western parts. Circulation presented by Bai et al. (2013) also shows a two-

gyre pattern but the line separating the northern anticyclonic and southern cyclonic gyres runs parallel to the longitudinal axes of the lake ‘, (Beletsky et al., 2013).

One main reason for the deficiency in the observed winds is that they are mostly measured at the land-based stations and the meteorological buoys are located rather close to the lakeshore. These can miss important details in the spatial wind structure over the lake. Finally, Beletsky et al. (2013), confirms that the GEM winds produce an exaggerated bowl-shaped thermocline and circulation pattern in the central basin, so the GEM model analysis may need improvement.

Figures 5.11b to 5.16b, show plots for the case where the POM model is driven by spatially uniform winds for which the wind vorticity effect would be eliminated. Beletsky et al., (2013), concluded that the resulting thermocline retained its dome shape in the eastern basin. Circulation in the shallow parts of the eastern basin switched from anti-cyclonic to cyclonic during the June to August period, while the current and thermocline in the deeper parts did not change and only current speed increased. In the central basin, circulation reversed and became mostly cyclonic. Another important effect of eliminating anticyclonic vorticity in the wind field was an increased hypolimnion thickness in the central basin and an extension of the stratification period to October.

In the warm months of June to August, when the NARR winds were more uniform, there is a better agreement between COHERENS water circulation results and with the POM results. The reason is the wind pattern. This uniformity decreases the effect of vorticity, which consequently diminish the anticyclonic effect in the water. However, September and October COHERENS water circulation plots are in better agreement with POM plots and with realistic winds (Figures 5.15a and 5.16a), and the dominant anticyclonic circulation prevailing in the central basin is more clearly observed. This can be explain by the building up of vorticity in the stronger winds of the cooler months which makes the COHERENS wind fields more compatible with GEM and NARR models.

5.2.2 Temperature

Air temperature, solar radiation, and wind stress are the main variables influencing the heat balance of the lake water. A mutual interaction between water and the atmosphere above determines the water temperature which follows the air temperature behavior but with a time phase lag. Water temperature is crucial for lake dynamics. Temperature is the primary driver of the vertical stratification, and thus directly affects vertical exchanges of mass, energy, and momentum within the water column. Water temperature plays a key role in influencing the aquatic ecosystem of lakes, which usually adapts to a specific range of physical and environmental conditions. Water temperature in lakes is governed by a complex heat budget. It is evident that any significant changes to water temperature directly affects the composition and richness of the ecosystem, (Piccolroaz et al., 2013). This is one reason to use a reliable numerical model to produce a reliable simulation.

Stratification affects the vertical water circulation. The static stability of a layer of warm water floating on cool water restricts vertical circulation. During periods of low wind, a substantial portion of the water column maybe stratified stably enough to virtually eliminate vertical turbulence, (Boyce et al., 1989). Prevailing meteorological conditions and bathymetry are principal among factors governing thermocline locations and depth so the thermocline depths vary from year to year. Generally, thermocline fluctuations correspond to the wind and the upper layers (hypolimnion) current speed fluctuations.

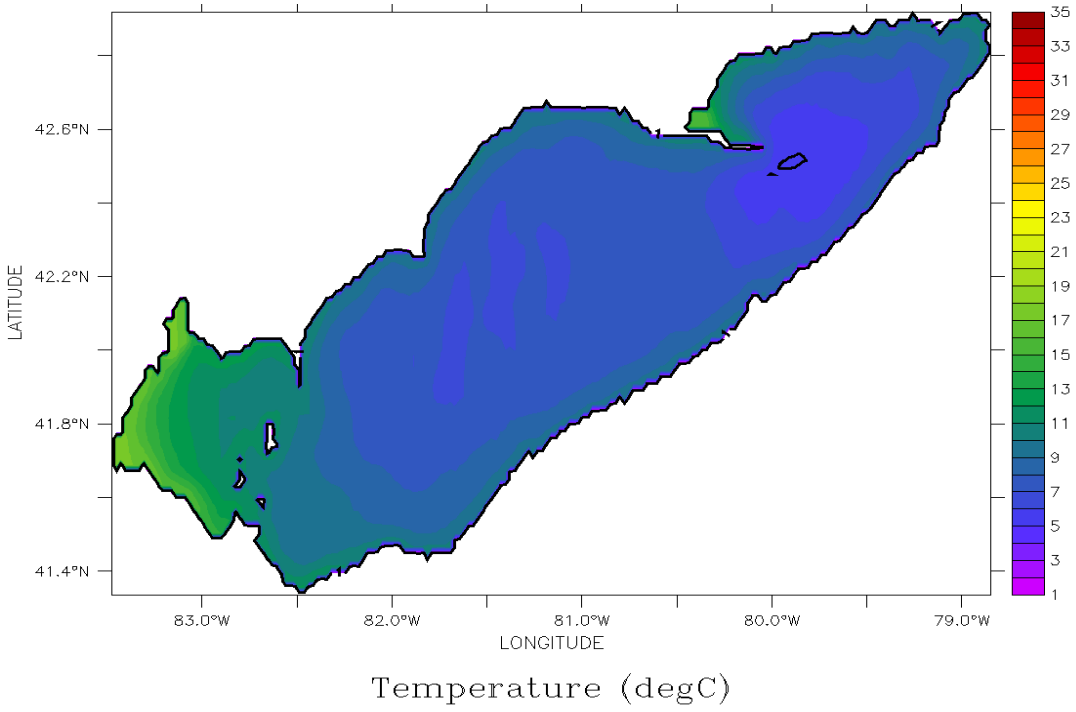

Figure 5.17: Depth-averaged water temperature in May 2005.

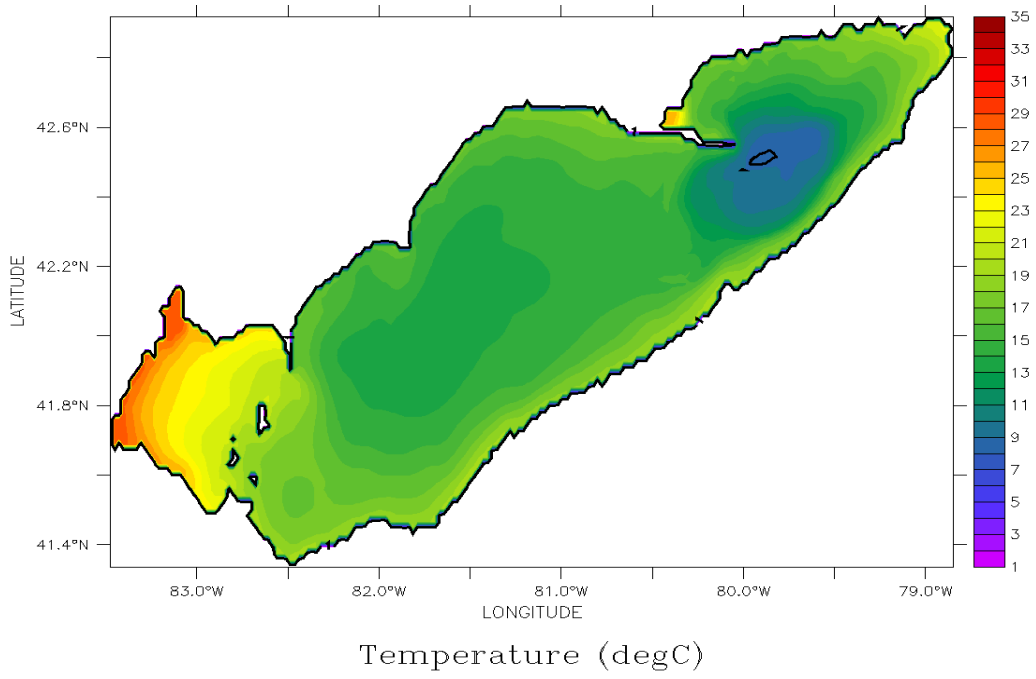

Figure 5.18: Depth-averaged water temperature in June 2005.

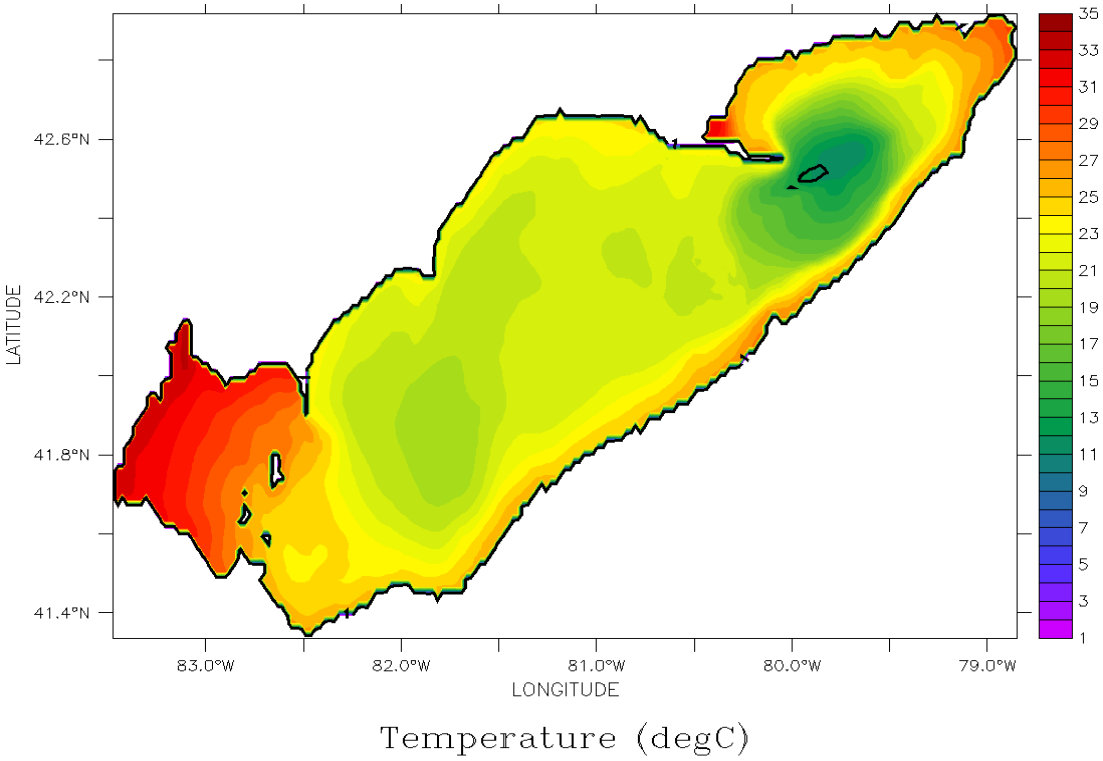

Figure 5.19: Depth-averaged water temperature in July 2005.

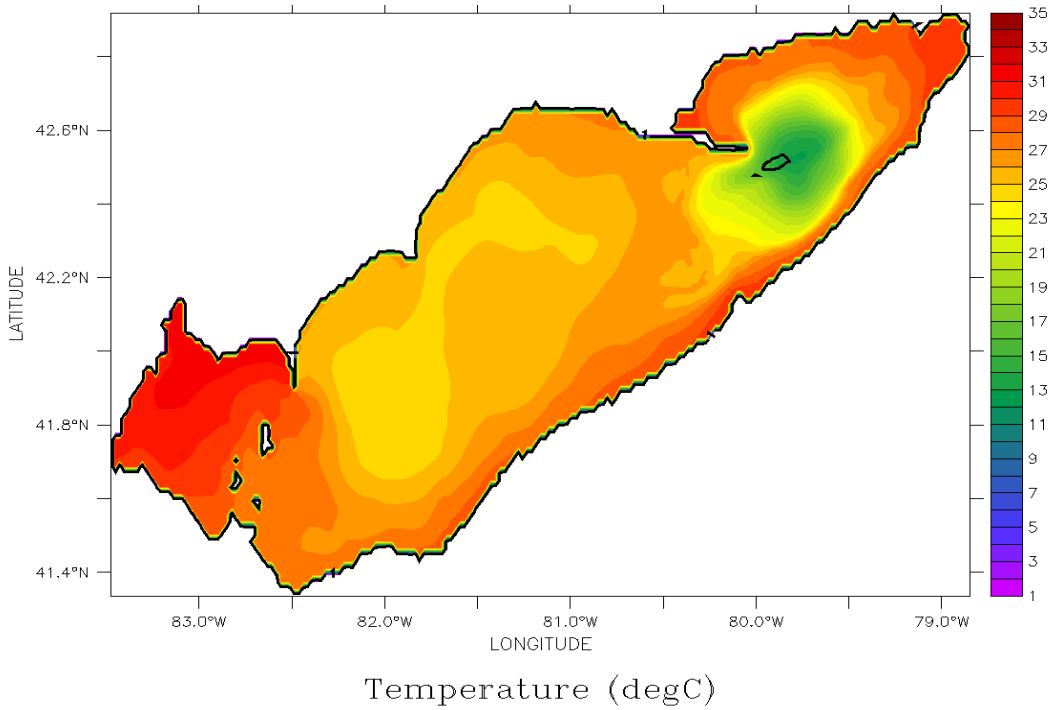

Figure 5.20: Depth-averaged water temperature in August 2005.

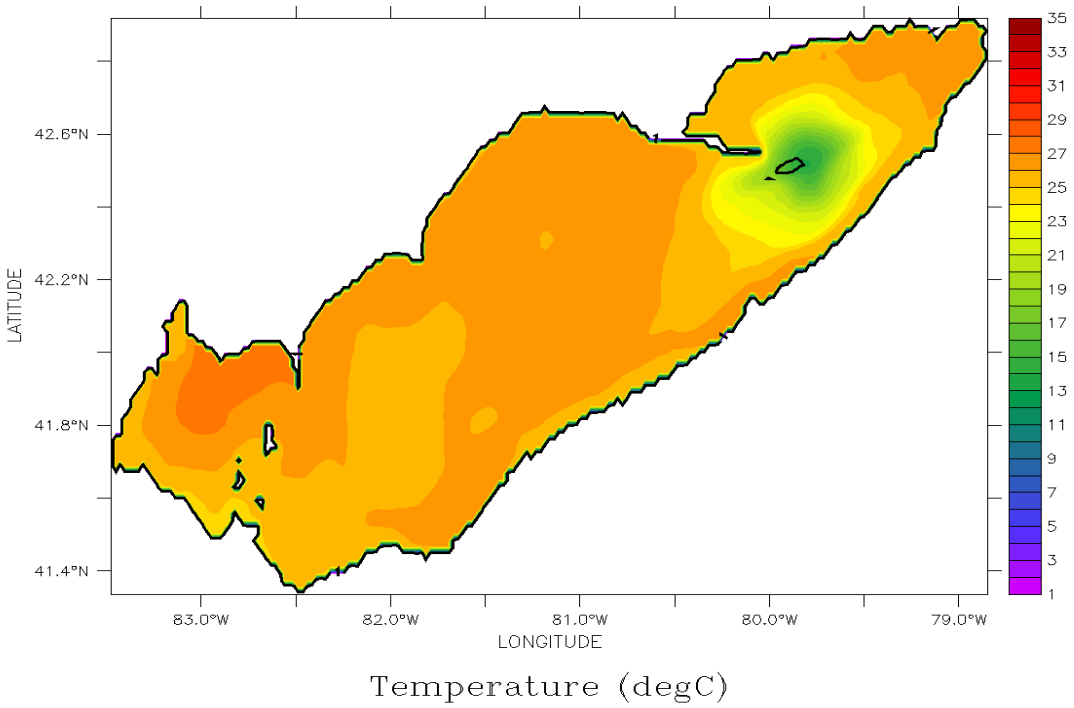

Figure 5.21: Depth-averaged water temperature in September 2005.

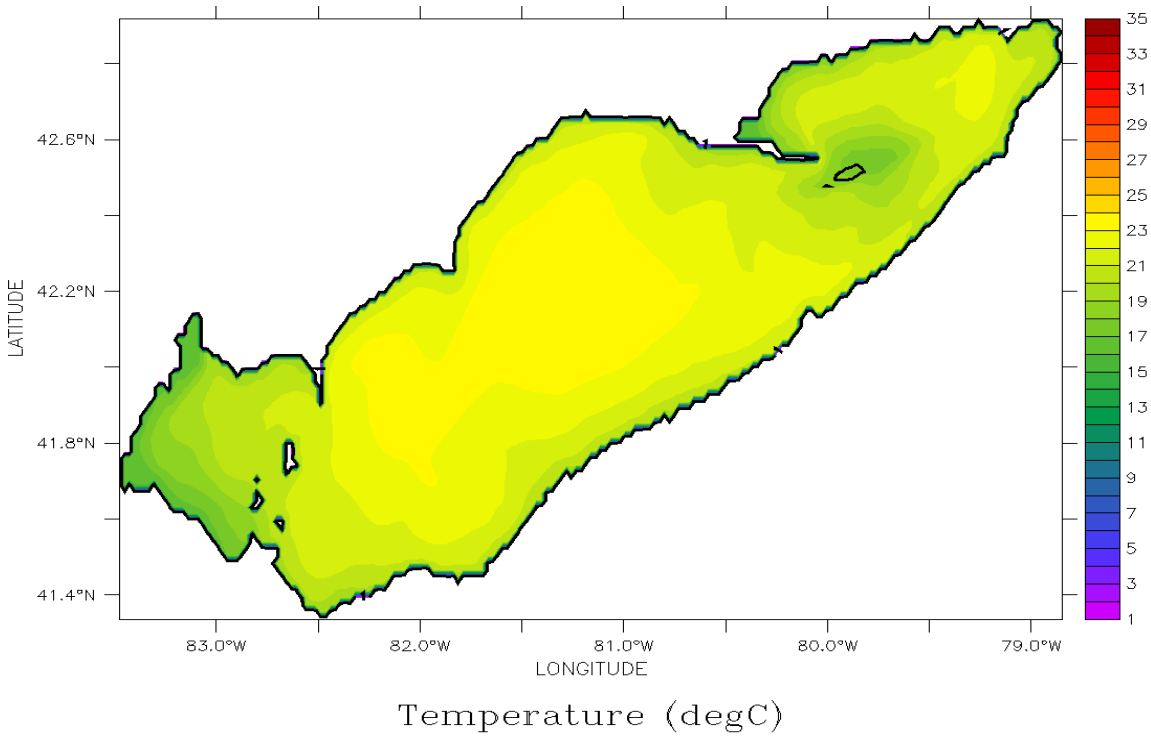

Figure 5.22: Depth-averaged water temperature in October 2005.

Figures 5.17 to 5.22 depict the monthly-averaged and depth-averaged modelled temperature of Lake Erie water from May to October 2005. Most of water is almost well mixed in May after winter ends. Average temperature decreases from 18-19 °C in the western basin to 4-5 °C to the eastern basin. As we expect, shorelines and shallow areas generally have higher temperature than the deeper parts. The maximum surface temperature difference in the lake reaches to 15 °C. The horizontal temperature difference within the western basin reaches 10 °C during May (Figure 5.17), while we observe a more uniform depth-averaged water temperature in the central and eastern basins, which have deeper waters. The solar radiation penetration into the shallower waters increases the shallower area's temperature more which leads to greater temperature gradient between shallow and deep parts. The eastern basin has colder water carrying the low temperature from cold winter months. The lowest temperature of 4-5 °C are seen in the deepest part of the central and eastern basins. In warm season areas of warmer water expand. While the deepest part of the eastern basin has an average water temperature of 7-8 °C, the temperature rises above 25 °C on the western shorelines of the lake. The temperature difference is still high in the lake but the average values are about 13-17 °C in the central and eastern basins and 22-25 °C for the shallowest basin of the lake.

In July (Figure 5.19), waters near the western boundary of the lake are about 30 °C on average. Ignoring the deepest part of the eastern basins leaves the central and eastern basins with temperatures of around 20-23 °C. The deepest eastern basin waters have the coolest water at 13-17 °C. Water temperature reaches to its maximum values in August (Figure 5.20) and temperature exceeds 25°C in the lake. However, temperature difference between the shallowest and deepest points of the lake keeps its value of 20°C. The highest intra-basin temperature difference of 15 °C occurs in the eastern basin. Water temperature starts to decrease after August (Figure 5.21) and we can see a more uniform lake with an average temperature of 24-25 °C, except in the deepest parts in the eastern basin with 16 °C temperature in September. A decaying trend in water temperature continues during October (Figure

5.22), and temperature varies from 14-15 °C in the West basin shorelines to 23 °C in the warmest parts of the central and eastern basins.

5.2.3 Thermocline

Figures 5.23 to 5.28 illustrate the temperature cross section along transect across the central and eastern basins. The transect is displayed in Figure 1.7 with a red line. However, the western basin is eliminated in plot frames as it has an imperceptible and non-significant stratification in the simulated period. In early spring (Figures 5.23c and 5.24c), if initial surface temperature is less than 4 °C surface heating causes convective overturning over the deep parts of the lake and the local incoming heat is distributed through the water columns. The surface temperature rises more in the shallow shoreline zones, which causes a large horizontal temperature gradient particularly in the deep parts of the eastern basin. In early May, the entire lake is almost well mixed and still cold at 4-5 °C. In spring, heating intensifies and temperature increases. A persistent temperature difference between the shallow western basin and the rest of the lake exists during the simulated period. As temperature increases, a weak stratification forms during spring in the central basin and in summer that merges into a thick thermocline with a moderate vertical temperature gradient. The thermocline moves higher in the water column during July-August, (Figures 5.25c, 5.26c). By the end of August, stratification rapidly decays in the central basin where near-bottom temperatures are still increasing, (Figure 5.27c).

The central basin has a weak bowl-shaped thermocline, which begins to form in June and matures in August. The thermocline depresses to a lower depth in the eastern basin as the surface water is pushed along by the southwest winds. However, the durable thermocline in the eastern basin is dome-shaped. The eastern basin thermocline persists over the summer and decays in September to October, (Figures 5.27c and 5.28c). In the early stages of stratification, a fragile stability is very susceptible to

strong wind impulses. In October, complete vertical mixing in response to high wind stress is observed and the whole lake is fully mixed, but in the eastern basin, stratification persists in the deepest parts.

The variety of processes of heat exchange across the water layers and the thermal inertia of water masses cause an overall temperature lag between the deepest parts of the eastern basin and the rest of the lake. Deep-water temperature typically changes on time scale much longer than the shallow water or surface waters. From temperature plots, water temperature of the deepest part does not present strong seasonal variations, and suggests that heat exchange in the deep layers can be reasonably assumed low in most situations. In light of results obtained from the depth-averaged temperature analysis, the deepest part of the eastern basin keeps a relatively low variable temperature of around 11-16 °C in most of the simulated period, while the other parts of the lake experience high fluctuations from 11-30 °C in lake temperature. The western basin, which is also the shallowest, is the warmest basin during the simulated period. We can speculate that it keeps its high variability in temperature behavior during the ice-free period and is the coolest basin during winter, while the eastern basin is the coolest among the Lake Erie's basins in warm months. Temperature plots also confirm this speculation, where the model produced the result in the occurrence of warm and cold periods. Near shore areas experience temperature increases exceeding 15 °C in some months while the temperature difference in other locations was much less. The deeper eastern basin lags the central basin in the heating season but retains its heat in storage for longer periods during the cooling phase.

The difference in temperature between the water surface and the lake bottom can be substantial in the summer months and varies considerably over the lake basins. Temperature decreases quite rapidly in all portions of the lake in the period of October. Temperature values for the summertime period indicate that the western basin has the highest values. The central basin showed higher temperatures generally in the west portion of the basin and the eastern basin has lower average temperature because of its greater depth. In the summer, stratification is firmly established in the central and eastern basins.

The upper mixed-layer depth of 10 meters in July is reduced to approximately 6 meters in August in response to meteorological forcing. Maximum heat storage generally occurs in mid-August. Stronger winds over Lake Erie during the fall months generally contribute to deepening of the upper mixed-layer. The central basin is isothermal and the eastern basin rapidly approaches an isothermal condition. The temperature distribution over the lake is related to the heat storage capacity of each basin. During warm months when the thermocline is thick, the mixing processes are confined to the upper portion of the thermocline. The temperature of the epilimnion is warm in summer and cools in winter. While the surface water temperature varies seasonally (monthly), the temperature of the bottom is almost constant in the eastern basin over the simulation period at about 12 °C. Twice a year, in spring and fall, surface water reaches the bottom temperatures, and thus the thermal stratification weakens. Under these conditions and in the presence of a sufficiently strong wind blowing at the surface the entire lake can mix (excluding the deep parts in eastern basin).

COHERENS thermal structure results (Figures 5.23c to 5.28c) are compared to POM results using GEM winds (Figures 5.23a to 5.28a) and POM results using uniform winds (Figures 5.23b to 5.28b). The bowl-shaped thermocline (central basin) and dome-shaped thermocline (eastern basin) are produced by both models and agree with observations. POM model stratification forms during May and persists to September, while COHERENS modelled thermocline decays in early September, as the water temperature in central basin is more uniform. The use of different wind data resources with different resolution can explain for this discrepancy. However, both models and observations predict the strong stratification and thick thermocline during July-August, which are reproduced by COHERENS.

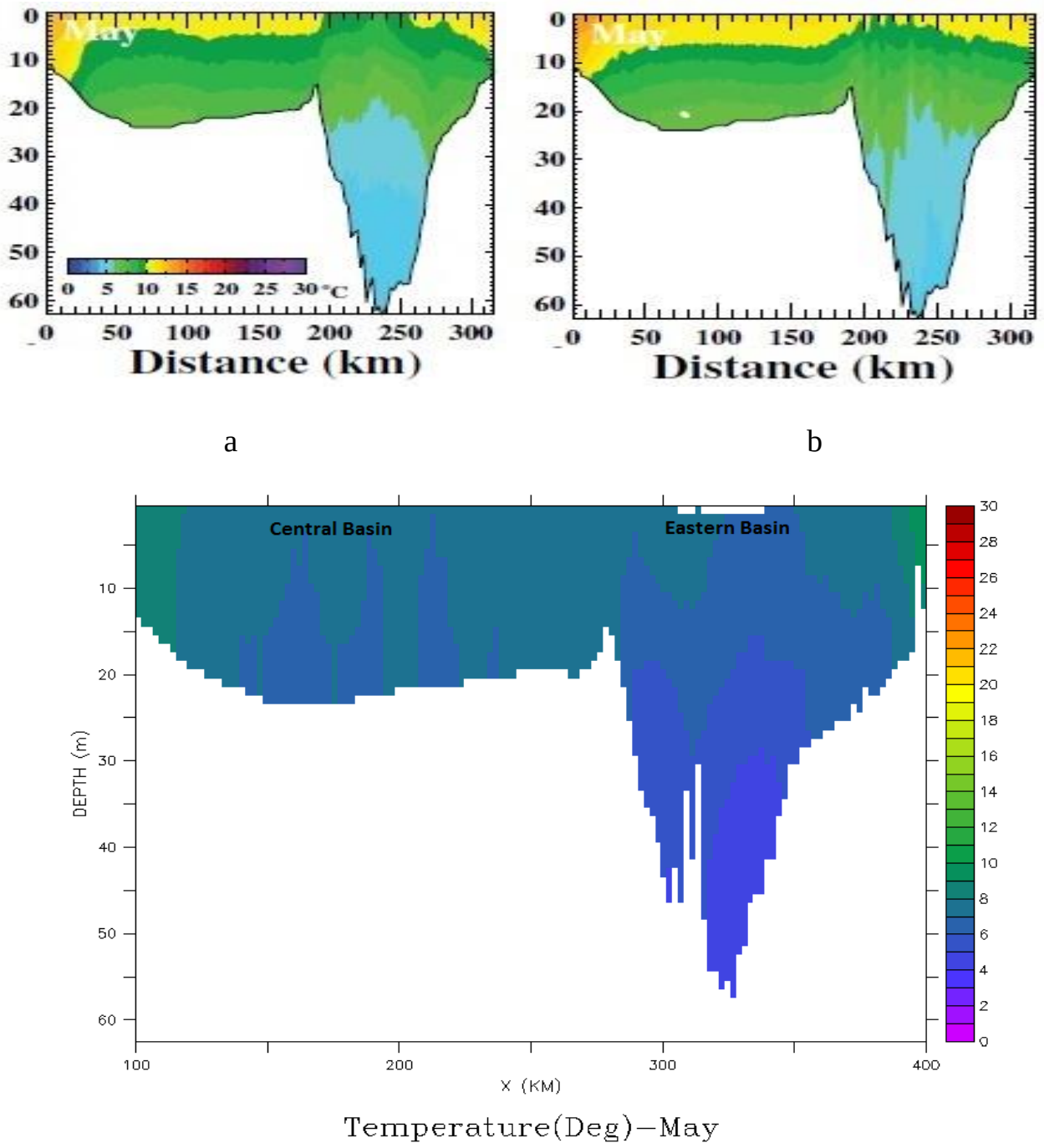

Figure 5.23: May averaged (a) POM model using GEM modelled winds, (b) POM model using spatially uniform winds (Beletsky et al., 2013) and (c) COHERENS model temperature, 2005.

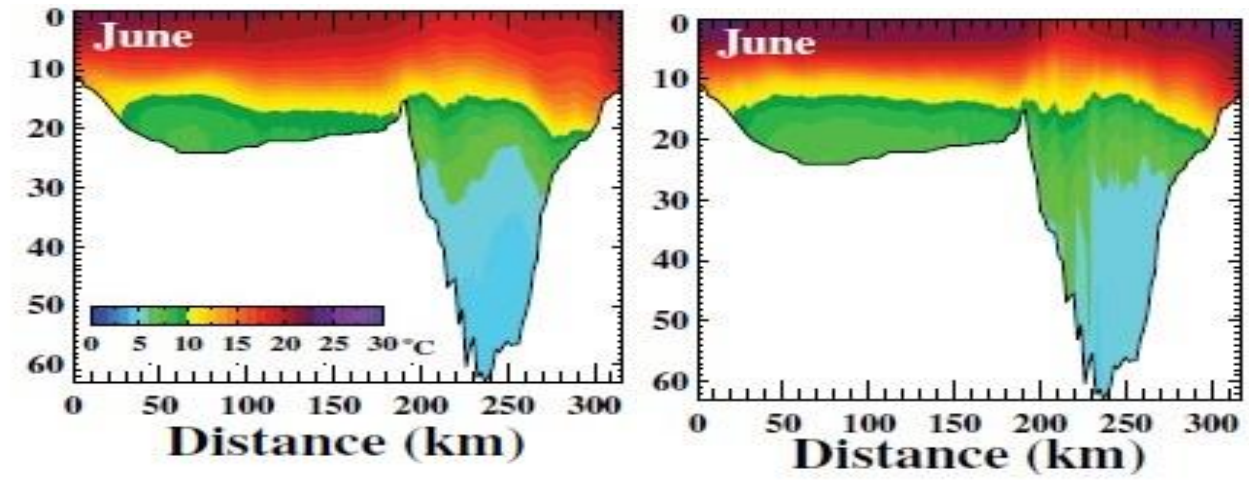

a b

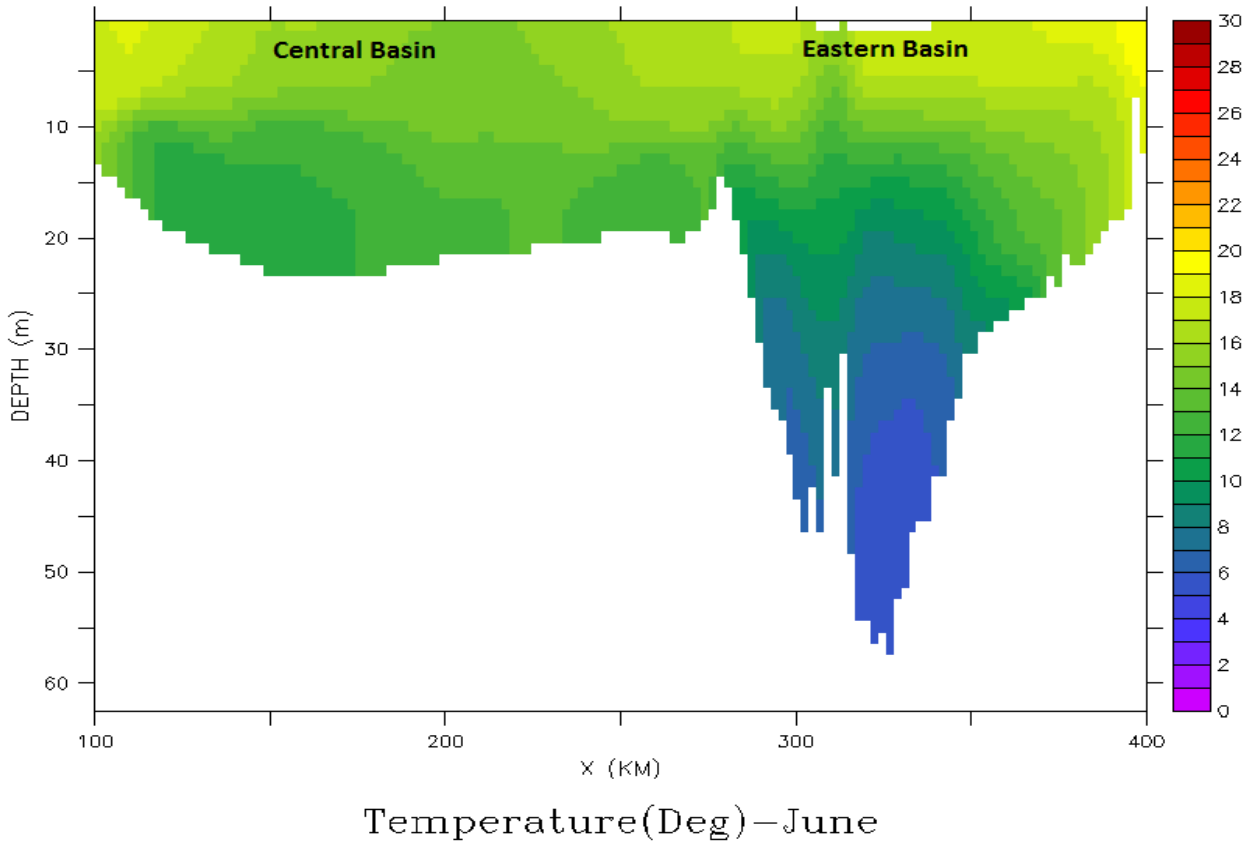

c

Figure 5.24: June averaged (a) POM model using GEM modelled winds, (b) POM model using spatially uniform winds (Beletsky et al., 2013) and (c) COHERENS model temperature, 2005.

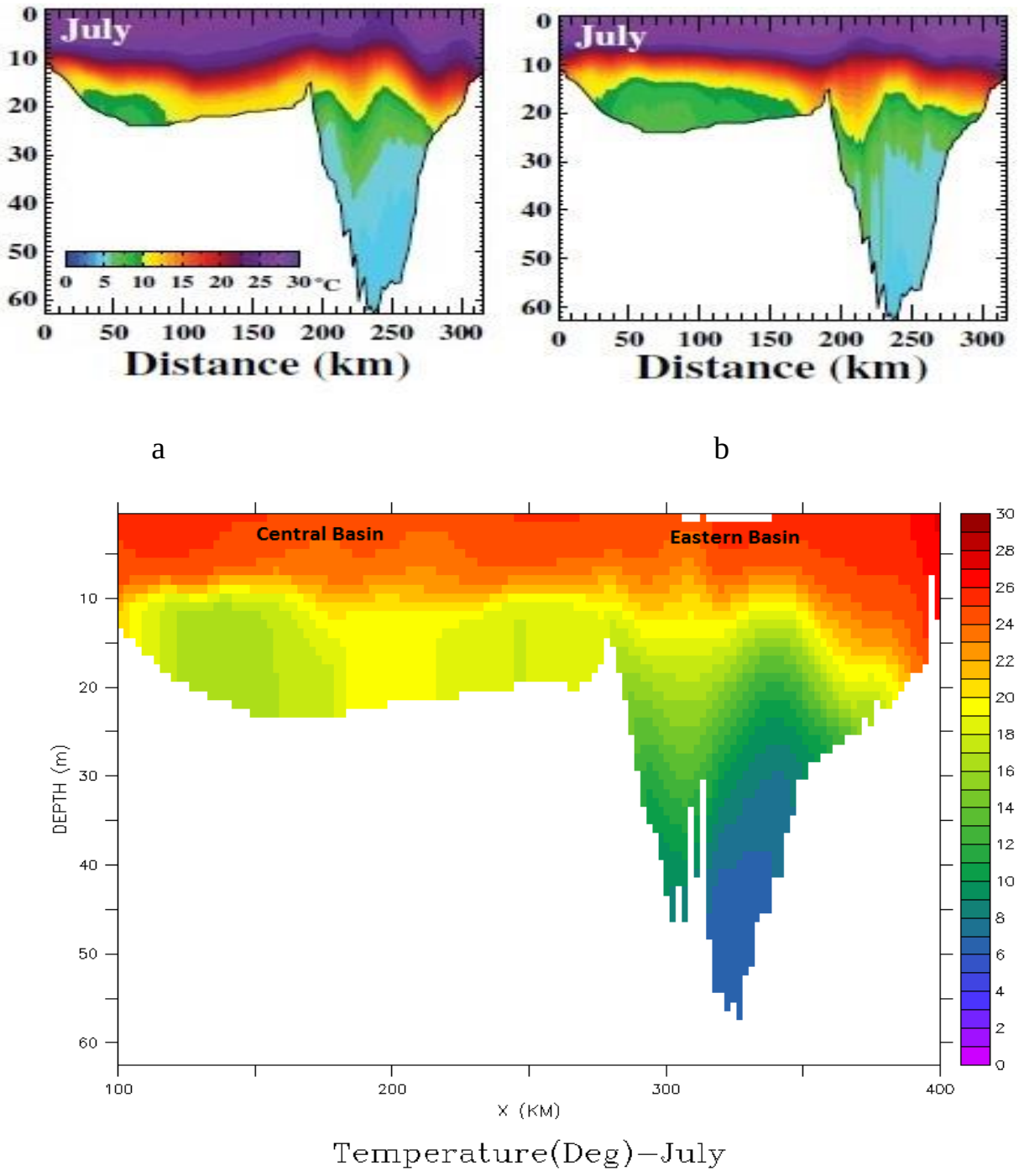

Figure 5.25: July averaged (a) POM model using GEM modelled winds, (b) POM model using spatially uniform winds (Beletsky et al., 2013) and (c) COHERENS model temperature, 2005.

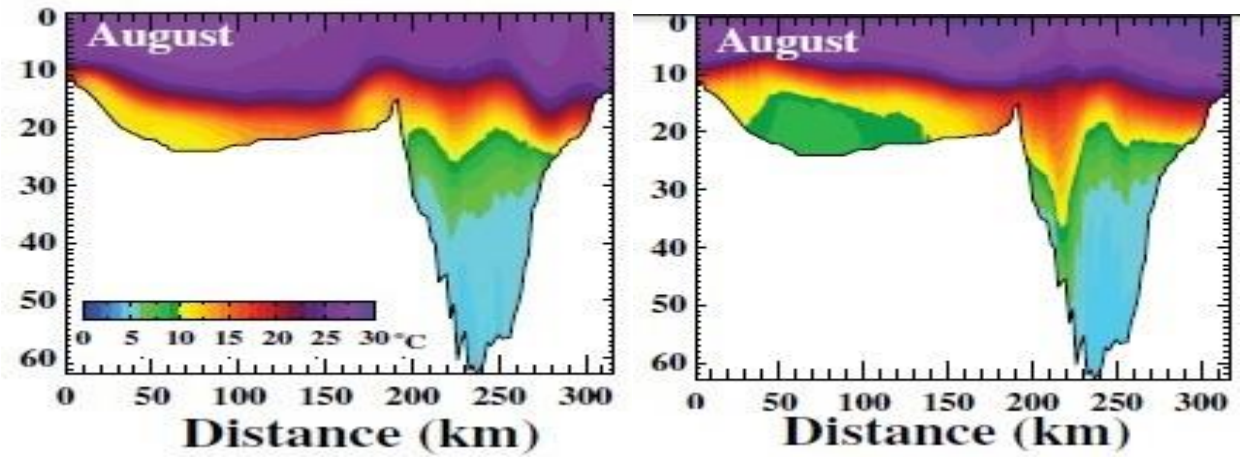

a b

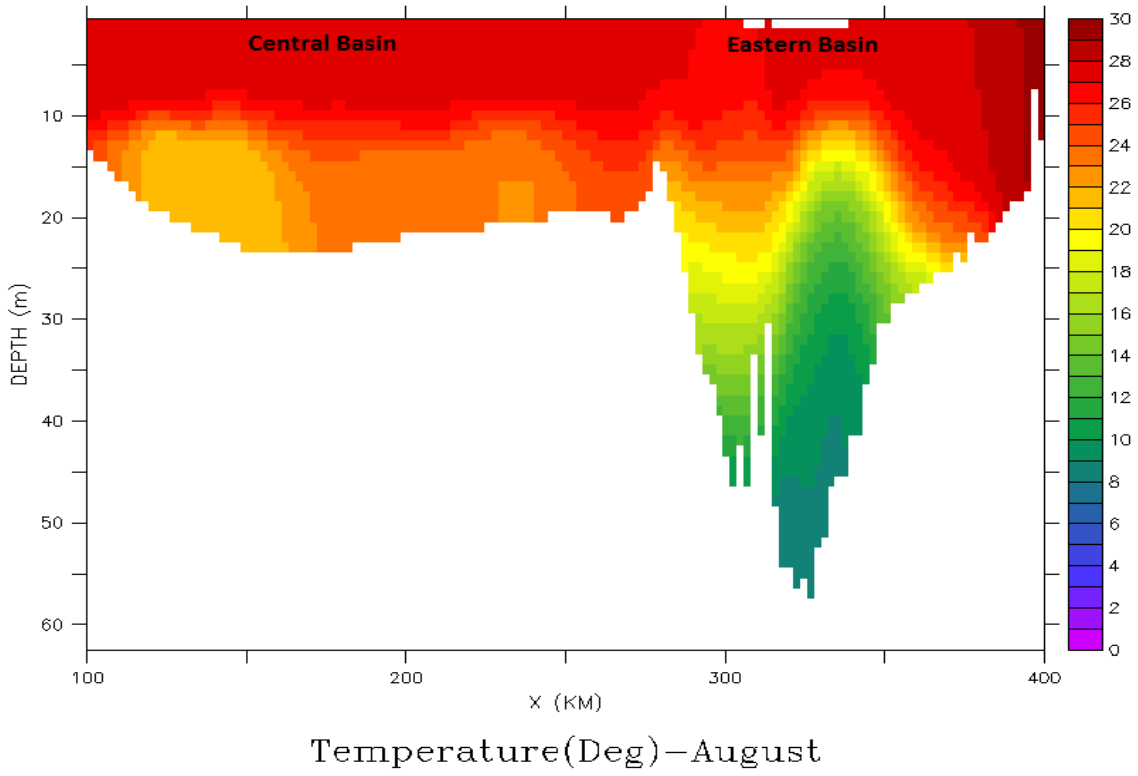

c

Figure 5.26: August averaged (a) POM model using GEM modelled winds, (b) POM model using spatially uniform winds (Beletsky et al., 2013) and (c) COHERENS model temperature, 2005.

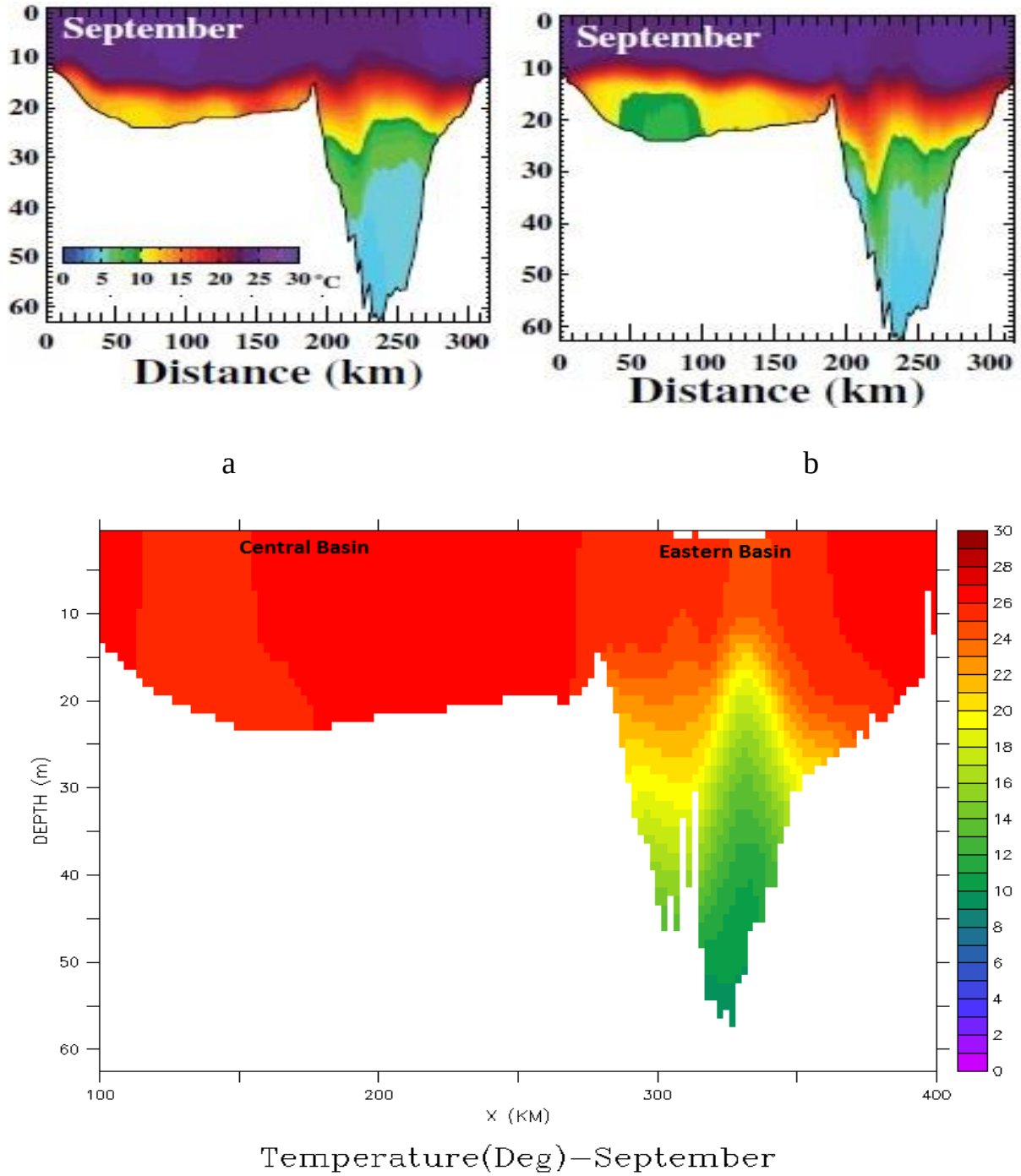

Figure 5.27: September averaged (a) POM model using GEM modelled winds, (b) POM model using spatially uniform winds (Beletsky et al., 2013) and (c) COHERENS model temperature, 2005.

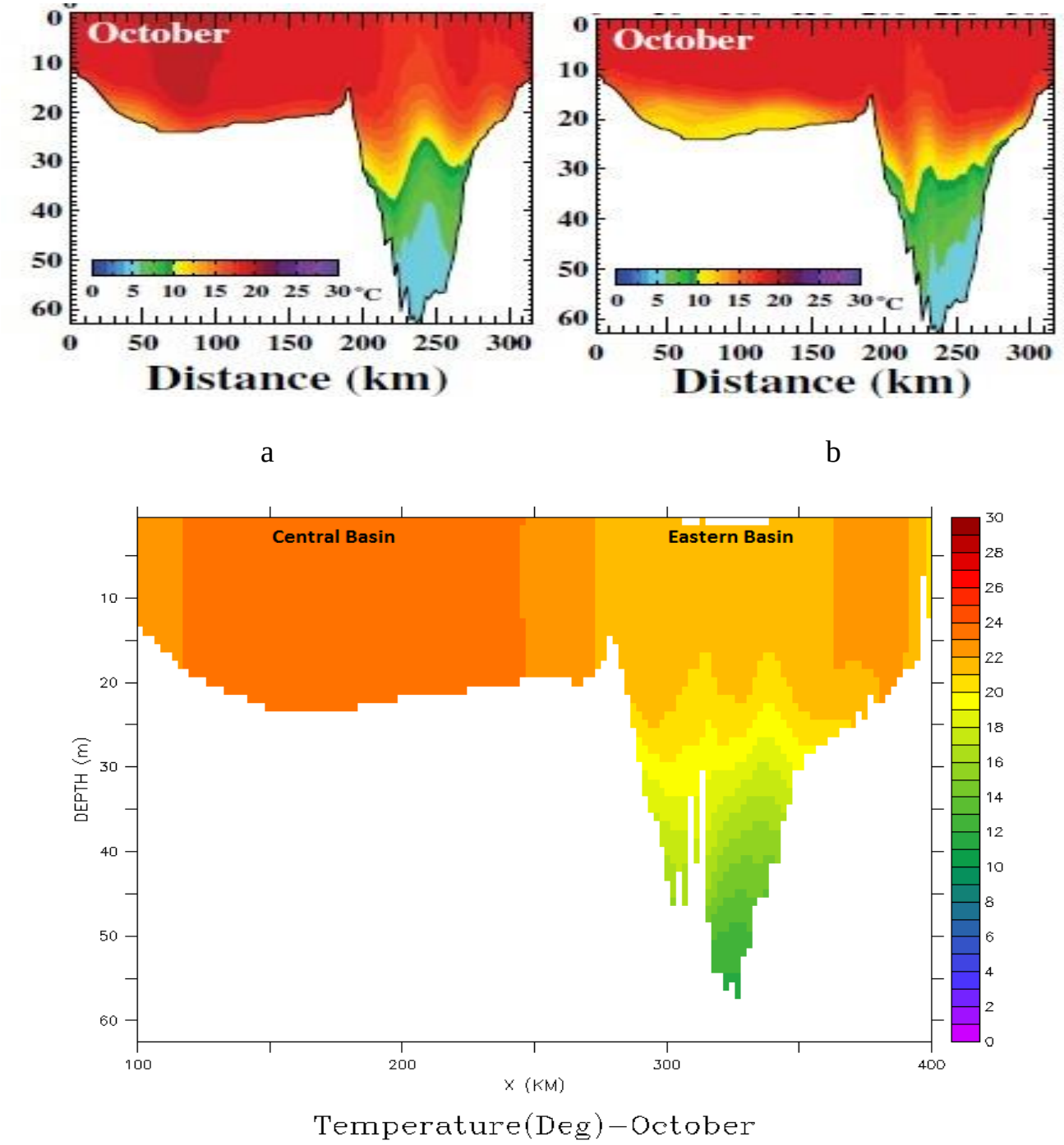

Figure 5.28: October averaged (a) POM model using GEM modelled winds, (b) POM model using spatially uniform winds (Beletsky et al., 2013) and (c) COHERENS model temperature, 2005.

5.3 Model Validation

Figures 5.29, 5.33a and 5.34a compare the observed and modelled time-series variation of surface temperatures at sites 45005, 45132 and 45142, (Figure 1.7).

A visual inspection of the modelled temperature plots with observations shows that while the COHERENS model obtains the same pattern and structure, the modelled temperature is slightly lower before DOY 230. Investigation of the wind time-series plots Figures 5.32, 5.33 b and 5.34 b, reveals that while the NARR reanalyzed winds used in COHERENS and the buoy-observed winds are comparable, the NARR adjusted-winds for station 45142 are slightly slower. Investigation of the air temperature reveals that the NARR air temperature is lower before DOY 230, and this is the reason for lower modelled temperature as the model uses the air temperature as an input, which affects the air-lake heat fluxes. There is close agreement between measurements and modelled temperature estimations which is further confirmed in temperature plots after August when the observed and NARR air temperature are more consistent with observations.

Wind speed was observed at 4 m above water level at all buoy stations and are adjusted to a standard measurement height of 10 m above the lake level to compare with NARR wind speed. This height was chosen since this is an elevation sufficiently near the water surface to have a direct relationship to processes at the air-lake surface, but high enough to be above storm wave crests. In order to estimate the mean wind speed at 10 m height based on that at 4 m, we used the log law formula for the wind speed through $W_{10} = W_4 [\ln (10/z_0) / \ln (4/z_0)]$ where W_4 and W_{10} are the mean speeds at 4 and 10 m and z_0 is the roughness length of 0.0004 m, (Wikipedia, 2018). To investigate the NARR winds reliability, a comparison of NARR winds with an on-shore station (Windsor A station) winds observed at 10 m, are displayed in Figure 5.35, which confirms the accuracy of NARR winds. It worth noting that NARR winds track the observations very well but the mean winds differ by almost 0.5 and 1 ms^{-1} at the Windsor A station and 45142 buoy.

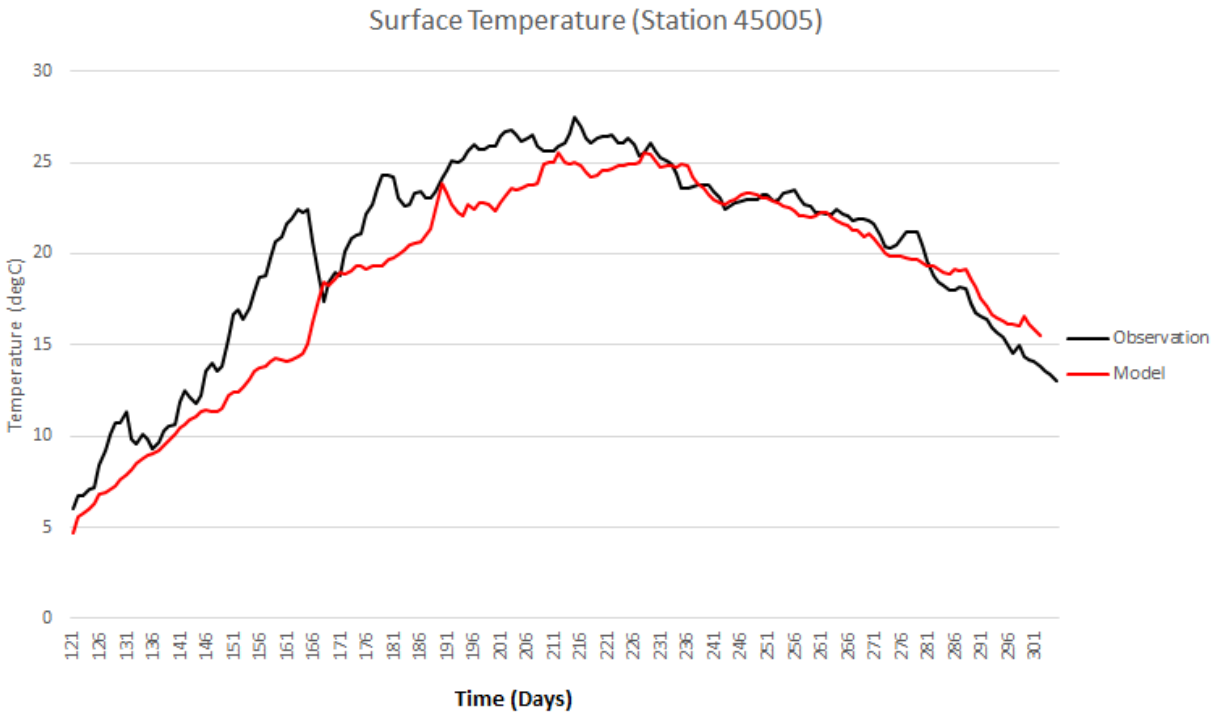

Figure 5.29: Time series water surface temperature, observation vs. COHERENS. (Station 45005)

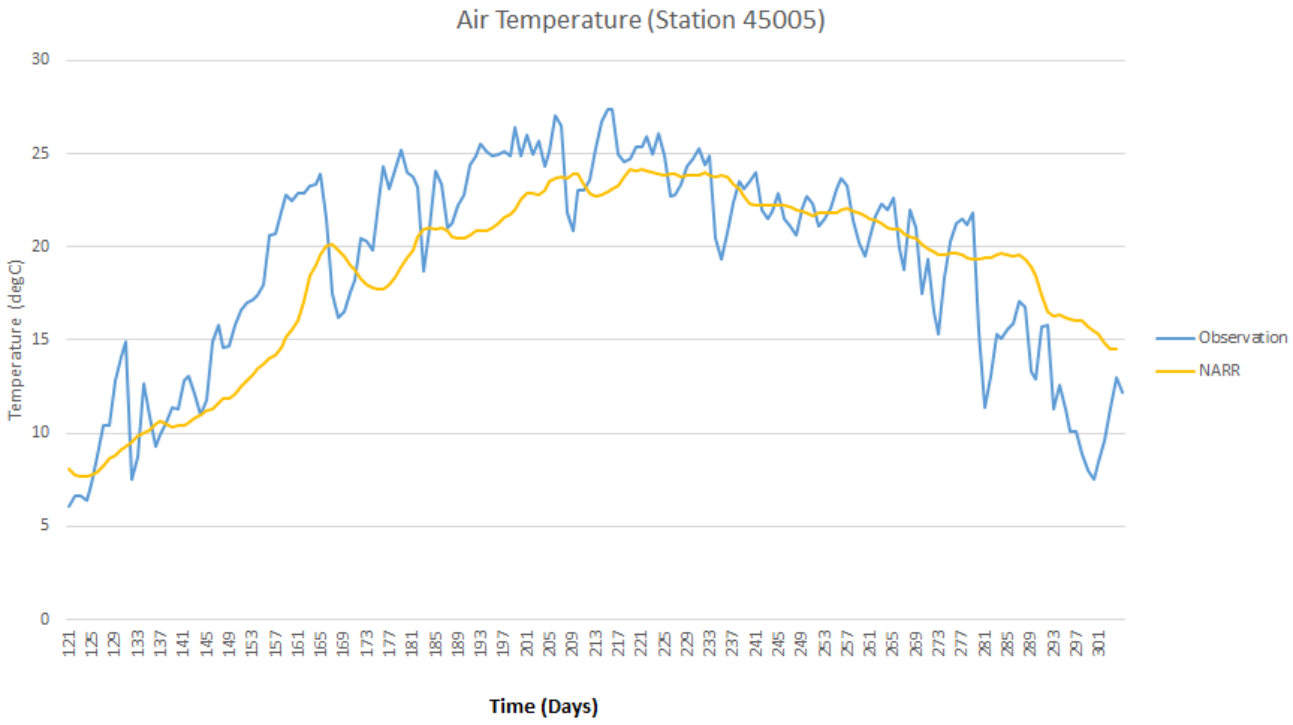

Figure 5.30: Time series air temperature, observation vs. NARR. (Station 45005)

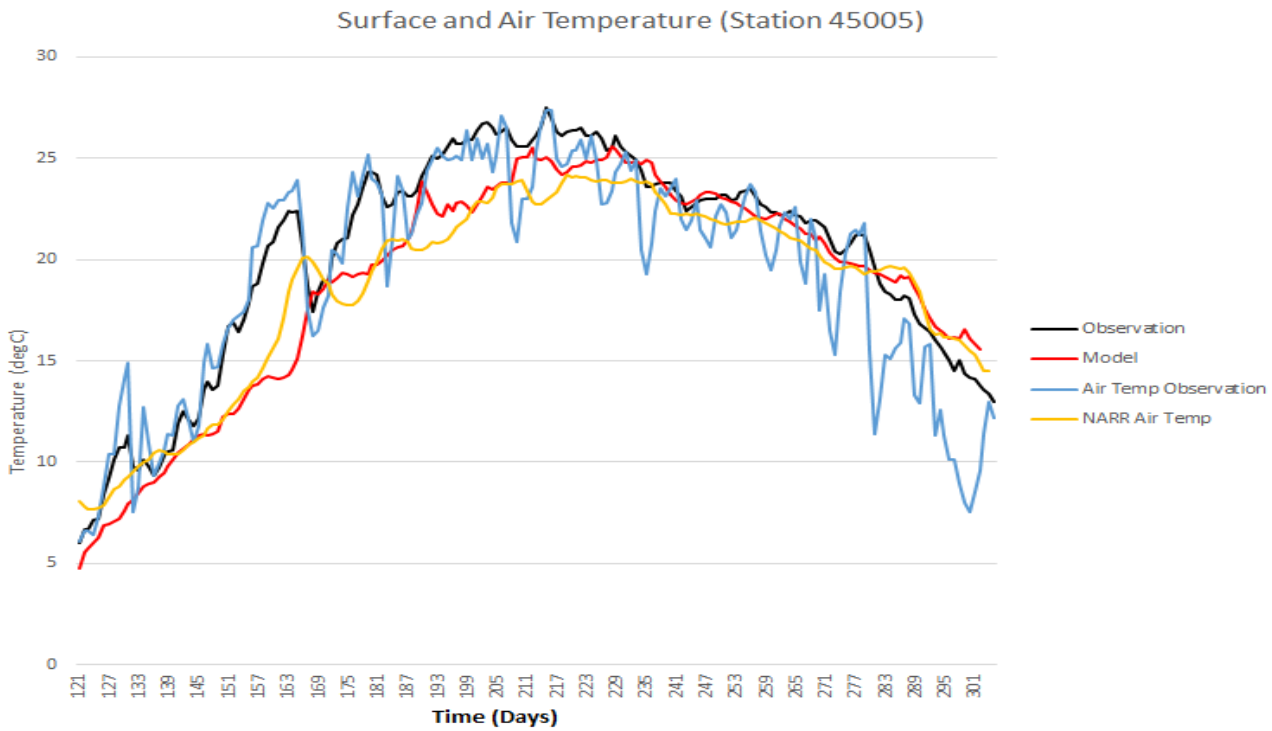

Figure 5.31: Time series surface water and air temperature, observation vs. COHERENS. (Station 45005)

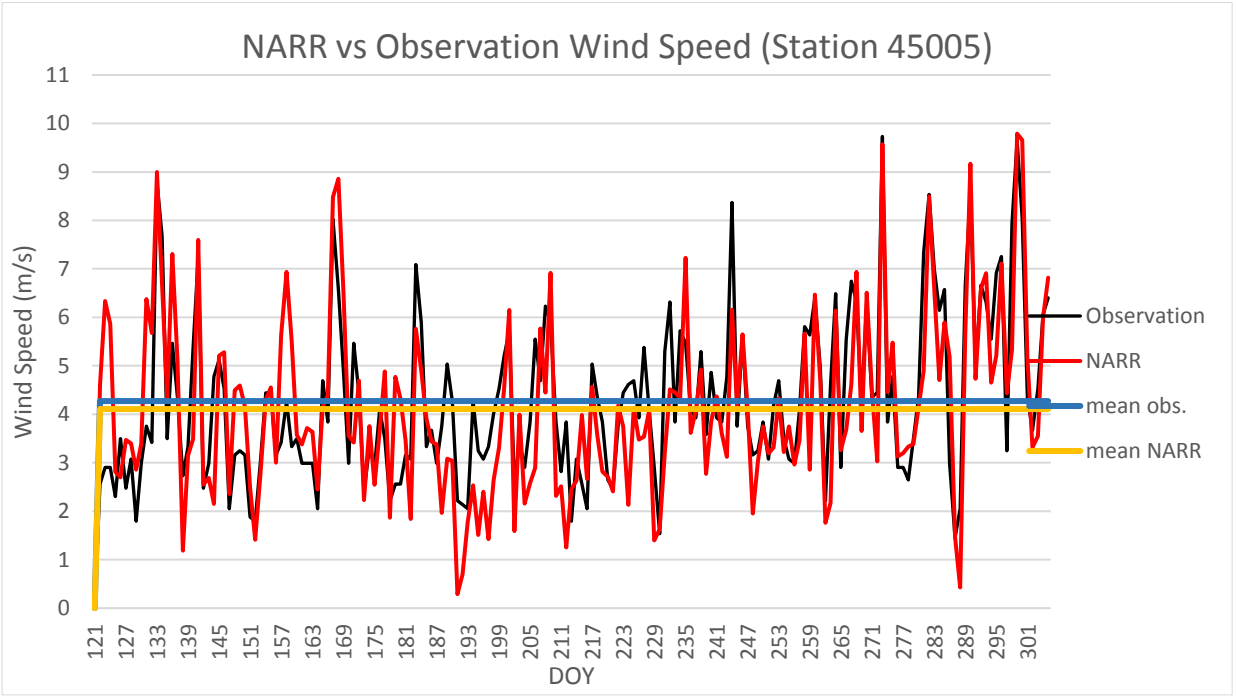

Figure 5.32: NARR (red) versus adjusted to 10m observation (black) wind speed at meteorological buoy 45005, in 2005.

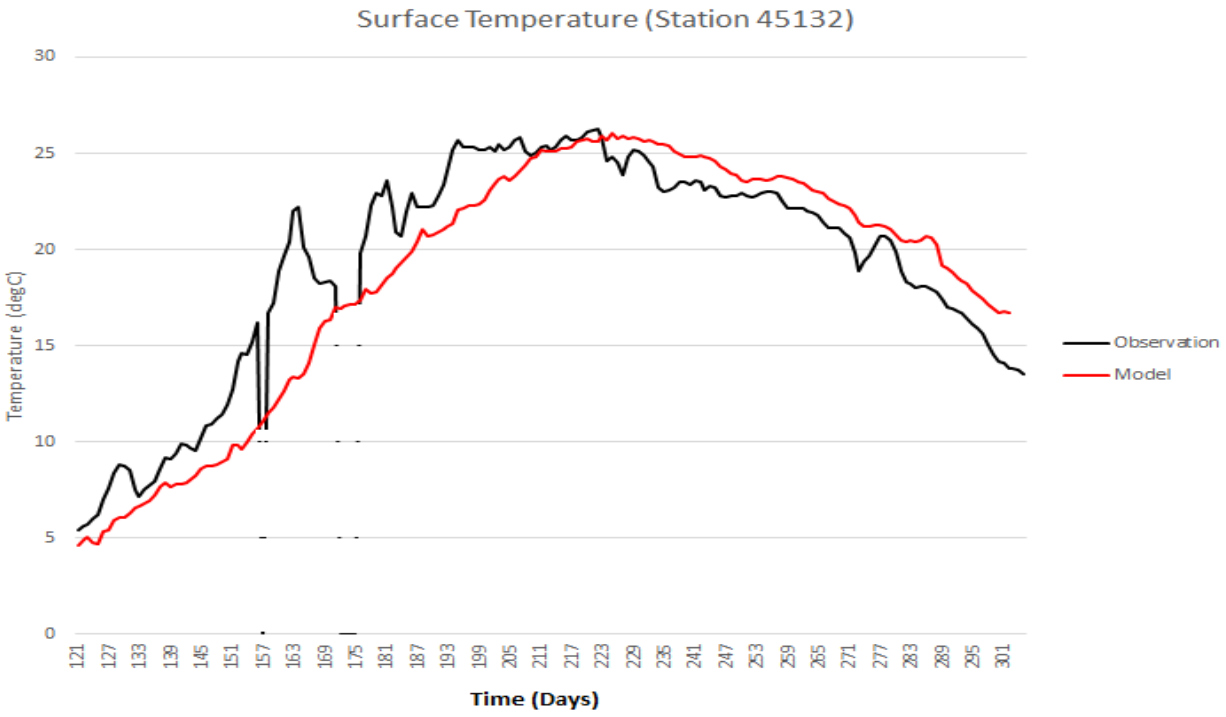

a

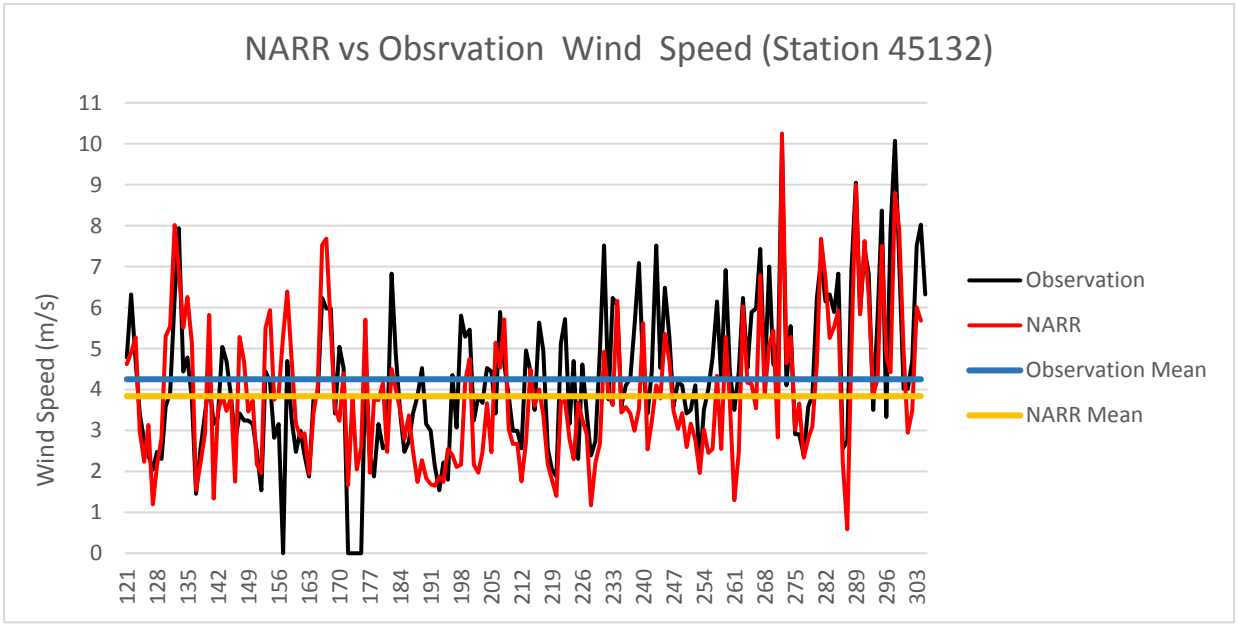

b

Figure 5.33: NARR (red) versus adjusted to 10 m observation (black) a) surface water temperature and b) wind speed at meteorological buoy 45132, in 2005.

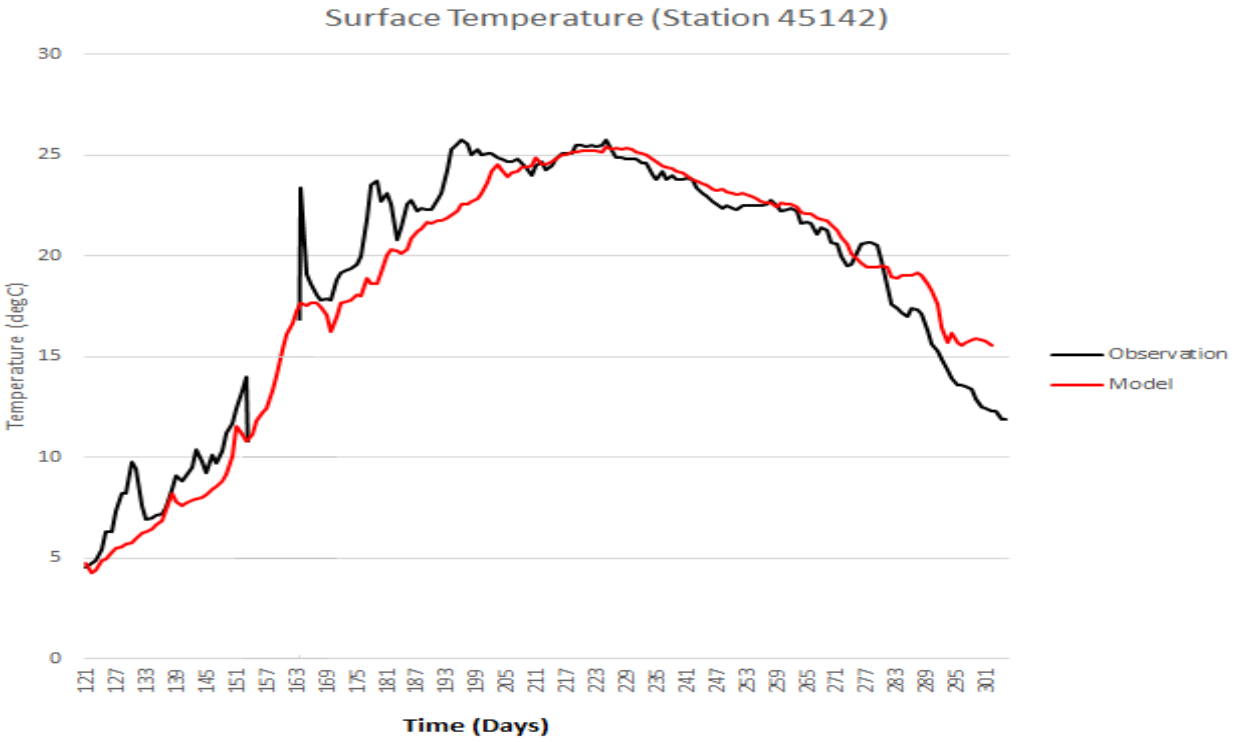

a

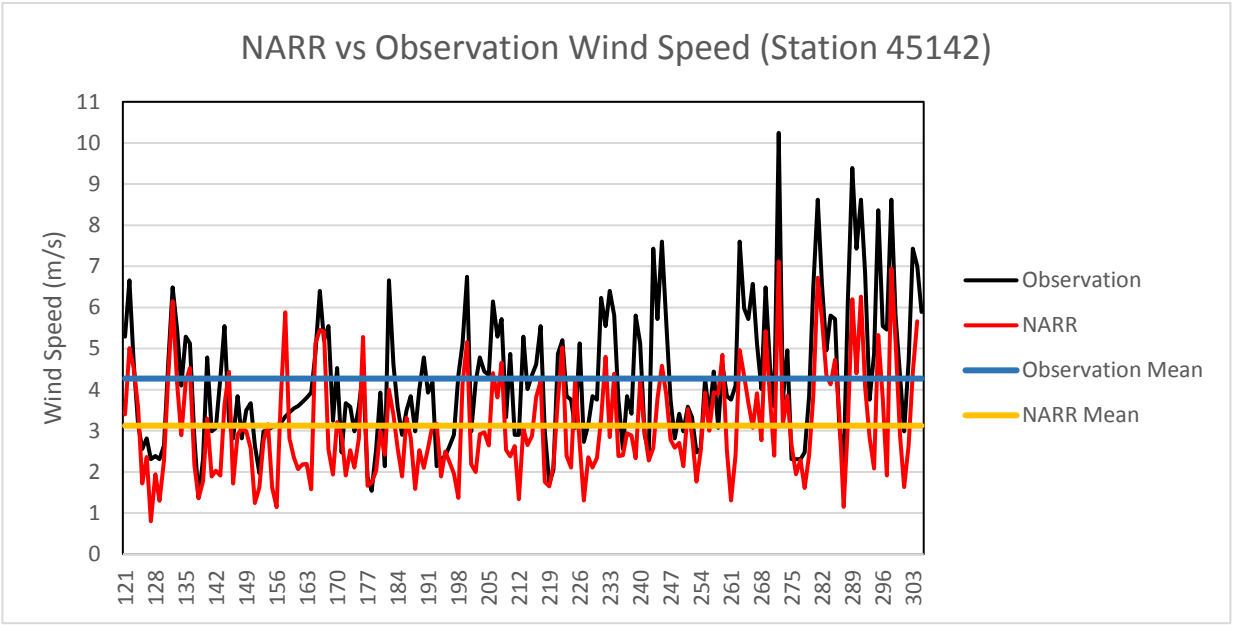

b

Figure 5.34: NARR (red) versus adjusted to 10 m observation (black) a) surface water temperature and b) wind speed at meteorological buoy 45142, in 2005.

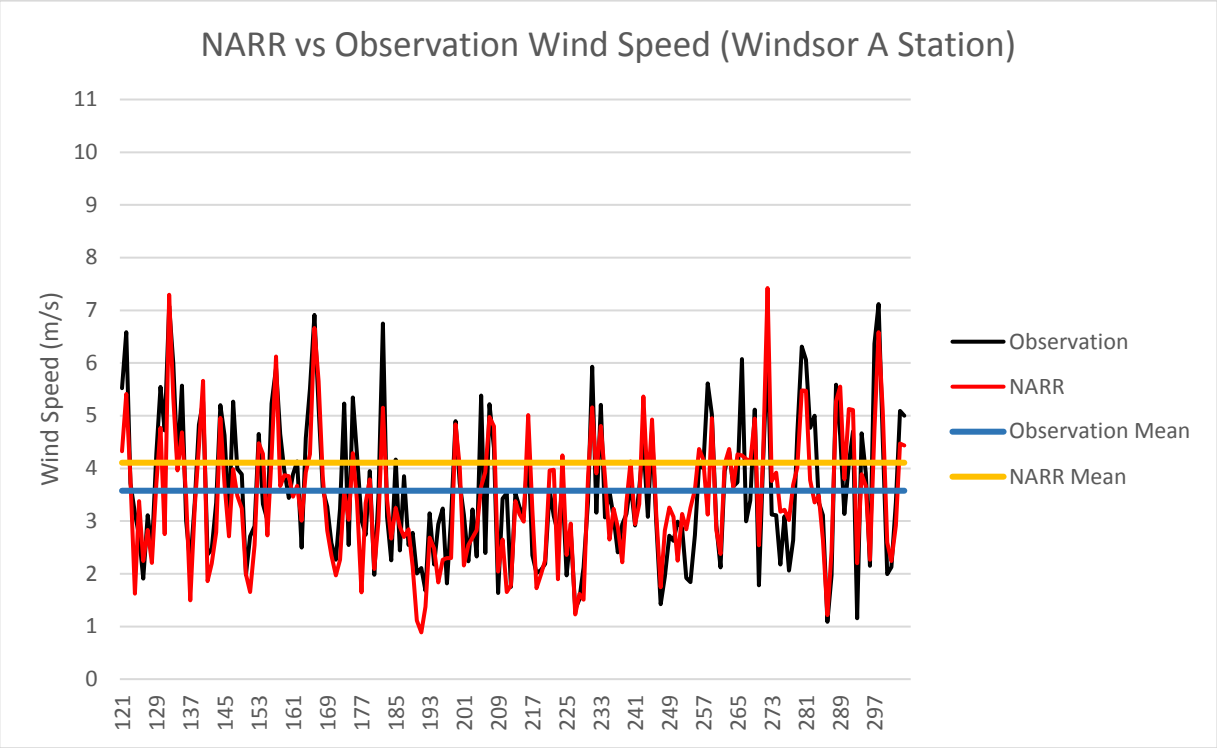

Figure 5.35: NARR (red) versus observed (black) wind speed at Windsor A station, in 2005.

CHAPTER SIX

COMPARING RESULTS WITH AND WITHOUT A LARGE WIND FARM

6.1 Comparing Some Plots in the Presence and Absence of a Large Wind Farm

In this section, some physical parameters such as surface temperature and water currents are compared in the presence and absence of a large wind farm. Developing a large wind farm in the central basin mostly impacts the central basin. The results of a small wind farm consisting of 6 wind turbines are illustrated in Appendix D. In order to capture a better spatial variability and plot resolution, only the central basin is depicted which is the main concern and focus of this part. As surface temperature and water current plots illustrate, the significant impact and substantial gradients are restricted to the southwest part of the central basin. Therefore, the focus on quantifying the temperature and current gradients is on the southwest part of the central basin. Details of the hypothetical wind farm are given in section 3.4. Also given in chapter 3 are the details of wake wind speed reductions.

6.2 Wind Field (In the Presence of a Large Wind Farm)

For May to October 2005, wind farm impacts on the wind field are shown in Figures 6.1 to 6.6. The plots illustrate the monthly-averaged wind vectors in the presence of a 432-turbine wind farm. This location has been selected to provide an example of the potential differences in wind and surface layer water current velocities and temperatures in the absence (hereafter termed “case 1”) and presence (hereafter termed “case 2”) of a large wind farm.

May vector-averaged wind velocities are relatively weak compared to other months (Figure 6.1). However, it worth is noting that the vector-averaged wind velocities are lower than the instantaneous wind speed because vector averaging takes into account the direction as well as the magnitude of the wind speed. Significant wind speed reduction occurs in the centre of wake zone displayed by the blue rectangle. On the north boundary of the wind farm zone, the vector-averaged wind blows from the north while on the south boundary the mean wind is from the south. Similarly, the winds on the west and east boundaries are from the west and east directions, respectively. The wind is reduced when it enters the wind farm zone and falls to its minimum value on the downwind side of the zone. This behavior is common to all wind directions. It seems the vector-averaged wind speed is reduced to below 1 m/s at the centre of wake (CW) location. From June to September, we also see downstream wind deficiency and the wind speed reduced typically 17 by percent of its original value within the wake zone north-east of the wind farm averaged over 12000 km^2 the area in downwind of turbines where the wake reduces to less than 2% from maximum, while the maximum wind speed reduction is approximately 60 percent in the centre of wake (CW). October winds are strongest among the simulated months and the mean wind is in the opposite direction to that observed in the summer winds. It can be interpreted from Figure 6.6 that like the warm months, the wind reduction occurs downstream of the wind farm. Since wind velocity vectors are based on monthly-averaged conditions over the lake, they do not show features specific to any particular day or hour. Their utility lies in providing the potential effect on the monthly-averaged surface temperature and current distribution for the simulated period over the central basin. To get a better idea of the wind turbine wake effect, a few episodes of the central basin wind pattern and related contours under the impact of the wind farm are plotted later in Figures 6.44 to 6.47. Also, a few plots of wind speed reduction (in percentage) in the presence of a wind farm are shown in 6.48 to 6.50.

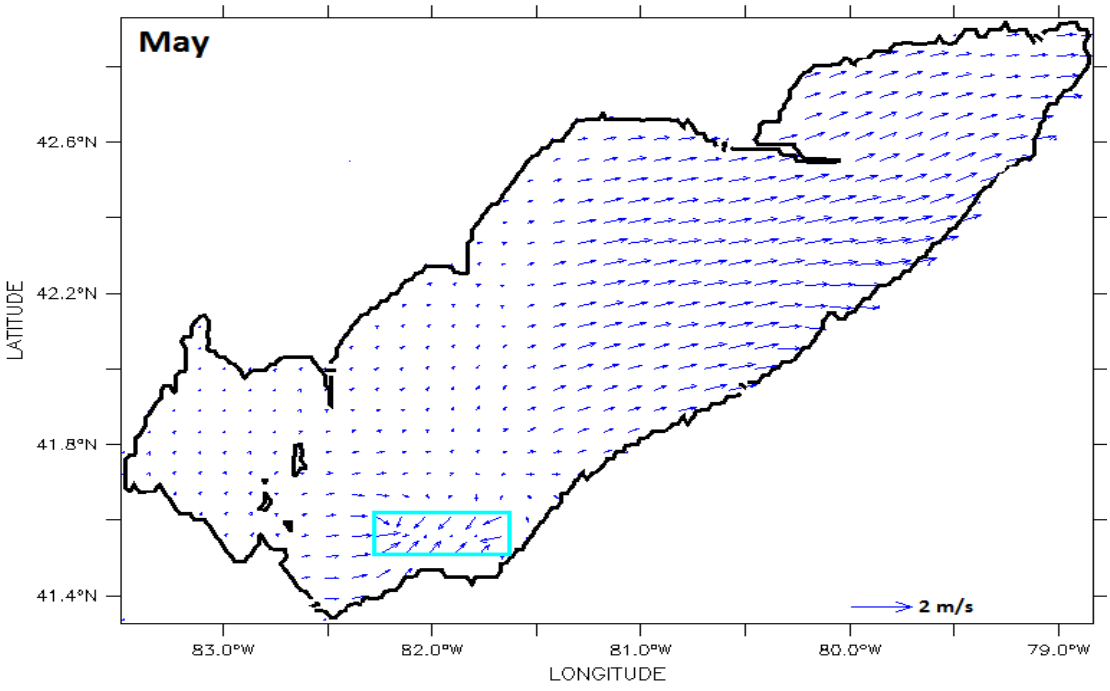

Figure 6.1: May averaged wind velocity

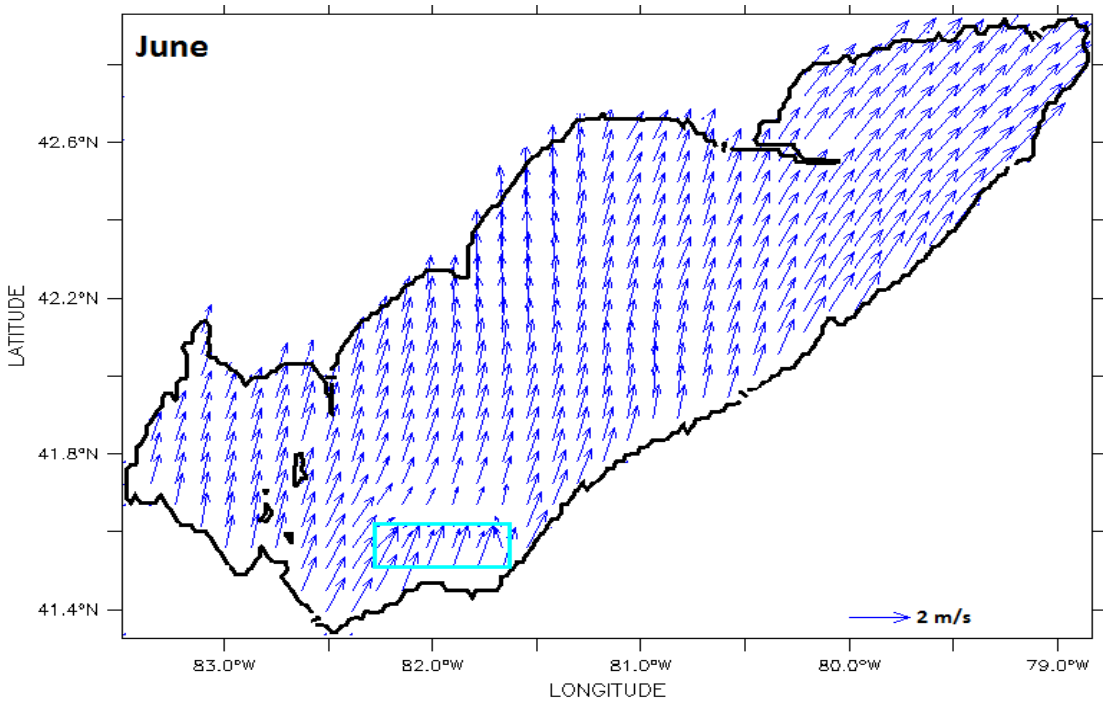

Figure 6.2:. June averaged wind velocity

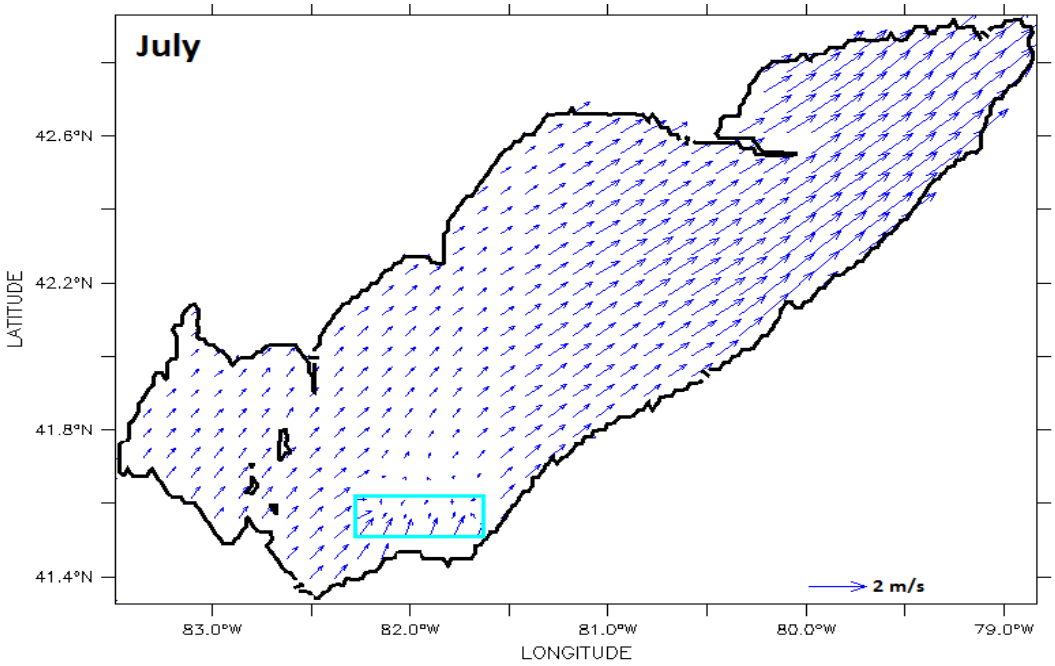

Figure 6.3: July averaged wind velocity

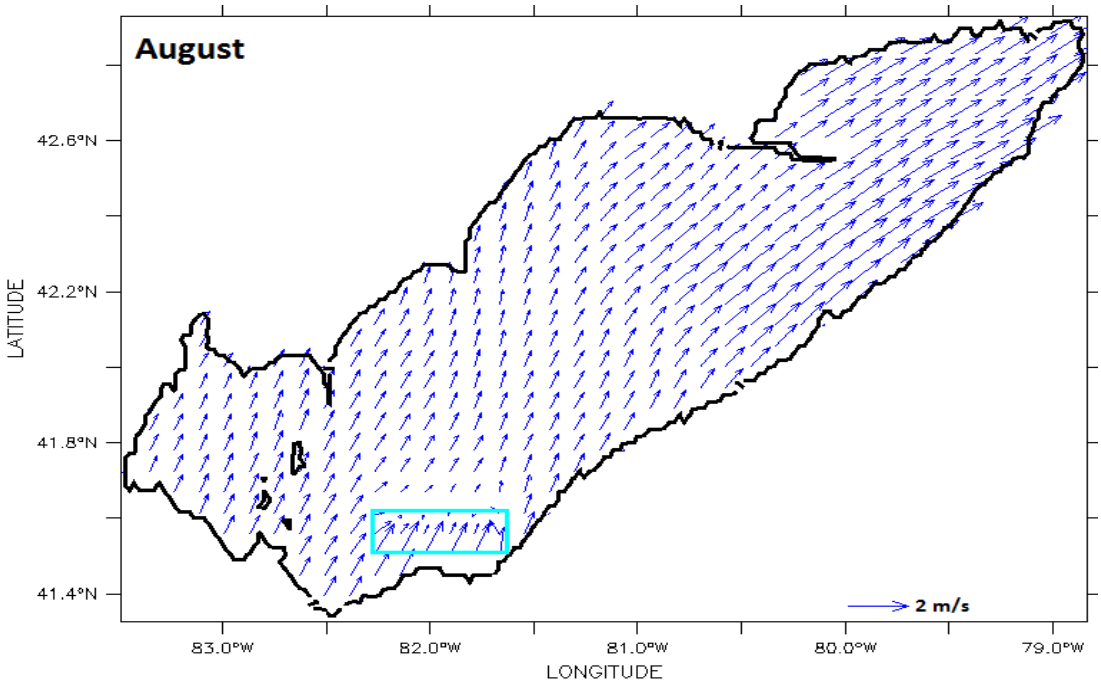

Figure 6.4: August averaged wind velocity

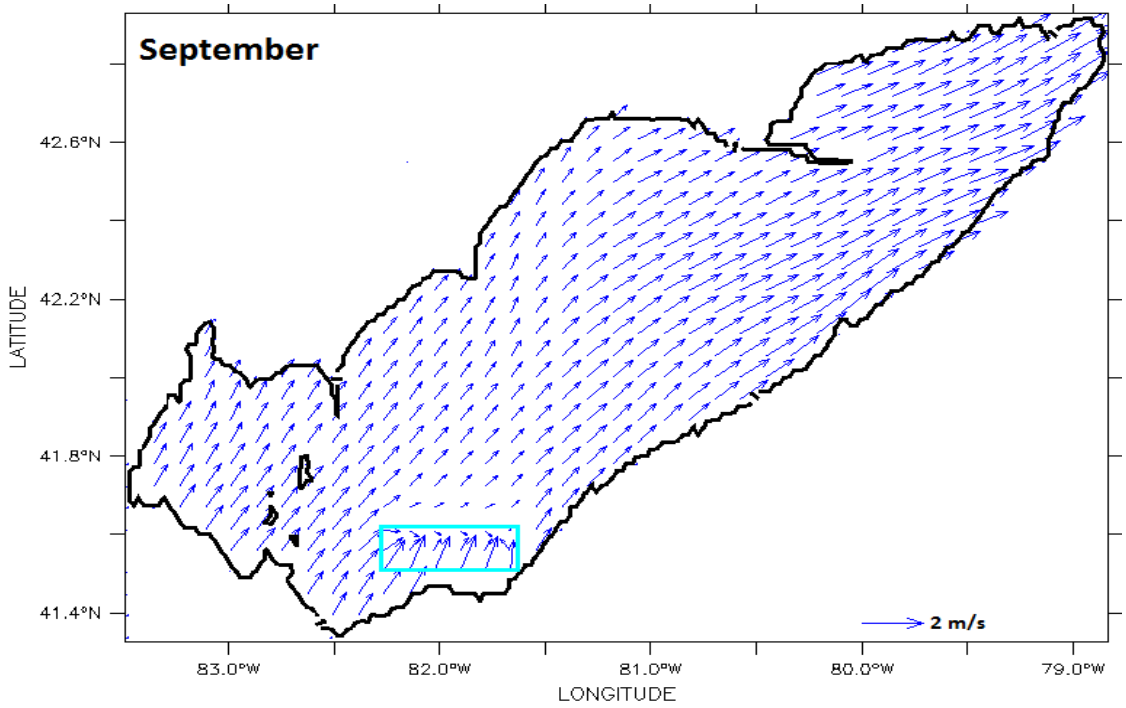

Figure 6.5: September averaged wind velocity

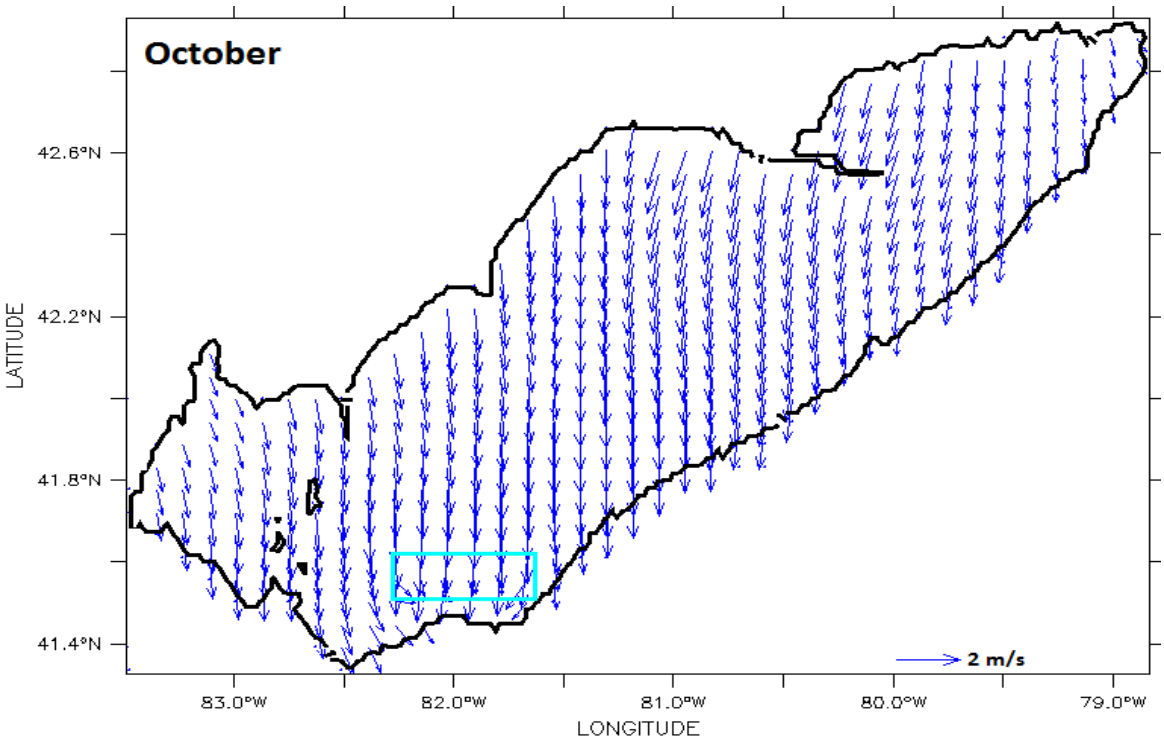

Figure 6.6: October averaged wind velocity

6.3 Wind Speed Contours

Monthly-averaged 10 m-wind speed (m/s), (Figures 6.7 to 6.12 a and b) contours based on NARR data, plus our imposed wind turbine wake reductions, for both cases (i.e, with and without the wind farm), are plotted for May-October 2005. To get a better view of the wind farm impact the monthly-averaged wind speed reduction in percentage are displayed in Figures 6.7c to 6.12 c. From these plots, we can conclude that July and October have the lowest and highest wind speeds of less than 3 m/s and above 4 m/s, respectively. Generally, the average 10m wind speed is between 3-4 m/s in most parts of the lake. Wind turbine hub height winds will be higher typically by a factor $\ln (100/z_0) / \ln (10/z_0)$ of order 1.25. The central basin generally experiences a slightly higher (generally by less than 1 m/s) wind speed compared to the other two basins which is probably due to its larger surface area and fetch. While wind speed increases in the central parts of the lake, it is lower closer to the shores due to the higher upstream surface roughnesses. When a wind farm is placed in the lake and the NARR wind field is modified, this wind speed variability increases significantly near and within the wind farm. However, away from the wind farm zone, as the wind turbine wake effect declines, there are only small changes in the imposed wind speed. The behavior of the monthly-averaged wind vector and speed are different as x and y components of the wind may be cancelled out in the averaging process. So, to understand better the wind farm effects of the wind fields over the lake, scalar wind speed contours are displayed. As mentioned earlier and as shown by the wind contour in case 2, the 10m-wind speed reduction can be of order 60 percent in the centre of the wake zone depending on the wind direction, but the average reduction is about 16-17 percent.

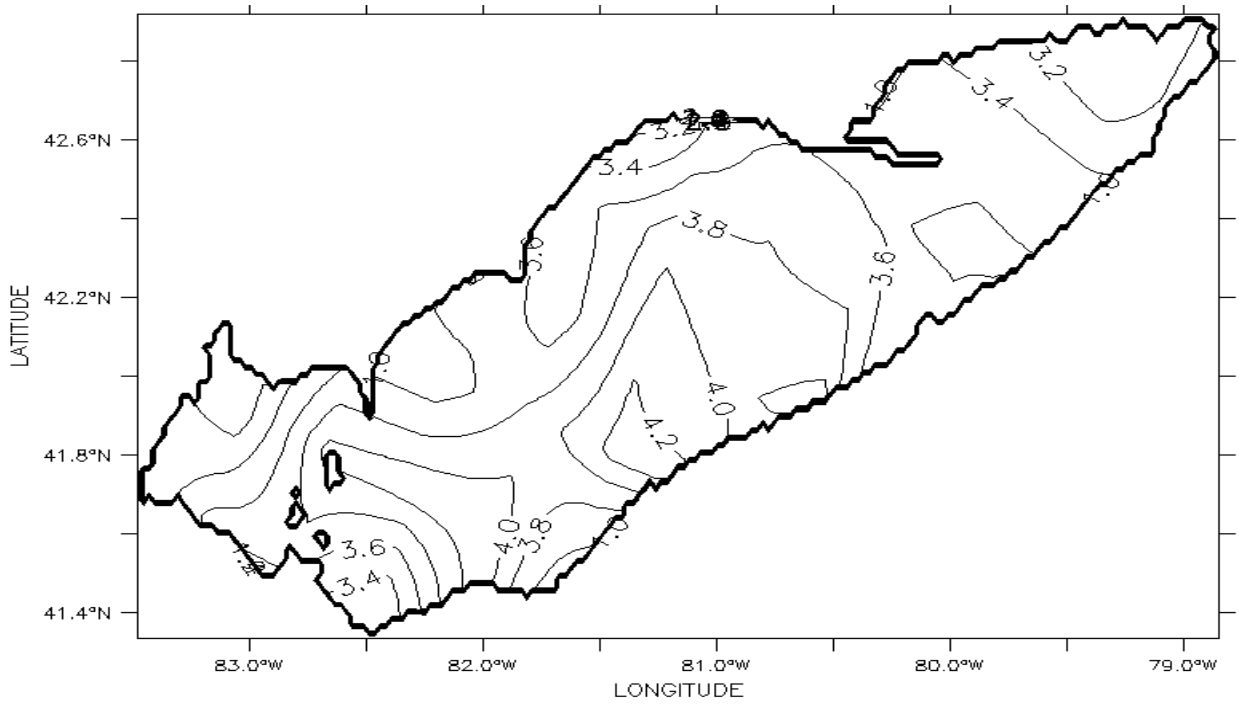
42.6°N
42.2°N
41.8°N
41.4°N
LATITUDE
83.0°W
82.0°W
81.0°W
80.0°W
79.0°W
LONGITUDE
3.2
3.4
3.6
3.8
4.0
4.2

a

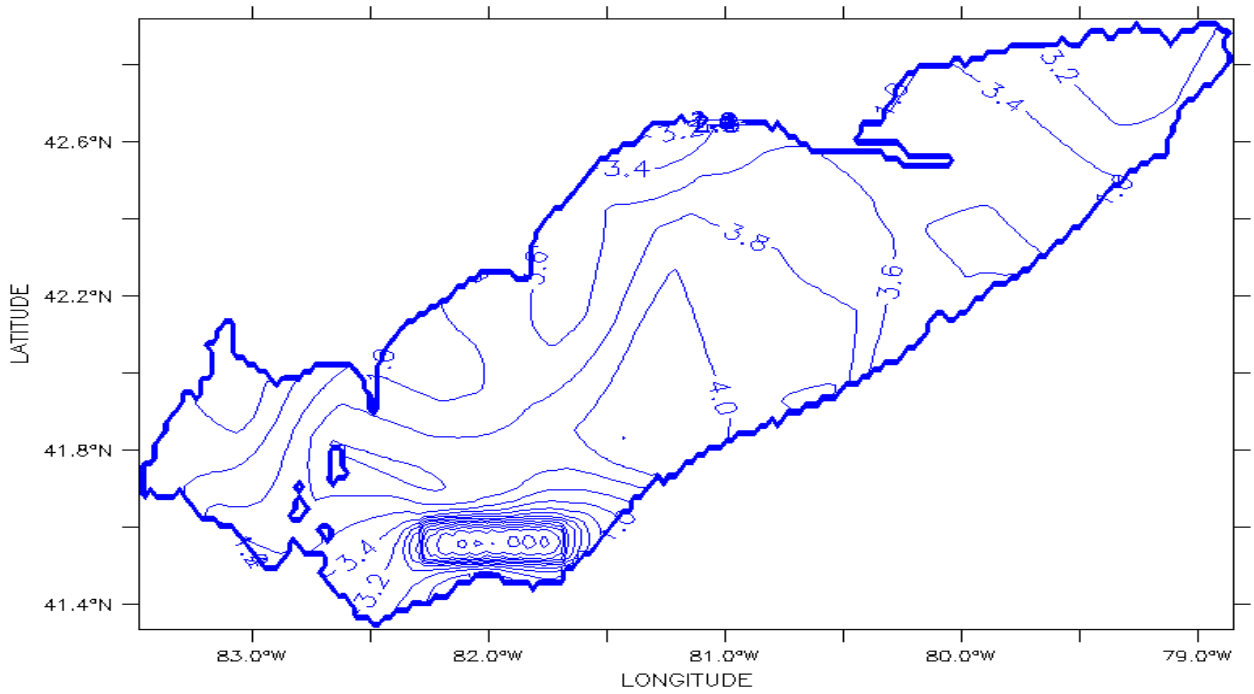
42.6°N
42.2°N
41.8°N
41.4°N
LATITUDE
83.0°W
82.0°W
81.0°W
80.0°W
79.0°W
LONGITUDE
3.2
3.4
3.6
3.8
4.0

b

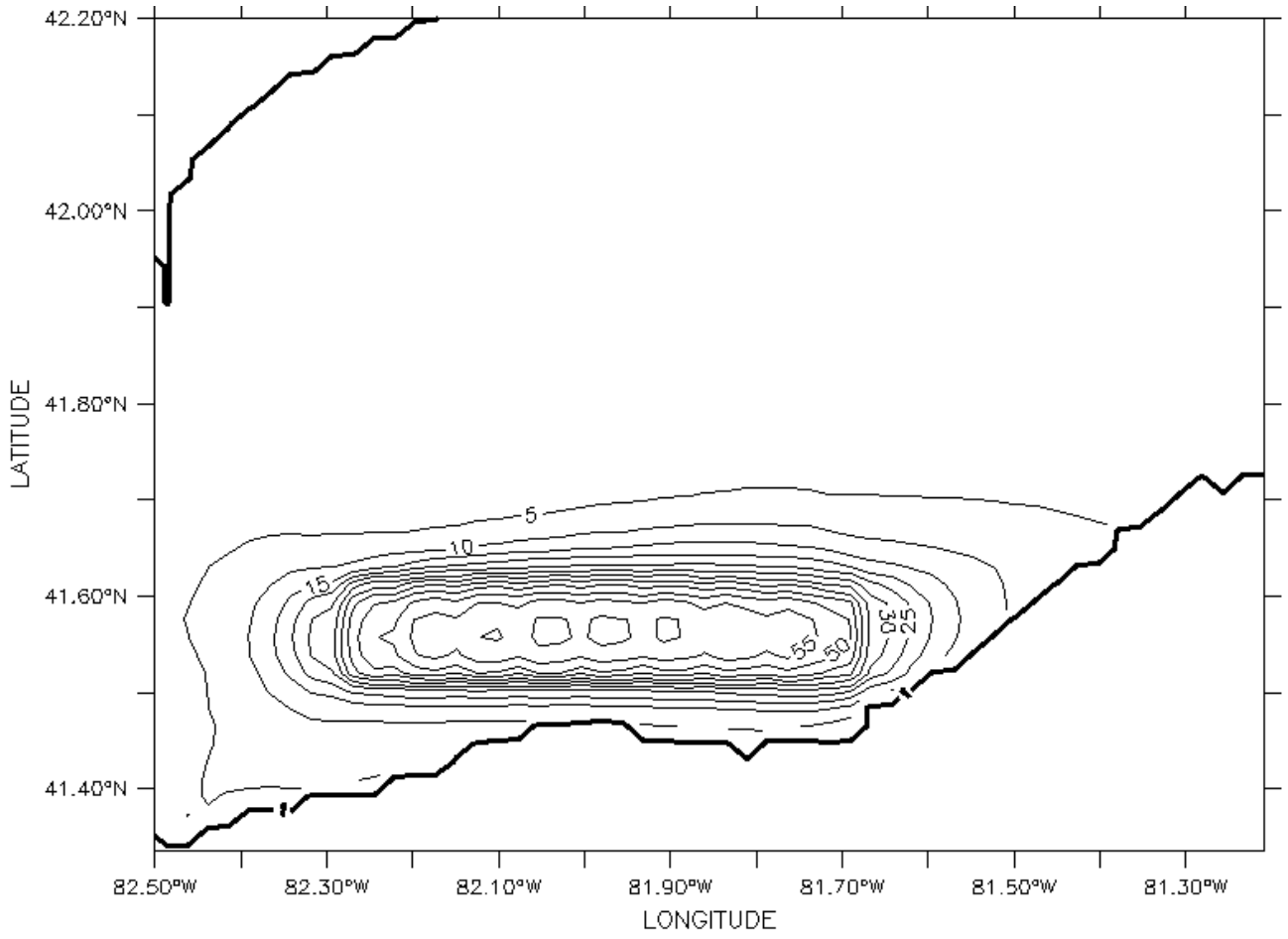

c

Figure 6.7: May-averaged wind speed (m/s) a) without a wind farm b) with a wind farm c) wind speed reduction in percent, 2005

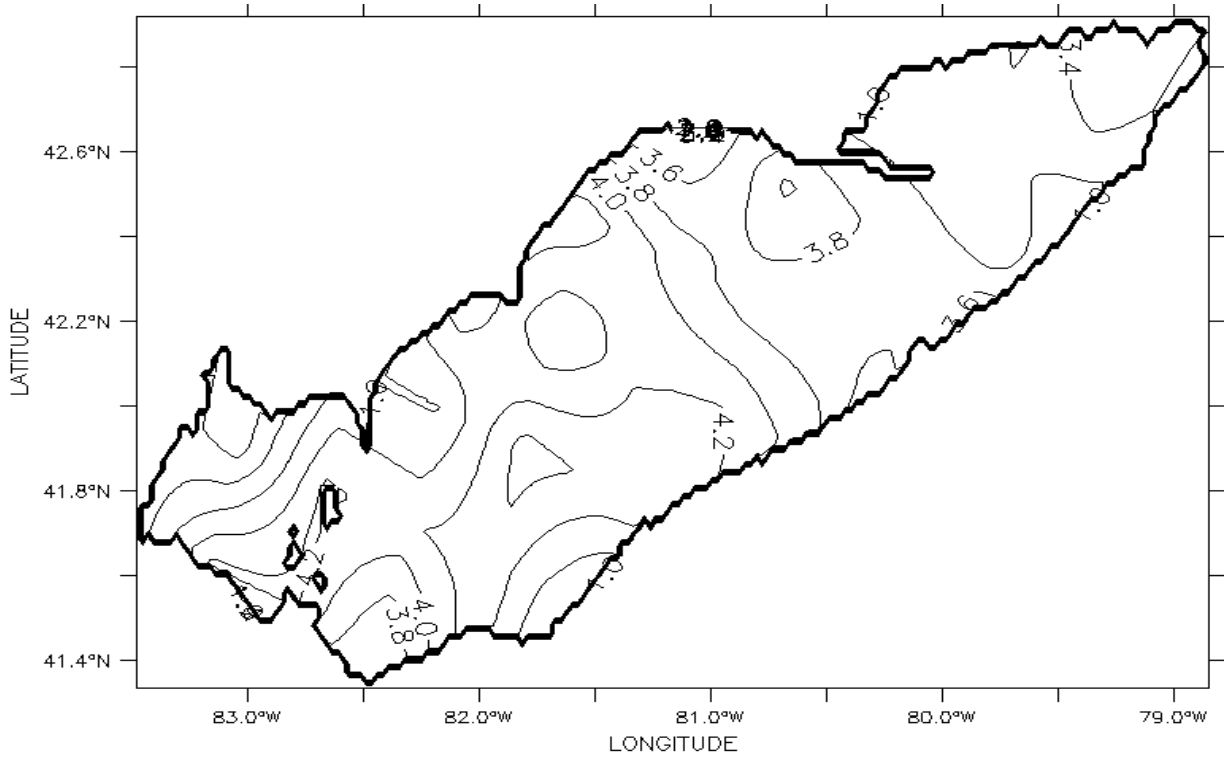
42.6°N
42.2°N
41.8°N
41.4°N
LATITUDE
83.0°W
82.0°W
81.0°W
80.0°W
79.0°W
LONGITUDE
3.4
3.6
3.8
4.0
4.2

a

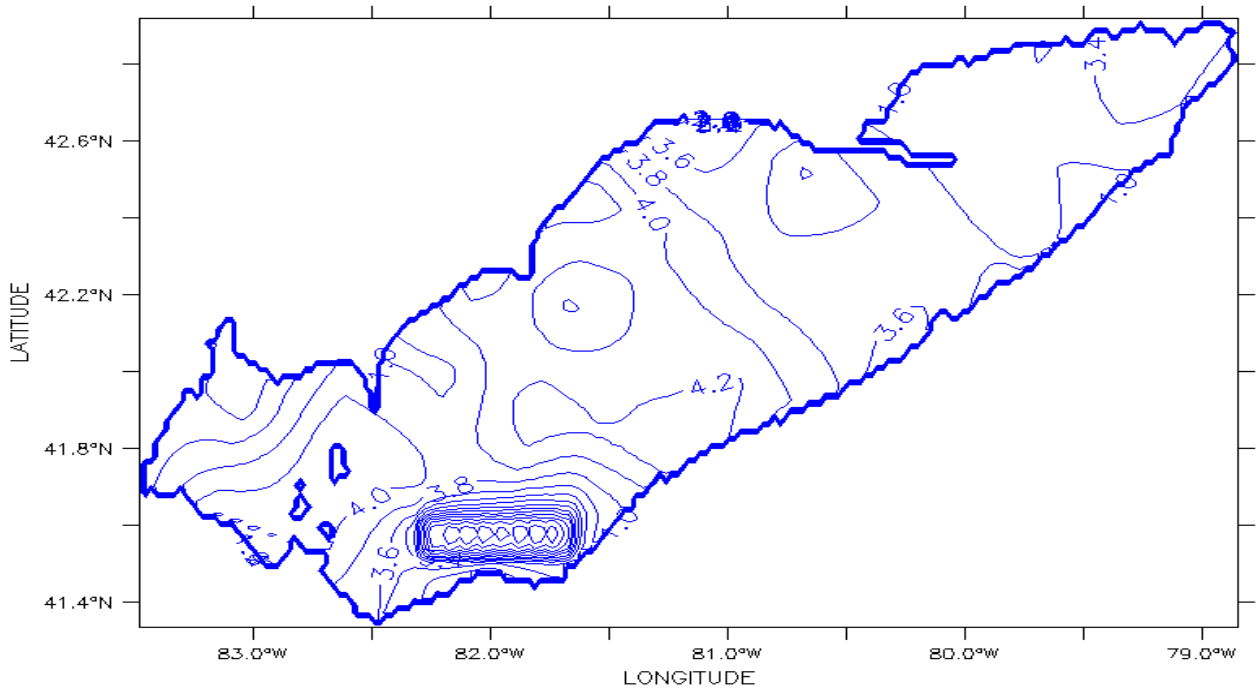
42.6°N
42.2°N
41.8°N
41.4°N
LATITUDE
83.0°W
82.0°W
81.0°W
80.0°W
79.0°W
LONGITUDE
3.4
3.6
3.8
4.0
4.2

b

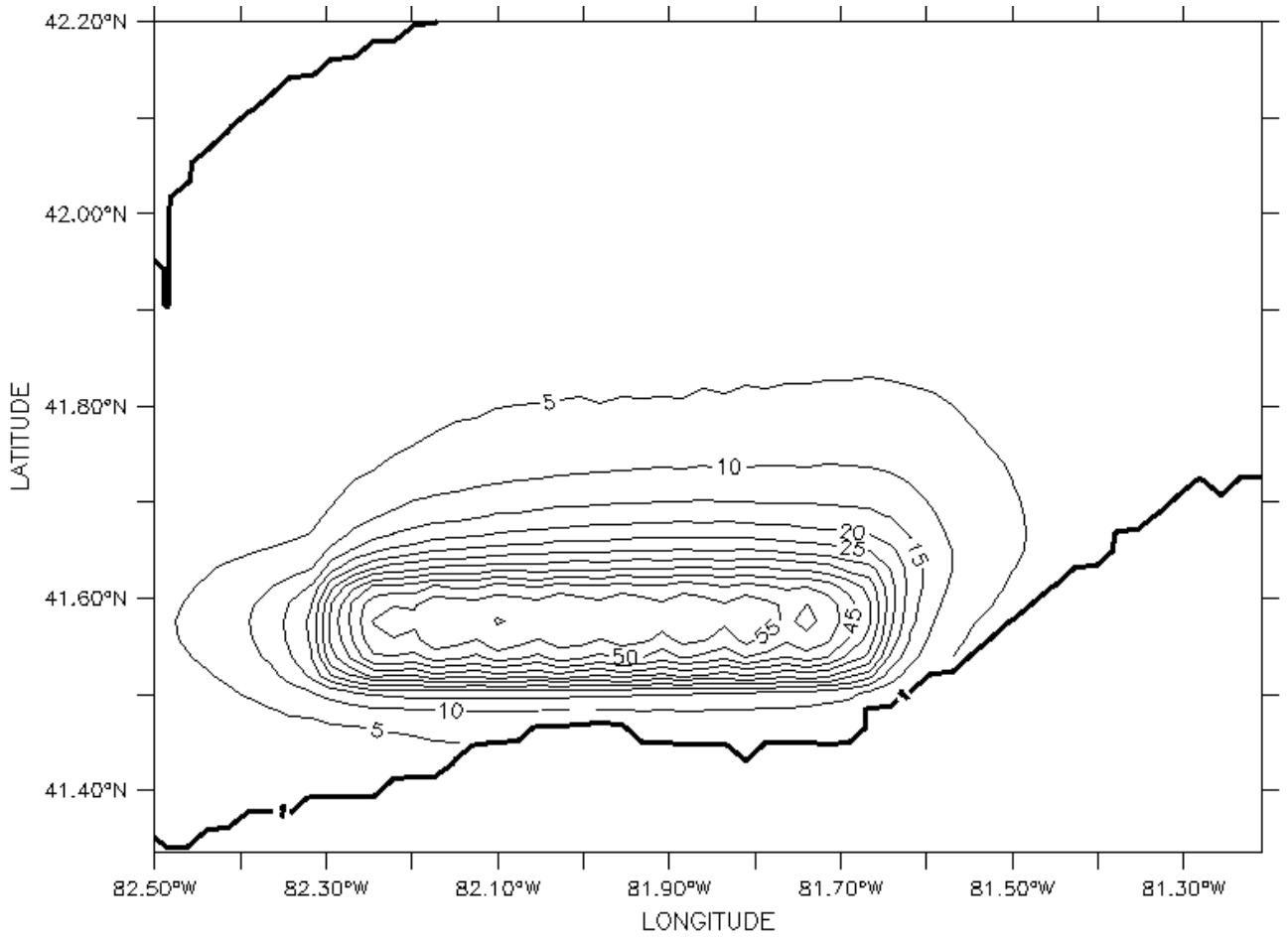

c

Figure 6.8: June-averaged wind speed (m/s) a) without a wind farm b) with a wind farm c) wind speed reduction in percent, 2005

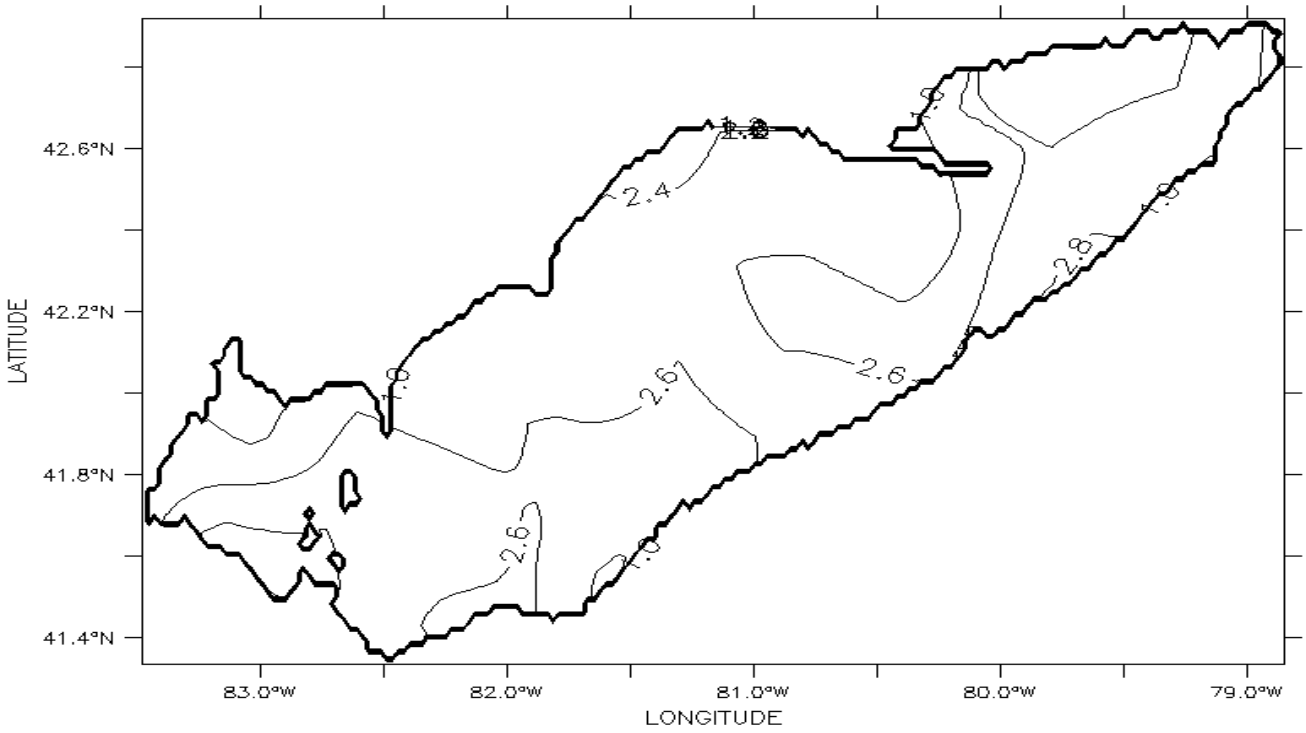
42.6°N
42.2°N
41.8°N
41.4°N
LATITUDE
83.0°W
82.0°W
81.0°W
80.0°W
79.0°W
LONGITUDE
2.4
2.6
2.8
3.0

a

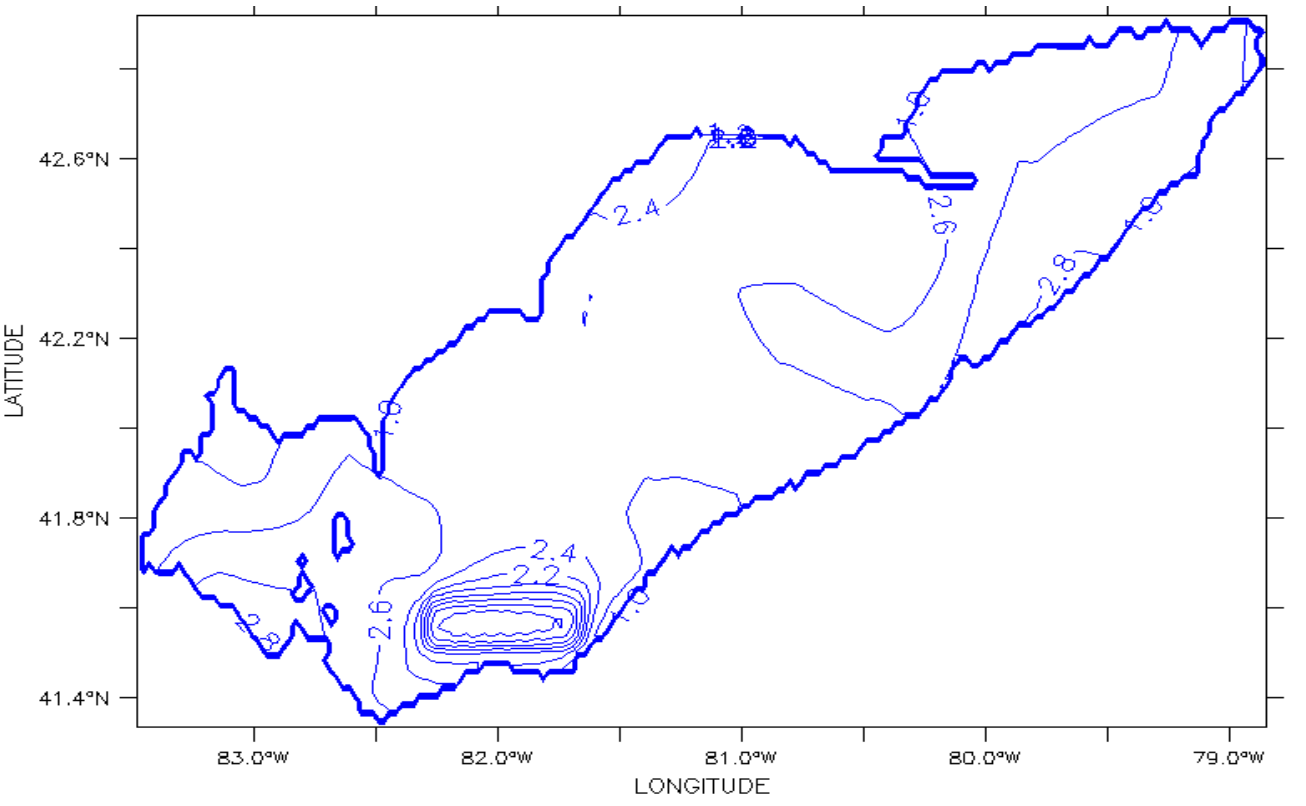
42.6°N
42.2°N
41.8°N
41.4°N
LATITUDE
83.0°W
82.0°W
81.0°W
80.0°W
79.0°W
LONGITUDE
2.4
2.2
2.6
2.8
3.0

b

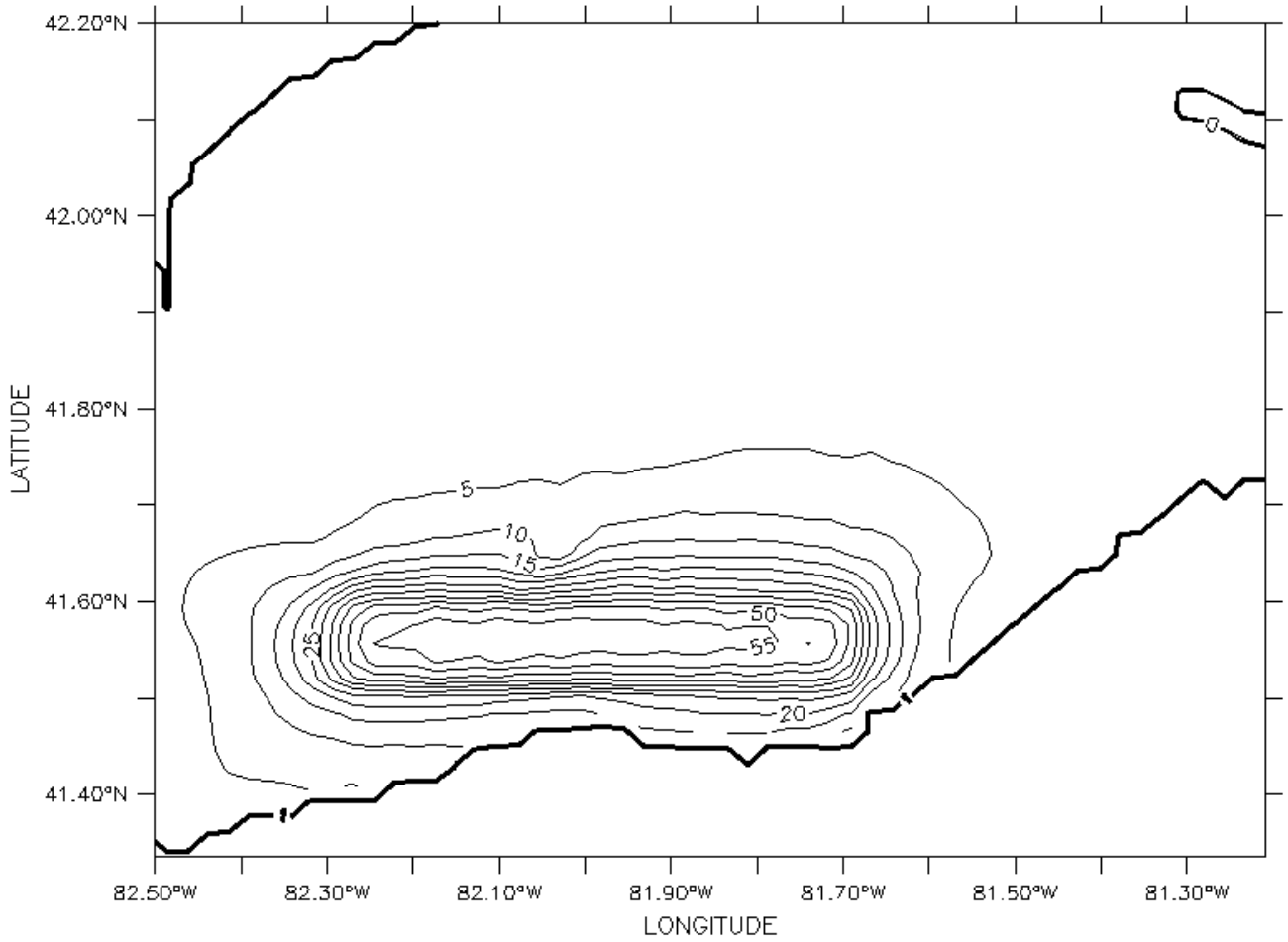

c

Figure 6.9: July-averaged wind speed (m/s) a) without a wind farm b) with a wind farm c) wind speed reduction in percent, 2005

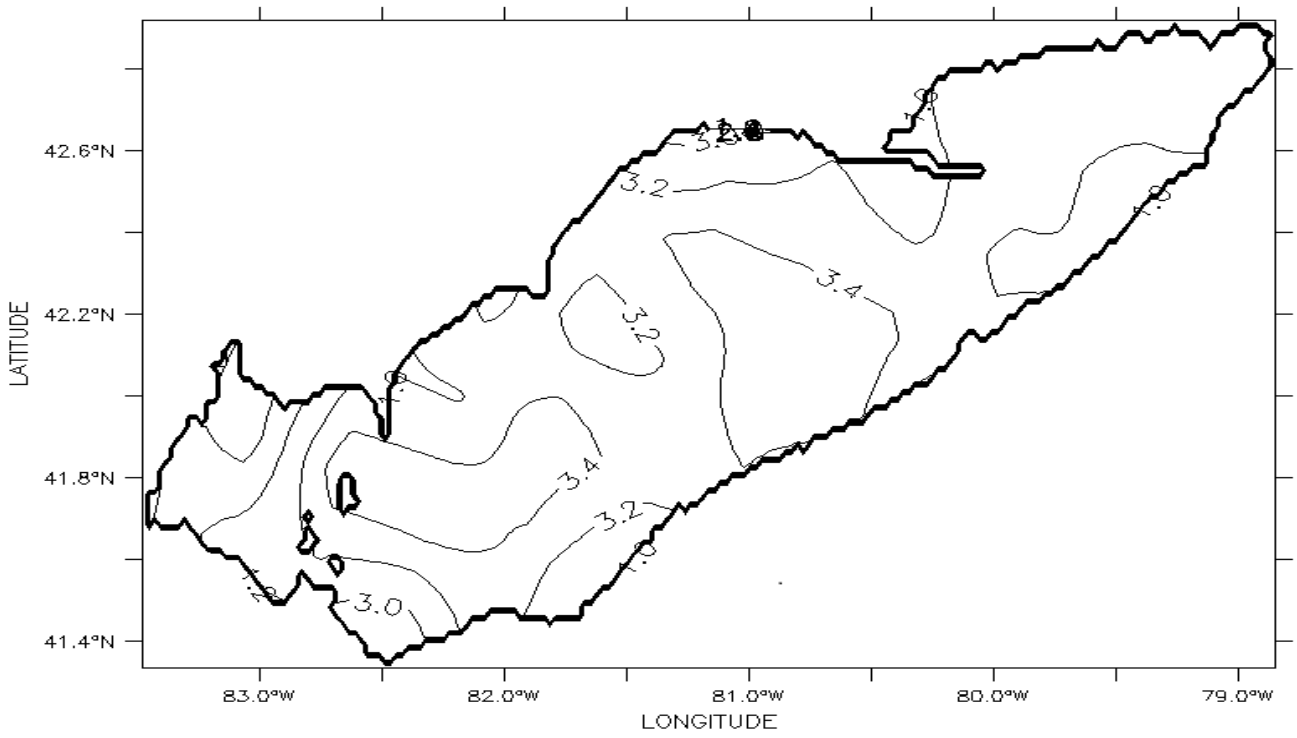
42.6°N
42.2°N
41.8°N
41.4°N
LATITUDE
83.0°W
82.0°W
81.0°W
80.0°W
79.0°W
LONGITUDE
3.2
3.4
3.0

a

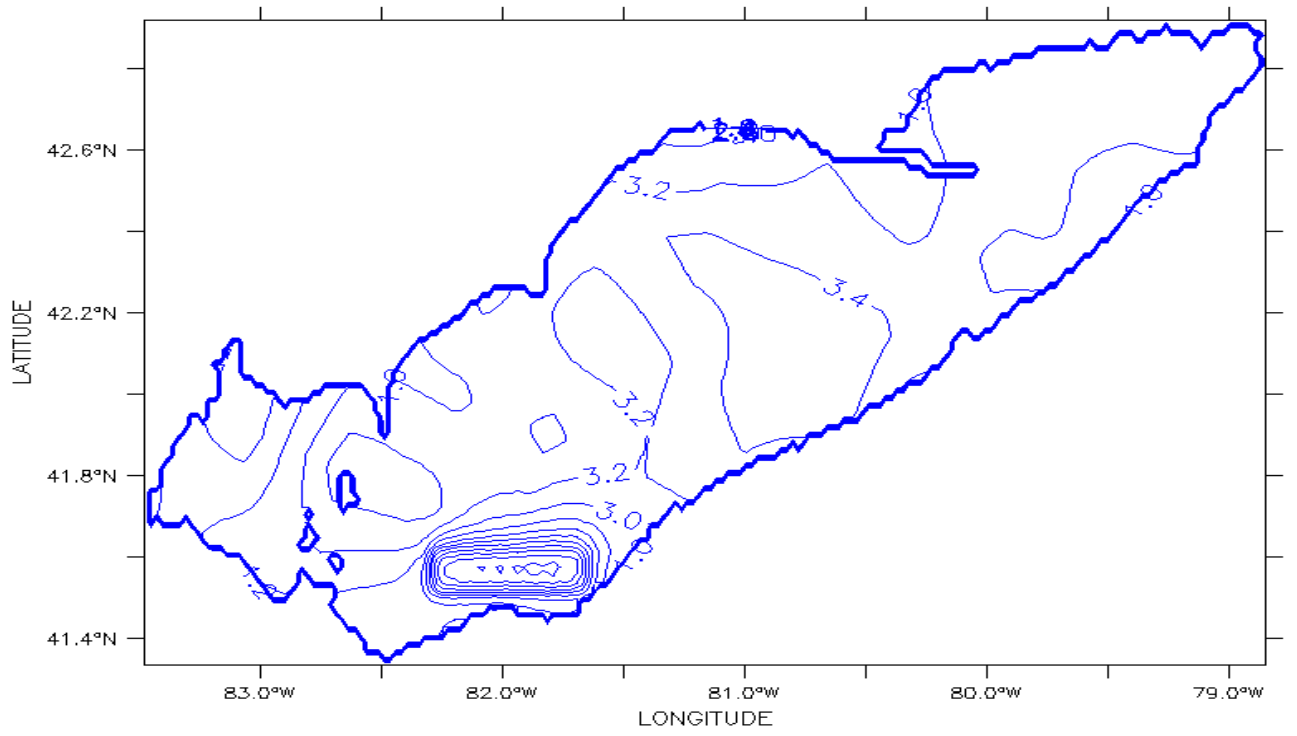
42.6°N
42.2°N
41.8°N
41.4°N
LATITUDE
83.0°W
82.0°W
81.0°W
80.0°W
79.0°W
LONGITUDE
3.2
3.4
3.0

b

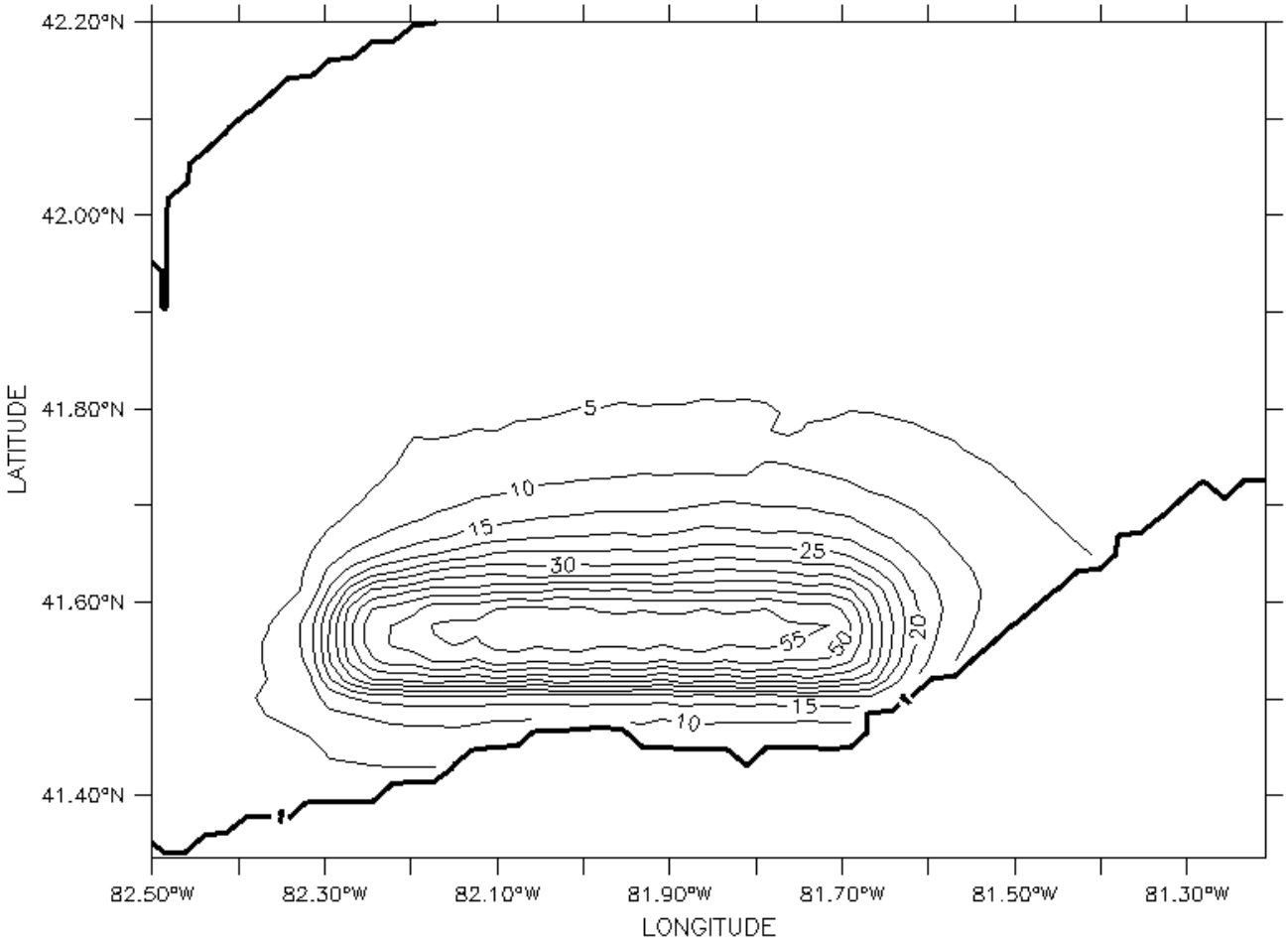

c

Figure 6.10: August-averaged wind speed (m/s) a) without a wind farm b) with a wind farm c) wind speed reduction in percent, 2005

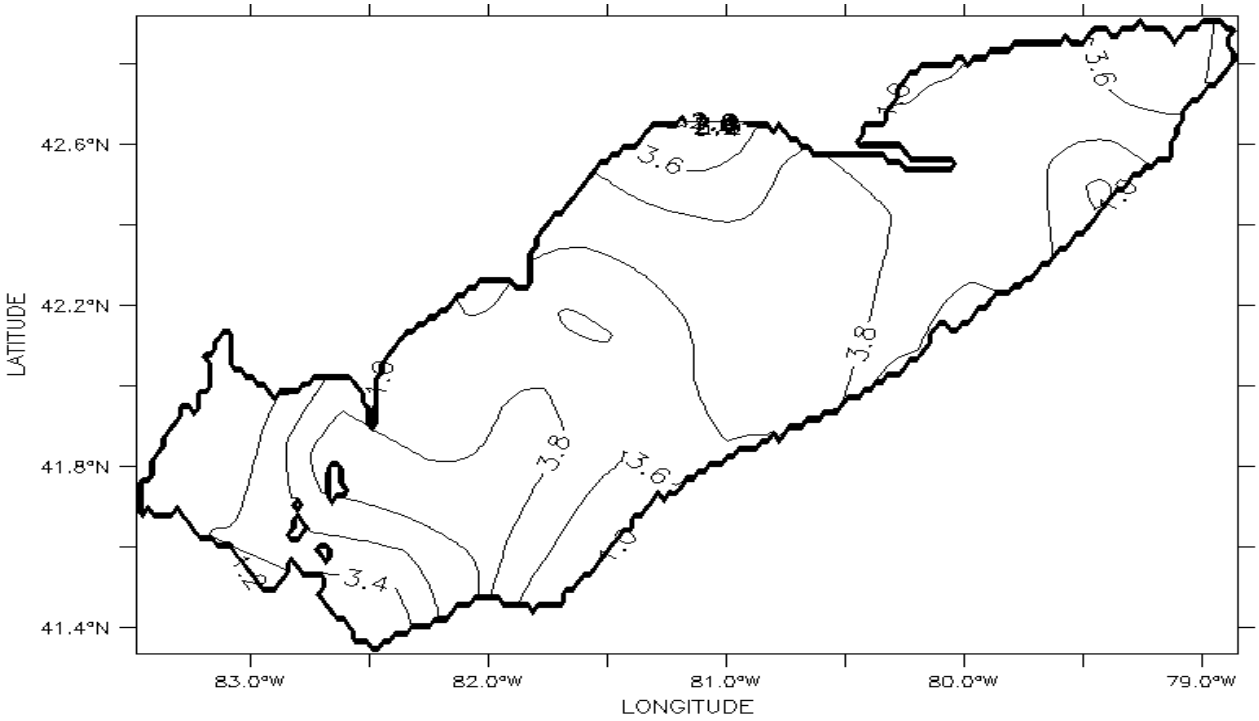
42.6°N
42.2°N
41.8°N
41.4°N
LATITUDE
83.0°W
82.0°W
81.0°W
80.0°W
79.0°W
LONGITUDE
3.6
3.8
3.4

a

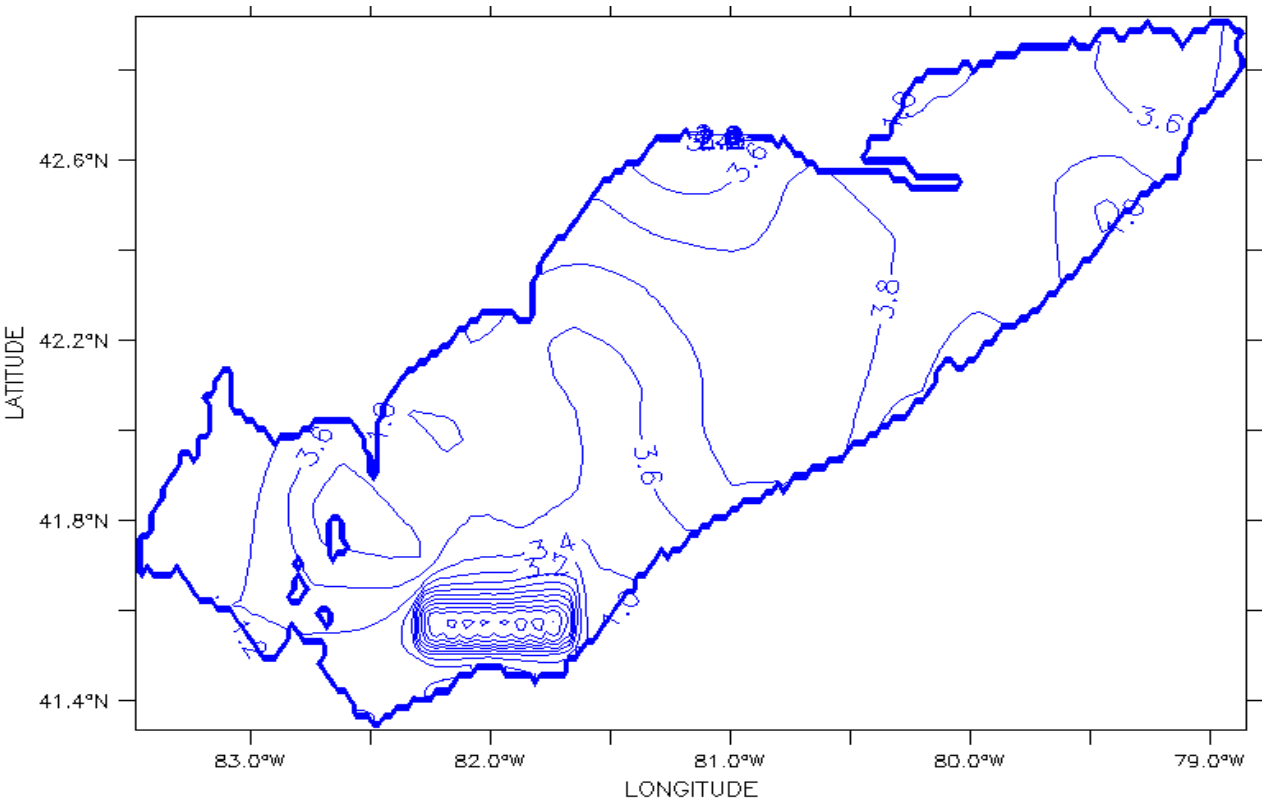
42.6°N
42.2°N
41.8°N
41.4°N
LATITUDE
83.0°W
82.0°W
81.0°W
80.0°W
79.0°W
LONGITUDE
3.6
3.8
3.4

b

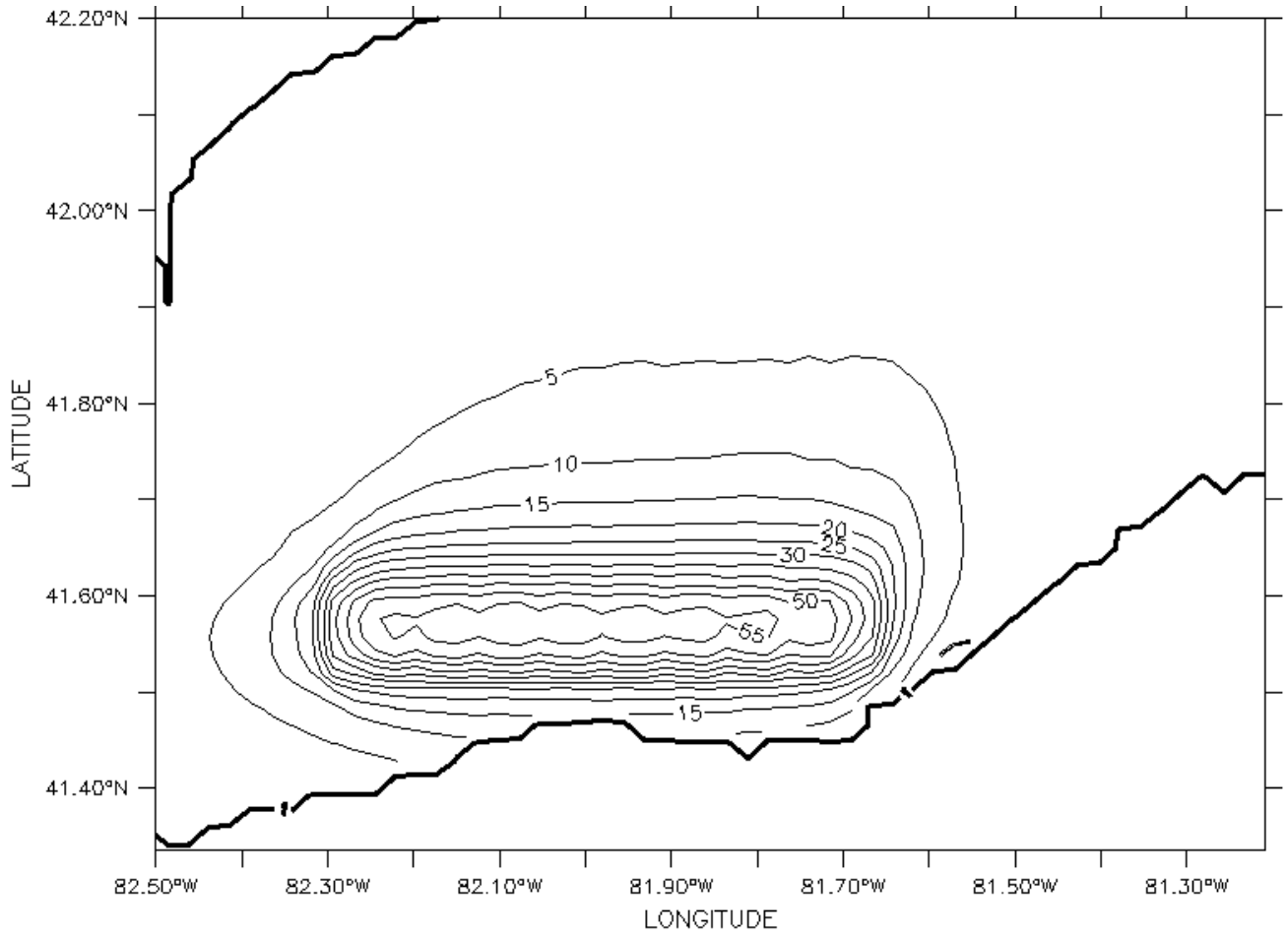

c

Figure 6.11: September-averaged wind speed (m/s) a) without a wind farm b) with a wind farm c) wind speed reduction in percent, 2005

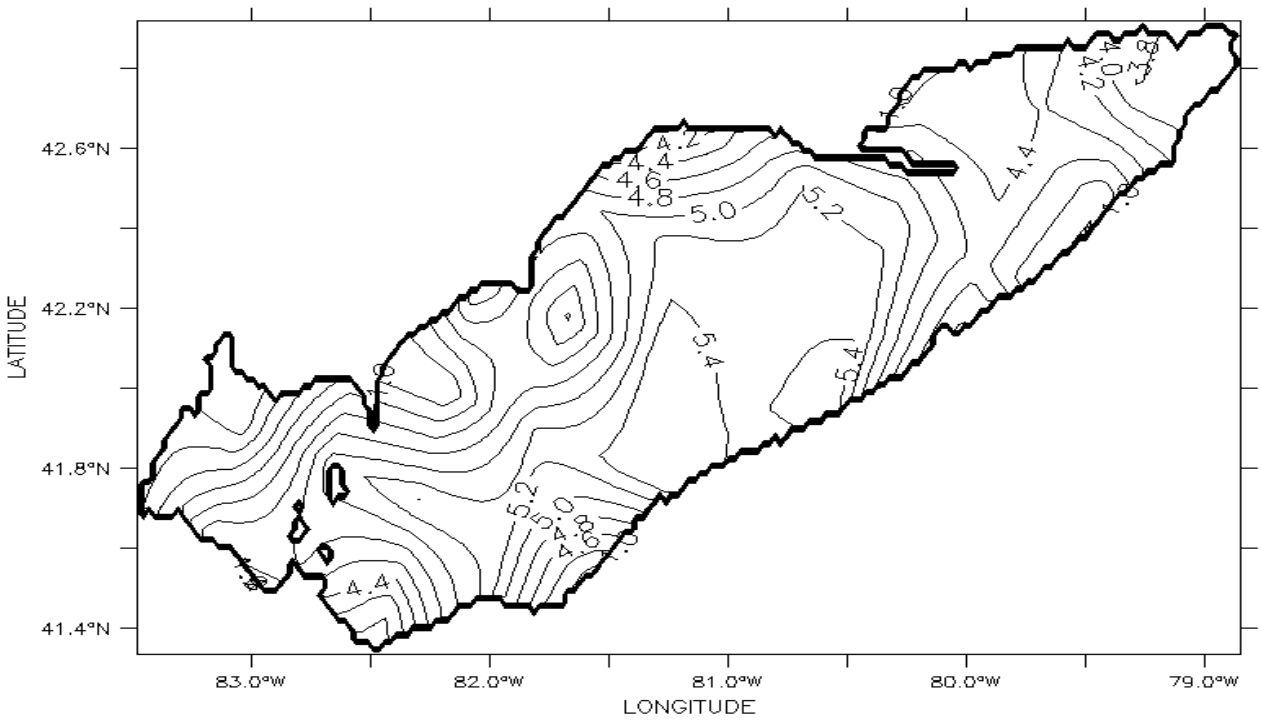
42.6°N
42.2°N
41.8°N
41.4°N
LATITUDE
83.0°W
82.0°W
81.0°W
80.0°W
79.0°W
LONGITUDE

a

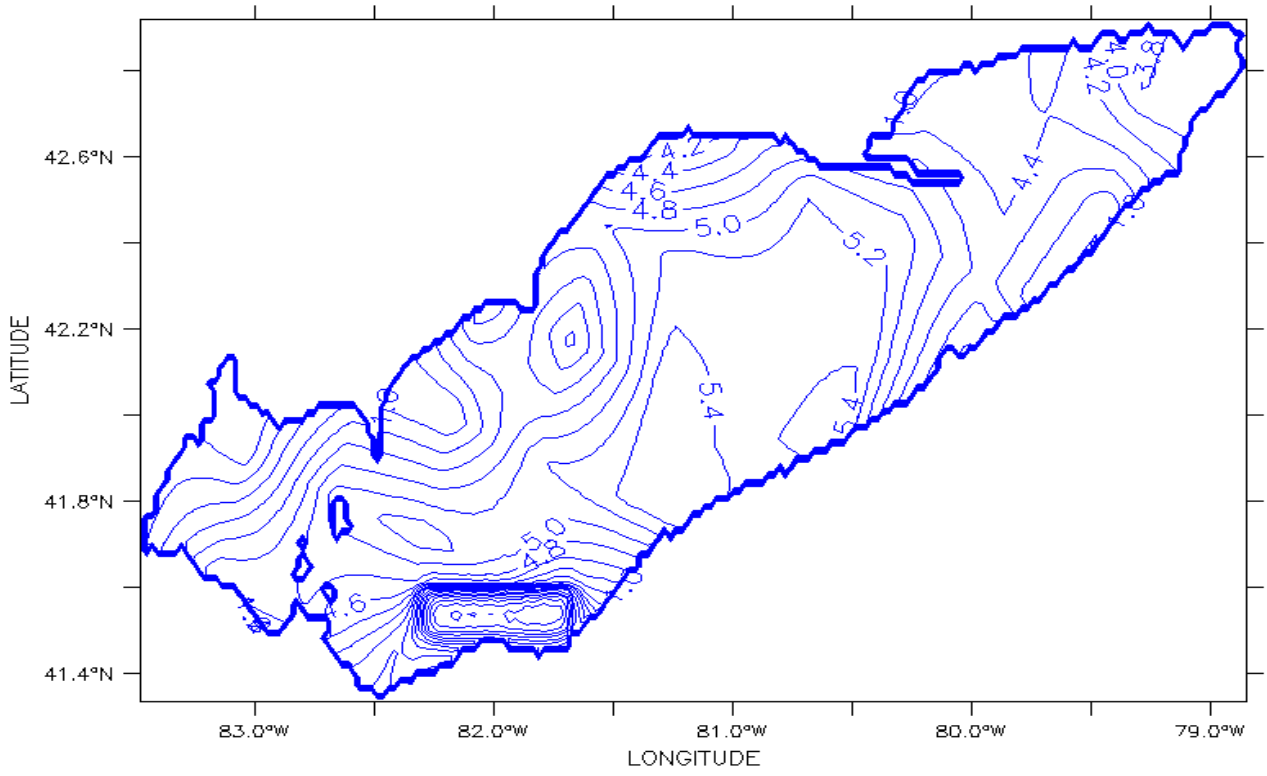
42.6°N
42.2°N
41.8°N
41.4°N
LATITUDE
83.0°W
82.0°W
81.0°W
80.0°W
79.0°W
LONGITUDE

b

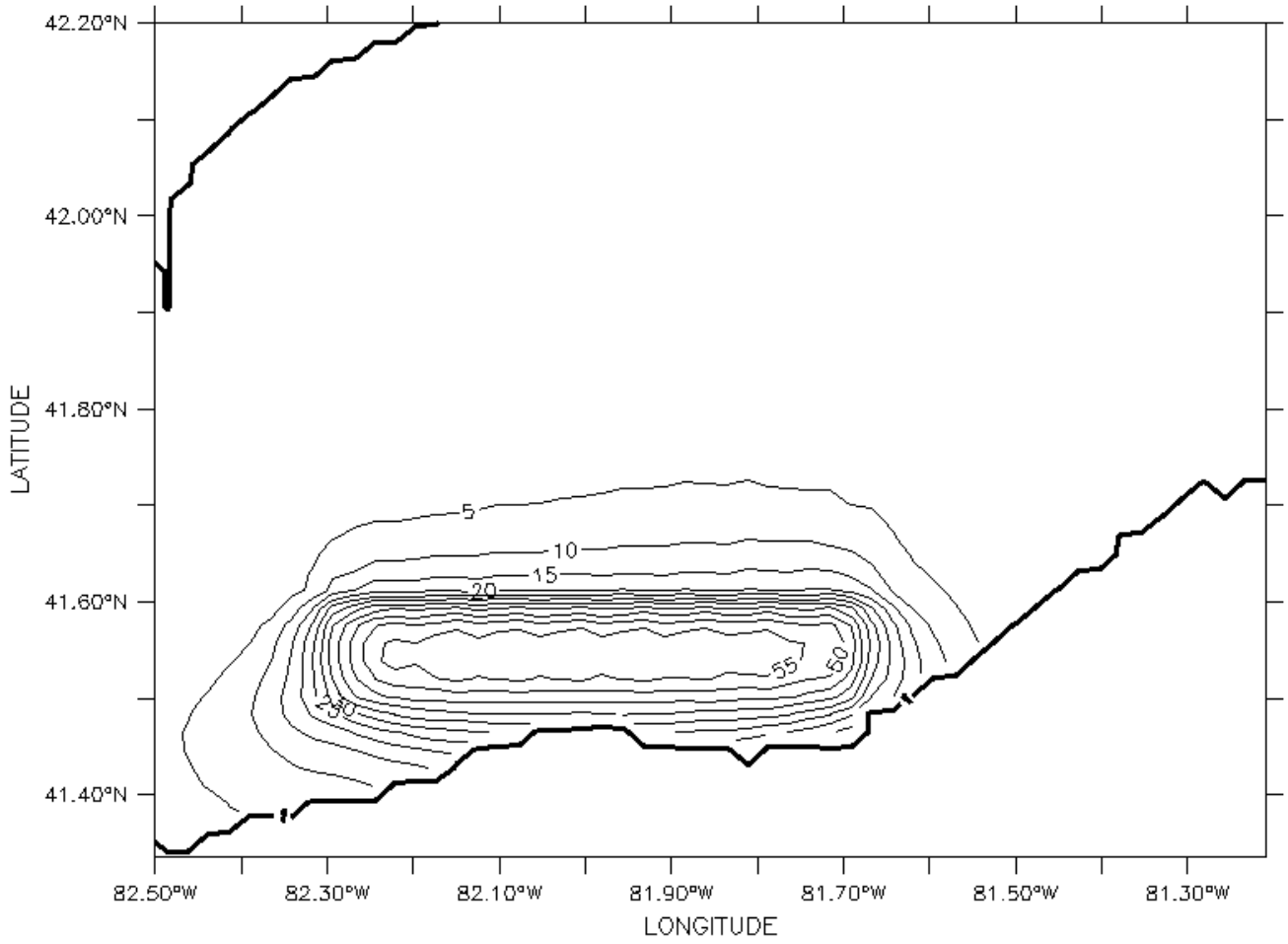

c

Figure 6.12: October-averaged wind speed (m/s) a) without a wind farm b) with a wind farm c) wind speed reduction in percent, 2005

6.4 Wind Rose at Centre of Wake (CW) When There Is No Wind Farm (Case 1)

Six-month and monthly NARR wind roses are displayed in Figures 6.13 to 6.19 a and b. There are 5 wind speed categories ranging from 1 to >8 m/s, also 16 wind direction (22.5-degree sectors) are considered in plotting the wind roses. The frequency counts up to 25 percent in each sector bin. Directions are those that the wind is coming from. See section 1.6.1 for the centre of wake location.

Figure 6.13a confirms that the dominant direction of the wind over the Lake Erie during May to October is S-SW. About 9 percent of time the wind speed is over 4 m/s. Dominant winds blow from the SW. In May (Figure 6.14), About 91 percent of the time winds are less than 4 m/s. Figure 6.15 shows June dominant wind speed of 2-4 m/s blows 59 percent of the time. N winds have a frequency of 18 percent while WSW and SW ones each blow with a frequency of 15 percent in the June wind rose. In July (Figure 6.16), we observe winds of less than 2 m/s blowing about 70 percent of the time. In August, Figure 6.17 the winds speed up but winds are less than 4 m/s for 90 percent of the time. In September winds are slightly stronger and frequently blow from W-SW, (Figure 6.18). The speed is still comparable with August winds. October winds, Figure 6.19, are the strongest and about 2 percent of times winds of above 6 m/s blow at this location. However, the most common winds are less than 4 m/s about 75 percent of the time, while for 24 percent of the time we observe winds of speed 4-6 m/s. Winds in October are from the NNE and NE sectors 23 percent of the time.

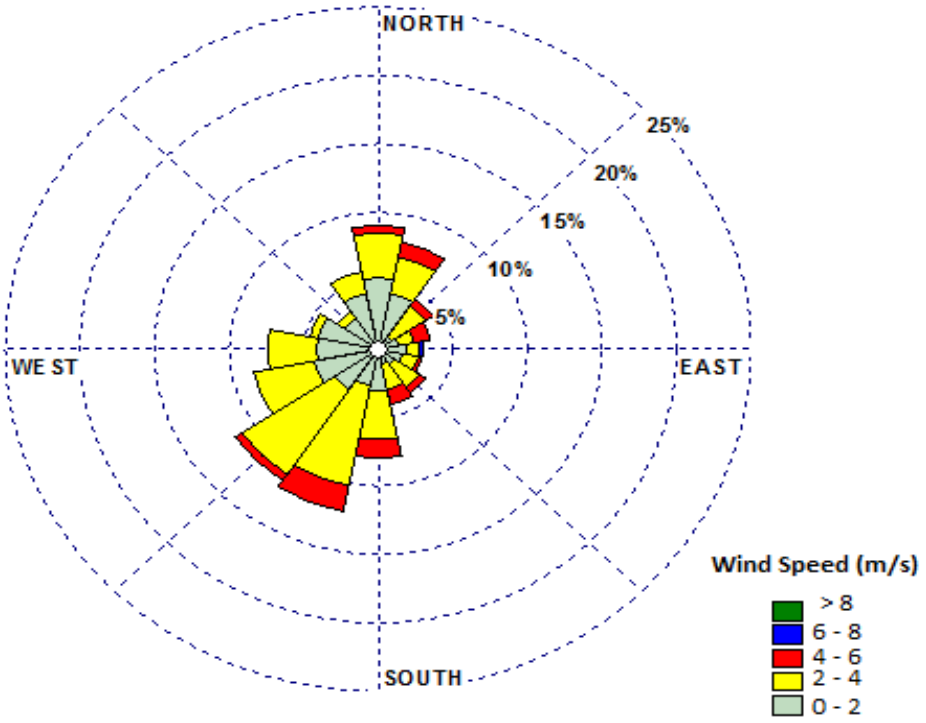

a

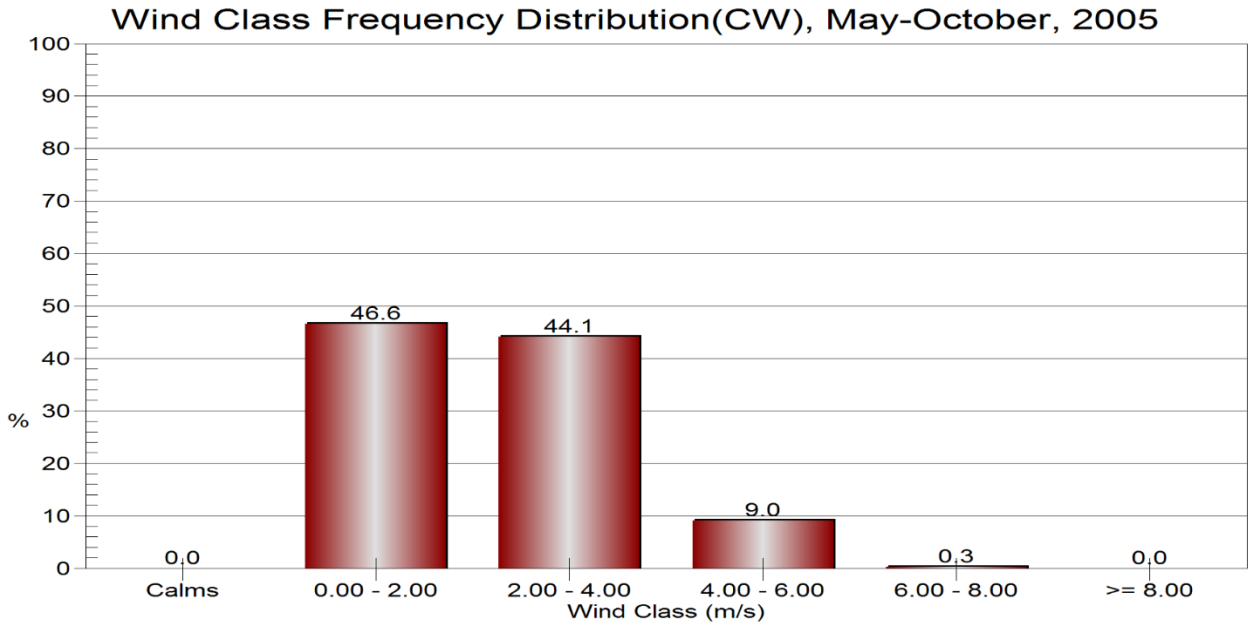

b

Figure 6.13: Twelve- hour a) Wind rose b) Wind class frequency distribution, May-October, 2005

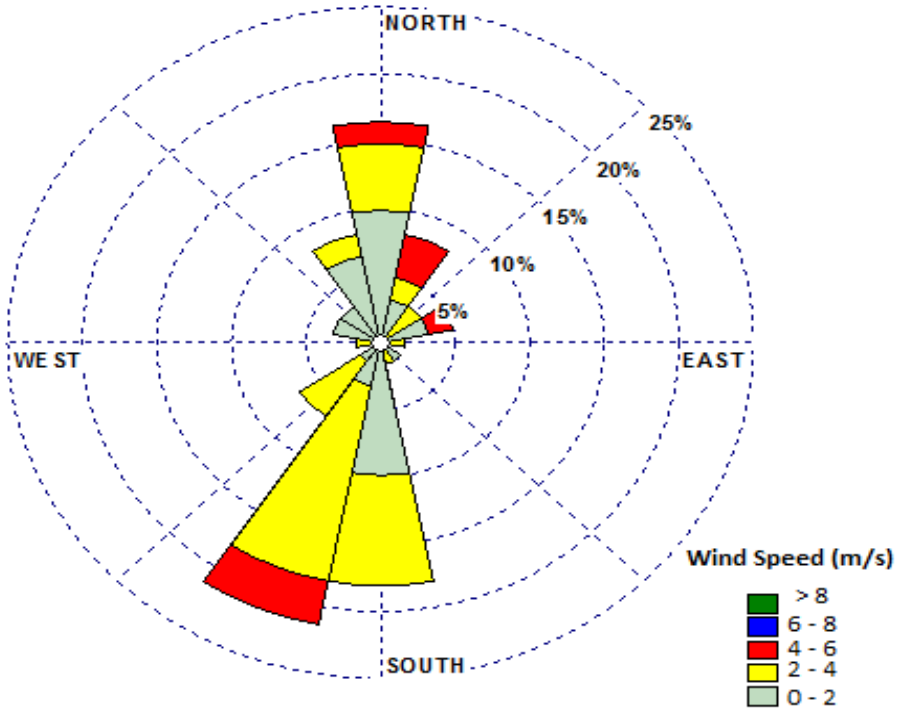

a

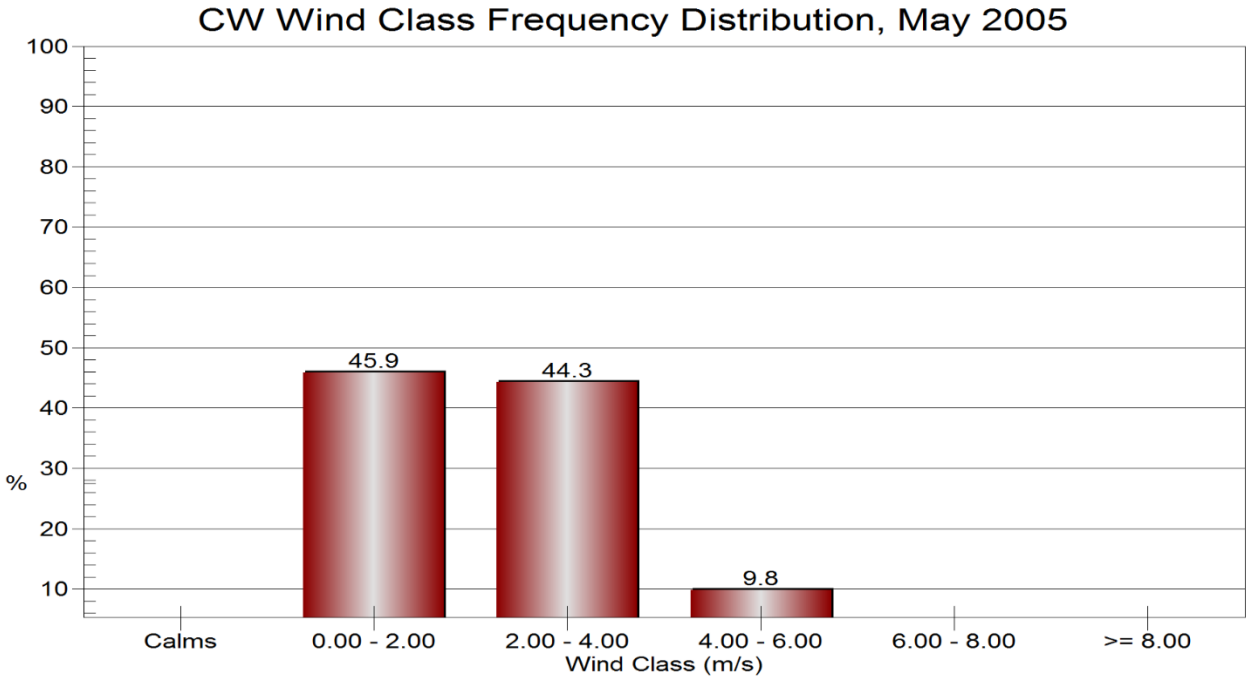

b

Figure 6.14: Twelve- hour a) Wind rose b) Wind class frequency distribution, May 2005

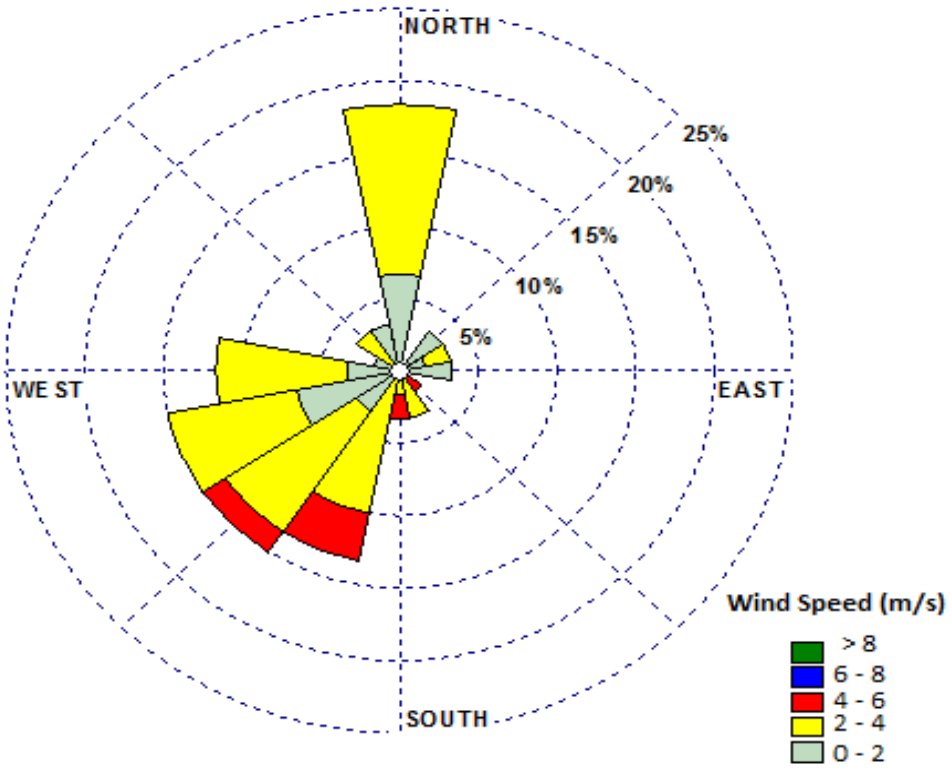

a

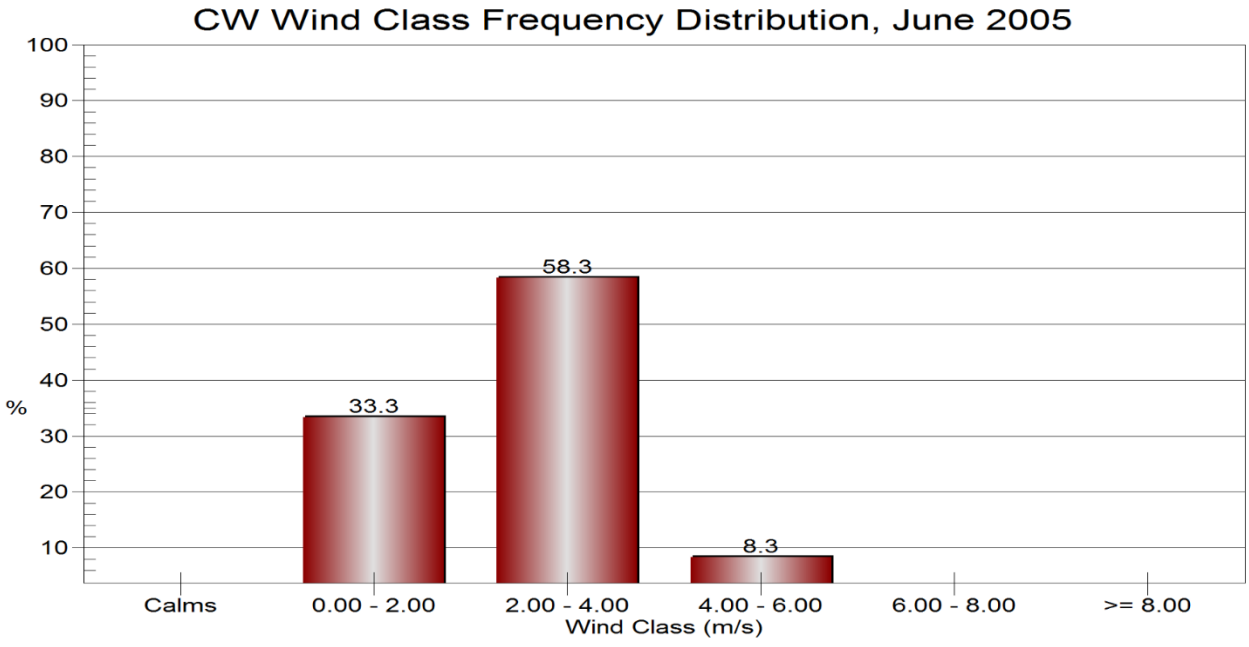

b

Figure 6.15: Twelve- hour a) Wind rose b) Wind class frequency distribution, June 2005

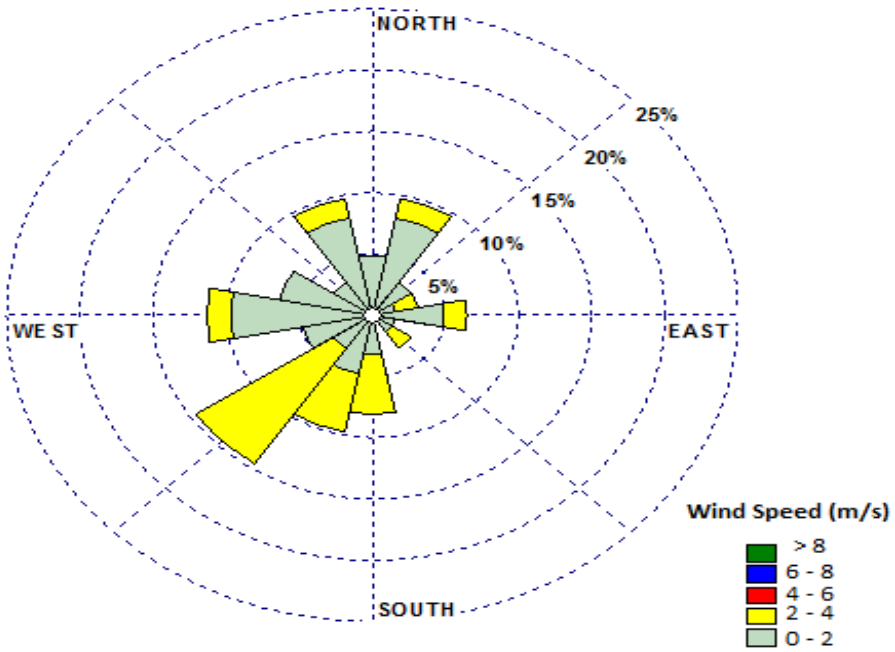

a

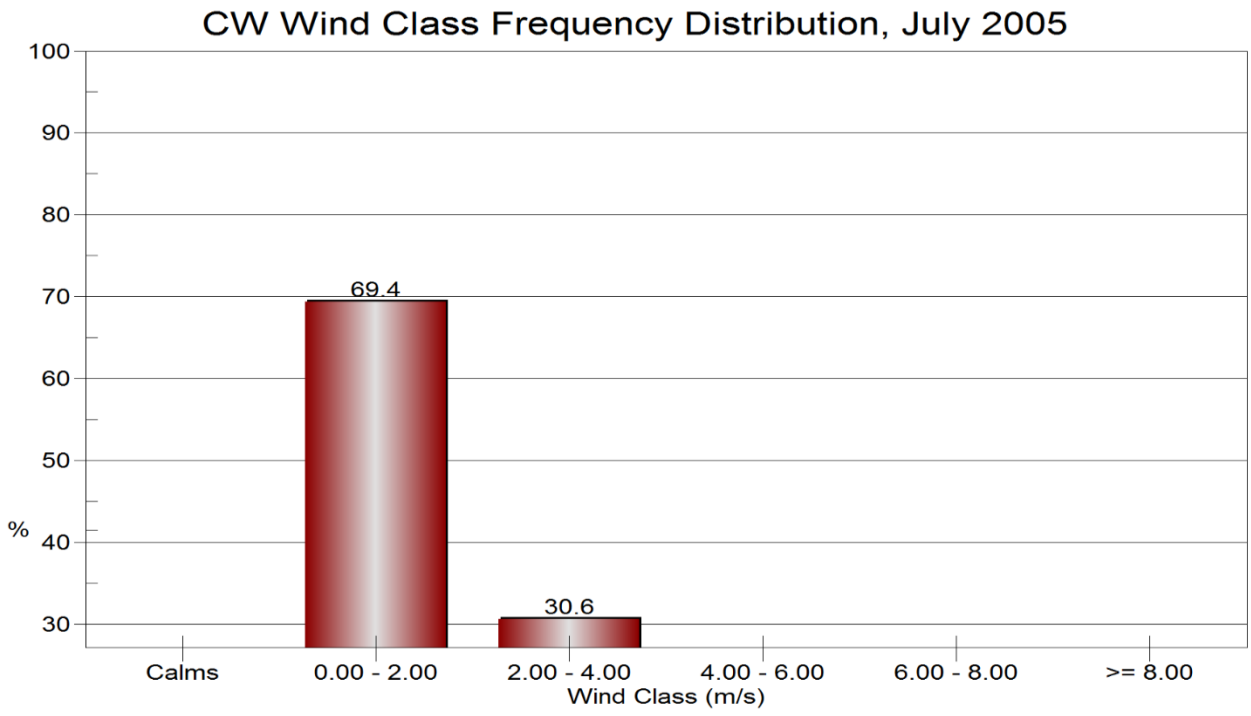

b

Figure 6.16: Twelve- hour a) Wind rose b) Wind class frequency distribution, July 2005

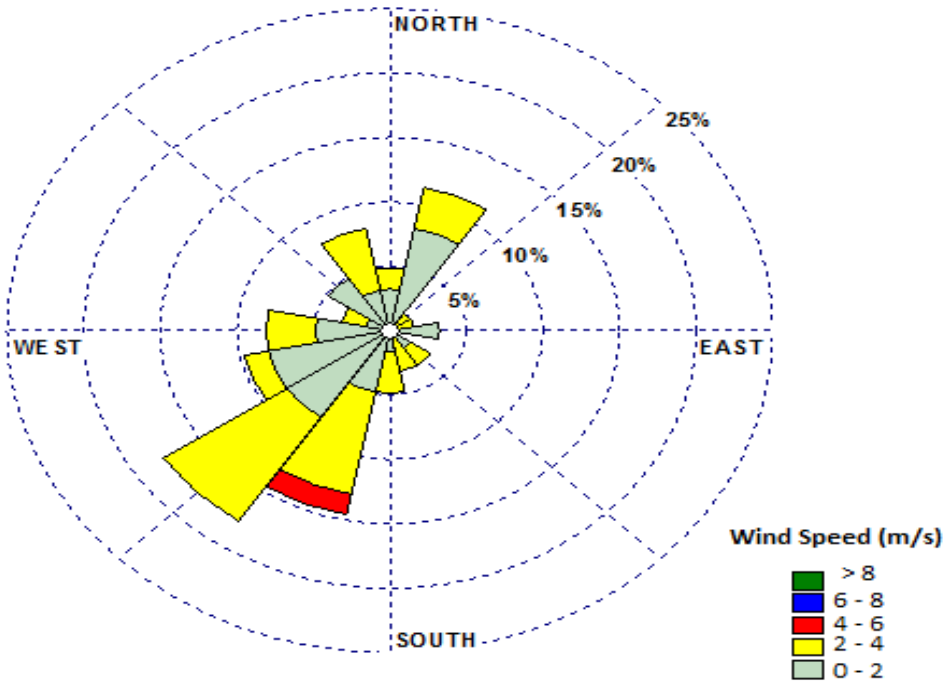

a

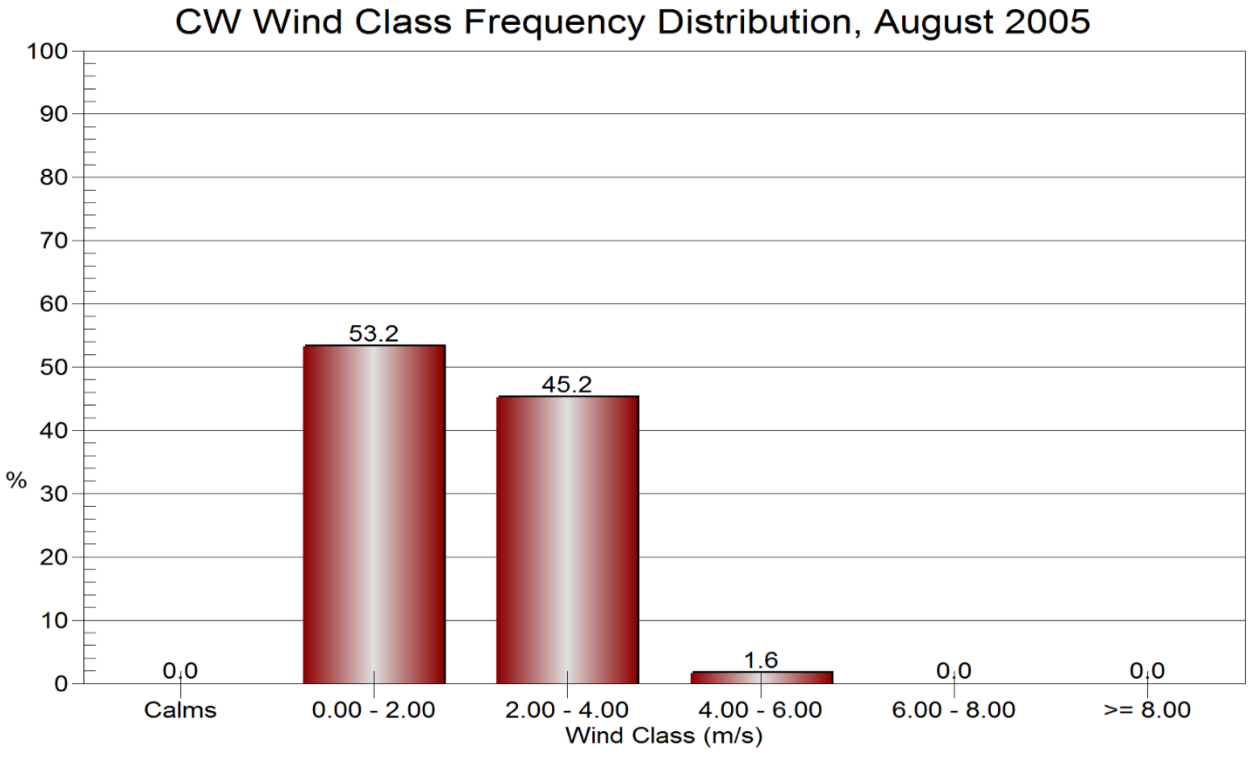

b

Figure 6.17: Twelve- hour a) Wind rose b) Wind class frequency distribution, August 2005

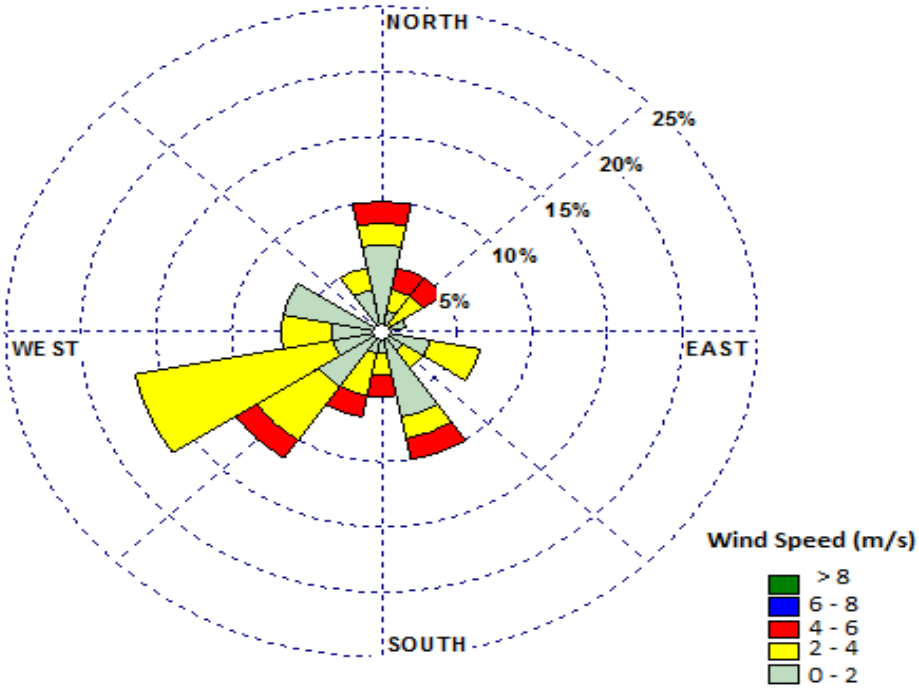

a

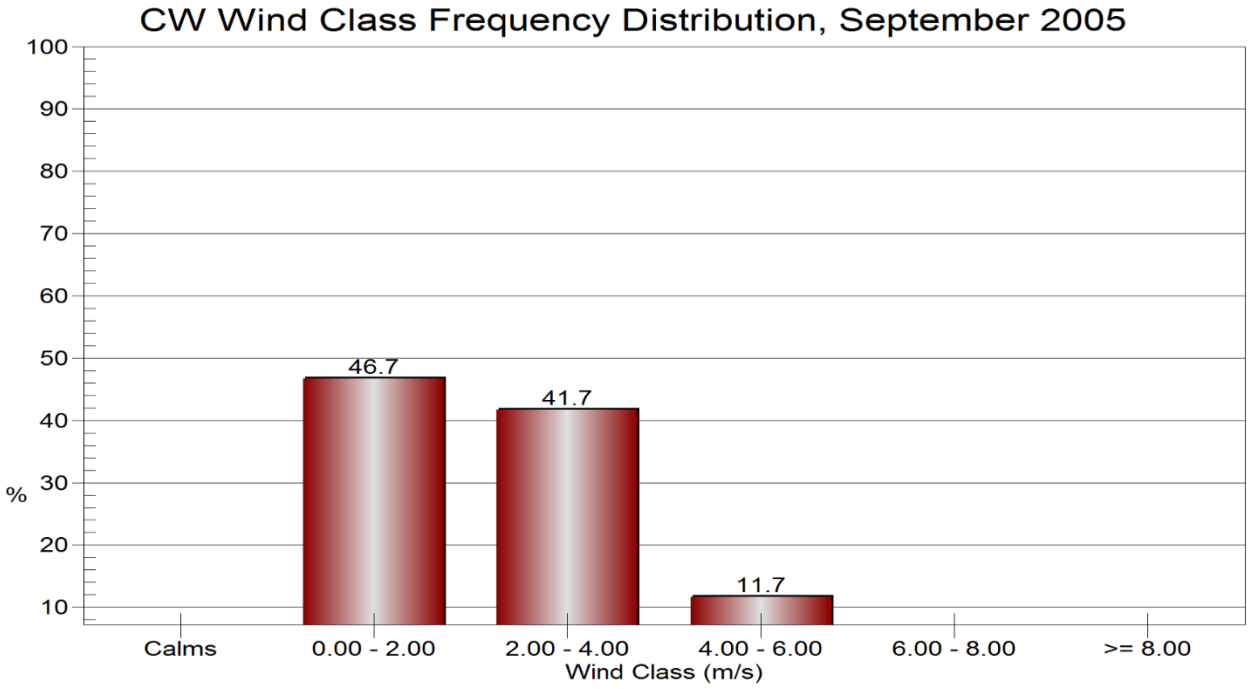

b

Figure 6.18: Twelve- hour a) Wind rose b) Wind class frequency distribution, September 2005

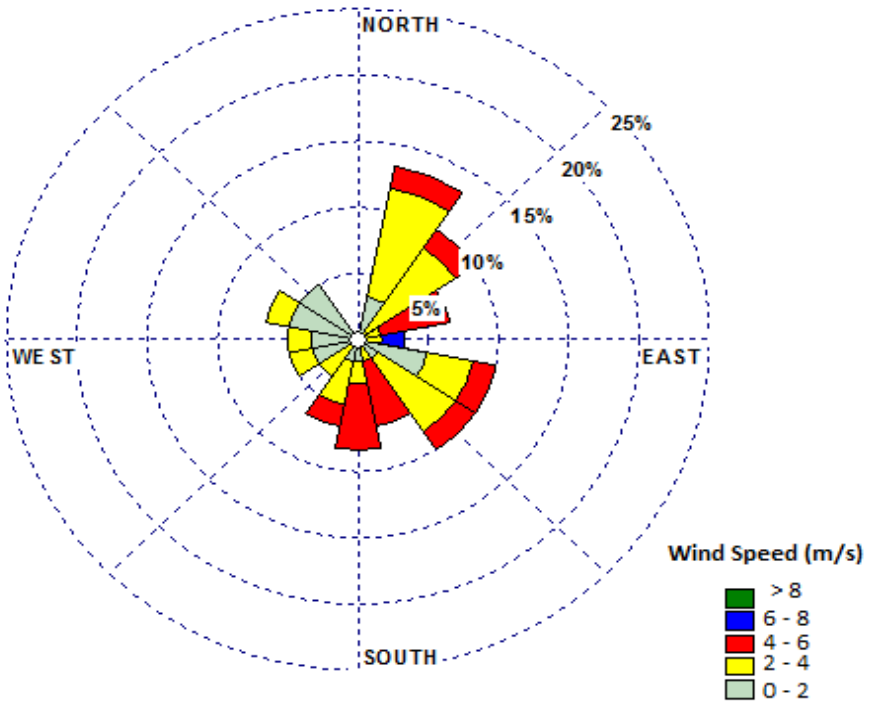

a

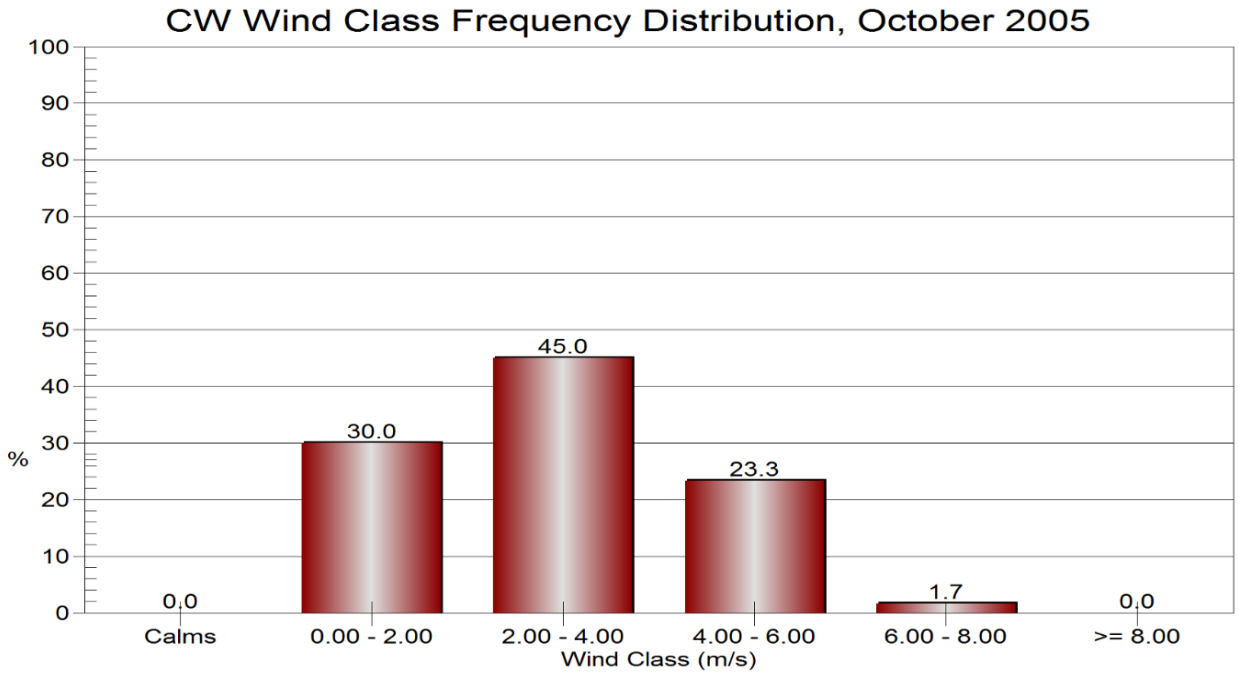

b

Figure 6.19: Twelve-hour a) Wind rose b) Wind class frequency distribution, October 2005.

6.5 central basin Surface Layer Water Temperature

The monthly-averaged distribution of the central basin surface layer water temperature in the presence (case 2) of a wind farm with 432 wind turbines from May to October (DOY 121 to 304) are illustrated in Figures 6.20b to 6.25b. The corresponding plots for the normal case when wind farm is absent (case 1) are shown in Figures 6.20a to 6.25a. Figures 6.20c to 6.25c show the surface temperature difference between case 1 and 2. These curves clearly demonstrate the potential impacts of the wind turbine wakes on the surface water.

The centre of wake's temperature difference in the presence (case 2) and absence (case 1) of the wind farm from May to October is approximately 1.5 °C, 2.5 °C, 1.3 °C, 2.8 °C, 1.5 °C and 1 °C, respectively. From these values, we can conclude that wind turbines impact the surface layer temperature the most during June and July and the temperature difference decreases after August with a minimum value of 1°C in October. (table 6.1)

Table 6.1: Centre of the wind farm wake surface layer water temperature (°C), May-October 2005

Centre of the wind turbine wake surface layer water temperature(°C)		
Month	**In the absence of a wind farm**	**In the presence of a wind farm**
May	9	10.5
June	17.5	20
July	23	24.3
August	25.7	28.5
September	22	23.5
October	18	19

In May, the southwest shore of the central basin has a water surface temperature of 9-10 °C in case 1, (Figure 6.20a), while the central part is about 2°C cooler with a temperature of 7.5 °C. In the presence of 432 wind turbines, the southwest shore is strongly influenced so that warmer and more variable temperature is seen near the wind farm. A maximum increase occurs in the centre of the wake zone, raising water temperature from 9 °C in case 1 to 10.5 °C in case 2. The wake effect diminishes gradually as it propagates downwind and far enough from the centre of the wake, temperatures are comparable with values in case 1.

While the surface layer water temperature in the centre of wake area experiences an increase of a few degrees, the rest of the central basin – out of the wind farm wake zone – does not experience a significant impact. Also, as illustrated in temperature plots, the surface temperature difference between the two cases (case 1 and 2) increases from May to August (except July) and then decreases in August onwards. The combination of an overall increase in the solar radiation and the wind speed reduction entering the summer months accounts for this increase. During the cooler months of September and October, wind speed increases while solar radiation decreases. Generally, the wind farm wake causes more reduction in stronger winds. Decreased winds cause an increase in temperature, while less solar input heat decreases the temperature. At the same time, water loses heat due to the air-water temperature gradient and stronger winds. So, wind reduction can't compensate for the water heat budget deficiency and the water gets cooler as a consequence and the temperature difference of two cases (case 1 and 2) decreases. In June, there is 4 °C difference between the mid-lake and near the south shore with temperatures of 15 °C and 19 °C, respectively, (Figure 6.21a). This difference can be explained by the dominant role of depth in determining temperature. During summer months, solar radiation intensifies, so water temperature increases as a consequence of the combination of incoming solar and raised atmospheric temperature. Equal input heat increases the shallower water column temperature more than the deep water one. This increase in temperature becomes even more significant

and accelerates with weaker winds, so the temperature rises even more in the wake zone as illustrated in Figures 6.20b to 6.25b. This temperature increase decreases moving away from the centre of the wake, as the wind farm wake declines (inversely proportional to distance) and the wind speed retains its original value far downwind. The north-west shore of the central basin (boundary of the western and central basins), experiences a minimal increase in the temperature, less than 0.3 °C as a result of the wind farm by comparing the temperature contours in two cases. This area is occasionally located in the wind farm downwind area, and the related wind turbine wake effect is very small. In July, the increasing trend of the temperature difference continues and intensifies so the corresponding surface layer water temperature reaches to 24.3 °C in case 2, from 23 °C in case 1, which causes a temperature difference of 1.3 °C, (Figure 6.22b). Also, a few locations in the eastern part of the southwest shores and north to south of the western and central basins's boundary, experience less than 1 °C increase in temperature. This shows that the wake effect applies to the mid-central basin on some occasions depending on the wind direction. Temperature differences significantly increase in the vicinity of the wind farm. As illustrated in Figure 6.22b, the difference between the ambient and the centre of the wind farm temperatures exceeds 1.5 °C (22.8 °C and 24.3 °C, respectively) within the wake zone. Surface temperature increases in August, (Figure 6.23b). As a result, differences in temperature and variations decrease within the centre and edges of the wake zone. In September (Figure 6.24b), the centre of wake temperature reaches to 23.5 °C, while the temperature around the edges is approximately 22.8 °C. More uniform water temperature is seen in October (Figure 6.25b), and the temperature difference between the wake zone centre (CW) and edges is of magnitude of a few tenths of degree.

As discussed above, the wind farm wake can play an important role in reducing the wind speed. As ambient temperature is warmer and the winds are weaker in June to August, the weaker winds

intensify the increasing trend of temperature which leads to a higher temperature. In cooler months of September and October, less temperature difference is seen between the two cases.

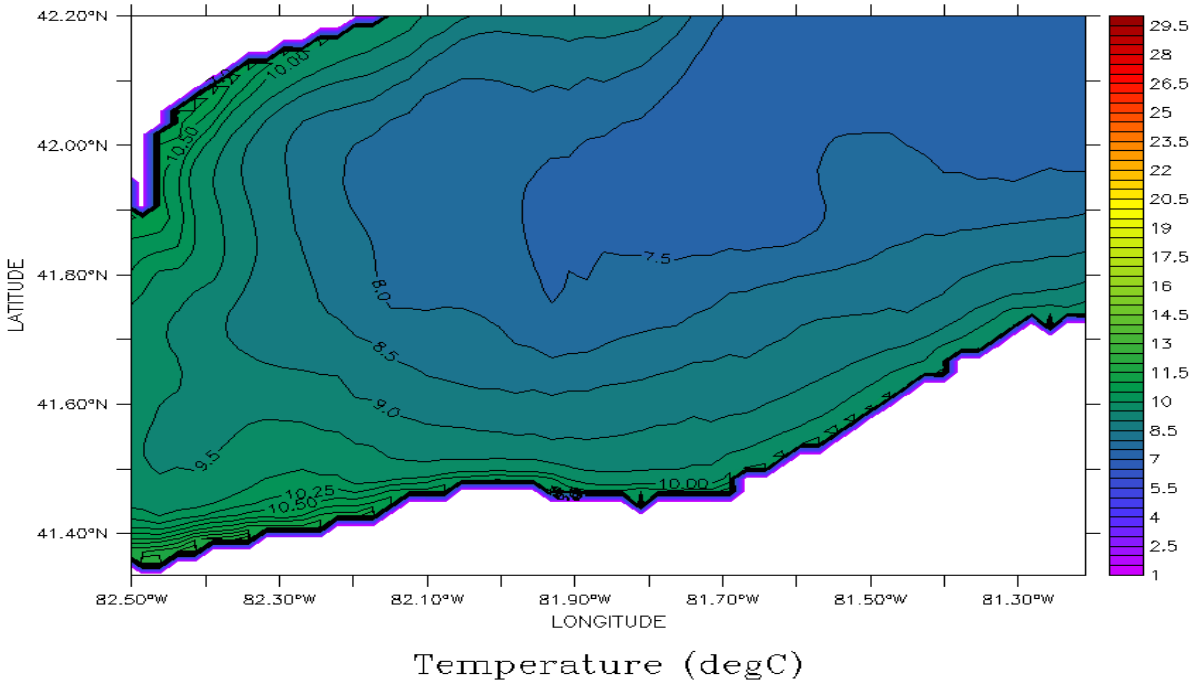

a

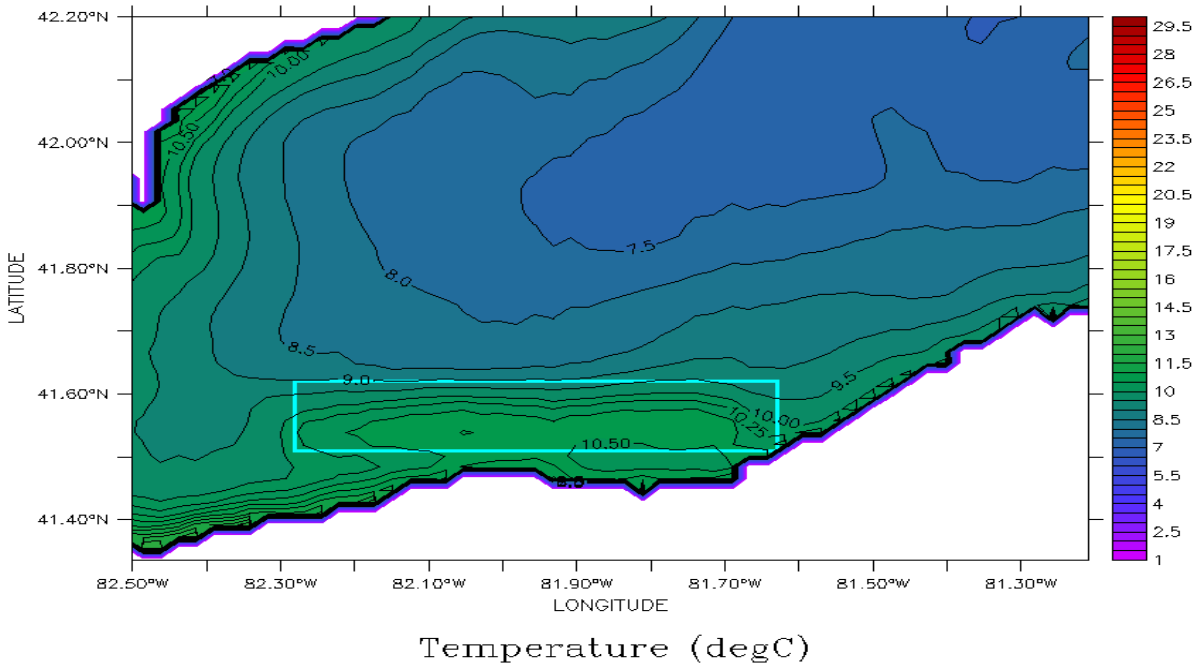

b

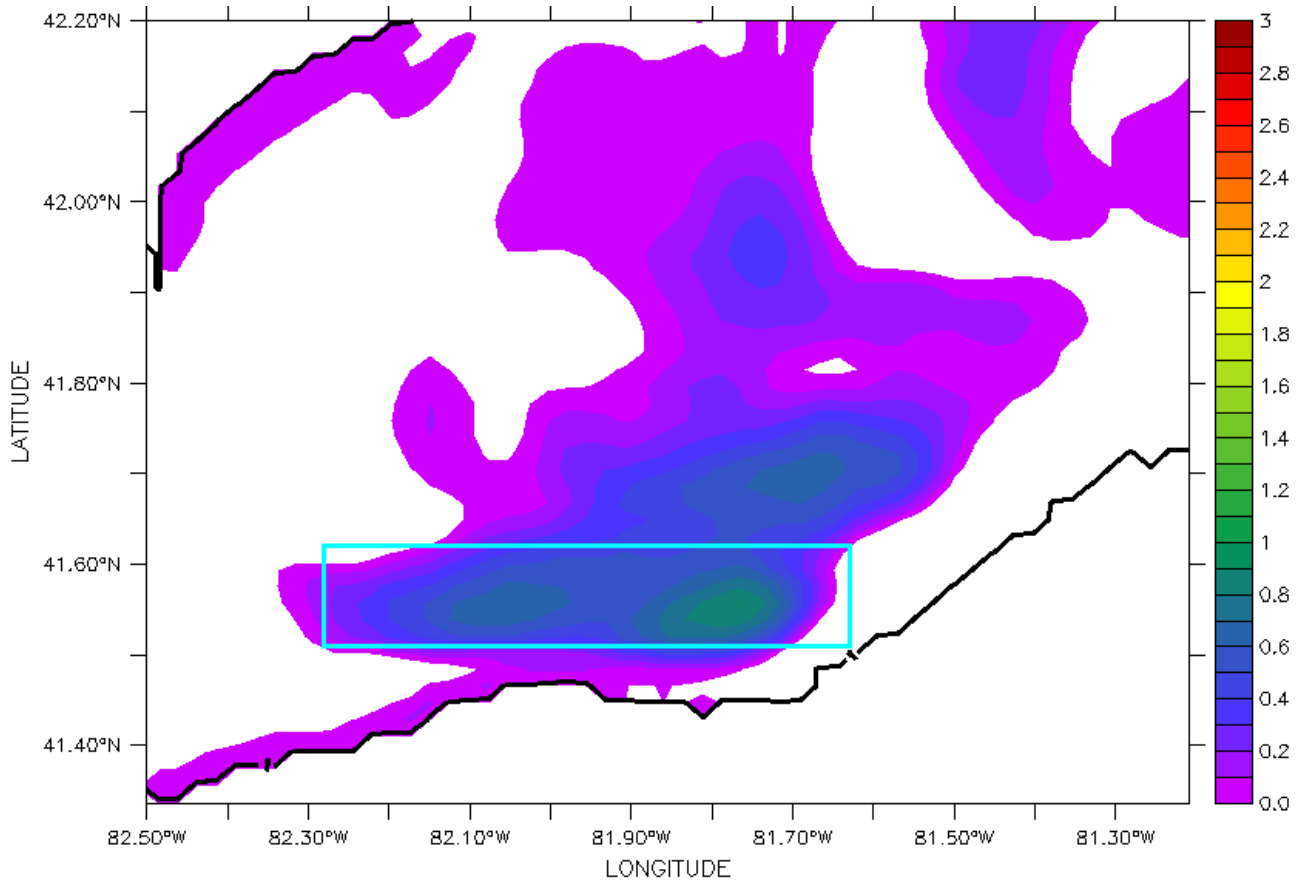

c

Figure 6.20: May-averaged surface water temperature in the a) absence, b) presence of a wind farm and c) the difference (deg C), 2005.

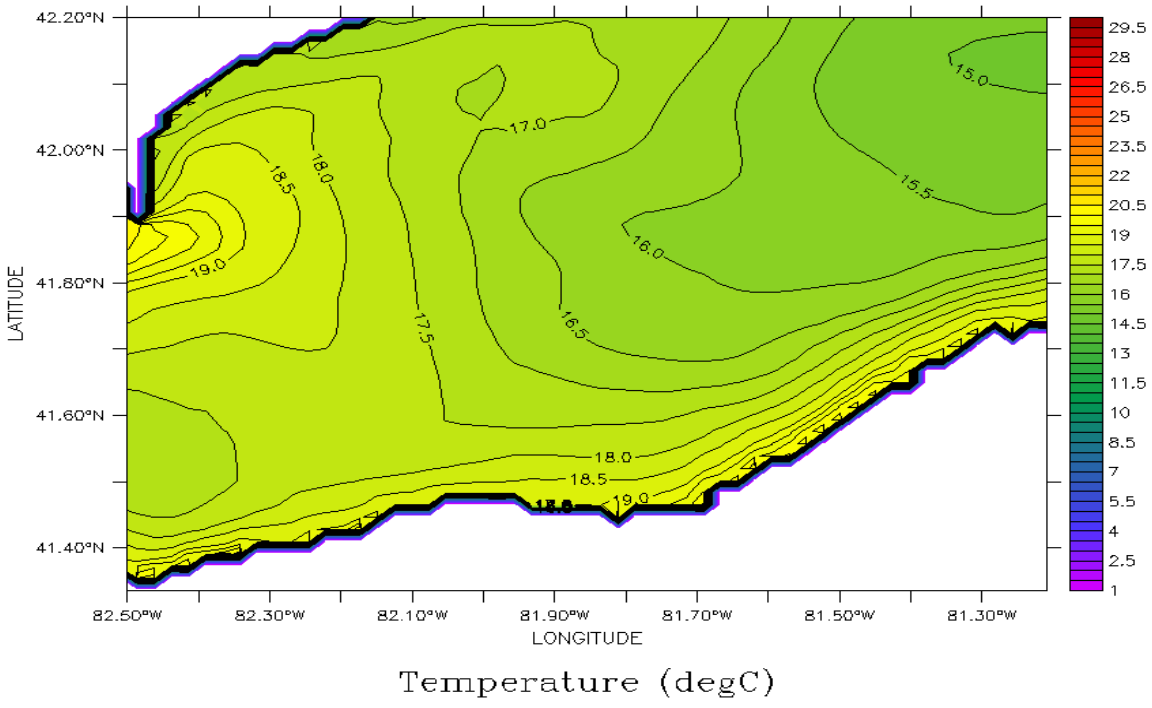
42.20°N
42.00°N
41.80°N
41.60°N
41.40°N
LATITUDE
82.50°W
82.30°W
82.10°W
81.90°W
81.70°W
81.50°W
81.30°W
LONGITUDE
15.0
15.5
16.0
16.5
17.0
17.5
18.0
18.5
19.0
29.5
28
26.5
25
23.5
22
20.5
19
17.5
16
14.5
13
11.5
10
8.5
7
5.5
4
2.5
1
Temperature (degC)

a

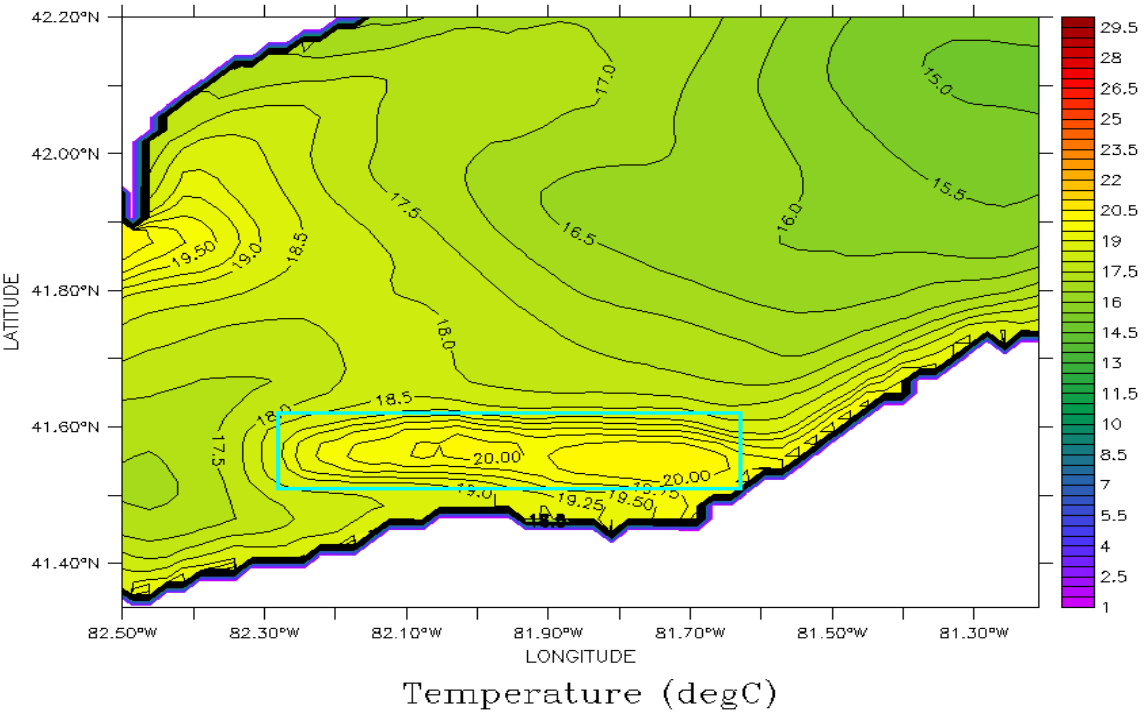
42.20°N
42.00°N
41.80°N
41.60°N
41.40°N
LATITUDE
82.50°W
82.30°W
82.10°W
81.90°W
81.70°W
81.50°W
81.30°W
LONGITUDE
15.0
15.5
16.0
16.5
17.0
17.5
18.0
18.5
19.0
19.50
20.00
19.25
29.5
28
26.5
25
23.5
22
20.5
19
17.5
16
14.5
13
11.5
10
8.5
7
5.5
4
2.5
1
Temperature (degC)

b

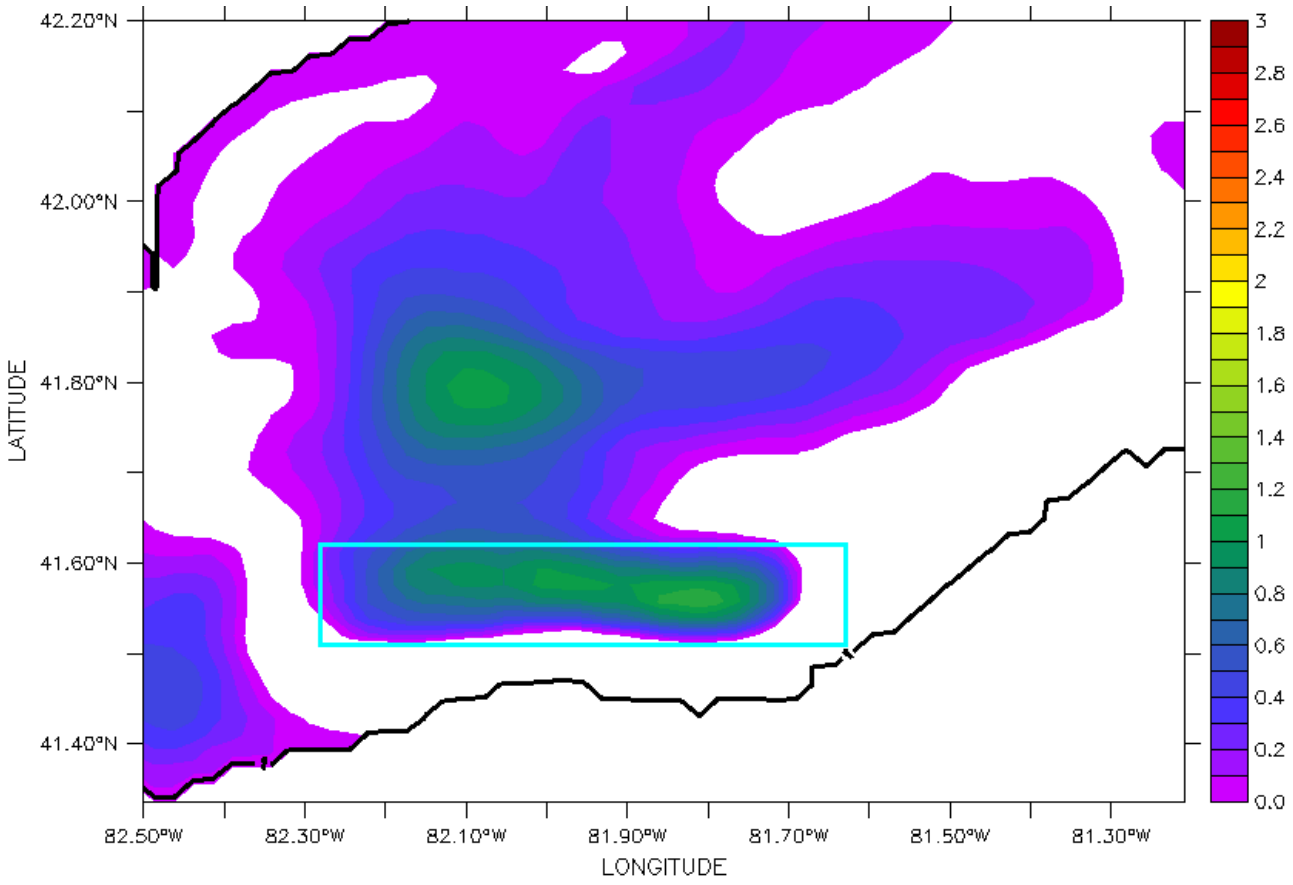

c

Figure 6.21: June-averaged surface water temperature in the a) absence, b) presence of a wind farm and c) the difference (deg C), 2005.

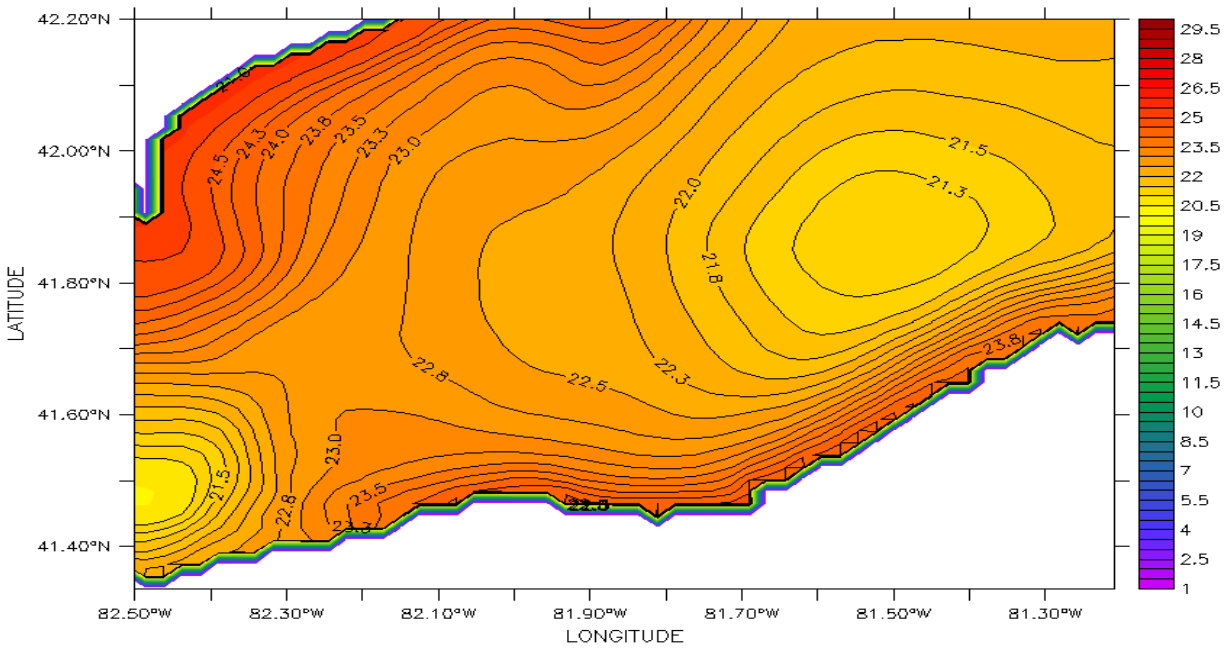
42.20°N
42.00°N
41.80°N
41.60°N
41.40°N
LATITUDE
82.50°W
82.30°W
82.10°W
81.90°W
81.70°W
81.50°W
81.30°W
LONGITUDE
29.5
28
26.5
25
23.5
22
20.5
19
17.5
16
14.5
13
11.5
10
8.5
7
5.5
4
2.5
1
Temperature (degC)

a

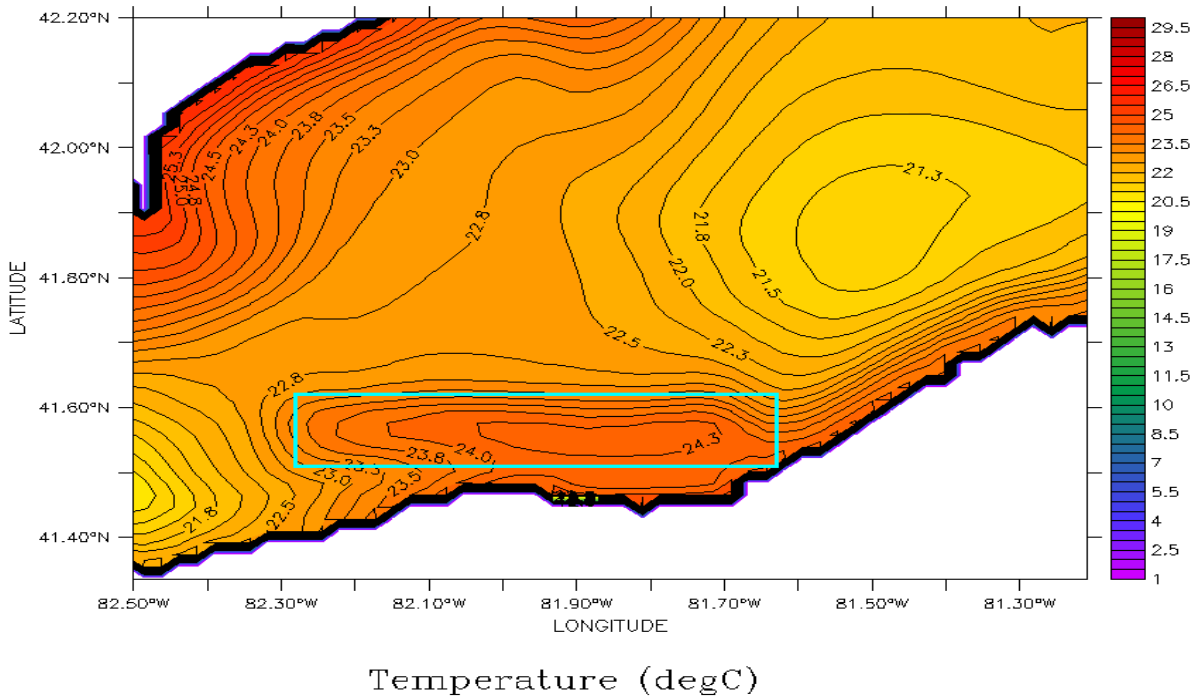
42.20°N
42.00°N
41.80°N
41.60°N
41.40°N
LATITUDE
82.50°W
82.30°W
82.10°W
81.90°W
81.70°W
81.50°W
81.30°W
LONGITUDE
29.5
28
26.5
25
23.5
22
20.5
19
17.5
16
14.5
13
11.5
10
8.5
7
5.5
4
2.5
1
Temperature (degC)

b

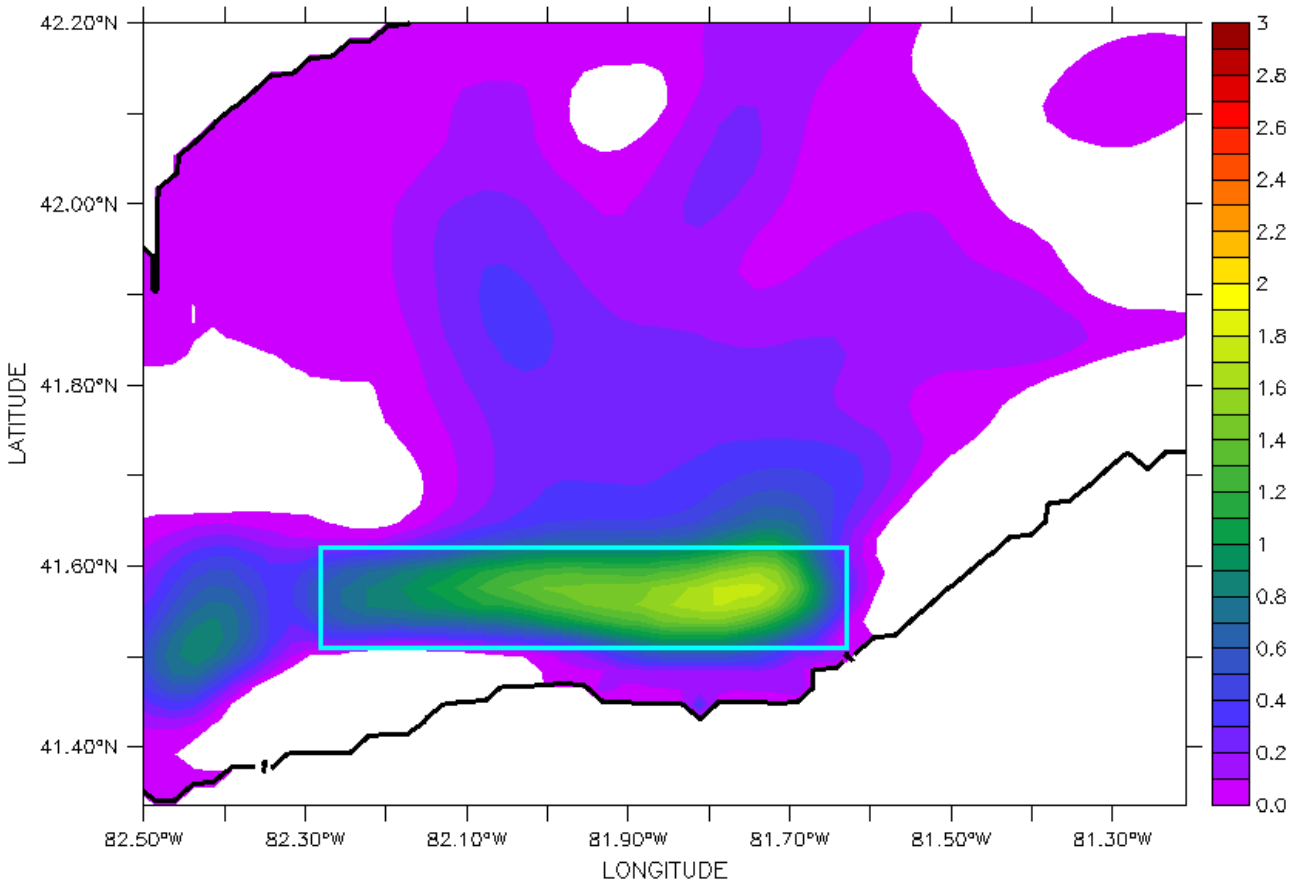

c

Figure 6.22: July-averaged surface water temperature in the a) absence, b) presence of a wind farm and c) the difference (deg C), 2005.

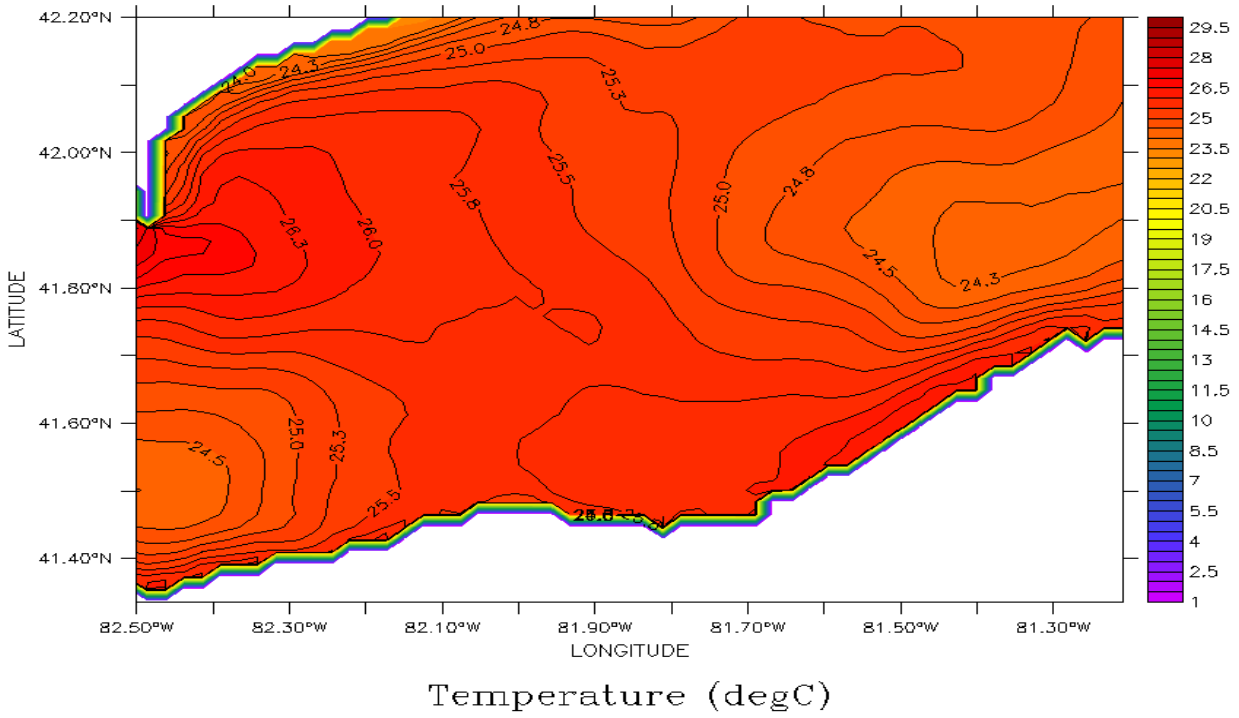
42.20°N
42.00°N
41.80°N
41.60°N
41.40°N
LATITUDE
82.50°W
82.30°W
82.10°W
81.90°W
81.70°W
81.50°W
81.30°W
LONGITUDE
29.5
28
26.5
25
23.5
22
20.5
19
17.5
16
14.5
13
11.5
10
8.5
7
5.5
4
2.5
1
Temperature (degC)

a

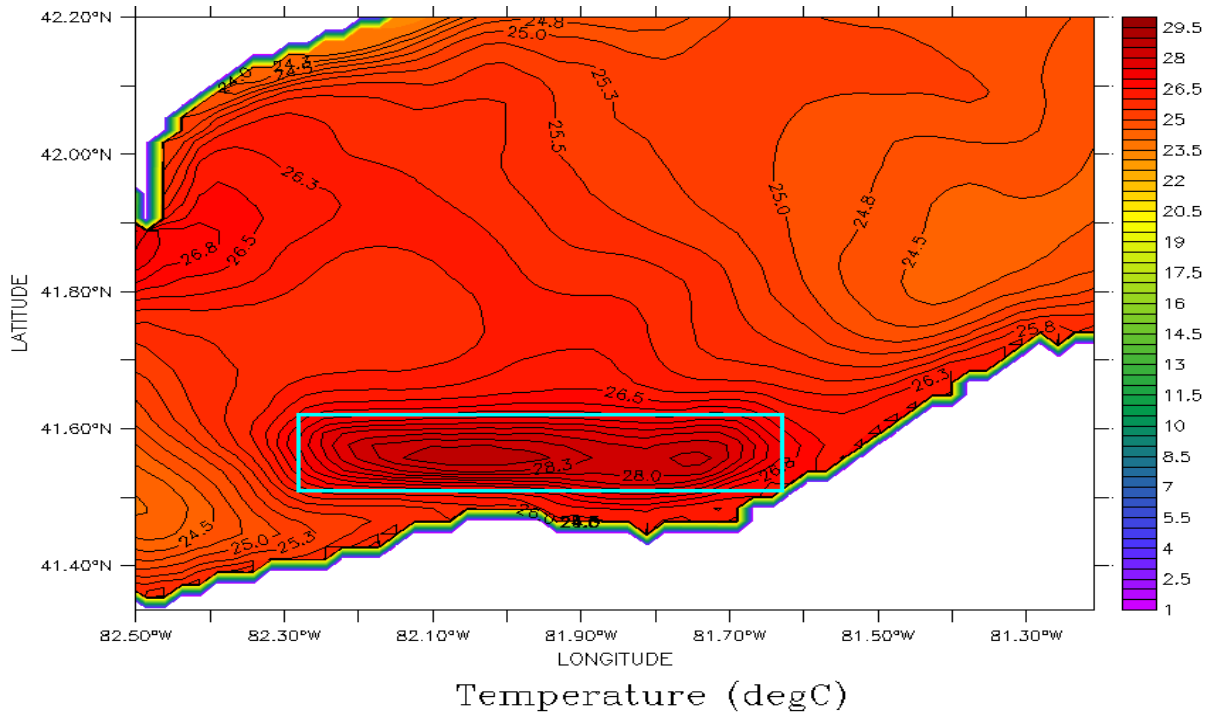
42.20°N
42.00°N
41.80°N
41.60°N
41.40°N
LATITUDE
82.50°W
82.30°W
82.10°W
81.90°W
81.70°W
81.50°W
81.30°W
LONGITUDE
29.5
28
26.5
25
23.5
22
20.5
19
17.5
16
14.5
13
11.5
10
8.5
7
5.5
4
2.5
1
Temperature (degC)

b

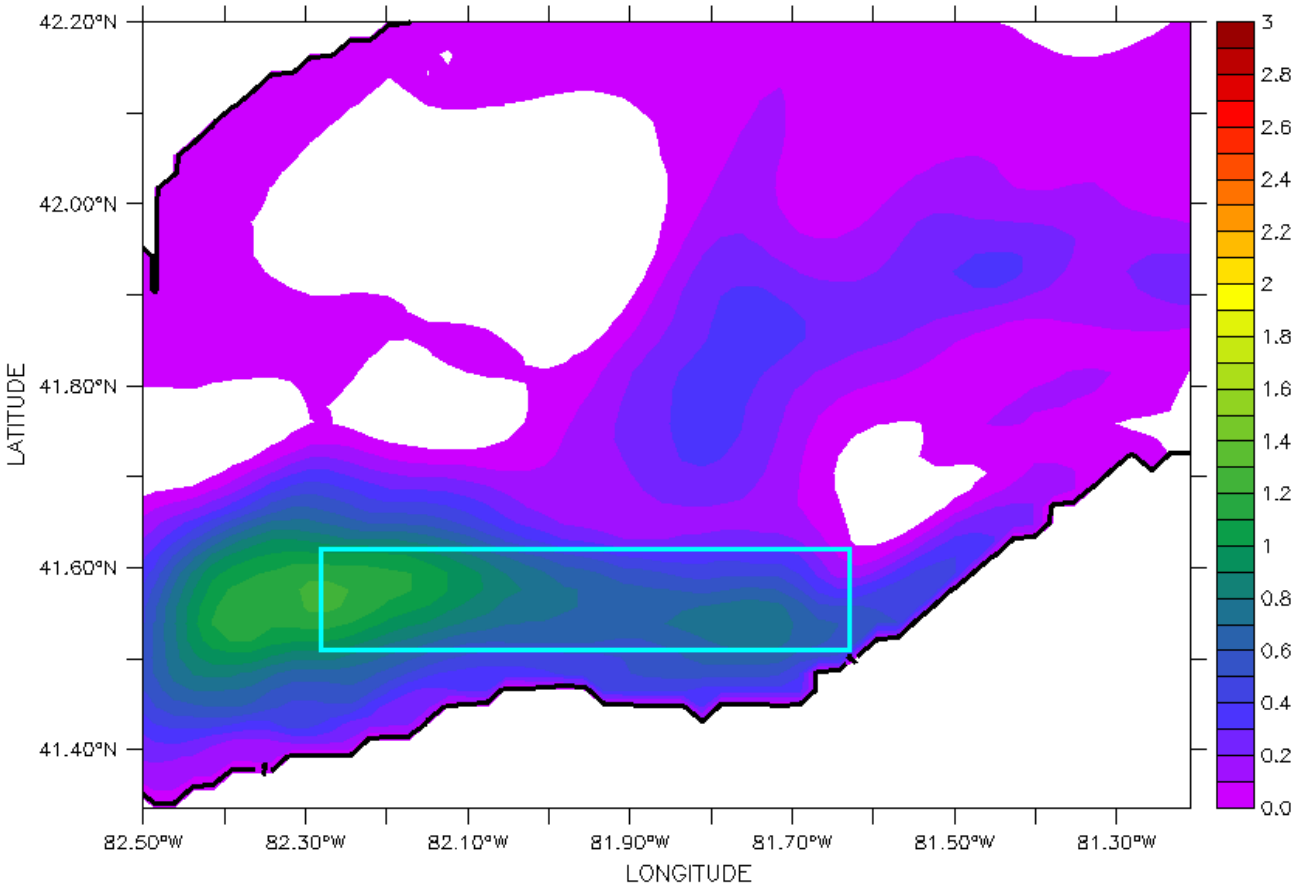

c

Figure 6.23: August-averaged surface water temperature in the a) absence, b) presence of a wind farm and c) the difference (deg C), 2005.

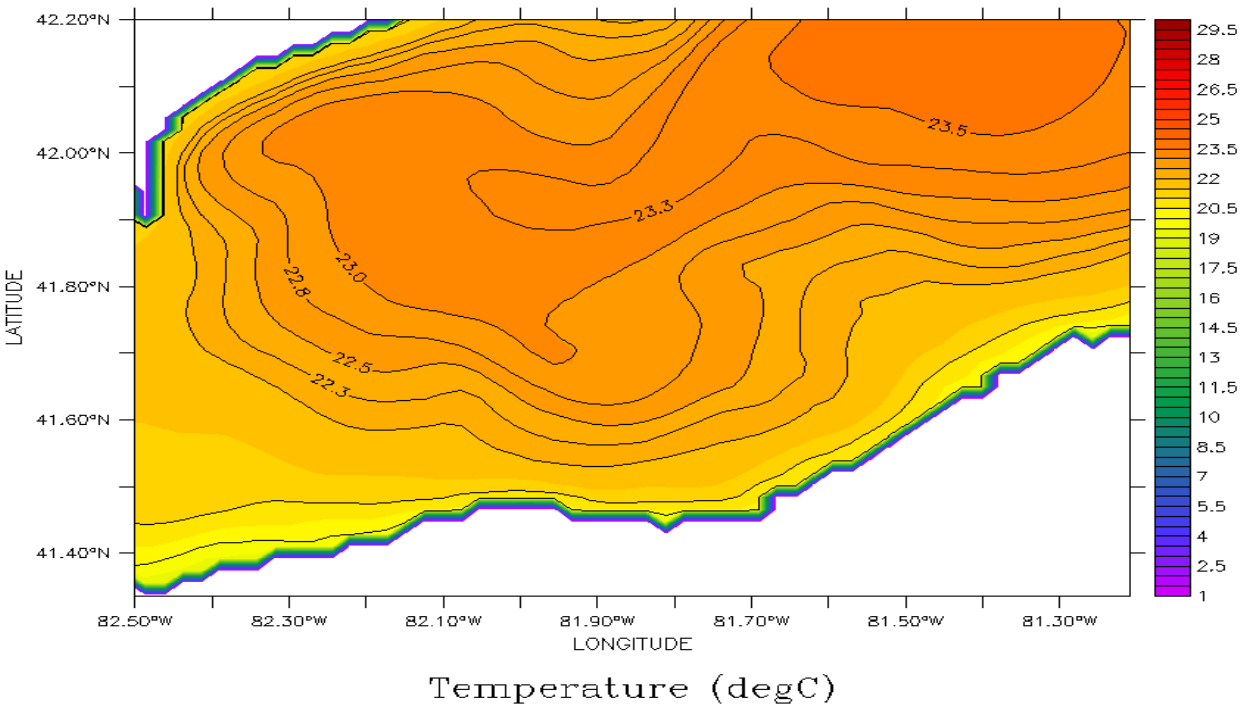
42.20°N
42.00°N
41.80°N
41.60°N
41.40°N
LATITUDE
82.50°W
82.30°W
82.10°W
81.90°W
81.70°W
81.50°W
81.30°W
LONGITUDE
23.5
23.3
23.0
22.8
22.5
22.3
29.5
28
26.5
25
23.5
22
20.5
19
17.5
16
14.5
13
11.5
10
8.5
7
5.5
4
2.5
1
Temperature (degC)

a

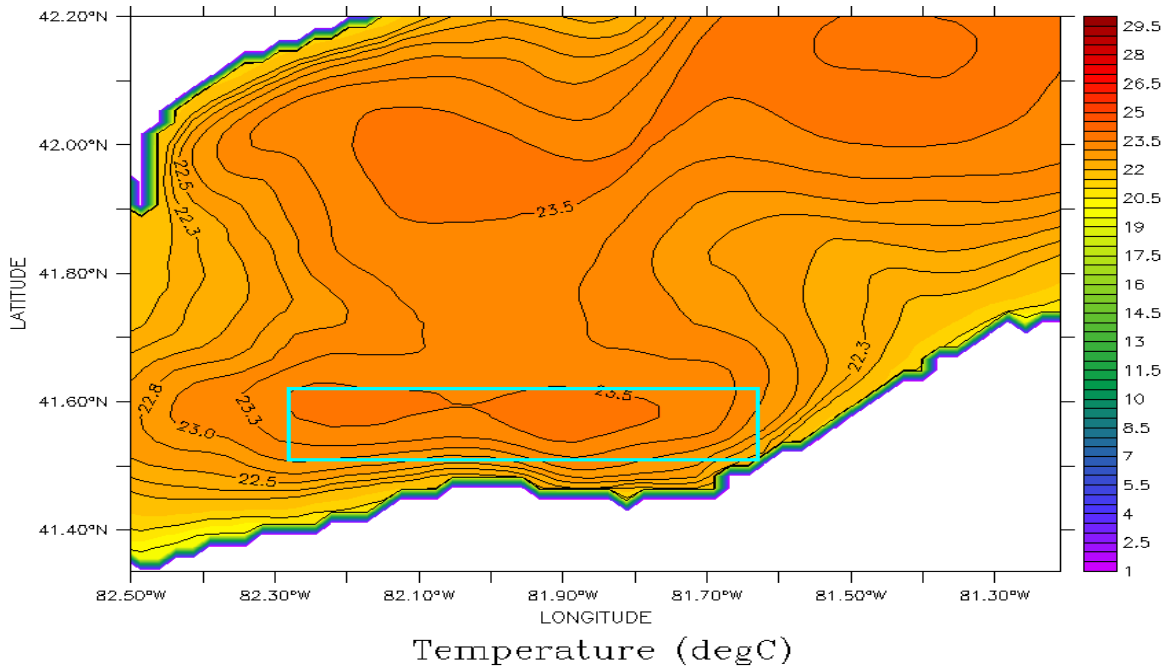
42.20°N
42.00°N
41.80°N
41.60°N
41.40°N
LATITUDE
82.50°W
82.30°W
82.10°W
81.90°W
81.70°W
81.50°W
81.30°W
LONGITUDE
23.5
22.5
22.3
22.8
23.0
23.3
29.5
28
26.5
25
23.5
22
20.5
19
17.5
16
14.5
13
11.5
10
8.5
7
5.5
4
2.5
1
Temperature (degC)

b

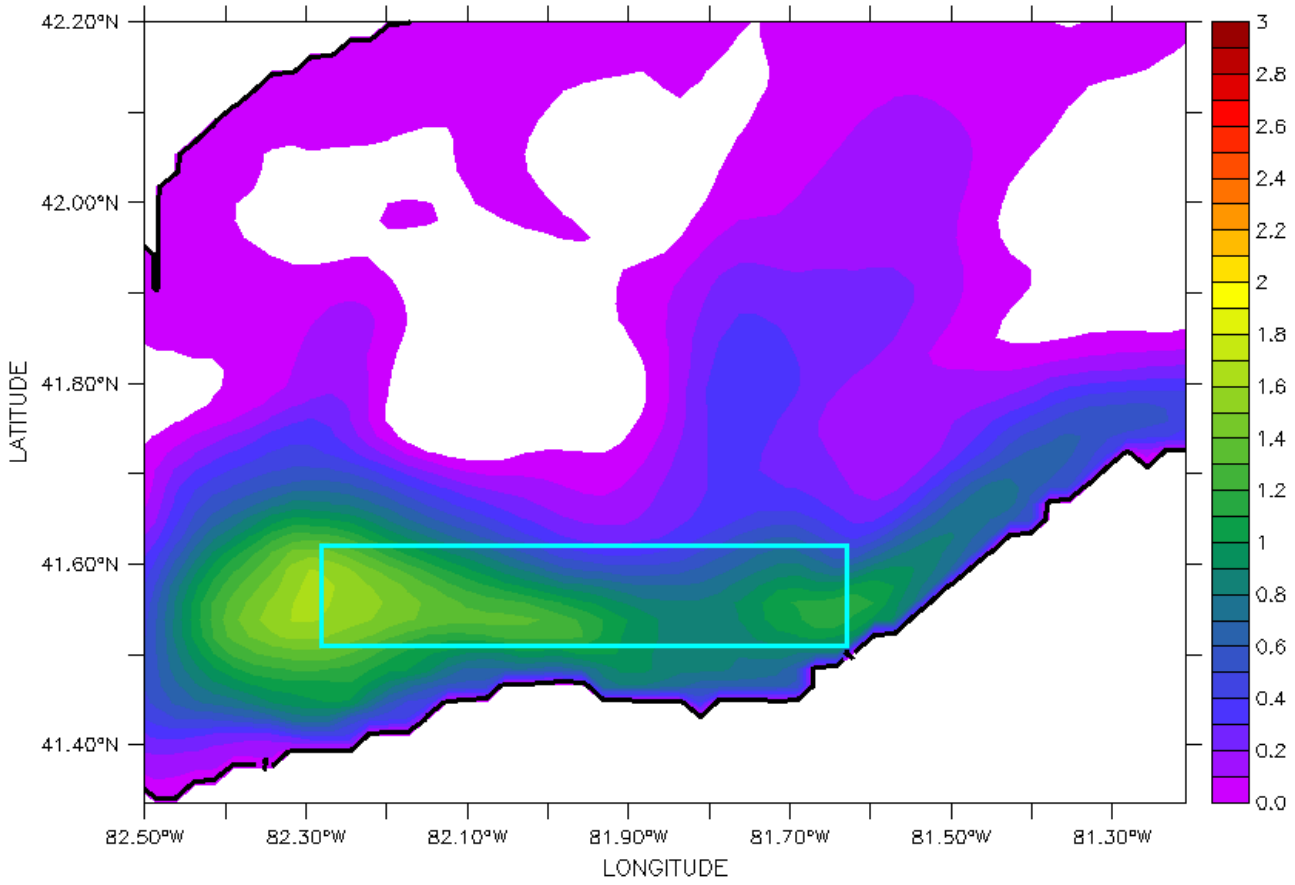

c

Figure 6.24: September-averaged surface water temperature in the a) absence, b) presence of a wind farm and c) the difference (deg C), 2005.

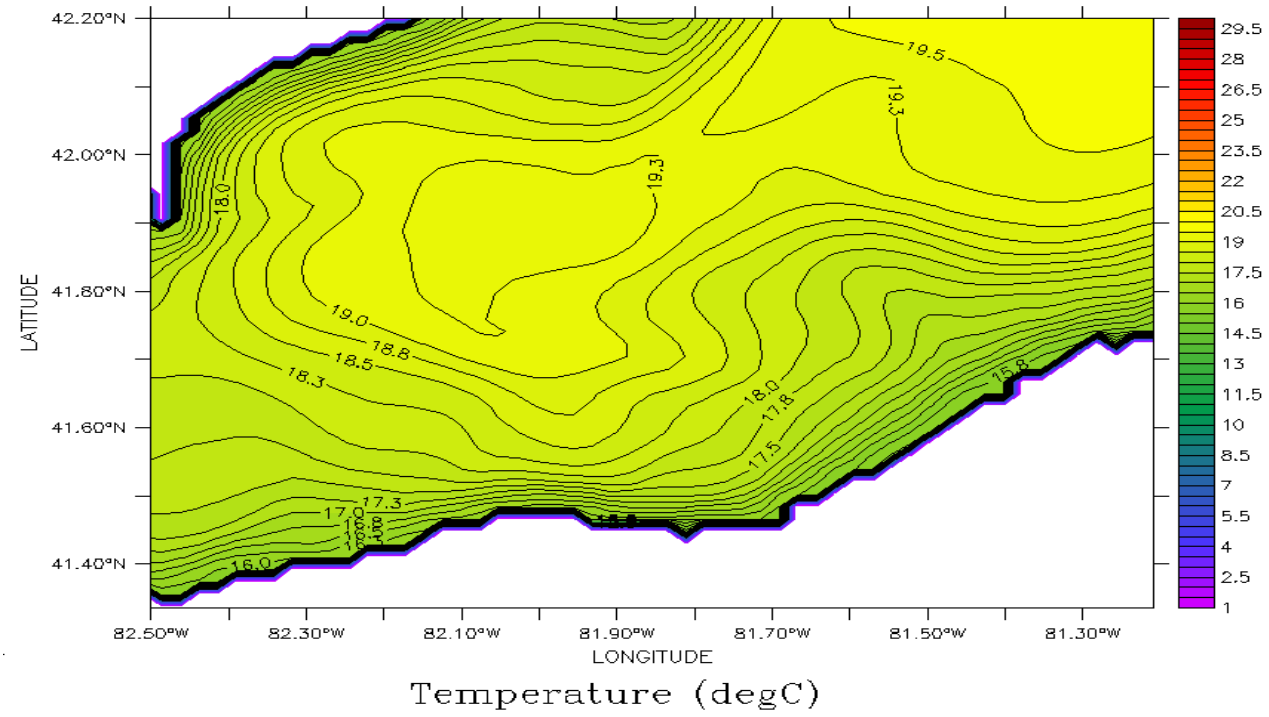
42.20°N
42.00°N
41.80°N
41.60°N
41.40°N
LATITUDE
82.50°W
82.30°W
82.10°W
81.90°W
81.70°W
81.50°W
81.30°W
LONGITUDE
29.5
28
26.5
25
23.5
22
20.5
19
17.5
16
14.5
13
11.5
10
8.5
7
5.5
4
2.5
1
Temperature (degC)

a

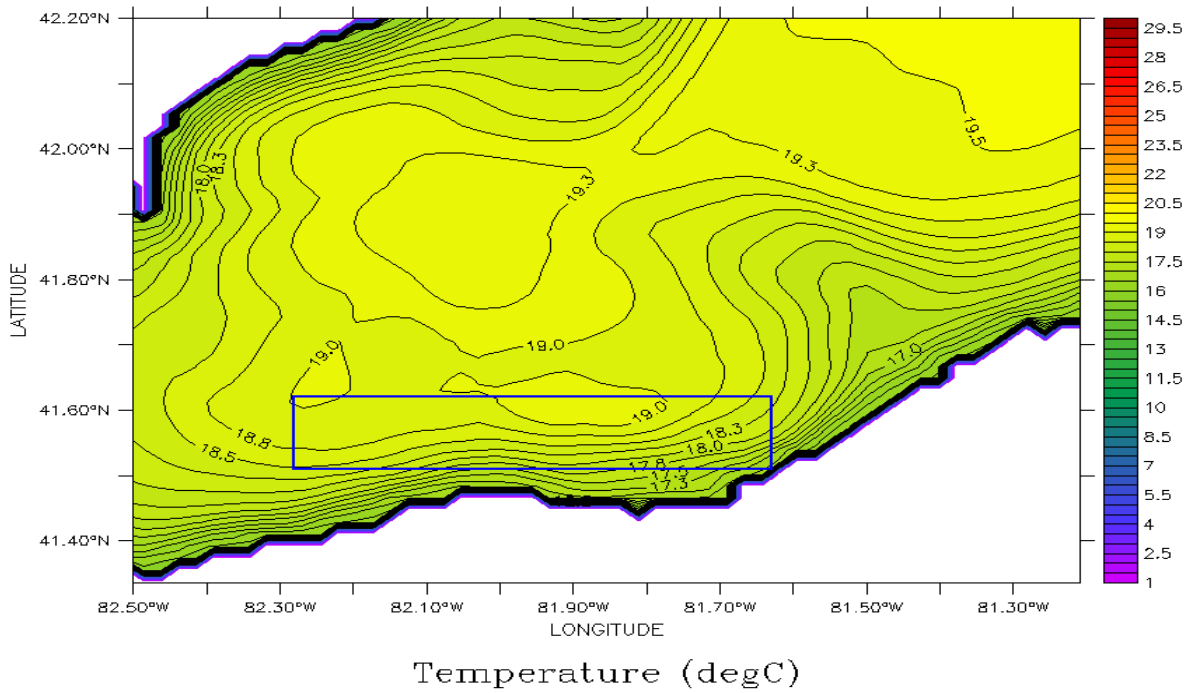
42.20°N
42.00°N
41.80°N
41.60°N
41.40°N
LATITUDE
82.50°W
82.30°W
82.10°W
81.90°W
81.70°W
81.50°W
81.30°W
LONGITUDE
29.5
28
26.5
25
23.5
22
20.5
19
17.5
16
14.5
13
11.5
10
8.5
7
5.5
4
2.5
1
Temperature (degC)

b

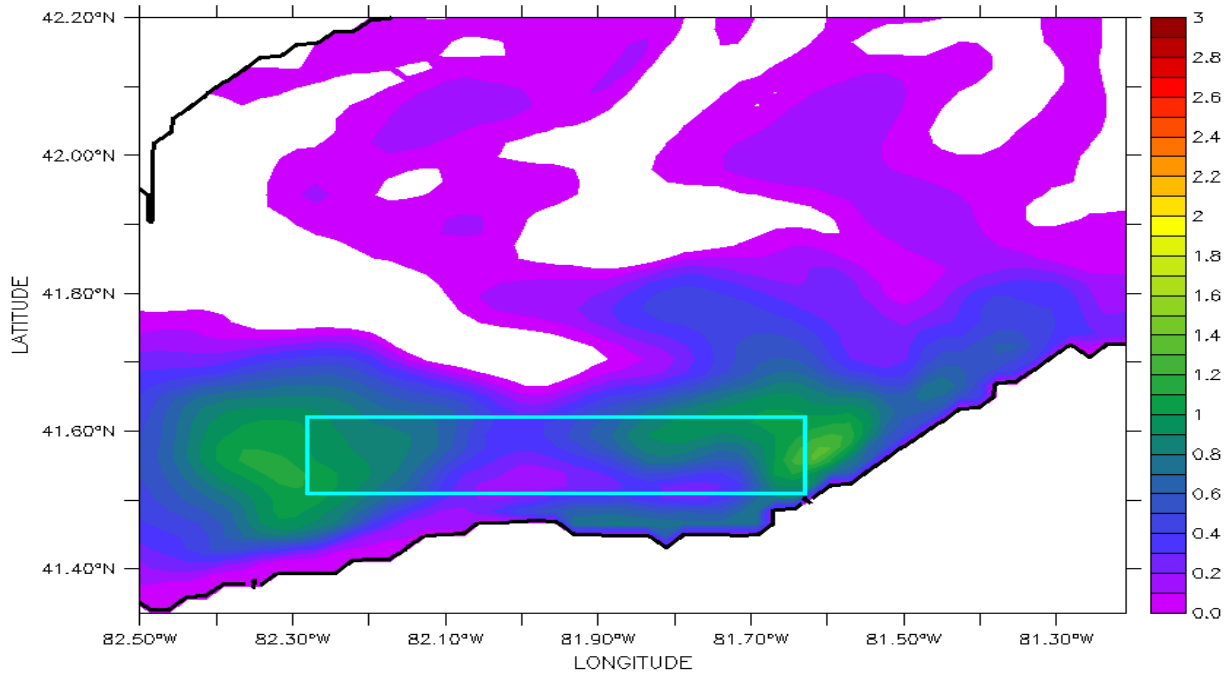

c

Figure 6.25: October-averaged surface water temperature in the a) absence, b) presence of a wind farm and c) the difference (deg C), 2005.

6.6 central basin Surface Layer Water Currents

Monthly-averaged (May-October) plots of the surface current velocities in the southwest portion of the central basin in the absence (case 1) and presence (case 2) of a large wind farm (with 432 wind turbines) are shown in Figures 6.26 to 6.31- the velocity vector scale in the figures is 5 cm/s. Figure 6.26 (a-b), compares the monthly mean surface current in May. In case 1, very little net water movement is observed in the west-east direction along the southern shoreline. COHERENS also portrays more east-directed water movement in the lower portion of the simulated area, (Figure 6.26a). The surface current is weak, and ranges between 0.1 to 2 cm/s; very seldom rising above 1 cm/s. Figure 6.26b displays the corresponding currents when a wind farm is applied. While currents in the west-east direction are aligned with the dominant wind direction, the southwest near-shore currents have a

different pattern. Most surface currents are correlated with the wind direction but in some parts, reverse patterns are observed- presumably because drag is proportional to the square of the wind speed, so higher wind speeds have more impact on the water currents. Despite a southwest dominant wind pattern, areas just north of the wind farm experience the opposite direction current pattern moving towards the west. Analysis shows mean velocity values are twice and in some events triple as large as those in case 1. Figure 6.26b portrays the surface water flowing west along the north boundary of the wake area while the southwest near-shore currents retain their easterly direction. However, they get significantly stronger. The presence of the wind farm accounts for the shift of the vectors to the west in the wake area. It is clear in Figure 6.26b that every time the current hits the wind farm boundaries, it deflects by 90 degrees. It seems that the wind farm acts like a barrier and deflects currents on its boundaries so that a cyclonic monthly-averaged circulation pattern forms within and around the wind farm area. When wind blows on a wind farm, generally a wake zone forms downwind of the turbines. While bigger mean current vectors are seen on the wind farm boundaries, the centre of wake has the lowest mean currents. From Figure 6.26b, southwest of the pictured area tends to have a small cyclonic circulation, and the current divides into two opposite directions in the north portion. Consistent southwest winds push water downwind as there is a strong correlation between surface water movement and wind direction. Currents in the north of the wind farm are in the opposite direction to the wind (Figure 6.1). For moderate and weaker winds, the west component dominates as the east component (which was generated by the wind stress) diminishes. So the resultant currents within the wind farm are in the order of 1-4 cm/s in case 2 compared to the westward currents of the order of 0.1-0.2 cm/s, in case 1. So introducing a wind farm can generate a small cyclonic gyre around the wind farm near the southwest shoreline.

In shallow parts of a lake with a sloping bottom, a steady wind stress over the lake pushes surface water downwind but when wind hits a barrier (here, a large wind farm), its speed decreases. In the

centre of the wake area, the wind stress drops to a minimum, so the dominant role of the wind stress on the surface water is reduced and other factors like bathymetry (depth), water temperature and bottom slope (topography) become more significant in determining the flow direction and magnitude. In June (Figure 6.27), surface current velocities are greater in magnitude compared to the previous month. Direction is more consistent towards the northeast. Near the south-shore currents reach to 10-12 cm/s (in the eastern part of the diagram), Figure 6.27a, and the general direction is towards the northeast. In case 2, Figure 6.27b, within the wake zone in the southwest of the central basin, a small cyclonic gyre is formed, and the ambient water current follows an anti-cyclonic pattern so that southward currents are seen in some parts in the eastern portion of wind farm. One explanation can be the weaker currents on the southwest side, appear in Figure 6.27a, which are relatively weaker compared to the rest of the lower portion of the region. This reveals that the west component of currents is a bit greater than the east component, which makes a small resultant vector to the east. Reduced wind stress in the wake zone weakens the east components and this leads to greater west-directed resultant vectors, in the range of 4-6 cm/s. As explained previously, in addition to the wind stress, the rotation of the earth, the shape of the lake floor, density and the shape of the coastlines are among the important factors that determine the complex patterns of surface currents. Although our COHERENS simulation portrays a few small gyres in some parts of the region during the simulated period, currents follow the general wind pattern (southwest to northeast) along the south shorelines in case 2. From Figure 6.27b, we can confirm that the centre of the wind farm is where the smallest water currents are found. Winds are weaker in July as expected and generate smaller current vectors, Figure 6.28a. Average currents are slower and have more directional variation than June has. However, the velocity field and surface current, still flow northeastward. This time, near south-shore currents, are weaker compared to the rest of the region while the north shore has stronger currents. The difference between the near south-shore currents in June and July can be due to the slower winds in July (Figure 6.9a), which divide near-shore currents

into two opposite directions of east and west, as shown in Figure 6.28a. This means west current components dominate the southwest winds on the west side and makes a westward current pattern.

In case 2, a strong anticyclonic gyre with an average current of 4-10 cm/s forms on the west side of the central basin. The surface current velocity closely follows vorticity in the wind. As southwest wind stress decreases, the current rotates anti-cyclonically due to the Coriolis force and topography. As well, the near south-shore current speeds up toward the northeast. Although the mid to southern portion of the central basin is impacted by the wind farm, the variation in the rest of the region is not significant and can be assumed as "far enough away to not be affected".

Comparing the surface current plots in August, Figure 6.29 a and b, the anti-cyclonic circulation which gradually formed since May becomes mature and stronger especially in case 2 since the wind farm wake decreases the southwest wind stress. Decreased winds lose their power in carrying the current. So, the anti-cyclonic circulation in case 1 becomes a full anti-cyclonic gyre in case 2 occupying most western parts of the central basin. The anti-cyclonic mean currents in case 2 are in the range of 4-20 cm/s, while in case 1, this value falls to, 1-10 cm/s. Small currents near the south shoreline, are replaced by the relatively strong (5 cm/s) northeast currents. This circulation is in response to the thick thermocline and the weak winds, which lead to a shallow mixed layer. After August, the mature anti-cyclonic gyre decays gradually and becomes weaker and west components dominate. There is a westward flow along the wake zone near the south portion of the affected zone. These currents are stronger and in the range of 2-4 cm/s (Figure 6.30b), relatively higher than that of the normal ones illustrated in Figure 6.30 a. Strong north winds blow during October which changes the circulation pattern and induces stronger currents (Figure 6.31a and b). The wake-affected zone has the smallest currents in the centre, the same as in the previous months' observation. As well, two small cyclonic and anti-cyclonic gyres are produced along the south shorelines. Because of the southward winds, the wake zone forms closer to the south boundaries of the central basin.

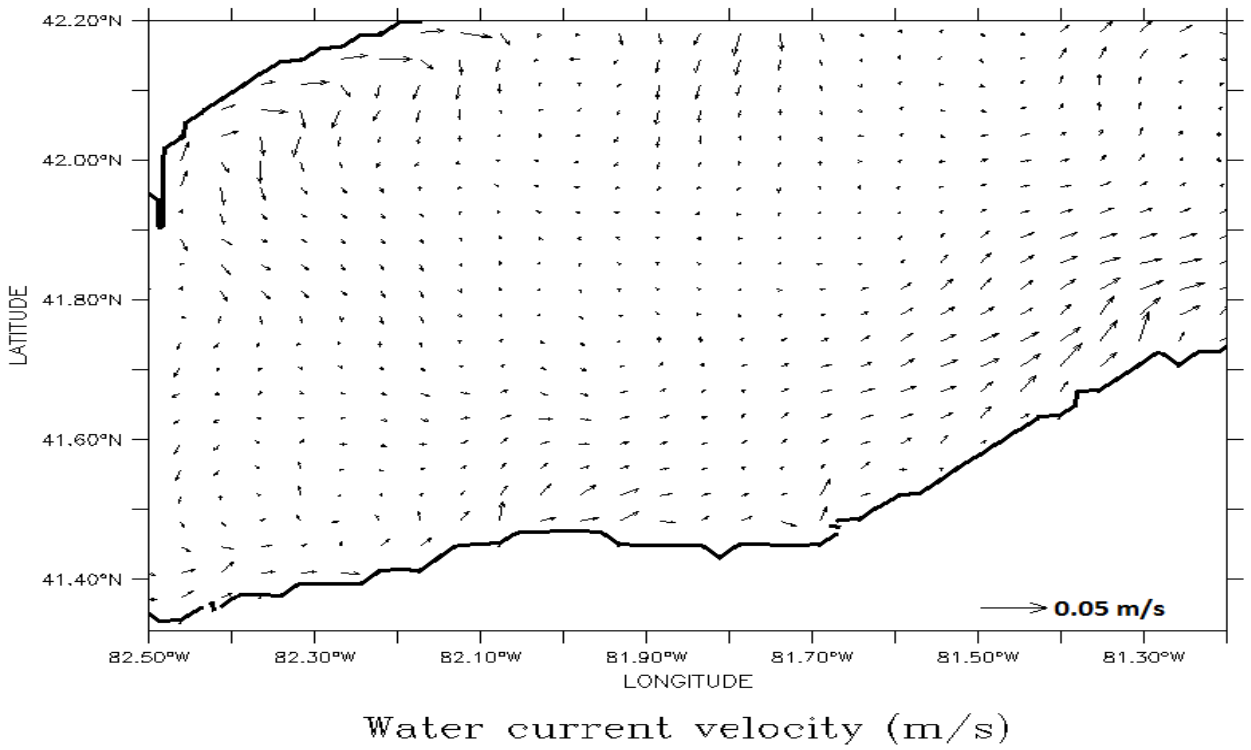

a

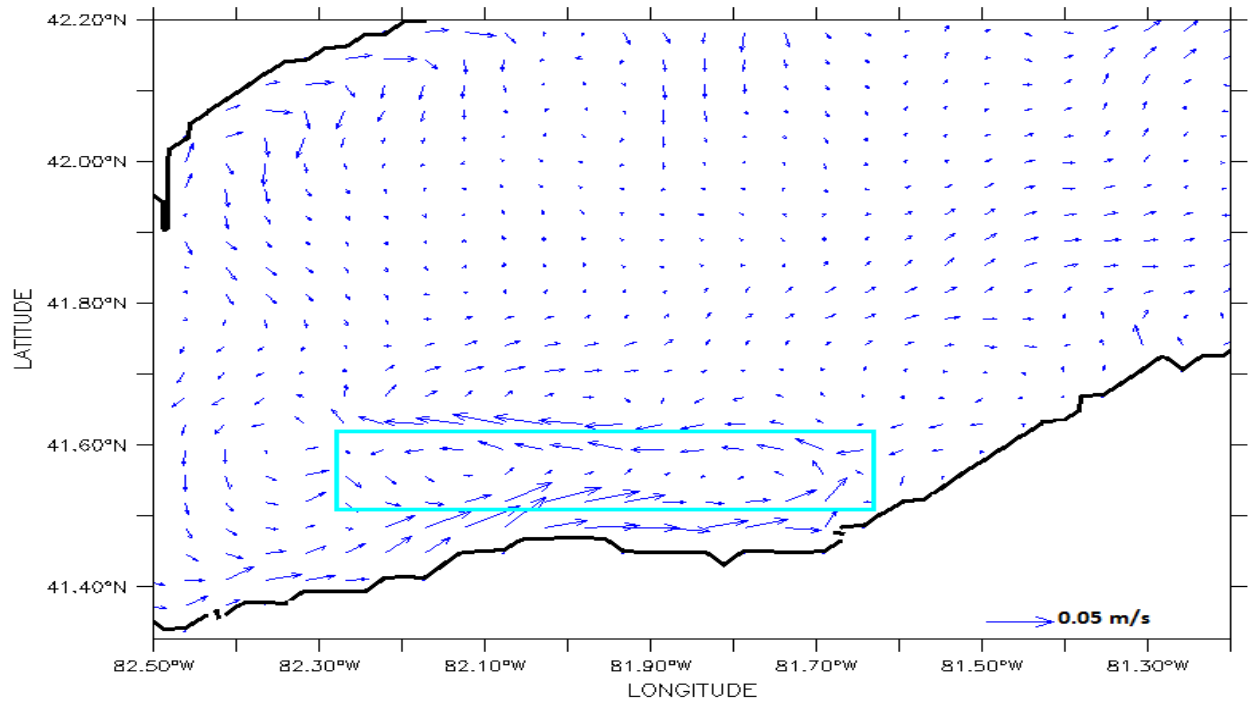

b

Figure 6.26: May-averaged surface water current in the a) absence and b) presence of a wind farm, 2005.

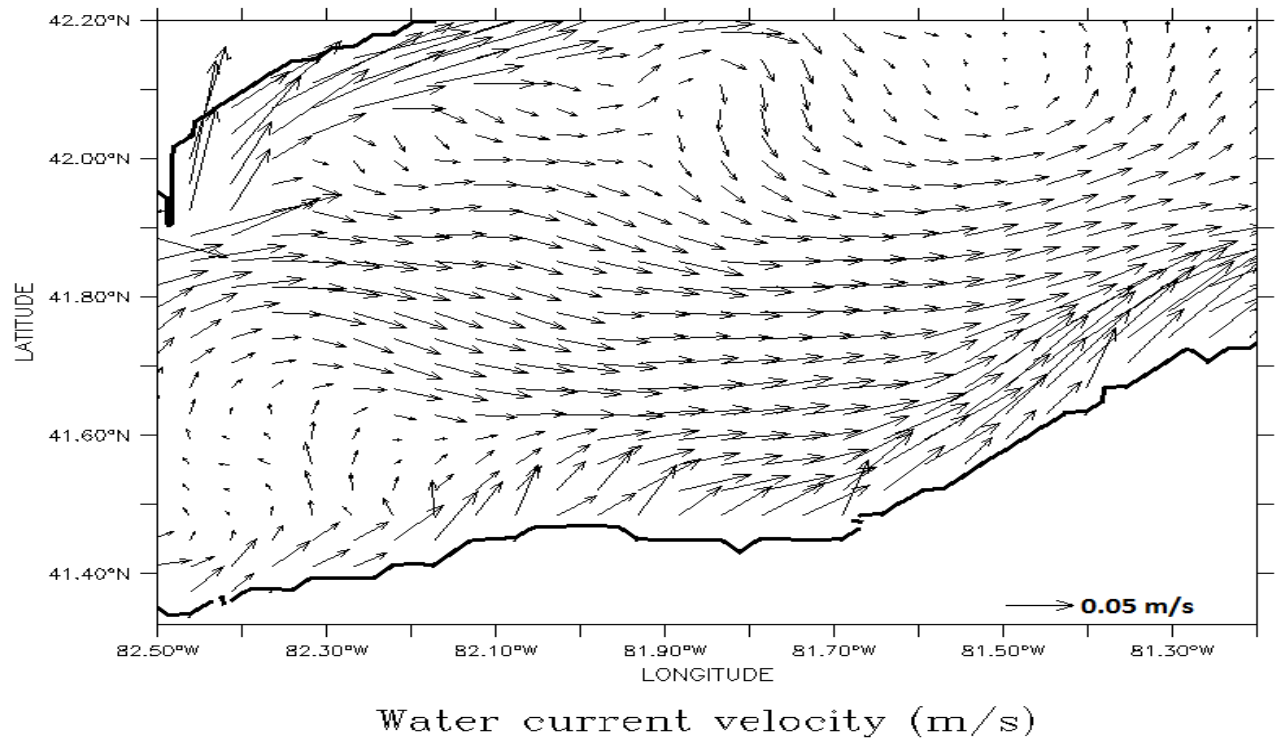

a

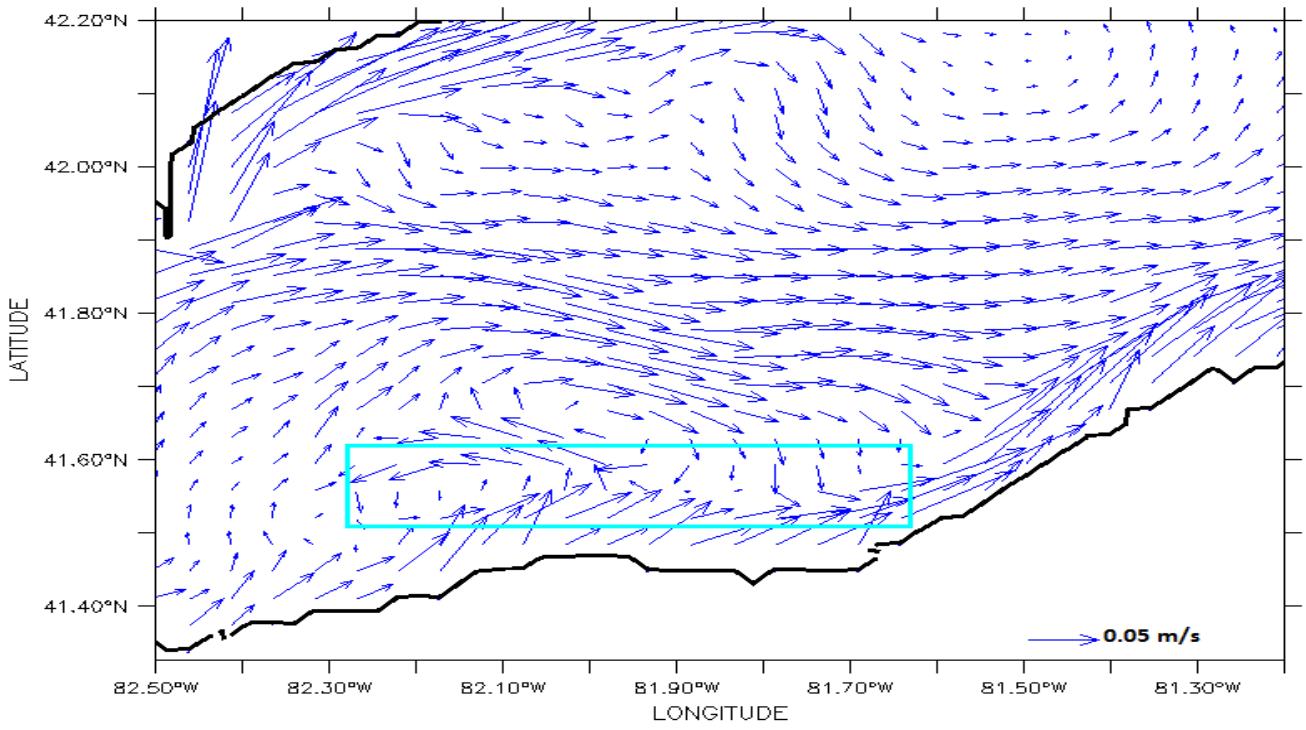

b

Figure 6.27: June-averaged surface water current in the a) absence and b) presence of a wind farm, 2005.

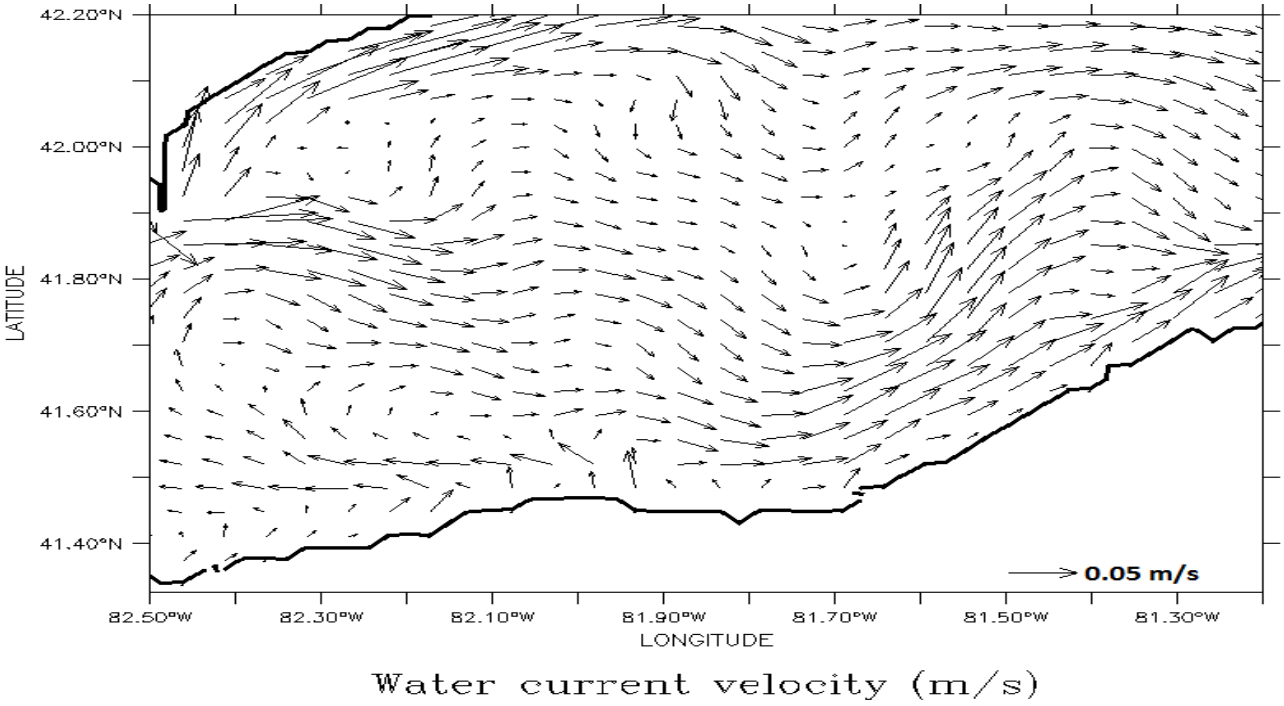

a

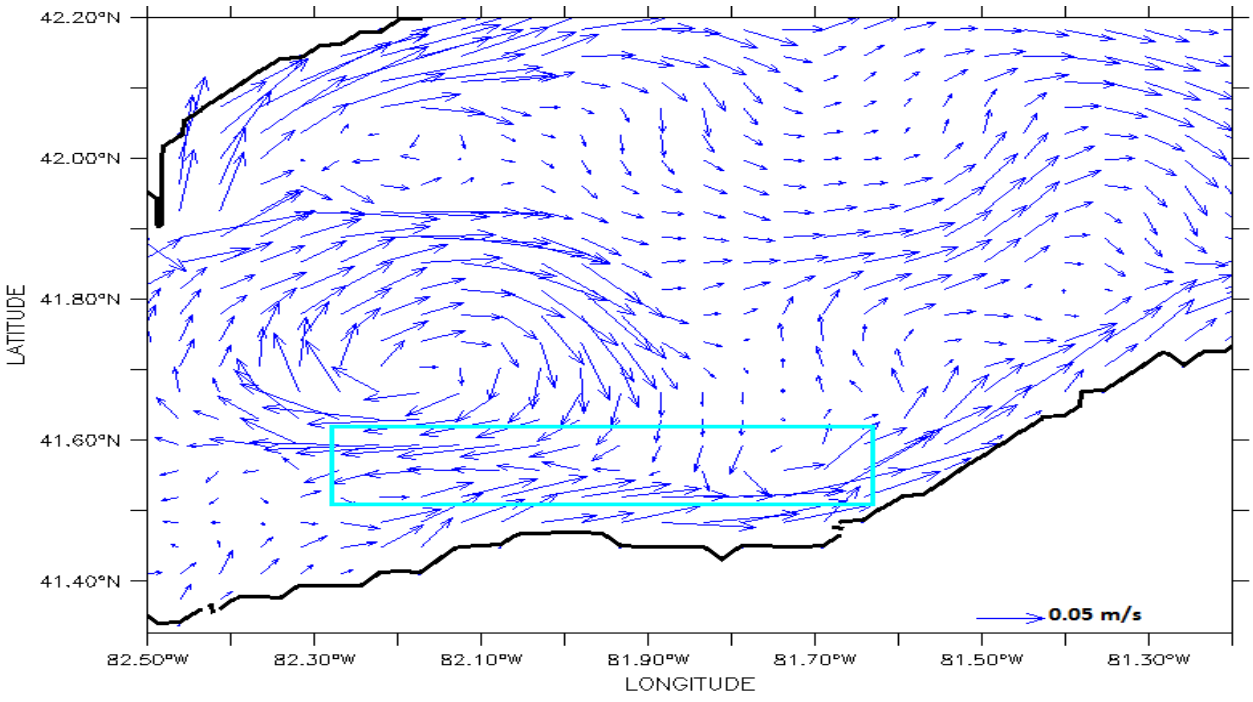

b

Figure 6.28: July-averaged surface water current in the a) absence and b) presence of a wind farm, 2005.

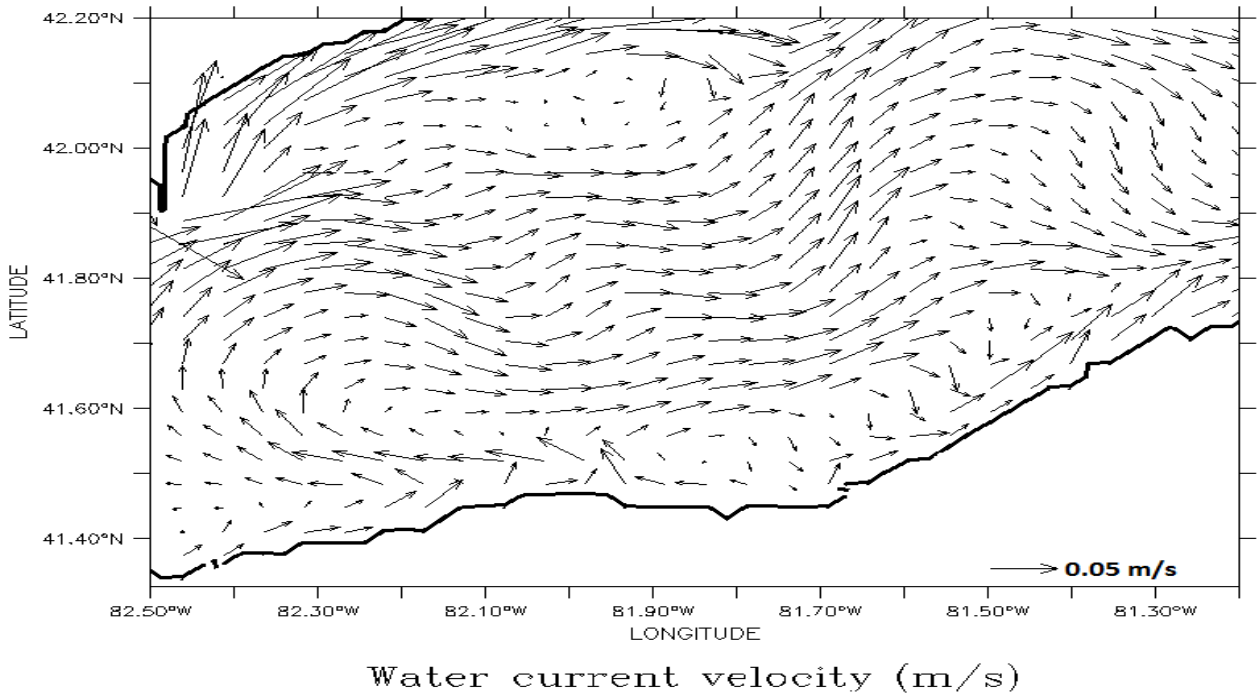

a

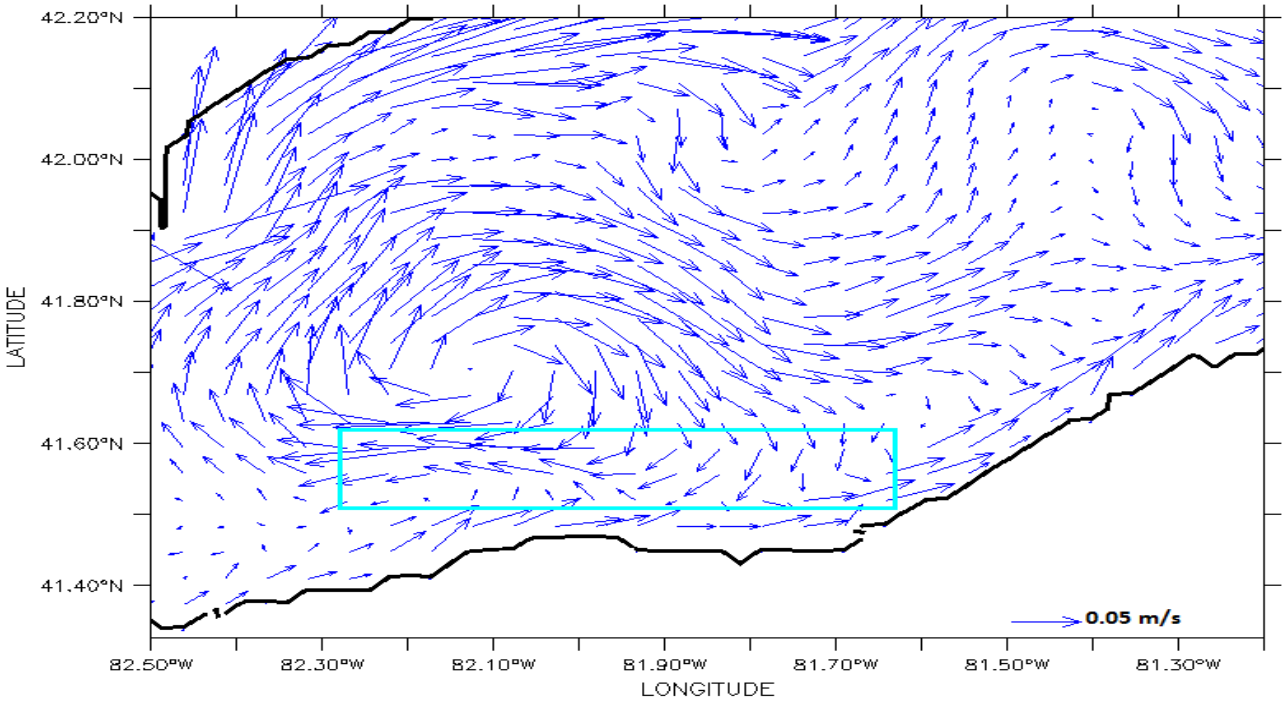

b

Figure 6.29: August-averaged surface water current in the a) absence and b) presence of a wind farm, 2005.

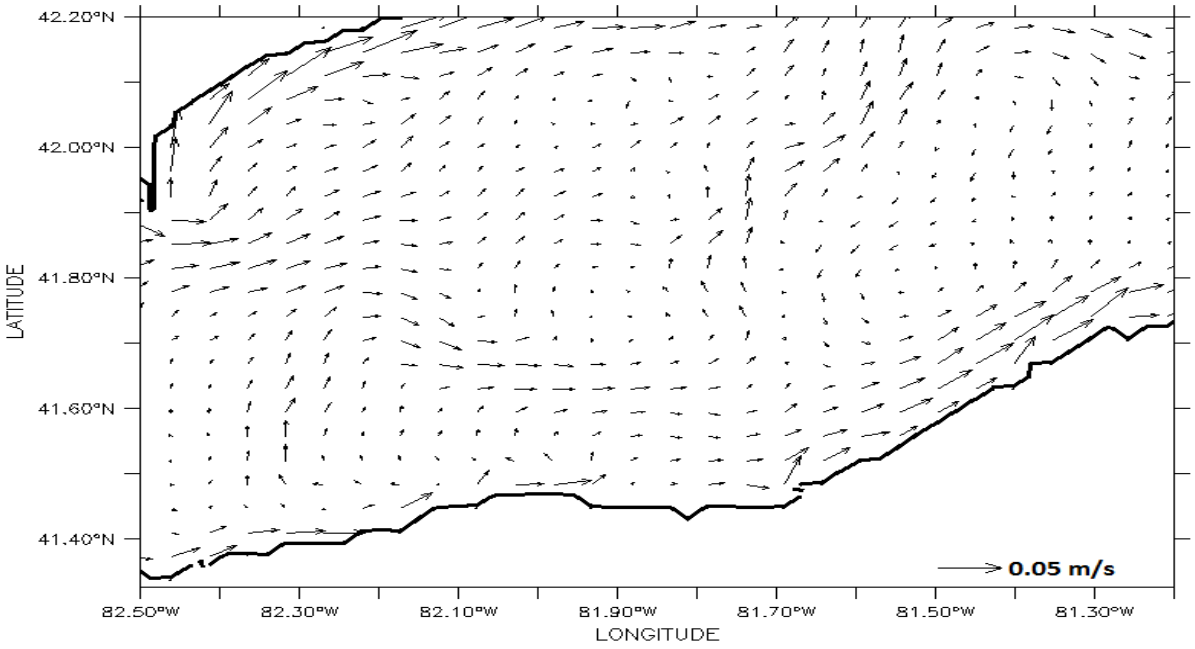

a

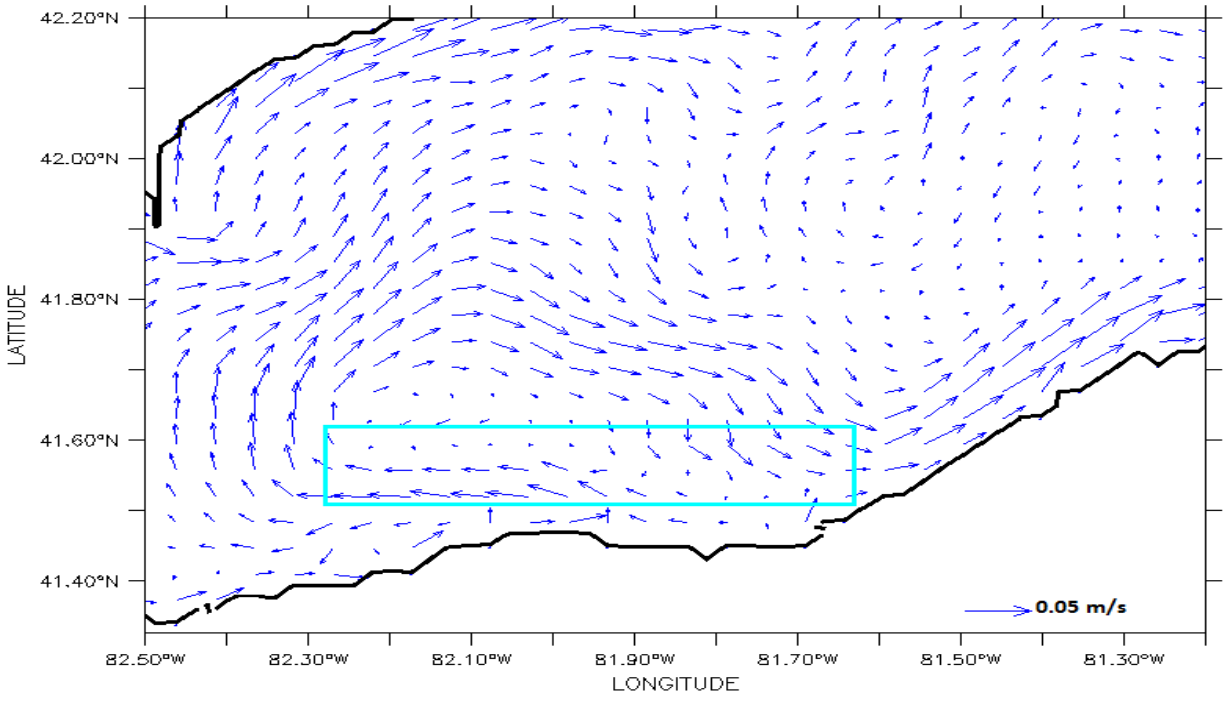

b

Figure 6.30: September-averaged surface water current in the a) absence and b) presence of a wind farm, 2005.

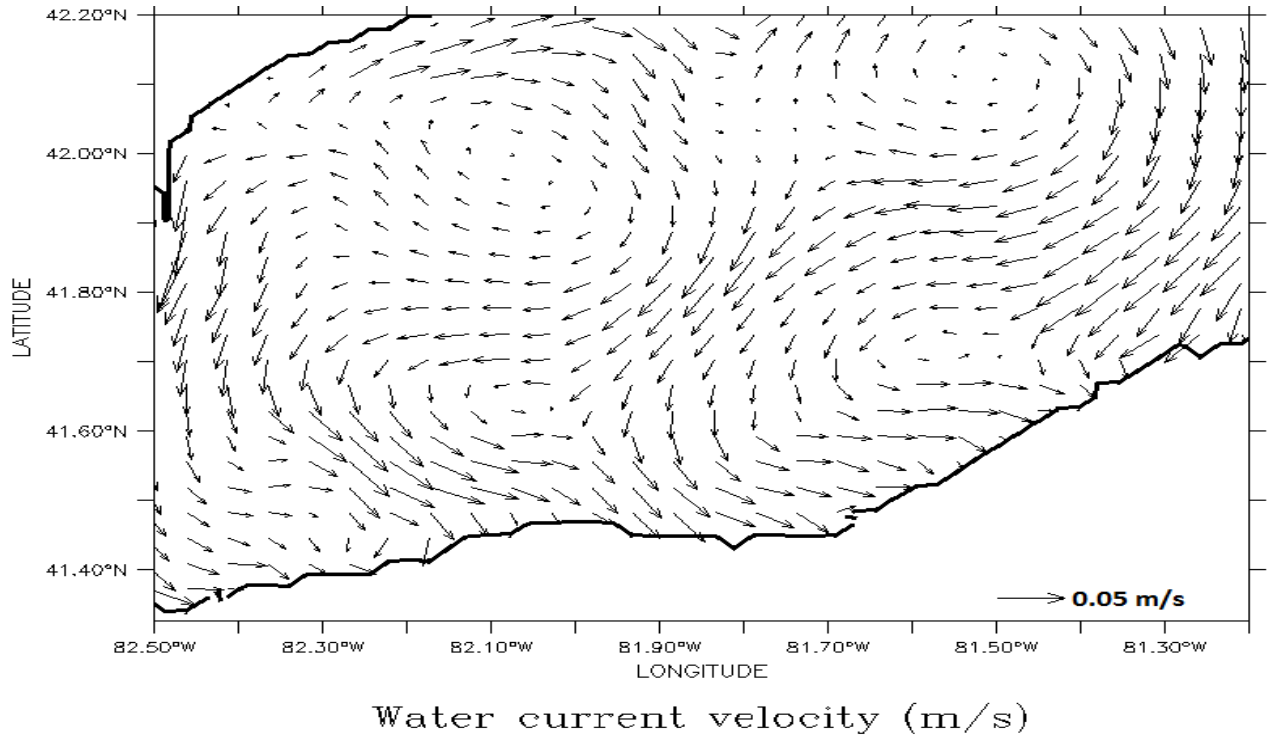

a

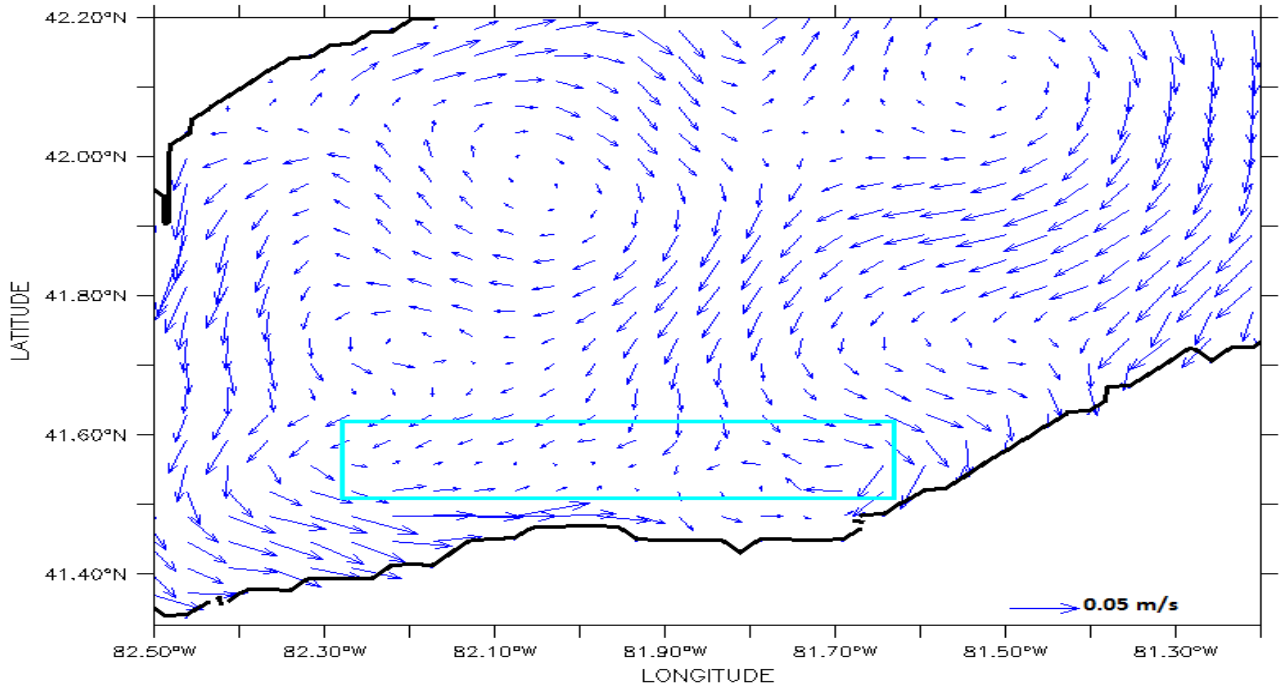

b

Figure 6.31: October-averaged surface water current in the a) absence and b) presence of a wind farm, 2005.

6.7 Near-Surface and Near-bottom Temperatures in the Centre of the Wake

The daily-averaged distribution of near-surface and near-bottom temperatures at point CW, located in the centre of the wake zone (Figure 1.7), from May to October (DOY 121 to 304) are illustrated in Figure 6.32a and b. This location is used to provide an example of differences between near-surface and near-bottom temperature and the potential range of temperature difference values, in the absence (case 1, Figure 6.32a) and presence (case 2, Figure 6.32b) of a wind farm, respectively. These curves clearly demonstrate the potential impact of the wind turbine wake on the water column.

The water column is essentially isothermal initially while weak stratification is formed during summer when the vertical temperature variation is more pronounced. In case 2, the temperature difference starts earlier and grows larger. Wind turbine wakes tend to force conditions away from neutral and stratification is established in a shorter time. Excluding summer, the difference between surface and bottom water temperature is mostly small, generally less than 2 °C on most days in both cases, indicating of vertically mixed condition. However, this difference reaches to its maximum value of approximately 12 °C (29 °C on the near-surface and 17 °C in near-bottom) in case 1, and 16 °C (32 °C on the near-surface and 16 °C in near-bottom) in case 2 in DOY 200 -202 (July). While almost well-mixed water exists in case 1 for most of May and sometimes during summer (for instance, DOY 170 or 240) in case 1, stratification onsets in early May, in case 2 and decays only in mid-September, DOY 250.

Maximum near-surface temperature reached 31°C and 33 °C in cases 1 and 2, respectively. The near-surface temperature is smoother in case 1 and has higher variability in case 2, which is caused by the effect of the reduced wind speed. Figure 6.33 compares the near-surface temperature difference in our 2 cases (with and without the wind farm). Despite considerable variability in the near-surface temperature before August (DOY 213-244), temperature is less variable afterward. During the summer, winds are weaker and solar radiation is the dominant factor in controlling temperature so the daily

variability is rather high. But, with the onset of cooler months' winds get stronger and solar radiation decreases. Consequently, the temperature and its fluctuations decrease. As illustrated in the previous plots, case 2 generally has higher temperature than case 1, while in the well-mixed water months the near-surface temperatures in two cases coincide, which means the wind farm impact is more restricted to summer.

Figure 6.34, highlights the role of wind turbine wake in the corresponding bottom temperature. Despite the near-surface temperature case where the wind wakes cause the higher temperature to persist during the whole simulation, near-bottom temperature values indicate that case 2 has slightly lower values before August and higher values afterwards. This is a reflection of the stratification effect, which prevents the water mixing mechanism so that spring's cooler bottom waters persist to early summer. The story repeats in autumn when warmer near-bottom waters mix less with the cooler surface layer ones as stratification onsets earlier in summer and decays later in fall when a wind farm is present. The near-bottom temperature difference between case 1 and 2 reaches a maximum of 5 °C, while the general average value is less than 1 °C. In some days around DOY 180, a time delay is seen between the two cases so that although following almost an identical pattern, but the temperature fluctuations and variations occur with a few days' time lag in case 2. Figures 6.35a and b display the corresponding near surface and near-bottom temperatures at a point beyond wake zone located in the mid-central basin (station T9). These plots reveal nearly identical values in the two cases, indicating that this point is not affected by the wind turbine wake and is beyond the impacted zone.

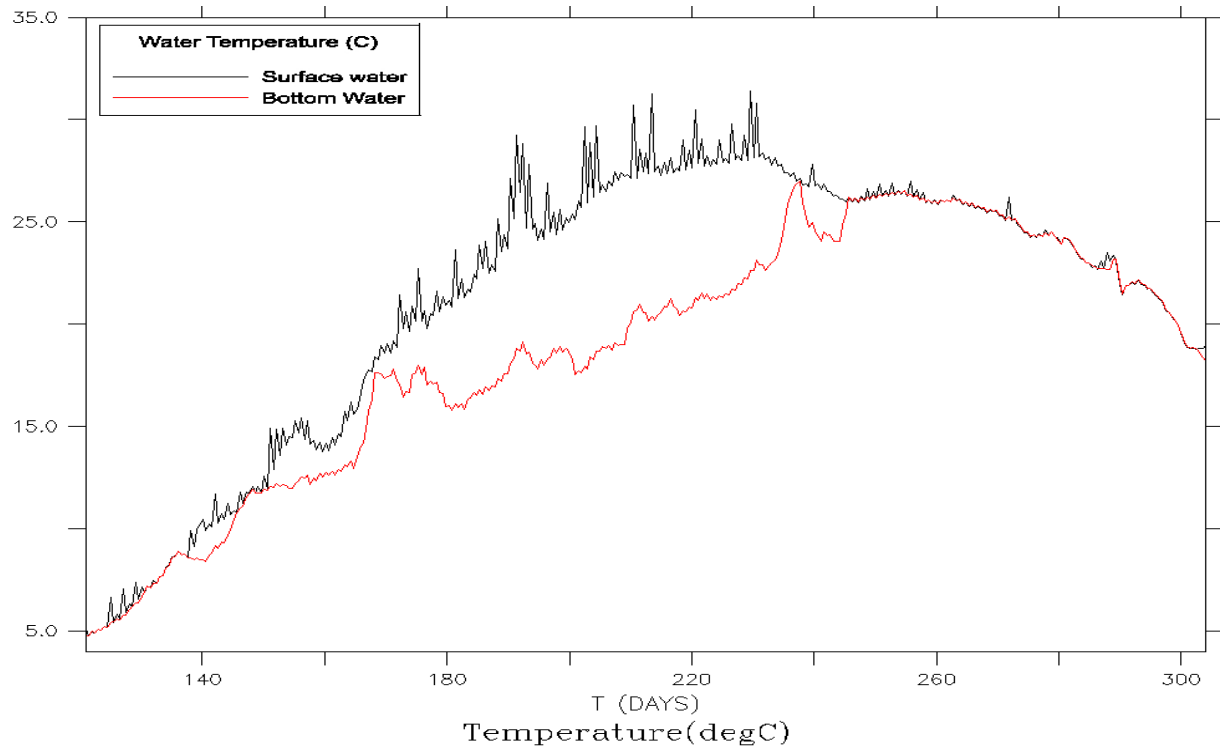

a

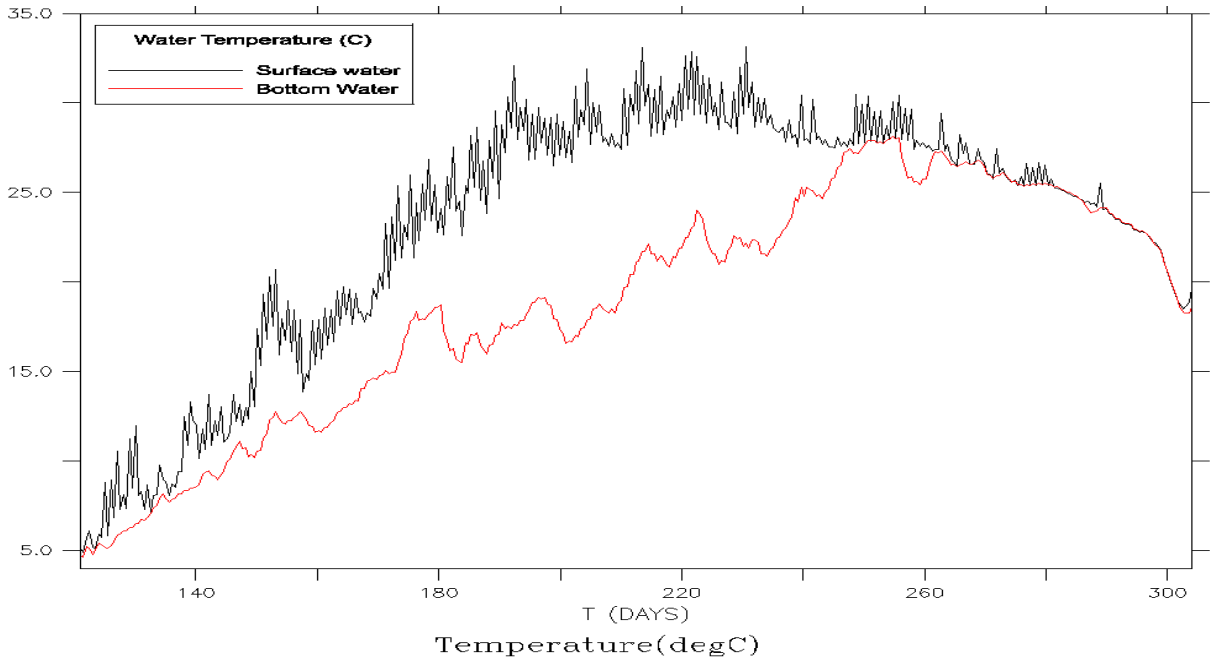

b

Figure 6.32: Near-surface and near-bottom temperatures in the a) absence and b) presence of a wind farm, 2005 (location: CW)

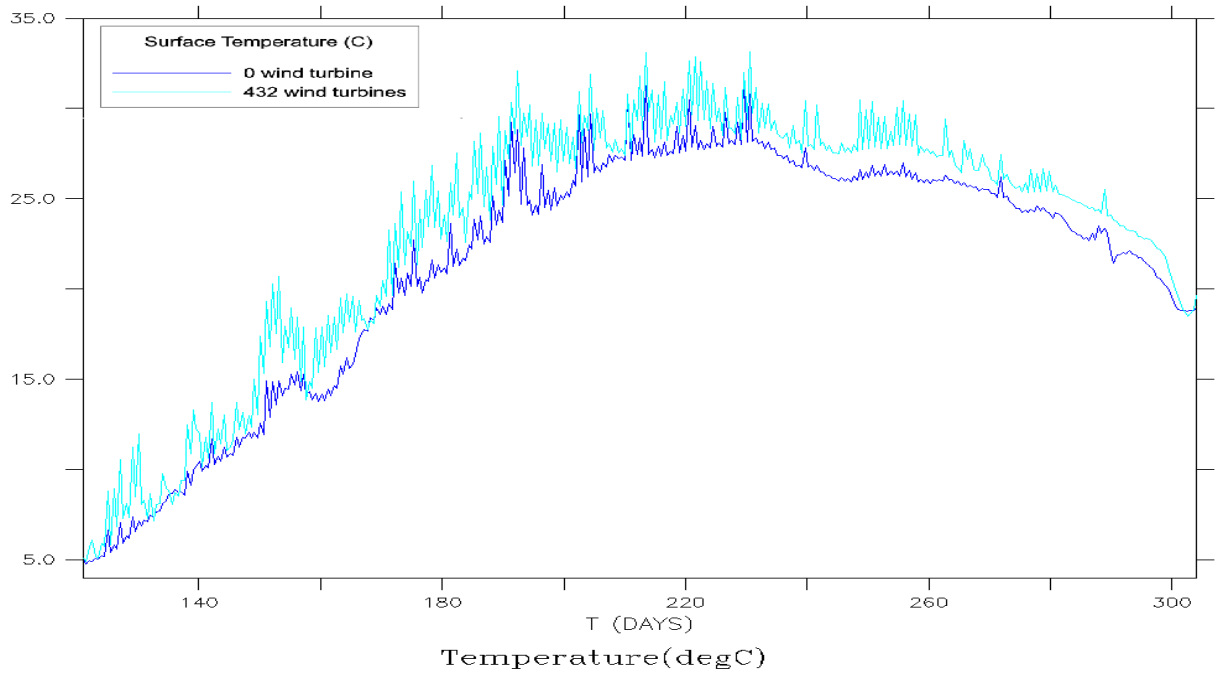

Figure 6.33: Near-surface temperature in the absence and presence of a wind farm, 2005 (location: CW)

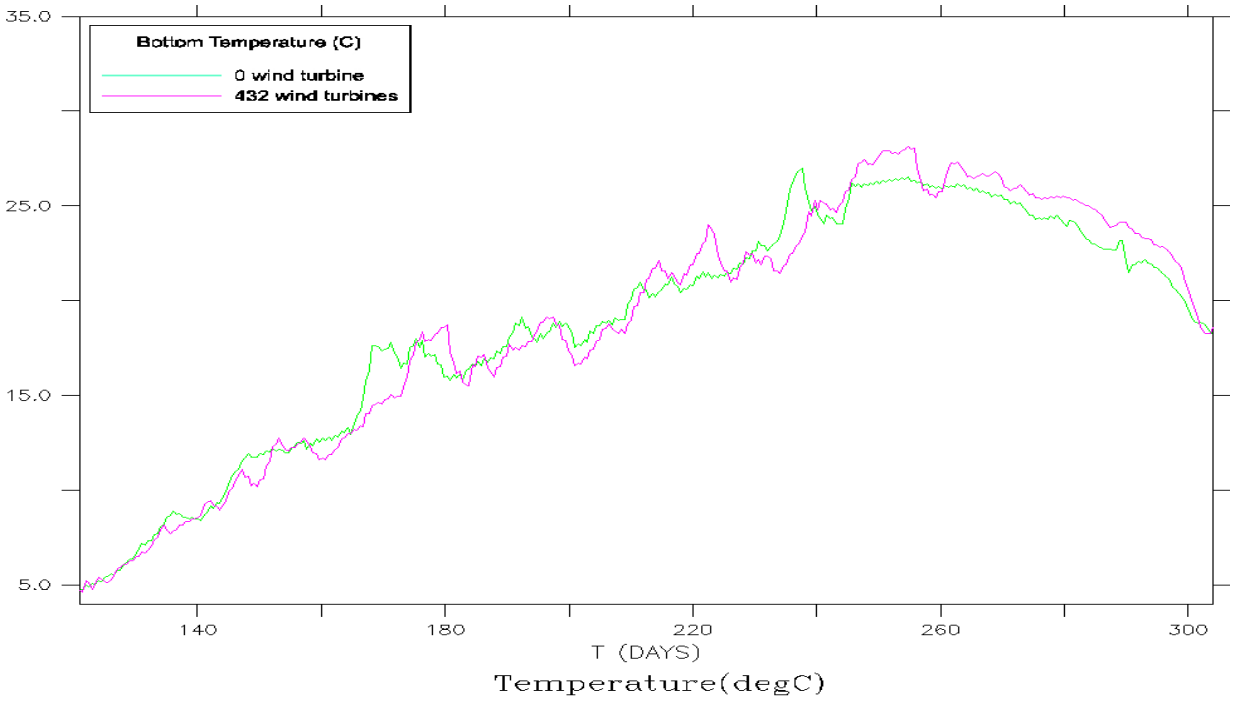

Figure 6.34: Near-bottom temperature in the absence and presence of a wind farm, 2005 (location: CW)

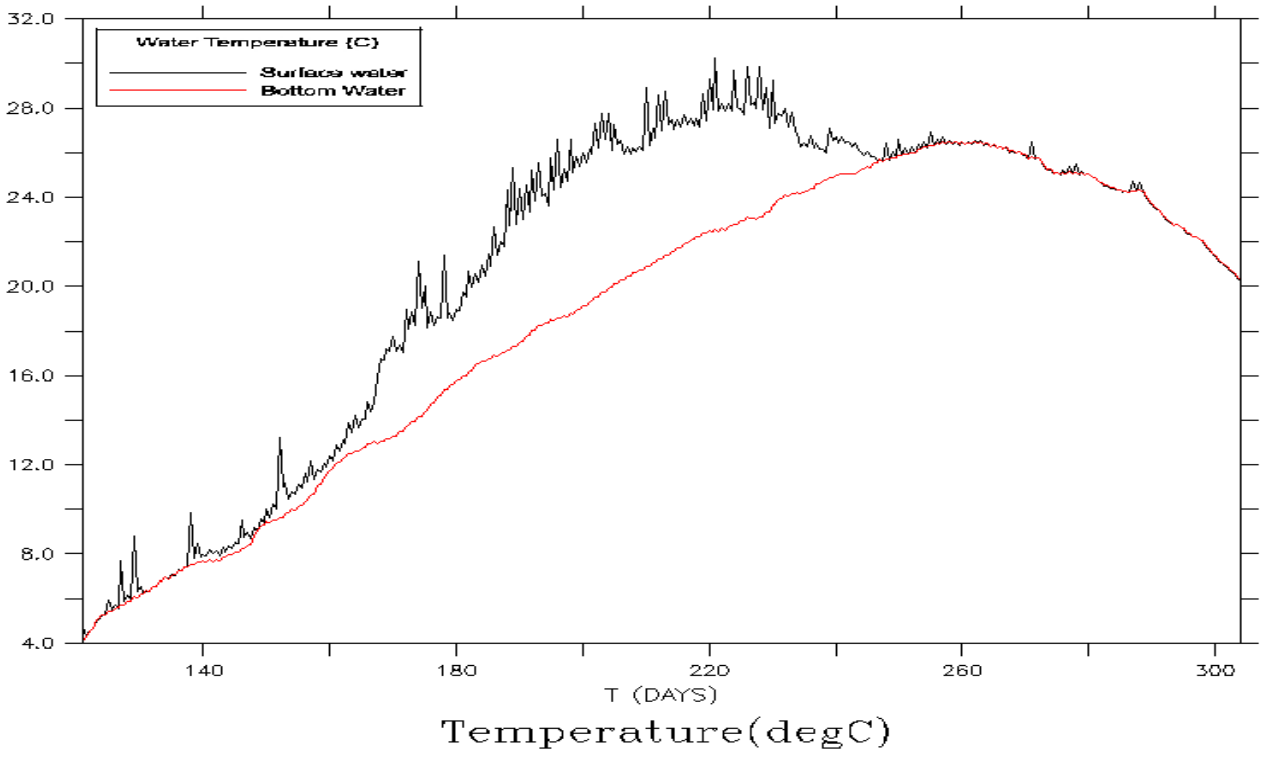

a

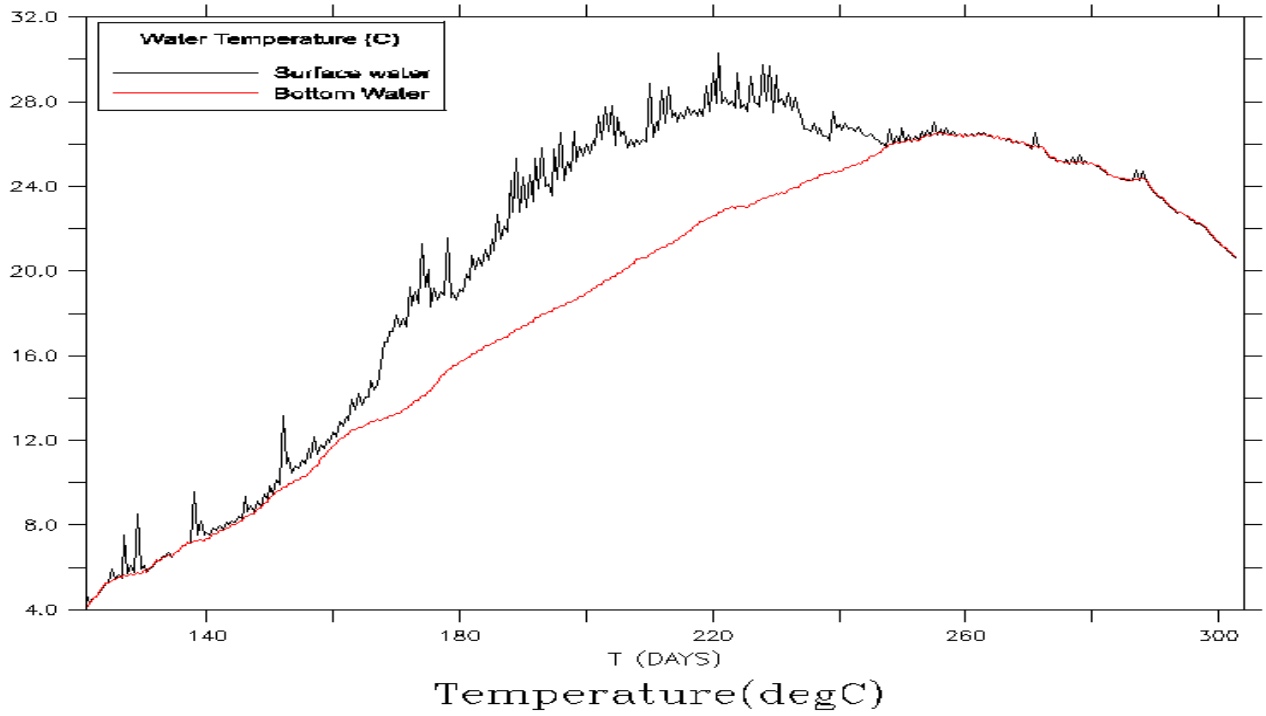

Figure 6.35: Near-surface and near-bottom temperatures in the a) absence and b) presence of a wind farm, 2005 (station T9)

6.8 A few Days Temperature Profiles

Figures 6.36 to 6.41 compare the temperature profiles and the modelled depth of the temperature mixed-layer and the strength of the thermocline in the centre of wake zone (CW) with a depth of 16.9 m, for DOY 130 (May 10), DOY 192 (July 11), DOY 200 (July 19), DOY 222 (August 10) and DOY 253 (September 10) in two cases. The results investigate the effects of a large wind farm on thermal stratification.

The temperature profiles of July and August are chosen as they have the deepest thermocline due to the high fluctuations in the wind speed and intensity of solar radiation. Also, May and September profiles illustrate the development and decay of the thermocline.

Simulation of the vertical structure of temperature is crucial for assessment of the wind farm effects on lake physics. But, it is worth noting that this point has been deliberately selected to show the significant loss due to the wind turbine wakes and is not representative of the whole data set. According to the temperature profiles, this location was isothermal in case 1 without the wind farm, while development of a weak stratification started on May 10, in case 2 with a wind farm of 432 wind turbines. Two months later, this point was stratified with a warm upper mixed-layer and cooler lower layer. On May 10, temperature difference between near-surface and near-bottom was less than 1 °C in case 2, while the water is well-mixed in case 1 with a temperature of 7°C. Bottom water is less than 0.5 °C warmer in case 1 than case 2, while surface water is about 1 °C cooler. Onset of stratification prevents warmer surface water from penetrating downward and this is the reason of having cooler bottom water in case 2. Two months later on July 11, the combination of the wind speed and solar radiation leads to strong heating of the surface layer, which clearly is shown in Figure 6.37. Stratification became mature in case 2 and deepens to a depth of 13 m, which starts approximately 2 m below the surface and penetrates 11 m downward. Surface-bottom temperature difference reaches approximately 10.5 °C (28 °C at surface and 17.5 °C at bottom), while the temperature gradient over

the upper 2 m (of the surface) is about 3.5 °C, (28 °C to 24.5 °C). Despite case 2, a mixed-layer of 4 m and a shallower thermocline from about 6 m to a depth of 12 m are seen in case 1. Also, the vertical temperature gradient decreases to a potential value of 6 °C (24.5 °C to 18.5 °C). Figure 6.38 shows the simulated temperature profile on July 19. COHERENS predicts a 4-m mixed-layer depth for case 2 and a deeper one of 9 m for case 1 in the centre of the wake (CW). The simulated profiles show that case 2 has slightly cooler water temperature (about 1 °C) in the bottom and warmer (about 2 °C), on the surface. Case 1 has shallower thermocline thickness of 4 m compared to 6 m in case 2. The thermocline erodes in both cases when the surface temperature starts to cool. But, the temperature profiles of August 10th (Figure 6.39) show an increase in temperature through the water column relative to July 10th. Solar radiation decreases in August and the whole water column is affected, so this cannot be explained by surface heating. The near-bottom layer on 10th of August is 21.5 and 24 °C about 6 and 5 °C cooler than the near-surface temperatures (27.5 and 29 °C) in case 1 and 2, respectively. There is a further increase in the near-surface temperature and decrease of the thermocline depths in both cases, which weaken the stratification. Wind stirring, as well as net surface heat flux, has an influence on stratification decay. Also, the depth of the near-bottom mixed-layer below the thermocline layer is greater by about 1 m in case 1 than case 2. From May 10th to August 10th, near-surface temperature gradually increases from 6 and 7 °C to 27 and 29 °C in case 1 and 2, respectively and the corresponding values on the near-bottom are 7 and 6.5 °C increasing to 21.5 and 24 °C. After August, water starts cooling down so that September 10 profiles (Figure 6.40) demonstrate the well-mixed temperatures of 25, 27 °C from surface to bottom in cases 1 and 2, respectively. As the plots illustrate, the profiles from May to August show a strong thermocline that is sharper and deeper in case 2 than case 1 and is weakened after August and destroyed by September. Case 2 has a shallower mixed-layer, which is probably due to insufficient mixing in their moderate winds caused by wind turbine wakes. From the plots. The depth of the mixed-layer is fairly sensitive to the wind stress. Figure 6.41 depicted

the development of thermocline in one episode. It presents a better image of how thermocline develops and decays during the simulated period. Generally, it can be concluded that the presence of a wind farm increases the surface temperature less than 2-3 °C on the selected days and also sharpens the thermocline, thickens its depth and increases its longevity. The July and August plots can be considered as representative for the stratification with average thermocline depths of around 8 and 5 m, for cases 1 and 2, respectively. However, a rough estimation of a depth of thermocline are given. After August, increased over-lake winds contribute to deepening of the upper mixed-layer. At the same time, further heat loss results in lowering of temperature. Similar responses are seen in both cases and the point continues to approach minimum temperature by end of October (not shown). The deepening of the thermocline and increase in thickness of the upper mixed-layer starts in late July and continues until the water column is again mixed from top to bottom. Surface heat loss and increased vertical mixing associated with strong winds are responsible for this deepening. The temperature in case 2 is warmer than case 1 value by 1-2 °C. in addition to local mixing there may be advective effects which differ from case 1 to case 2 and play a role in determining the local thermal structure.

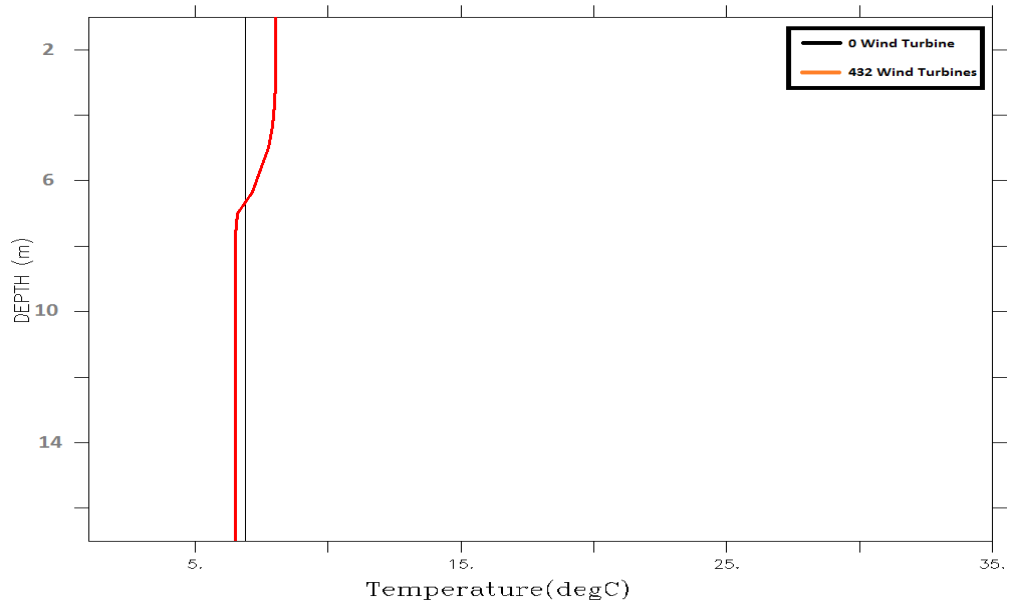

Figure 6.36: Centre of wake depth-averaged vertical temperature profile, May 10- 2005.

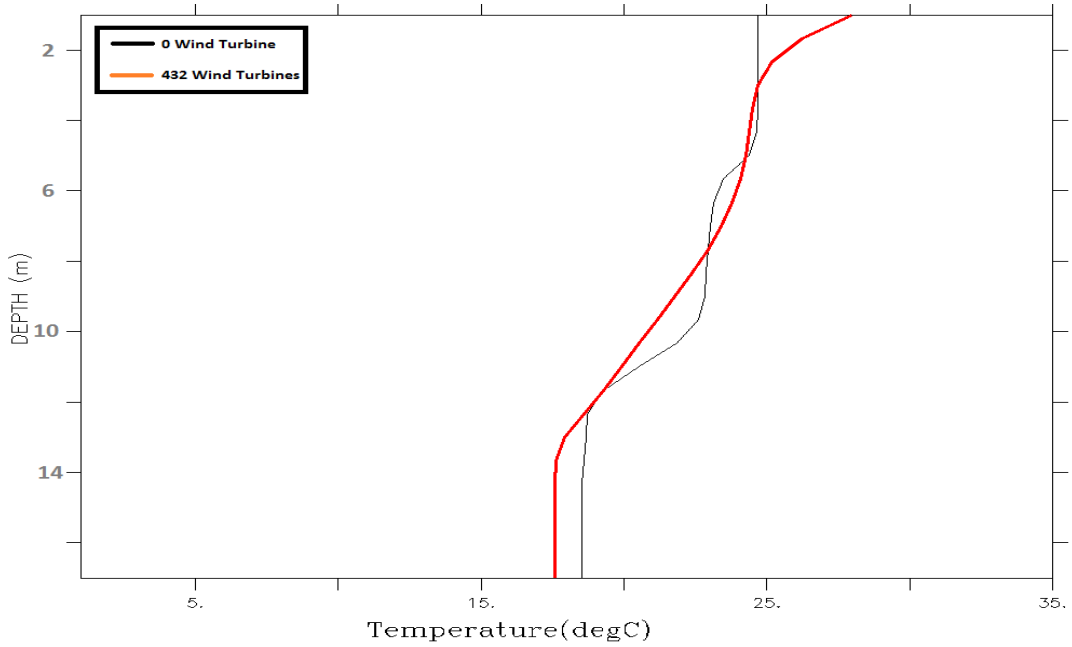

Figure 6.37: Centre of wake vertical temperature profile, July 11- 2005.

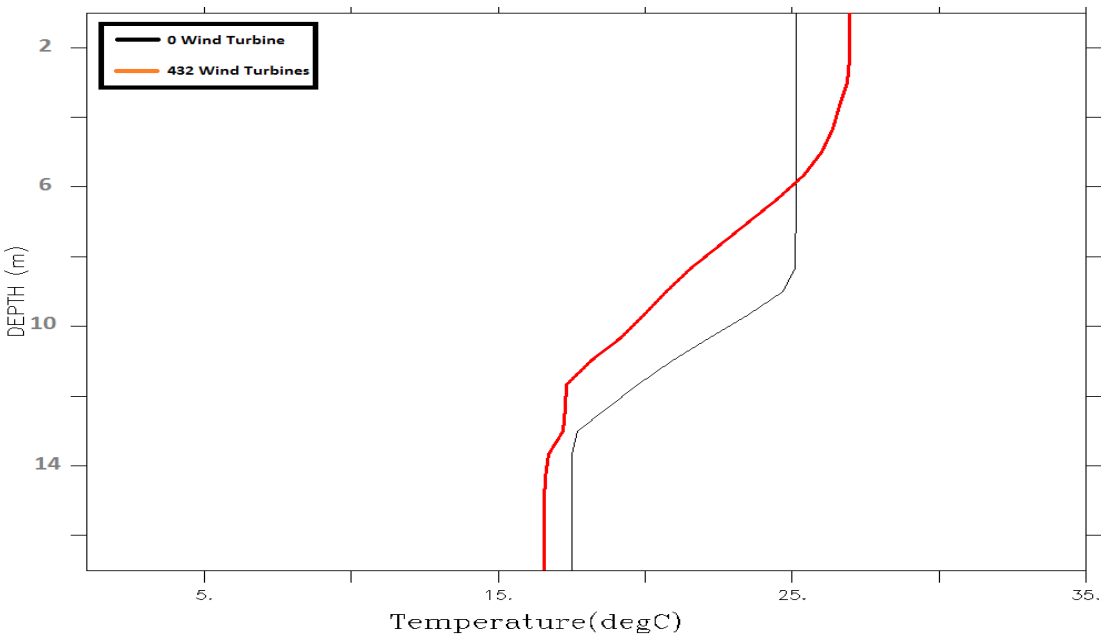

Figure 6.38: Centre of wake vertical temperature profile, July 19- 2005.

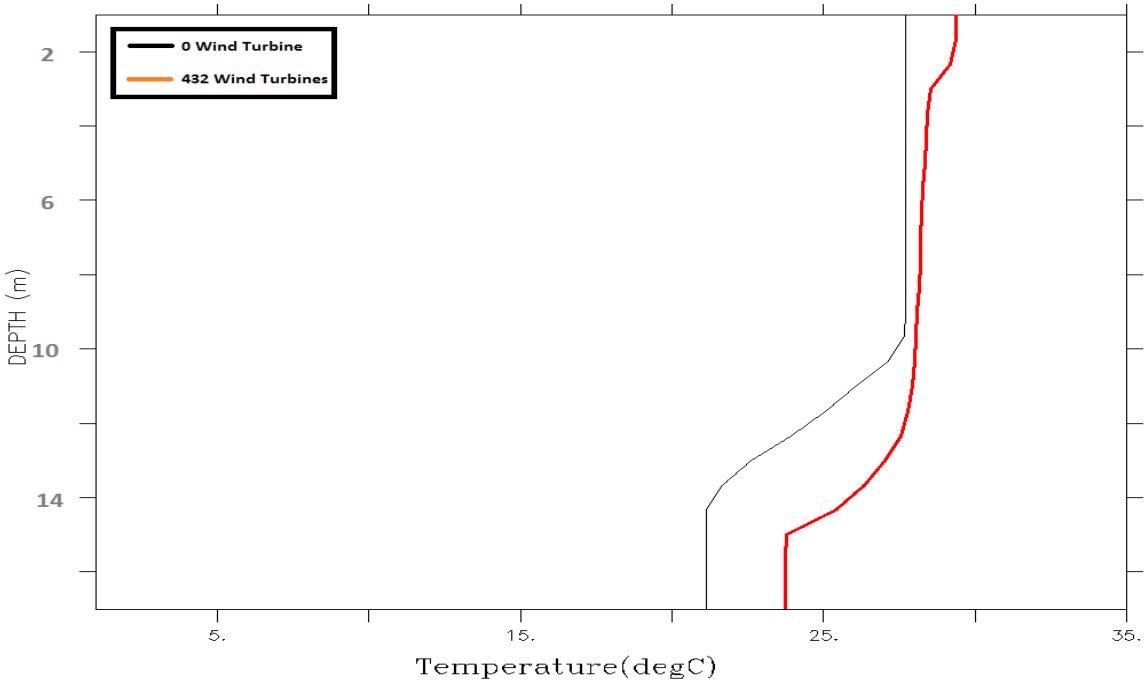

Figure 6.39: Centre of wake vertical temperature profile, August 10- 2005.

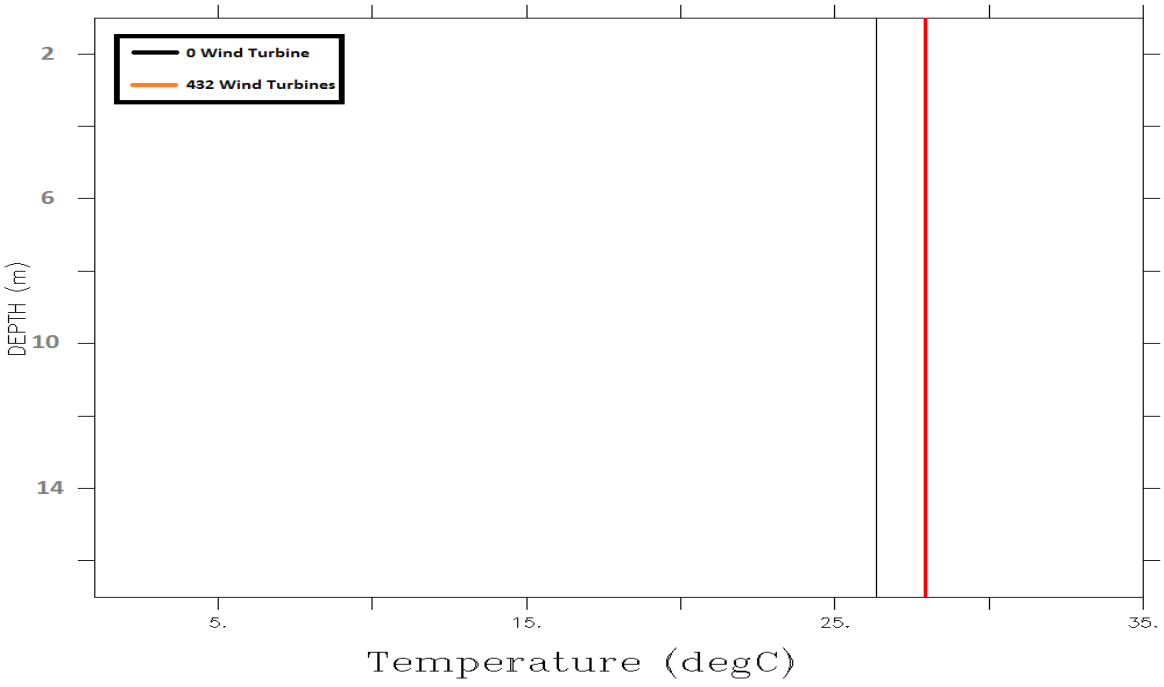

Figure 6.40: Centre of wake vertical temperature profile, September 10- 2005.

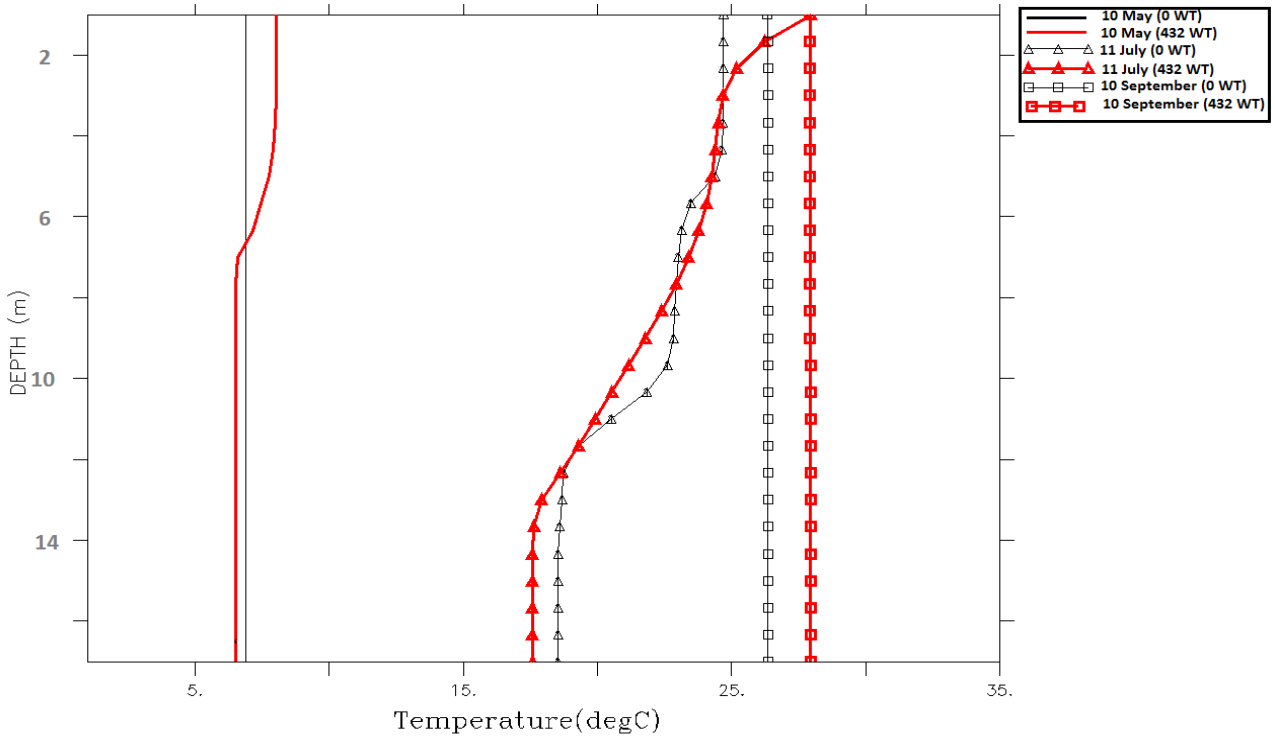

Figure 6.41: Centre of wake vertical temperature profile, May to September- 2005.

6.9 Thermocline Plots in Presence of a Large Wind Farm

Thermocline depth was observed to vary over the months and between basins. Fluctuations in the thermocline depth is a consequence of the fluctuations in the dominant winds and input heat budget. While almost an identical thermocline of case 1 was modelled in the simulated period in case 2, a sharp thermocline was established by July at approximate depth of 10 m in the central basin and a bit deeper of 10-20 m in the eastern basin. The position of the 19 °C isothermal was used to define the thermocline depth in July. During July and August, when the thermocline is thicker, the mixing processes are confined to the upper portion of the thermocline. Comparison between Figure 5.24c with Figure 6.42 reveals warmer water in the western part of the central basin so that in July, temperatures in shallower depths of 15 m, are mostly 23-26 °C. While the main effect is seen on the west part of the central basin (near to the wind farm), the rest of the lake retains its normal thermal structure and is not affected by

the wind farm. The model indicates that the central basin thermocline is more variable in depth and sharper when a wind farm is applied. Again, in August warmer water of 29 °C penetrates to depths of 10-12 m in the western part of the central basin, (Figure 5.26c compare to Figure 6.43). Also, in case 2, in some bottom parts water is cooler than case 1 by less than 1 °C, as a thicker thermocline prevents and slows the mixing process.

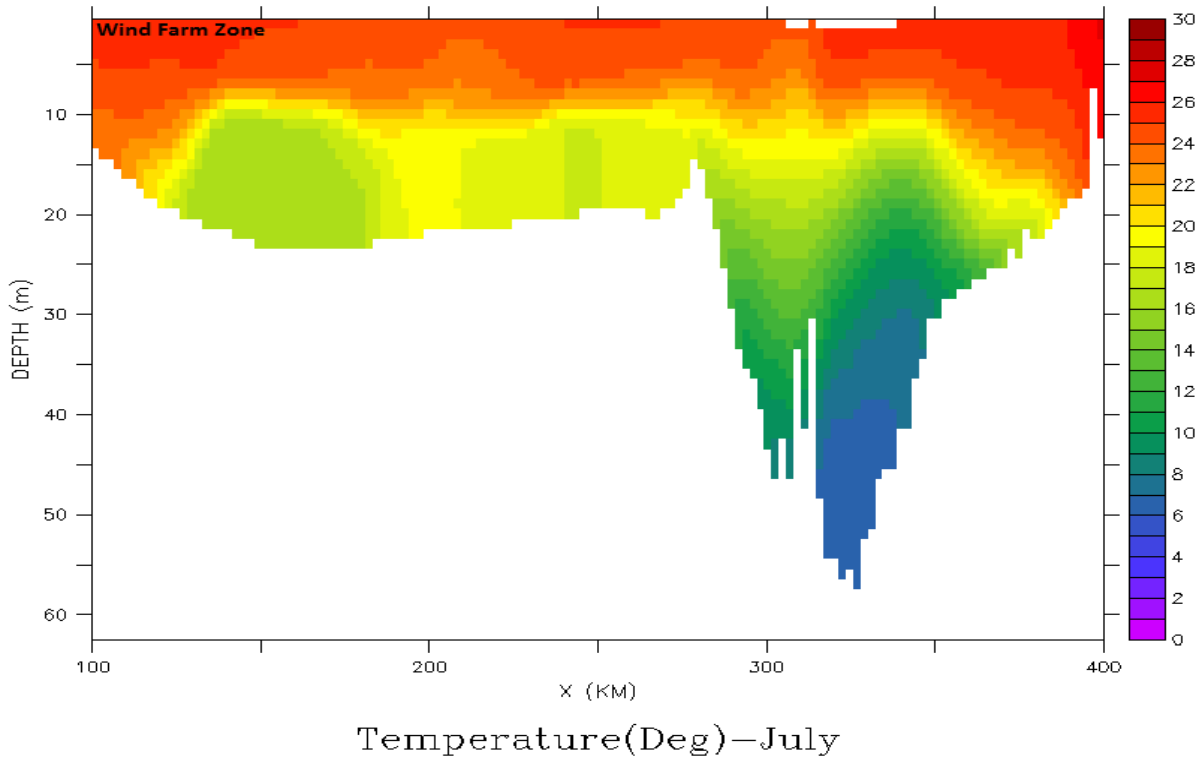

Figure 6.42: July averaged COHERENS model temperature (west to east) in the presence of a wind farm, 2005.

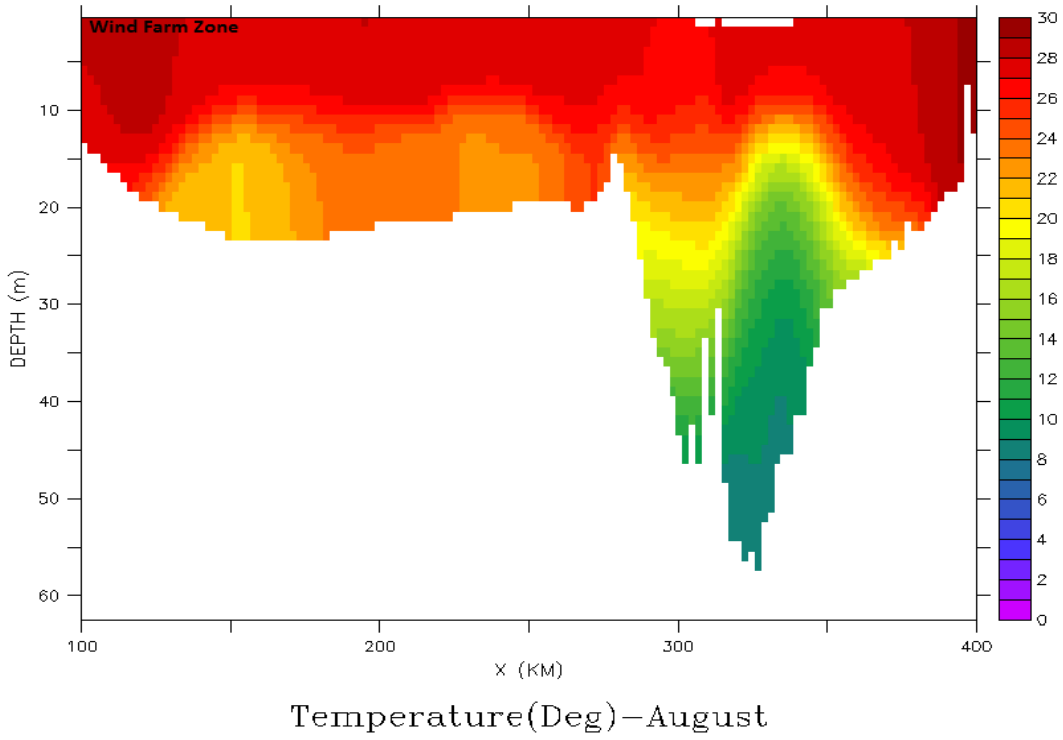

Figure 6.43: August averaged COHERENS model temperature (west to east) in the presence of a wind farm, 2005.

6.10 A few Days Wind Plot in the Presence of a Wind Farm

Figures 6.44 to 6.47 show the instantaneous wind plots of DOY 130 (10 May), DOY 170 (June 19), DOY 205 (July 24), and DOY 283 (October 10) at UTC 5:00 pm, in the west part of the central basin for the 2005 simulation. There was not any preference in selecting these four days and the main purpose was to choose different wind directions to investigate the model's response to the wind turbine wake effect and further assessment by examining the distribution of the wind when a wind farm is present. Wind speed contours overlay the wind vectors in the plots. The wind speed difference away from the wind farm tends to be small and quite smooth. But wind speed reduction within the wind farm area is predicted to be about 60 percent in the centre of the wake zone (CW). May 10th (Figure 6.44) shows the ambient wind speed of 5 m/s compare to a reduced 2 m/s wind at the centre of wake where

the wind blows to the northeast. Wind speed contours clearly present the downwind wake zone. On June 19th (Figure 6.45), wind blows to southwest and smaller wind vectors are recognized within the wake zone. This time, the wake zone forms at the very southwest part of the central basin. Figure 6.46 presents winds blowing from the south directed to the north so a wake zone is formed downwind on the north boundary of the wind farm. This figure presents a more detailed pattern of the wind turbine wake as the lateral (x-direction) turbine spacing is six times more than the y-direction. (3 km in the x-direction compared to 0.5 km in the y-direction). The October 10th wind pattern, in Figure 6.47 is almost similar to June 19th but is more southward.

Figures 6.48 to 6.50 illustrate the wind speed reduction of about 60 percent in the centre of wake (CW), in all selected directions (west, south and southwest, respectively).

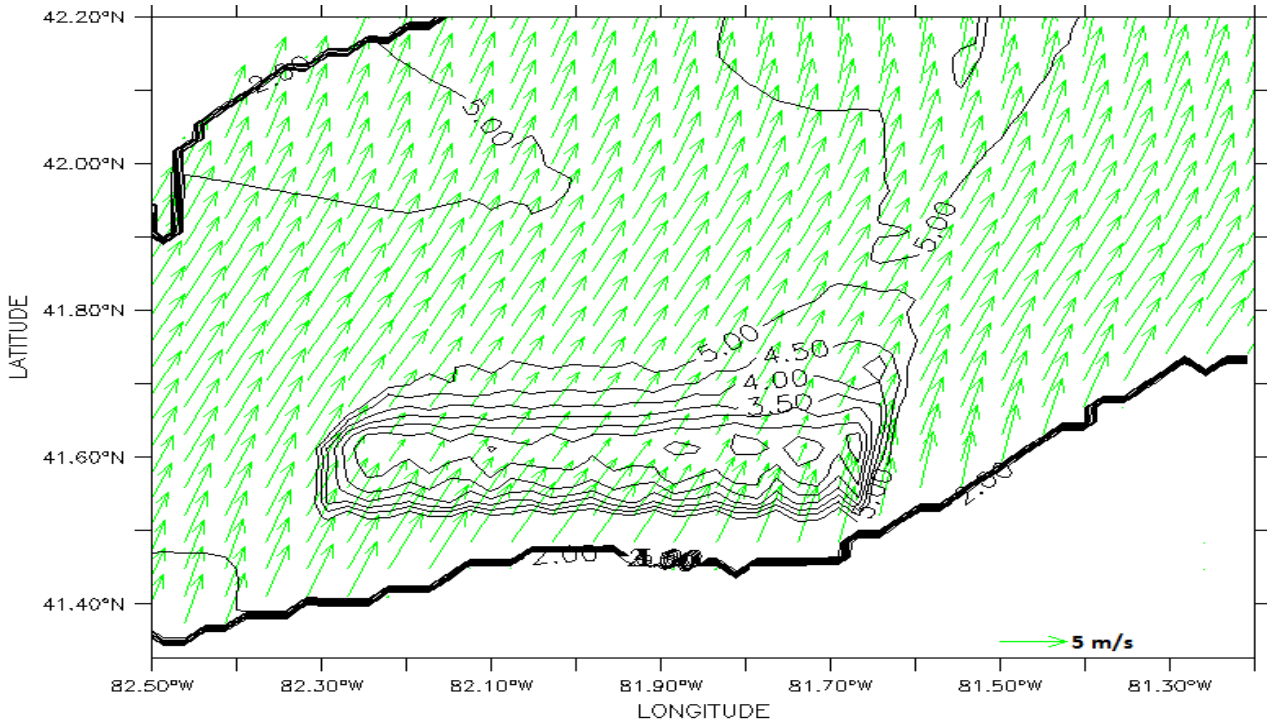

Figure 6.44: Spatial plot of wind in the presence of a wind farm, May 10, 2005.

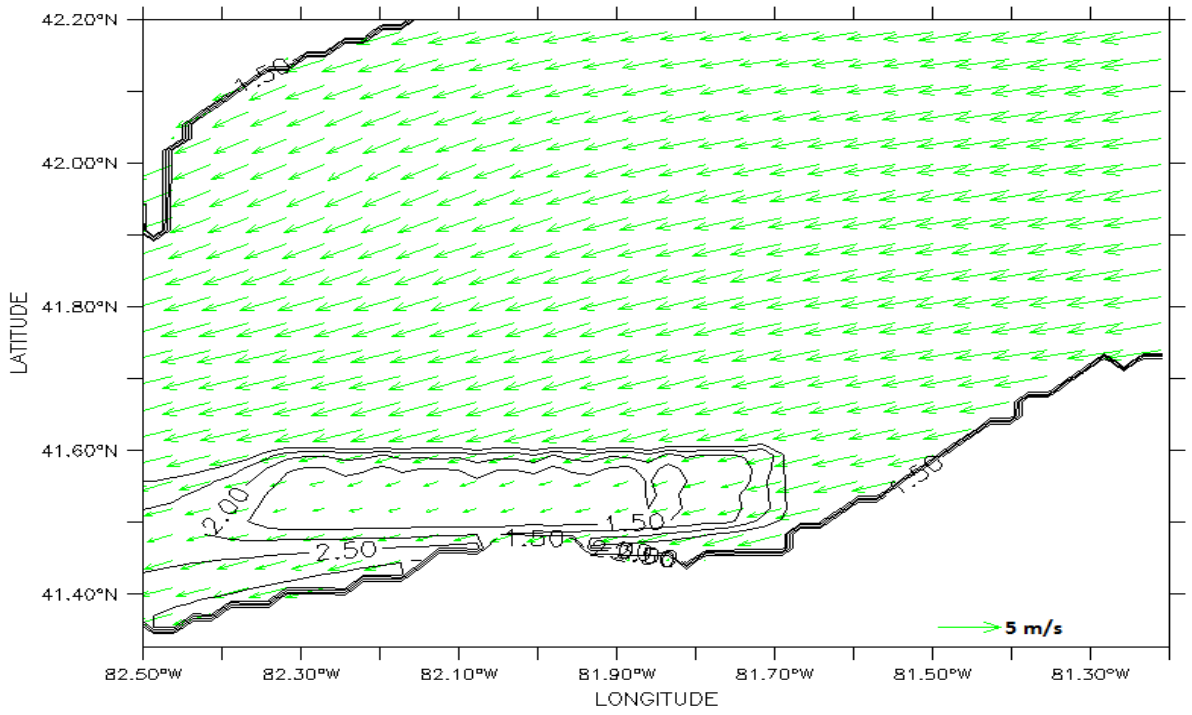

Figure 6.45: Spatial plot of wind in the presence of a wind farm, June 19, 2005.

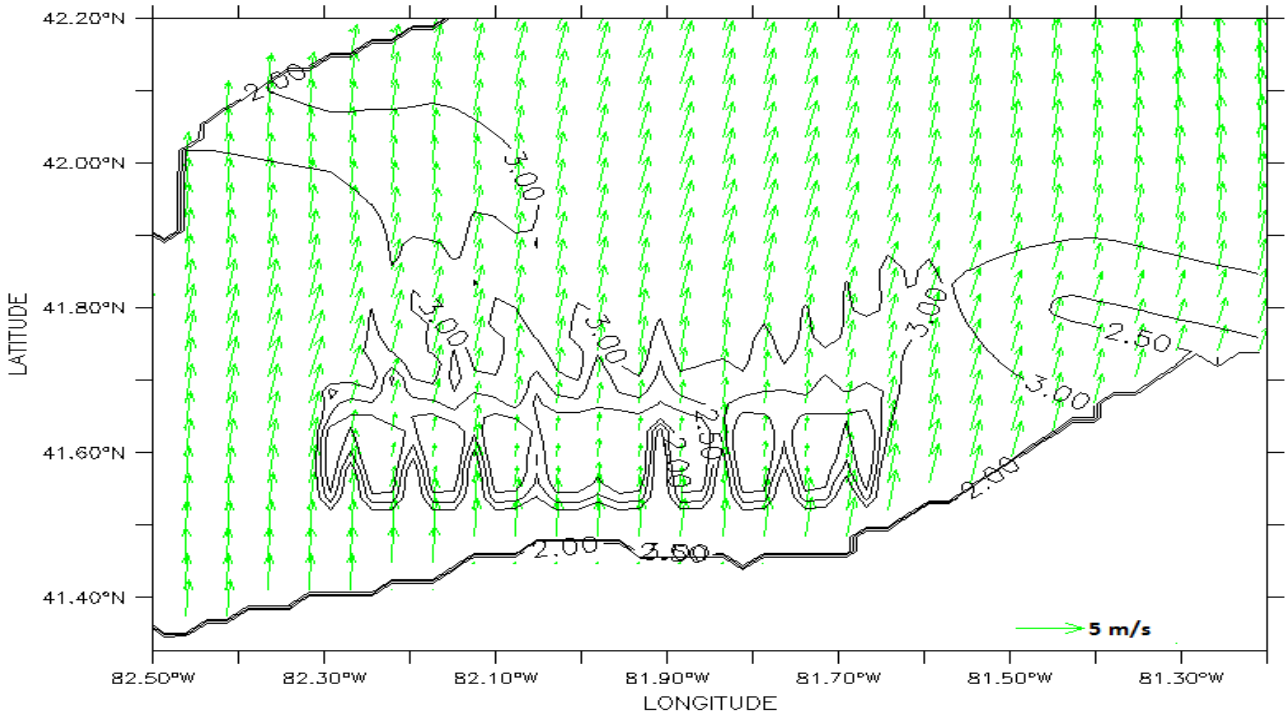

Figure 6.46: Spatial plot of wind in the presence of a wind farm, July 24, 2005.

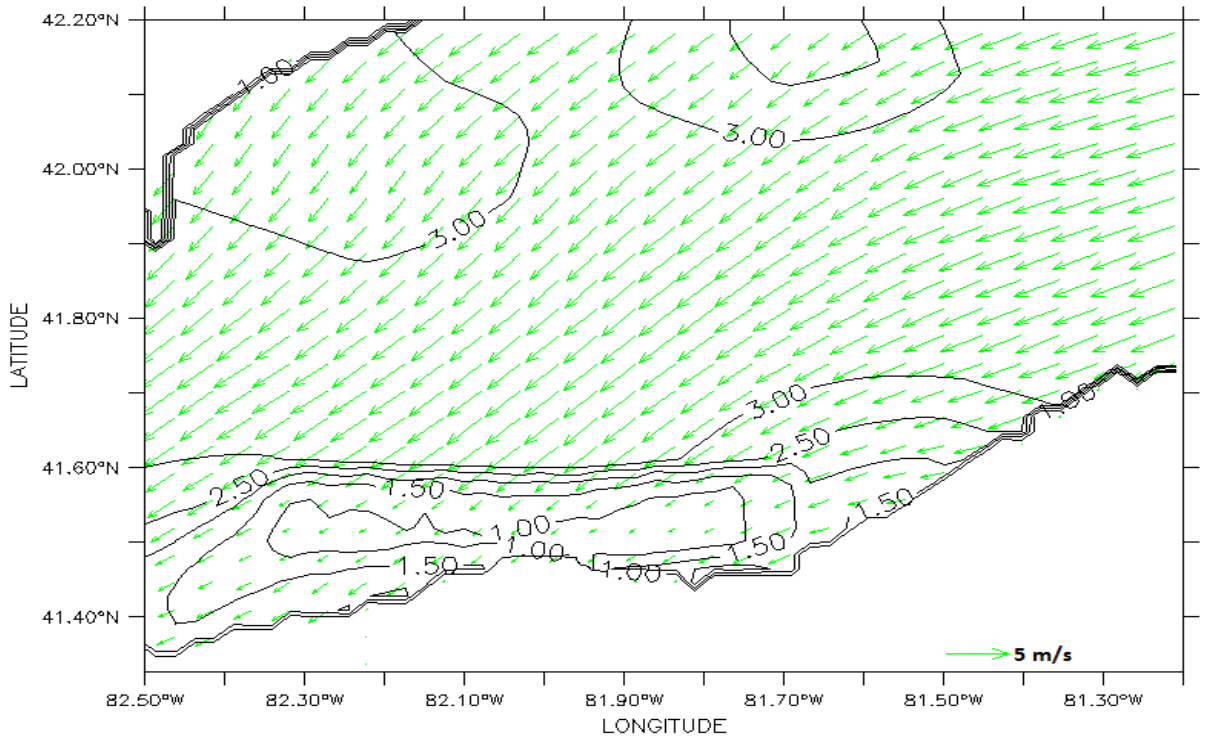

Figure 6.47: Spatial plot of wind in the presence of a wind farm, October 10, 2005.

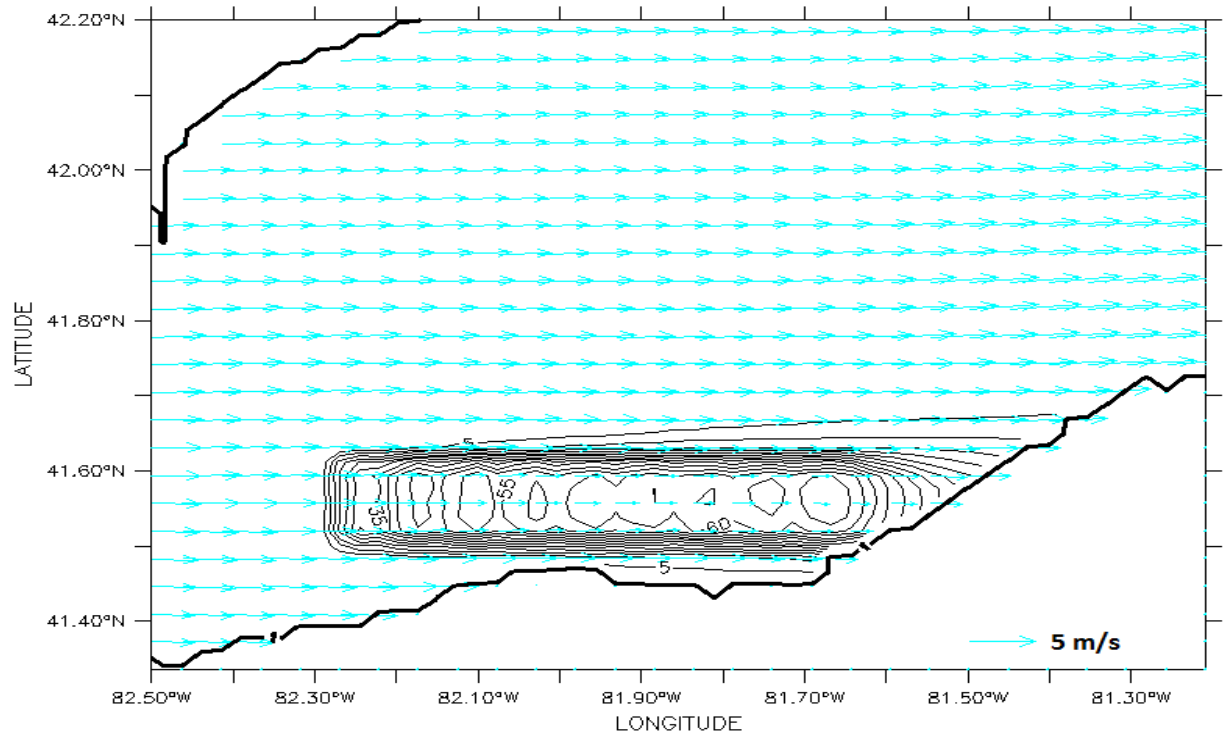

Figure 6.48: Spatial plot of wind speed reduction (percentage) in the presence of a wind farm, May 3, 2005.

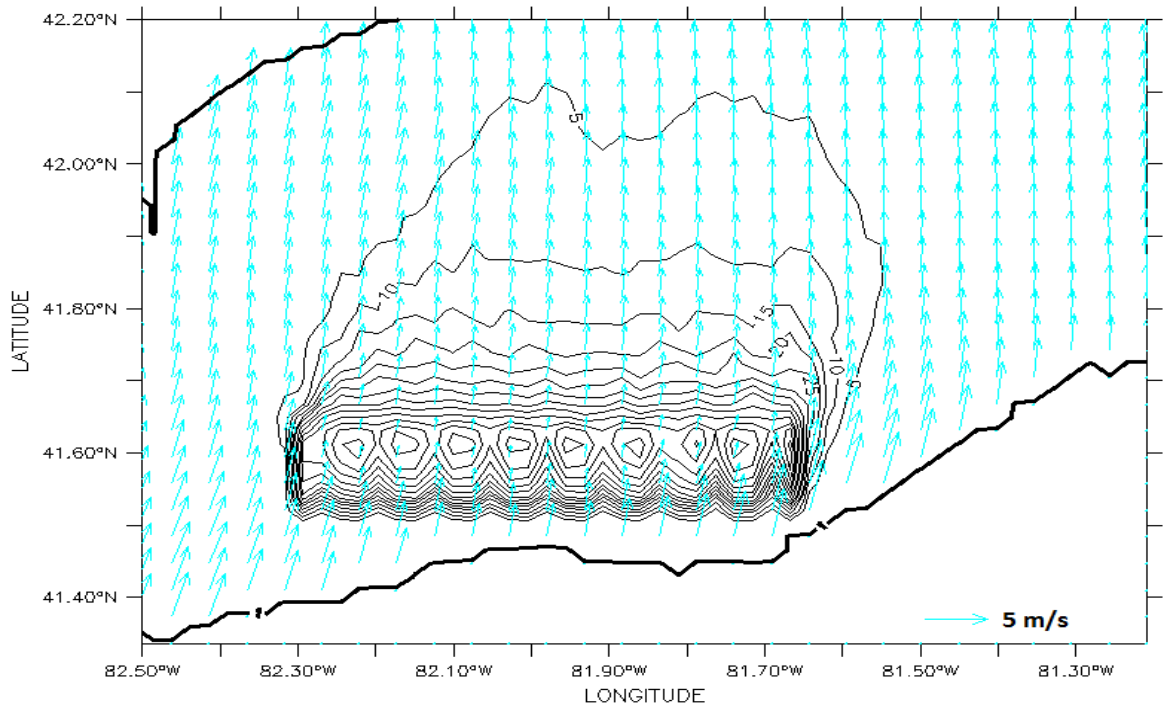

Figure 6.49: Spatial plot of wind speed reduction (percentage) in the presence of a wind farm, July 24, 2005.

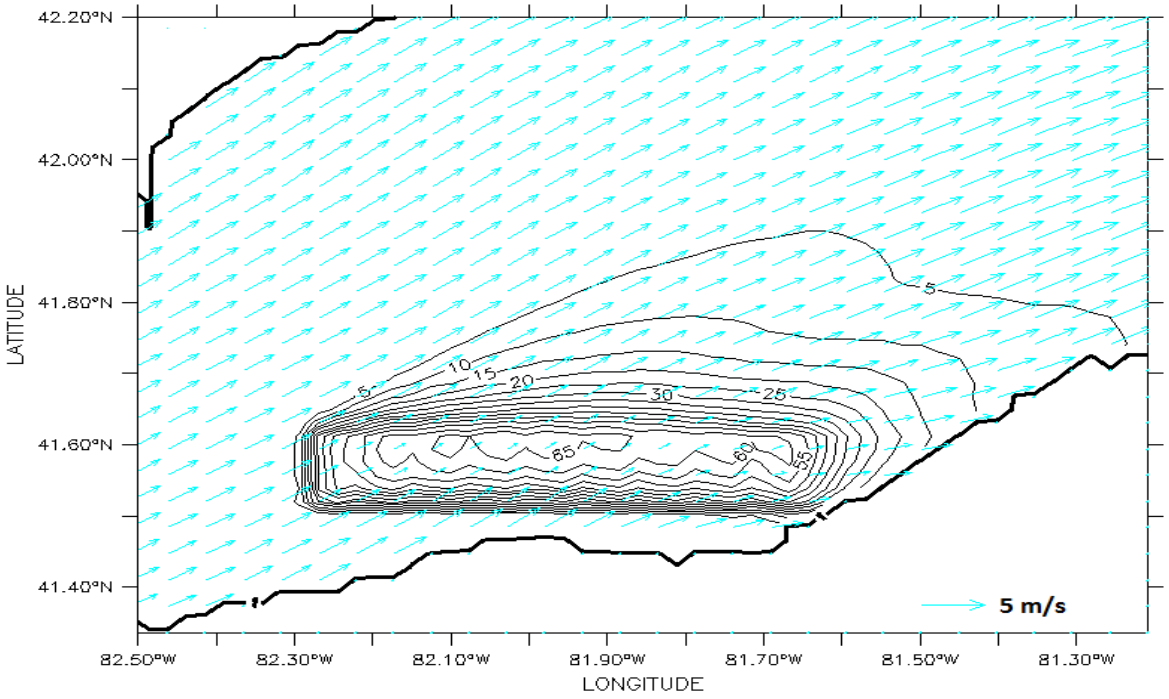

Figure 6.50: Spatial plot of wind speed reduction (percentage) in the presence of a wind farm, August 24, 2005.

6.11 Temperature Mixed-layer Depth (TMLD)

Figures 6.51 to 6.54 present the time-depth distribution of the temperature mixed-layer depth (TMLD) at stations T8, T9, T12 and centre of wake (CW). To highlight the similarities and differences between two cases three plots in each case are displayed, including an individual TMLD for each case and a combined plot of the two cases. These stations represent TMLD conditions from shallow to deep depths. Stations T12 and T9 almost have not been affected in accordance with our expectations as they are located in the eastern basin and the northeast central basin far enough away to not be impacted by the wind farm. However, station T12 has much stronger stratification in most of the simulated period and that prevents the water mixing.

The mixed-layer depth has significant spatial variability, due to the influence of the currents that can transport and redistribute the heat obtained from the atmosphere both horizontally and vertically. The mixed-layer increases when entering the cooler months. The spatial distribution and variability of the TMLD is mainly a consequence of the prevailing winds.

At station T12 (Figure 6.51), the TMLD barely reaches below 10 m after May and before September, but reaches 30 m in October. Therefore, it reveals a persistent stratification before the cold months in the simulated period. At station T9 (Figure 6.52), stratification forms around DOY 160 and decays completely on DOY 245. One reason for this shorter stratification period is that water is shallower at this station compared to the station T12. At station T8 (Figure 6.53), the wind farm causes a deeper TMLD, especially after July. This station is close enough to the wind farm so it is expected to be impacted by the wind turbine wakes. Normally, a shallower mixed-layer depth is expected in the presence of a wind farm, but this point is located on the northwest side of the wind farm and does not follow the behavior within the wind farm wake zone. Considering Figures 6.26 to 6.31, bigger mean currents exist in the western gyre formed on the west side of the wind farm, where T8 is located, when a wind farm is included in the model. Because of wind speed reduction and the averaging process, the

water current velocity changes and, as mentioned above, get bigger outside of the wind farm zone. Current velocity increases after June, and that is why a deeper TMLD is seen. During July and August, the TMLD is more diffuse and has higher variations as currents reach their maximum values (in the mature western gyre). However, slower currents combined with lower temperature decrease this variability and we can see a deeper and smoother TMLD after August. Despite the T8-station results, in centre of wake (CW) (Figure 6.54), the opposite behavior applies. TMLD decreases in the presence of a wind farm because wind speed and current reach to their minimum value in the centre of wake as a consequence of the wind speed reduction. Also, stratification forms earlier and decays later while a sharp and strong thermocline exists during June, July, and early August. Surface temperature increases, associated with reduced-wind speed and prevents surface water from entraining downward. To better present the impact of a wind farm on TMLD, Figure 6.55 illustrates a 10-day block of TMLD for both cases in July. It can be concluded that the mixed-layer depth is zero in July (our model calculates the results at the near-surface and not at the exact surface) for case 2 and barely reaches to 8 m in case 1. This means that by introducing a wind farm a strong stratification forms, which reduces the TMLD during summer by increasing the temperature more, due to the wind speed reductions. Also, the plots confirm that high-frequency changes in wind stress are responsible for deepening the surface mixed-layer. Comparing the wind speed plots and TMLD reveals the high sensitivity of thermal stratification to changes in wind speed.

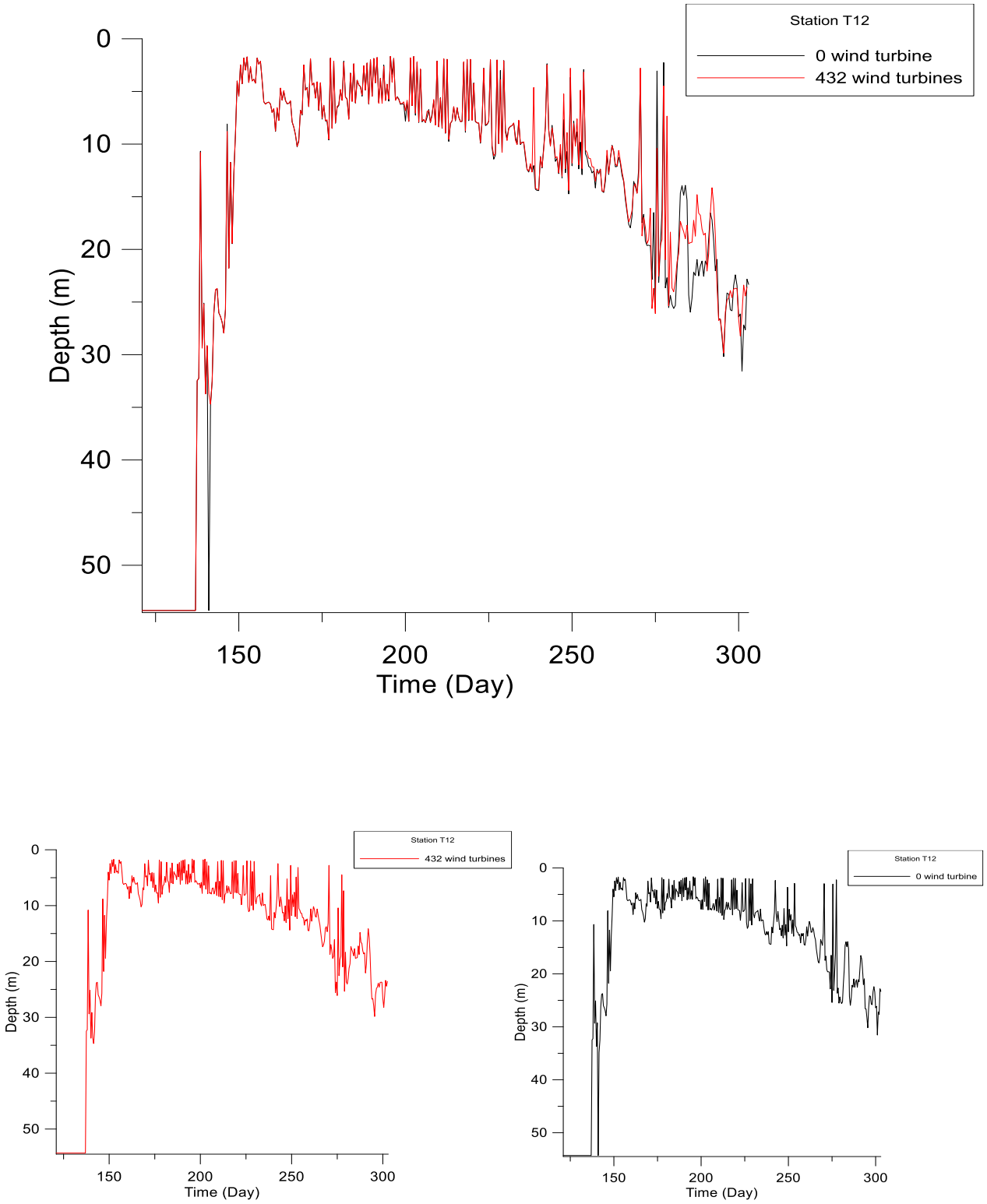

Figure 6.51: Computed temperature mixed-layer depth throughout in the presence (red) and absence (black) of a wind farm for station T12 in Lake Erie, May-October 2005.

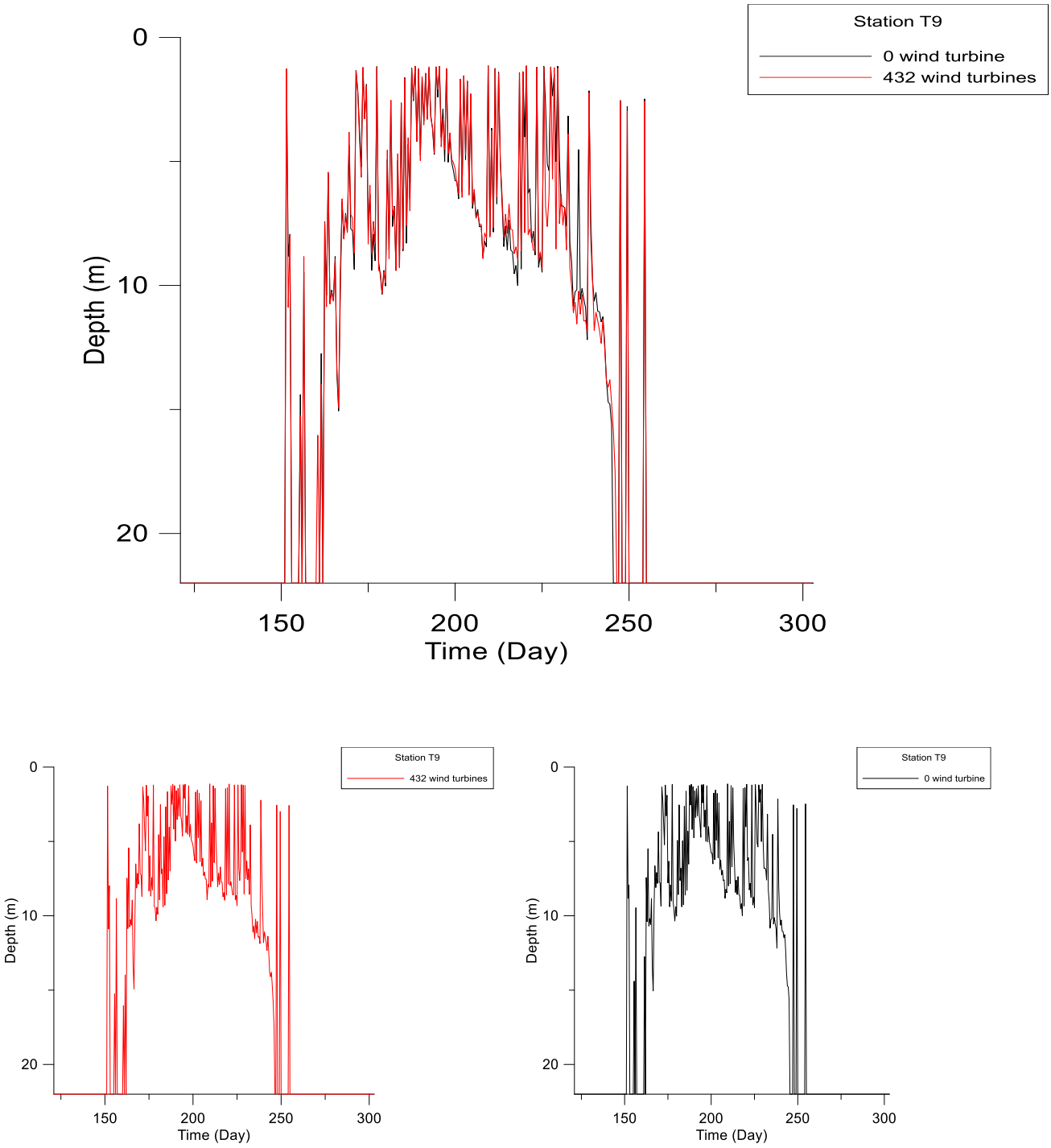

Figure 6.52: Computed temperature mixed-layer depth throughout in the presence (red) and absence (black) of a wind farm for station T09 in Lake Erie, May-October 2005.

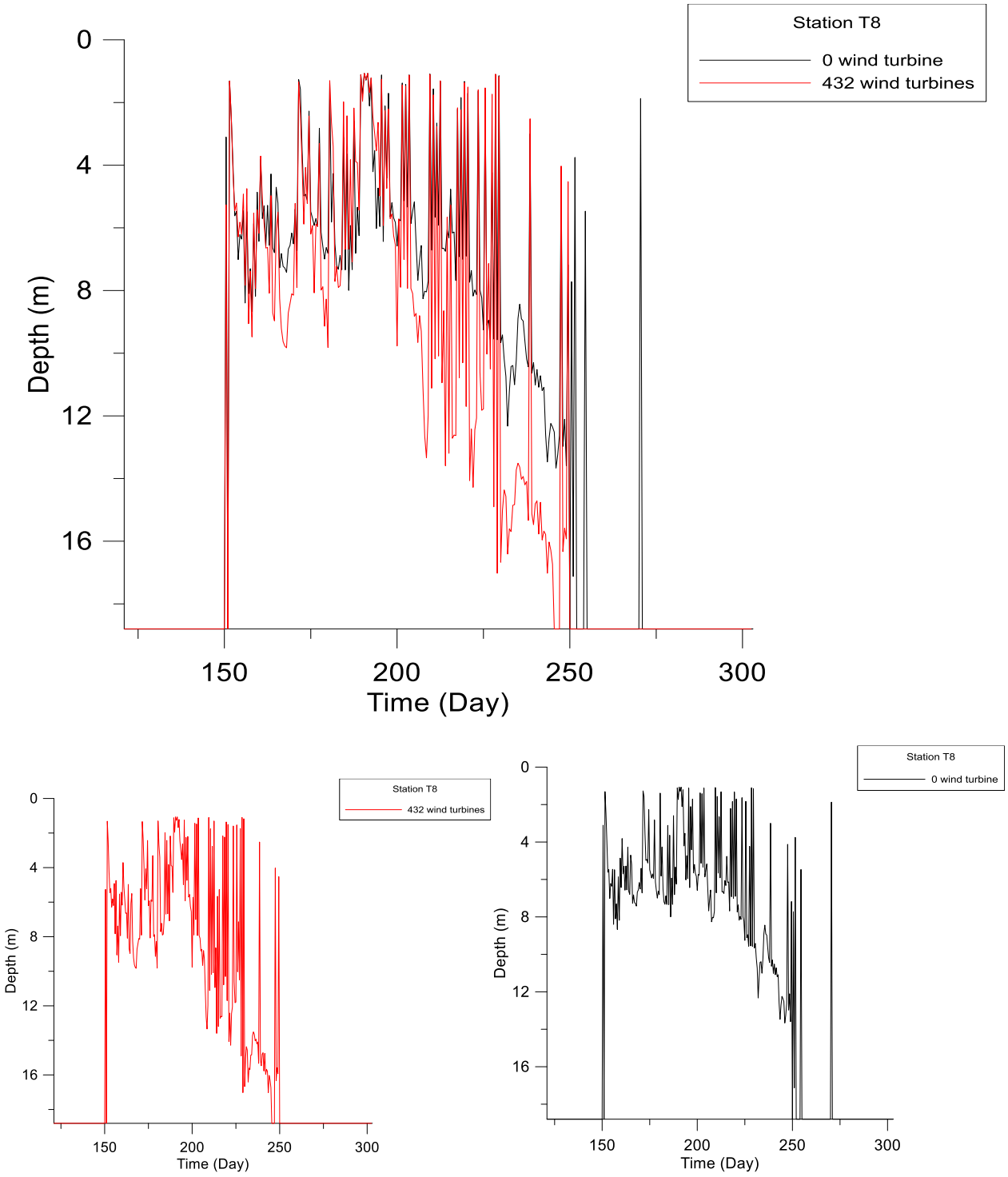

Figure 6.53: Computed temperature mixed-layer depth throughout in the presence (red) and absence (black) of a wind farm for station T08 in Lake Erie, May-October 2005.

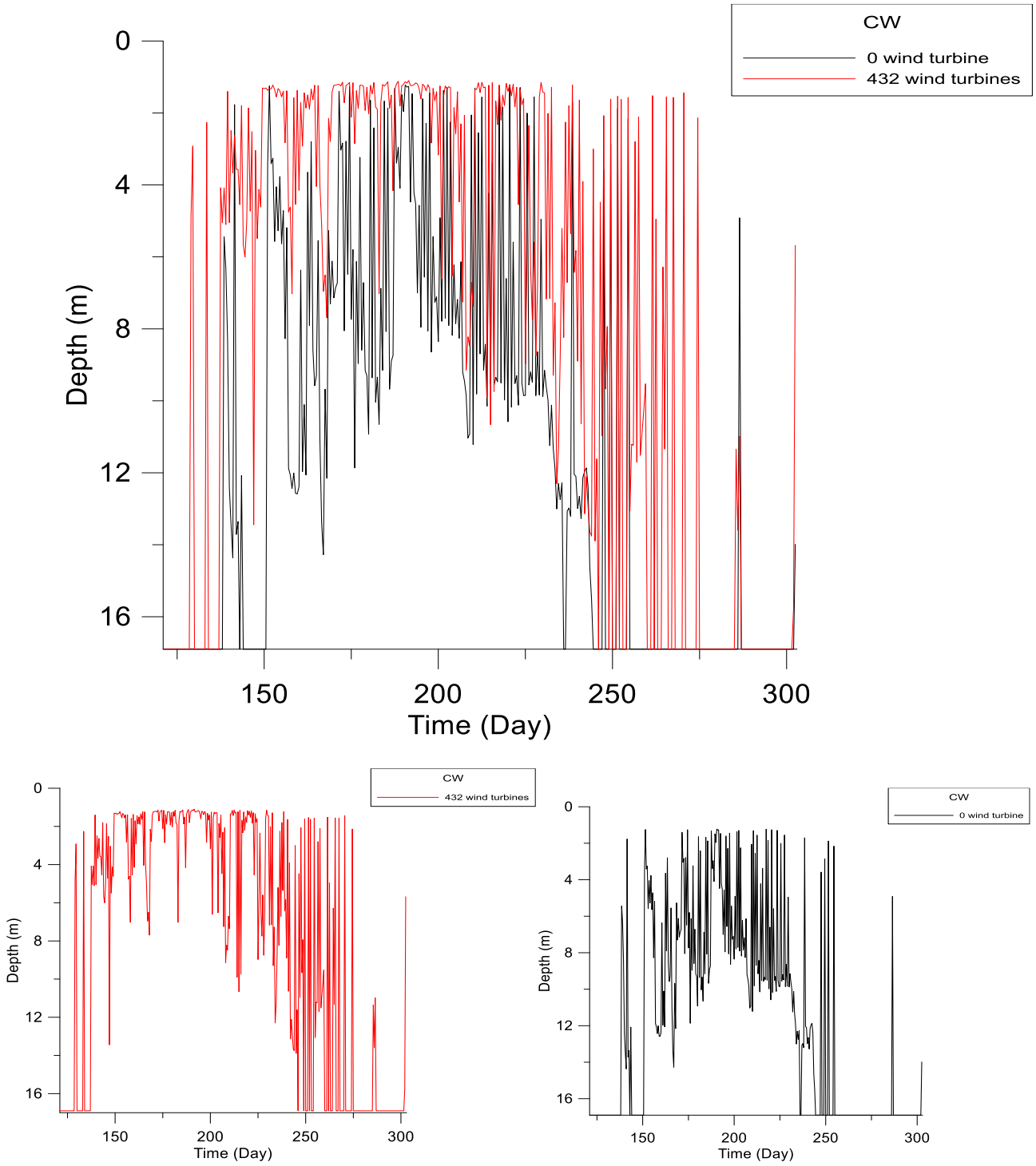

Figure 6.54: Computed temperature mixed-layer depth throughout in the presence (red) and absence (black) of a wind farm for centre of wake (CW) in Lake Erie, May-October 2005.

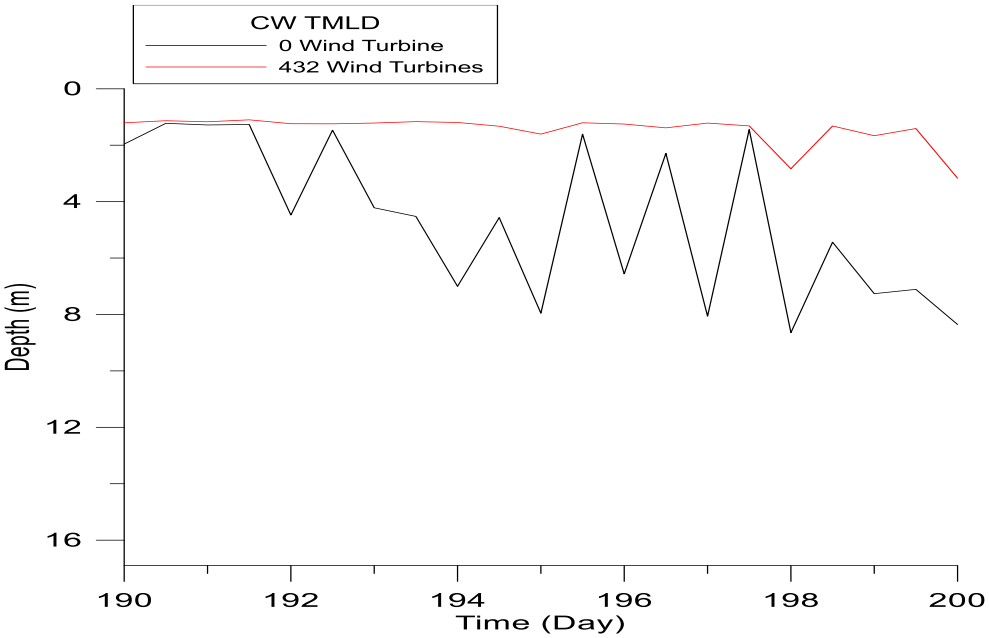

Figure 6.55: Computed mixed-layer depths during DOY 190-200.

CHAPTER SEVEN

CONCLUSION

Because of significant ecological implications, it is important for us to examine the potential effect of a large wind farm (our example has 432 9.5MW-turbines for a total capacity of 4,104 MW) on the water temperature and hydrodynamics of Lake Erie. Lake Erie has a large and relatively shallow basin (central) which could be used for wind farms and is impacted by the wind strength and vorticity. NARR reanalyzed winds used in the model match well with observed winds (Figure 5.32). However, NARR air temperature is a few degrees lower than those observed by buoys in the lake, from May to August. This leads to a lower surface water temperature prediction for that period of time as shown in Figures 5.29, 5.33 and 5.34. Lake Erie mixing behavior investigations are important as algal blooms depend on both water temperature and the nutrient concentrations, which are impacted by the lake water turnover and circulation. This characteristic along with thermal structure are important because understanding the physics that govern the thermocline developments leads to a better comprehension of the vertical transfer of mass and energy controlling factors, (McCormick, 1988). The mixing in the surface layer is mainly due to the wind stress and the surface heat flux. Stratification and turbulence are the main factors governing the vertical mixing. Stratification affects the mixing and circulation as a consequence.

Model results presented in this research provide a description of the estimated temperature and water currents and how they vary with time. An important and critical assumption in the temperature

profile is that the local factors like surface wind stress and heat flux and the initial temperature profile govern the thermal structure so by knowing those factors we can predict the thermal behavior. Water temperature in lakes follow a complex dynamic and is a result of a combination of different fluxes. The net heat flux is often small compared to the individual terms, particularly for a well-mixed surface layer (epilimnion) during stratified conditions, The epilimnion experiences strong oscillations at a variety of temporal scales: from short (hourly and daily) to long (annual and Interannual). In general, large uncertainties are associated with the estimates of the various heat exchange components, (Piccolroaz, 2013). The main heat exchanges occur at the interface between the epilimnion and atmosphere, and between the epilimnion and lower water layers (hypolimnion). Lake Erie is stratified during the summer months, but during the rest of the year, its temperature and, hence, density are fairly constant throughout. In Lake Erie, the thermal structure has a shallow unstratified western basin, and more deeply stratified central and eastern basins. As the western basin is the shallowest, it heats to maximum temperature at a faster rate rather than the other basins.

Most large thermally stratified lakes have a dome-shaped thermocline with a shallower depth offshore than close to the shore. The Ekman transport in cyclonic surface winds is a key mechanism, (Beletsky et al., 2013). Lake Erie has a bowl-shaped thermocline and anti-cyclonic circulations in the central basin.

The surface water temperature and vertically integrated water temperature vary significantly in different basins due to the heat storage and bathymetry. Wind mixing and surface heat flux are dominant processes for the development of thermal stratification in Lake Erie. The exact determination of stratification is important for phytoplankton production. Wind variations have an important influence on the depth of the thermocline, especially in the spring and autumn.

Water current circulation in Lake Erie on monthly time scales is affected mostly by wind stress and baroclinic effects, associated with horizontal temperature gradients. Baroclinic effects are more

important in summer, while winds play a more important role in the cold months. Also, the eastern basin is more influenced by baroclinic effects while wind vorticity impacts are predominant in the central basin. The western basin currents are mostly determined by Detroit River inflow.

Wind stress curl is a major factor in the Great Lakes, becoming dominant in winter when considerable vorticity in the wind field is present, (Beletsky et al., 2013). The mean circulation of the surface of the lake followed the mean winds over the region.

By modelling a large wind farm in Lake Erie, wind speed is reduced by maximum and average values of 60 and 17 percent of the undisturbed values in the centre of the wind turbine wake zone. This wind reduction leads to a potential increase of a few degrees (1 to 3°C), in the water surface temperature, which varies with time and has a maximum impact in summer. Another effect is reducing the surface current magnitude and changing the surface water current directions. The combination of these two, in turn, affects the thermocline and TMLD (temperature mixing length depth). The thermocline onsets earlier and decays later when a wind farm is present, with a deeper and sharper thermocline. The COHERENS model predicts higher surface temperature and cooler bottom temperature during warm months and vice-versa in cooler months compared to the case when there is not any wind farm. The persistent thermocline and slower winds lead to a shallower TMLD. Reduced wind speeds over the water surface will reduce latent heat fluxes and, when the water temperature is higher than that of the air, will also reduce sensible heat loss and increase water temperatures relative to those at higher wind speeds. In addition, there will be less mixing in the water column and, a stronger thermocline and a shallower surface mixed later.

The agreement between the modelled temperature plots with the previous results and observations confirms that the model is able adequately describe the seasonal thermal structure and fluctuation. However, the application of the model is limited to a specific period of the year (ice-free months).

A drawback of the numerical models is the requirement of detailed time series of meteorological data input, which are often not available or accurate enough on a forecasting basis. So this leads to impossibility in predicting the future trend of the physical-bio properties of the lake if the meteorological data are insufficient. General predictions can be verified if good meteorological forcing data are collected near to any wind farms in Lake Erie and the model output compared against temperature profiles and current velocities measured at the selected wind farm locations in Lake Erie.

REFERENCES

American Geophysical Union (2012), Lake Erie's thermal structure and circulation are backward. Retrieved from https://phys.org/news/2012-04-lake-erie-thermal-circulation.html

ArcGIS (2008), Lambert Conformal Conic. Retrieved from http://webhelp.esri.co/arcgisdesktop /9.3/ index.cfm?TopicName=Lambert_Conformal_Conic

AWS Truewind LLC (2010), New York's offshore wind energy development potential in the Great Lakes: feasibility study. Retrieved from https://www.awstruepower.com/assets/ New-Yorks-Offshore-Wind-Energy-Development-Potentila-in-the-Great-Lakes1.pdf

Barthelmie RJ., Folkerts L., Larsen GC., Rados K., Pryor SC., Frandsen ST., et al. (2005), Comparison of wake model simulations with offshore wind turbine wake profiles measured by sodar. Journal of Atmospheric and Oceanic Technology 2005, vol. 23, pages 881 – 901.

Barthelmie RJ., Frandsen ST., Nielsen MN., Pryor SC., Rethore PE., Jørgensen HE. (2007), Modelling and measurements of power losses and turbulence intensity in wind turbine wakes at Middelgrunden offshore wind farm. Journal of Wind Energy 2007, vol. 10, pages 517–528.

Barthelmie RJ. and Jensen LE. (2010), Evaluation of wind farm efficiency and wind turbine wakes at the Nysted offshore wind farm Wind Energy, vol. 13, pages 573–86. Retrieved from

https://institute.lanl.gov/ei/_docs/Annual_Workshops/Wind_Workshop_2011/BarthelmieLosAlamos.pdf

Barthelmie RJ., Pryor SC., ,Frandsen ST., Hansen KS., Schepers JG., Rados K., Schlez W., Neubert A., Jensen LE., And Neckelmann S. (2010 a), Quantifying the Impact of Wind Turbine Wakes on Power Output at Offshore Wind Farms. Journal of Atmospheric and Oceanic Technology vol. 27, pages 1302–1317.

Barthelmie R., Giebel G., Jørgensen B., Badger J., Pryor S., and Hasager C. (2004), Comparison of corrections to site wind speeds in the offshore environment: value for short-term forecasting.

Bastankhah M. and Porté-Agel F. (2014), A new analytical model for wind-turbine wakes. Elsevier Ltd. 10.1016/j.renene.2014.01.002

Beletsky D., Schwab D. J., Roebber P. J., McCormick M. J., Miller G. S., and Saylor J. H. (2003), Modelling wind-driven circulation during the March 1998 sediment resuspension event in Lake Michigan, Journal of Geophysical Research, vol. 108(C2), 3038 pp., doi:10.1029/2001JC001159, 2003.

Beletsky D., Hawley N. and Rao Y. R. (2013), Modelling summer circulation and thermal structure of Lake Erie, Jornal of Geophysical Research, vol. 118, pages 6238-6252, doi:10.1002/2013JC008854

Beletsky D., Schwab J., Ruberg S. A. (2012), Summer thermal structure and anticyclonic circulation of Lake Erie. Geophysical Research Letters, vol. 39, 6 pp.

Blumberg A.F. and Mellor G.L. (1987), A description of a three-dimensional coastal ocean circulation model. Pages 1–16 of: Heaps, N.S. (Editor), Threedimensional Coastal Ocean Models. Coastal and Estuarine Sciences. Washington D.C.: Americal Geophysical Union.

Bolsenga S. J. and Herdendorf C. E. (1993), Lake Erie and Lake St. Clair Handbook (Editors.), Wayne 427 State University Press, 467 pp.

Boyce F., Donelan M., Hamblin P., Murthy C. and Simons T. (1989), Thermal Structure and Circulation in the Great Lakes, Journal of Atmpsphere and Oceanic Technology, vol. 27 (4), pages 607–642, doi: 10.1080/ 07055900.1989.9649358.

Boyer Montégut C., Madec G., FischerLazar A., Iudicon D. (2004), Mixed-layer depth over the global ocean: An examination of profile data and a profile-based climatology, Journal of Geophysical Research, vol. 109, C12003.

Broström G. (2008), On the influence of large wind farms on the upper ocean circulation, Journal of Marine Systems, vol. 74, pages 585–591.

CANWEA (2017a), Installed Capacity. Retrieved from http://canwea.ca/wind-energy/installed-capacity/

CANWEA (2017b), Wind Energy Ontario. Retrieved from http://canwea.ca/wind-energy/ontario/

Chamorro LP. and Porté-Agel F. (2010), Effects of thermal stability and incoming boundary-layer flow characteristics on wind-turbine wakes: a wind-tunnel study. Bound-Layer Meteorol 2010, vol. 136, pages 515–533.

Charnock H. (1955), Wind stress on a water surface. Quarterly Journal Royal Meteorological Society, vol. 81, pages 639–640.

Cleve J., Greiner M., Enevoldsen P., Birkemose B. and Jensen L. (2009), Model-based analysis of wake-flow data in the nysted offshore wind farm. Wind Energy 2009, vol. 12(2), pages 125–135.

Crespo A., Hernandez J., Frandsen ST. (1999), Survey of modelling methods for wind turbine wakes and wind farms. Wind Energy 1999, vol. 2(1), pages 1–24.

Douwe J. Renkema (2007), Validation of wind turbine wake models Using wind farm data and wind tunnel measurements thesis report.

Dupont F., Chittibabu P., Fortin V., Rao Y. R., and Lu Y. Y. (2012), Assessment of a NEMO-based hydrodynamic modelling system for the Great Lakes, Water Quality Research Journal of Canada, vol. 47 (3–4), pages 198–214, doi: 10.2166/ Wqrjc.2012.014.

Dvorak P. (2015), Offshore wind provides opportunities for U.S. manufacturers in the Midwest. Available online at: http://www.windpowerengineering.com/construction/offshore-wind-provides-opportunities -u-s-manufacturers-midwest/.

Encyclopaedia-Britannica (2017), Retrieved from https://www.britannica.com/science/Ekman-layer

Ezer T. (2000), On the seasonal mixed-layer simulated by a basin-scale ocean model and the Mellor-Yamada turbulence scheme, Journal of Geophysical Research, doi: 10.1029/2000JC900088

Ferguson R. (2016), Ontario extends moratorium on offshore wind turbines. Retrieved from https://www.thestar.com/news/queenspark/2016/12/22/ontario-extends-moratorium-on-offshore-wind-turbines.html

Ferziger J., (2005), Turbulence: its origins and structure. Pages 4–13 of: Baumert H.Z., Simpson J., and S¨undermann J. (Editors), Marine Turbulence. Theories, Observations and Models. Cambridge University Press.

Fujisaki A., Wang J., Hu H. G., Schwab D. J., Hawley N., and Rao Y. R. (2012), A modelling study of ice-water processes for Lake Erie applying coupled ice-circulation models, Journal of Great Lakes Research, vol. 38(4), pages 585–599, doi:10.1016/J.Jglr.2012.09.021.

Galperin B., Kantha L.H., Hassid S. and Rosati A. (1988), A quasi-equilibrium turbulent energy model for geophysical flows. Journal of the Atmospheric Sciences, vol. 45, pages 55–62.

Gill A.E. (1982), Atmospheric-Ocean Dynamics. International Geophysics Series, vol. 30. Orlando: Academic Press.

Gendney R. (1972), Wind-Driven Currents in Lake Erie, Journal of Geophysical Research, vol. 77 (15).

GLERL (2005), Lake Erie Physical Data Sets. Retreived from: https://www.glerl.noaa.gov/res/ projects/ ifyle/data/Mooring/therm/eriemap.html

Gonzalez F. and Longatt (2011), Wake effects in the wind farms performance: Steady-state and dynamic behavior, Renewable Energy, doi:10.1016/j.renene.2011.08.053.

Great Lakes Atlas (1995), Environment Canada and U.S. Environmental Protection Agency Lake Erie brochure, 1990, Michigan Sea Grant.

Hamilton T. (2016), Ontario's love-hate relationship with Great Lakes wind turbines. Retrieved from https://tvo.org/article/current-affairs/climate-watch/ontarios-love-hate-relationship-with-great-lakes-wind-turbines

Hawley, Johengen N. T., Yerubandi R., Ruberg S., Beletsky D., Ludsin S., Eadie B. J., Schwab D. J., Croley T., and Brandt S. (2006), Lake Erie hypoxia prompts Canada-US study, Eos Trans. AGU, vol. 87(32), pages 313–319.

Heathershaw A.D. (1981), Comparisons of measured and predicted sediment transport rates in tidal currents. Marine Geology, vol. 42, pages 75–104.

Hill J.S. (2016), Global offshore wind market reached nearly 12 GW In 2015, Offshore_Wind_Growth_Navigant. Retrieved from: https://cleantechnica.com/2016/09/28/global-offshore-wind-market-reached-nearly-12-gw-2015/

Hill J.S. (2015), US offshore wind energy potential is staggering. Available online at: http://cleantechnica.com/2015/01/13/us-offshore-wind-energy-potential-staggering/.

Hossain M.S. and Rodi W. (1982), A turbulence model for buoyant flows and its application to vertical buoyant jets, pages 121–178 of: Rodi, W. (Editor), Turbulent buoyant jets and plumes. HMT-Series, vol. 6. Oxford: Pergamon Press.

IESO (2017), Demand Overview. Retrieved from http://www.ieso.ca/en/power-data/demand-overview/historical-demand

Ifpress (2016), Retrieved from http://www.lfpress.com/2016/10/23/offshore-wind-plan-in-lake-erie-criticized-internationally

IJC (2014), A balanced diet for Lake Erie: Reducing Phosphorus Loadings and Harmful Algal Blooms, Report of the Lake Erie Ecosystem Priority. International Commission on the Great Lakes, 96 pp.

Jacket D.R. and McDougall T.J. (1995), Minimal adjustment of hydrographic profiles to achieve static stability. Journal of Atmospheric and Oceanic Technology, vol. 12, pages 381–389.

Jones A. (2017), Ontario signals offshore wind moratorium will continue for several more years. Retrieved from https://www.thestar.com/news/canada/2017/02/13/ontario-signals-offshore-wind-moratorium-will-continue-for-several-more-years.html

Juwi GmbH (2009), Lake Erie wind resource assessment: Results from the Cleveland Water Intake Crib (JW Great Lakes Wind LLC and juwi GmbH, 2008).

Kantha L.H. and Clayson C.A. (2000a), Small scale processes in geophysical fluid flows. San Diego, California: Academic Press.

Kowalski K.M., (2014), Despite funding setback, Lake Erie wind project pushes ahead. Retrieved from http://www.midwestenergynews.com/2014/06/23/despite-funding-setback-lake-erie-wind-project-pushes-ahead

Lange M., Burkhard B., Garthe S., Gee K., Kannen A., Lenhart H. and Windhorst W. (2010), Analyzing Coastal and Marine Changes: offshore wind farming as a case study. Zukunft Küste - Coastal Futures Synthesis Report. LOICZ Research and Studies, GKSS Research Centre, Geesthacht, vol. 36, 212 pp.

LEEDCO (2017), Draft Environmental Assessment LEEDCo Project Icebreaker Lake Erie, City of Cleveland, Cuyahoga County, Ohio, U.S. Department of Energy.

Ludewig E. (2014), Influence of offshore wind farms on atmosphere and ocean dynamics, PhD dissertation, Max Planck Research School for Maritime Affairs, Hamburg, 198 pp, also available (2015) as "On the Effect of Offshore Wind Farms on the Atmosphere and Ocean Dynamics" : Hamburg Studies on Maritime Affairs, vol. 31, Springer.

Luyten P. (2012), User documentation version 2.4, Royal Belgian Institute of Natural Sciences (RBINS-MUMM), Belgium. Retrieved from https://odnature.naturalsciences.be/coherens/manual

Manwell J. F., Wind energy explained: theory, design, and application / James Manwell, Jon McGowan, Anthony Rogers. (2009) – second edition. ISBN 978-0-470-01500-1 (cloth)

May G. (2017), Turbines in our lakes - too keen to be green in Ontario, battle lines drawn in wind power debate on the waterfront. Retrieved from http://www.mynewwaterfronthome.com/turbineslakes.aspx

McCormick M. (1988), An intercomparision of four mixed-layer models in a shallow inland sea, Journal of Geophysical Research, vol. 93C6, pages 6774-6788, June 15, 1988, doi: 0148-0227/88/008C-0175.

McDougall T.J., Jackett D.R., Wright D.G., and Feistel, R. (2003), Accurate and computationally efficient algorithms for potential temperature and density of seawater. Journal of Atmospheric and Oceanic Technology, vol. 20, pages 730–741.

Mellor G.L. and Yamada T. (1974), A hierarchy of turbulence closure models for planetary boundary layers. Journal of the Atmospheric Sciences, vol. 31, pages 1791–1806.

Mesinger F., and Arakawa A. (1976), Numerical methods used in atmospheric models. Technology report Global Atmospheric Research Programme (GARP) publication series.

Michigan Great Lakes Wind Council (2010), Report of the Michigan Great Lakes Wind Council. Available at: www.michiganglowcouncil.org. Accessed 21 December 2010.

Natural Resources Canada (2017), Canada's low-carbon energy future, designed by you. Retrieved from https://www.generationenergy.ca/learn/making-energy

NOAA (2016), Lambert Conformal Format. Retrieved from: https://www.esrl.noaa.gov/psd/data/narr/format.html

NOAA (2017), Bathymetry of Lake Erie and Lake Saint Clair. Retrieved from https://www.ngdc.noaa.gov/mgg/fliers/98mgg01.html, https://oceanservice.noaa.gov/facts/bathymetry.html

O'Connor W. P., Schwab D. J., and Lang G. A. (1999), Forecast verification for Eta Model winds using Lake Erie storm surge water levels, Weather Forecast, vol. 14(1), pages 119–133, doi:10.1175/1520-0434(1999)014 <0119:Fvfemw>2.0.Co;2.

Offshorewindbiz (2017), Offshore capacity. Retrieved from: http://www.offshorewind.biz/2017/02/10 /global-offshore-wind-capacity-reaches-14-4gw-in-2016/

Offwind (2016), Wake model. Retrieved from: http://offwind.eu/static/eng-tools/wake-model/wake-model-that-assumes-linear-expansion-of-wake-cone.png

Ontario.ca (2017), Retrieved from: https://www.ontario.ca/page/assessment-offshore-wind-farm-decommissioning-requirements

Ornl.gov (2017), Retrieved from: https://www.phy.ornl.gov/csep/CSEP/OM/NODE23.html

Paskyabi M.B. and Fer I. (2012), Upper ocean response to large wind farm effect in the presence of surface gravity waves. Energy Procedia, vol. 24, pages 245–254, doi:10.1016/j.egypro.2012.06.106

Paulson C.A. and Simpson J.J. (1977), Irradiance measurements in the upper ocean. Journal of Physical Oceanography, vol. 7, pages 952–956.

Payne R. E. (1972), Albedo of the sea surface. Journal of the Atmospheric Sciences, vol. 29, pages 959–970.

Phillips N.A., (1957), A coordinate system having some special advantages for numerical forecasting. Journal of Meteorology, vol. 14, pages 184–185.

Phys.org (2012), Summer thermal structure and anticyclonic circulation of Lake Erie, Geophysical Research Letters, doi: 101029/2012GL051002, 2012 Read more at: https://phys.org/news/2012-04-lake-erie-thermal-circulation.html#jCp

Piccolroaz S., Toffolon M., and Majone B. (2013), A simple lumped model to convert air temperature into surface water temperature in lakes, Hydrology Earth Systems Science, vol. 17, pages 3323–3338, doi: 10.5194/hess-17-3323-2013

Planning.gov (2017), Draft PPS 18: Renewable Energy Annex 1 Wind Energy: Spacing of Turbines. Retrieved from https://www.planningni.gov.uk/de/index/policy/planning_statements/pps18/_pps18_annex1/pps18_annex1_wind/pps18_annex1_technology/pps18_annex1_spacing.htm

Pryor S., Shahinian M., and Stout M. (2005), Offshore wind energy development in the Great Lakes: A preliminary briefing paper for the Michigan renewable energy program.

Reevely D. (2016), Ontario suspended offshore wind farms so it could do more science, then did not do any for years. Retrieved from http://ottawacitizen.com/news/national/reevely-ontario-suspended-offshore-wind-farms-so-it-could-do-more-science-then-didnt-do-any-for-years

Roe P.L. (1986), Characteristic-based schemes for the Euler equations. Annual Review of Fluid Mechanics, vol. 18, pages 337–365.

Ryan J. (2016), Next U.S. offshore wind farm set to emerge from Lake Erie. Retrieved from https://www.bloomberg.com/news/articles/2016-10-26/next-u-s-offshore-wind-farm-set-to-emerge-from-lake-erie

Schertzer W. M., Saylor J. H., Boyce F. M., Robertson D. G., Rosa F. (1987), Seasonal thermal cycle of Lake Erie. Journal of Great Lakes Research, vol. 13 (4), pages 468-486.

Schwab D. J. and Bennett J. R. (1987), Lagrangian comparison of objectively analyzed and dynamically modelled circulation patterns in Lake Erie, Journal of Great Lakes Research, vol. 13(4), pages 515–529.

Schwab D. J., Beletsky D., DePinto J., and Dolan D. M. (2009), A hydrodynamic approach to modelling phosphorus distribution in Lake Erie, Journal of Great Lakes Research, vol. 35(1), pages 50–60, doi:10.1016/J.J glr.2008.09.003.

Simons T. (1976), Continuous dynamical computations of water transports in Lake Erie for Journal of the Fisheries Board of Canada, 1976, vol. 33(3), pages 371-384, doi: 10.1139/f76-060.

Song Y. and Haidvogel D. (1994), A semi-implicit ocean circulation model using a generalized topography-following coordinate system. Journal of Computational Physics, vol. 115, pages 228–244.

Soulsby R.L. (1983), The bottom boundary layers of shelf seas. Johns, B. (Editors), Physical Oceanography of Coastal and Shelf Seas, vol. 35, pages 189–266. Elsevier Oceanography Series.

Statoil (2017), World's first floating wind farm has started production. Retrieved from https://www.statoil.com/en/news/worlds-first-floating-wind-farm-started-production.html

Stewart R. (2008), Introduction to physical oceanography, Department of Oceanography Texas A & M University. URL: http://oceanworld.tamu.edu/resources/ocng_textbook/PDF_files/_book_PDF_files.html

Sweby P.K. (1984), High resolution schemes using flux limiters for hyperbolic conservation laws. SIAM Journal of Numerical Analysis, vol. 21, pages 995–101.

Taylor P. A. (1988), Turbulent wakes in the atmospheric boundary layer, Proceedings of International Symposium On Flow and Transport in the Natural Environment: Canberra 1987, Steffen W.L. and Denmead O.T. (Editors), published by Springer, pages 270–292.

Taylor P. A. (1983), On wakes and the net forces produced by surface mounted obstacles in neutrally stratified atmospheric boundary-layers. Boundary-Layer Meteorology, vol. 27, pages 393–412.

The Canadian Atlas (2017), Wind energy, how offshore wind farms work. Retrieved from http://www.canadiangeographic.com/atlas/themes.aspx?id=windenergy&sub=windenergy_farms_offshore&lang=En

UCS (2017), Benefits of renewable energy use. Retrieved from http://www.ucsusa.org/clean-energy/renewable-energy/public-benefits-of-renewable-power#.WbV9JbKGPIW

Vestasoffshore (2017), V164-9.5 MW. Retrieved from http://www.mhivestasoffshore.com/category/v164-9-5-mw/

Wang J., Hu H. G., Schwab D., Leshkevich G., Beletsky D. et al., Hawley N., and Clites A. (2010), Development of the Great Lakes Ice-circulation Model (GLIM): Application to Lake Erie in 2003–2004, Journal of Great Lakes Research, vol. 36 (3), pages 425–436, doi:10.1016/J.Jglr.2010.04.002.

Weather.gov (2017), Retrieved from https://.wwwweather.gov/cle/marine_thermocline

Weng W., Taylor P. A. and Salmon J. R. (2010), A 2-D numerical model of boundary-layer flow over single and multiple surface condition changes, Journal of Wind Engineering and Industrial Aerodynamics, vol. 98, pages 121–132.

Wikipedia (2017), Ekman layer. Retrieved from https://en.wikipedia.org/wiki/Ekman_layer

Windpowerengineering (2017), Monster deep-water offshore floating wind turbines are the new horizon for renewable energy. Retrieved from http://www.windpowerengineering.com/offshore-wind/monster-deep-water-offshore-floating-wind-turbines-new-horizon-renewable-energy/

Wikipedia (2018), Log wind profile. Retrieved from https://en.wikipedia.org/wiki/Log_wind_profile

Wu Y.T. and Porté-Agel F. (2012), Atmospheric turbulence effects on wind-turbine wakes: an LES study. Energies 2012, vol. 5, pages 5340–5362, doi: 5:5340e62.

Wu YT. and Porté-Agel F. (2011), Large-eddy simulation of wind-turbine wakes: evaluation of turbine parametrisations. Bound-Layer Meteorol 2011, vol. 138, pages 345–366, doi: 138:345e66

4C Offshore (2015), Lake Erie alternative power. Retrieved from http://www.4coffshore.com/windfarms/lake-erie-alternative-power-united-states-us96.html

4C Offshore (2017), Icebreaker United States. Retrieved from http://www.4coffshore.com/windfarms/icebreaker-united-states-us82.html

APPENDIX A

Thermocline

A thermocline is a transition layer between deep and surface water (mixed-layer). The definition of these layers is based on temperature. The mixed-layer is near the surface where the temperature is roughly that of surface water. In the thermocline, the temperature decreases rapidly from the mixed-layer temperature to the colder deep-water temperature. The mixed-layer and the deep-water layer are relatively uniform in temperature, while the thermocline represents the transition zone between the two. In our plots thermocline depth is defined as the depth where the maximum vertical temperature gradient onsets and thermocline thickness is considered as the difference in a depth where thermocline (under the mixed layer) onsets and the depth where it ends (above deep water).

In spring and summer, the mixed-layer warms the fastest due to the absorption of solar radiation and warm air interacting with the water, while the bottom layers stay cooler. (weather.gov, 2017)

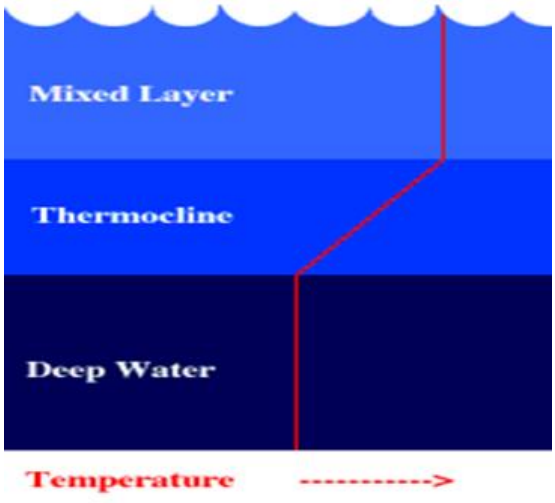

Figure A1: Thermocline Layer [weather.gov, 2017]

APPENDIX B

The Ekman Layer

The Ekman layer is the layer in a fluid where there is a force balance between pressure gradient force, force and turbulent drag. It was first described by Vagn Walfrid Ekman. Ekman layers occur both in the atmosphere and in the ocean, (Wikipedia, 2017). Steady winds blowing on the lake surface produce a thin (at most a few hundred meters), horizontal boundary layer. A similar boundary layer exists at the bottom of the ocean, the bottom Ekman layer. (Stewart, 2008).

The wind stress on the lake depends on the wind speed magnitude and direction. Within the oceanic Ekman layer, the wind stress is balanced by the Coriolis and frictional forces. Generally, the wind tends to draw current in its direction when there is no or a weak Coriolis force but in the presence of the Coriolis force the surface water is directed at an angle of 45° to the wind (assuming a constant eddy viscosity), to the right in the Northern Hemisphere and to the left in the Southern Hemisphere. The current speed reduces as depth increases. On the surface, water current is in the direction of the wind but it forms a spiral as the depth increases and becomes antiparallel to the surface flow at the base of the layer where in an idealised model, the speed is 1/23 of the surface speed. The average water particle within the Ekman layer moves at an angle of 90° to the wind (to the right of the wind direction in the Northern Hemisphere and to its left in the Southern Hemisphere). This phenomenon is called Ekman transport, and its effects are widely observed in the oceans. (Encyclopaedia-Britannica, 2017)

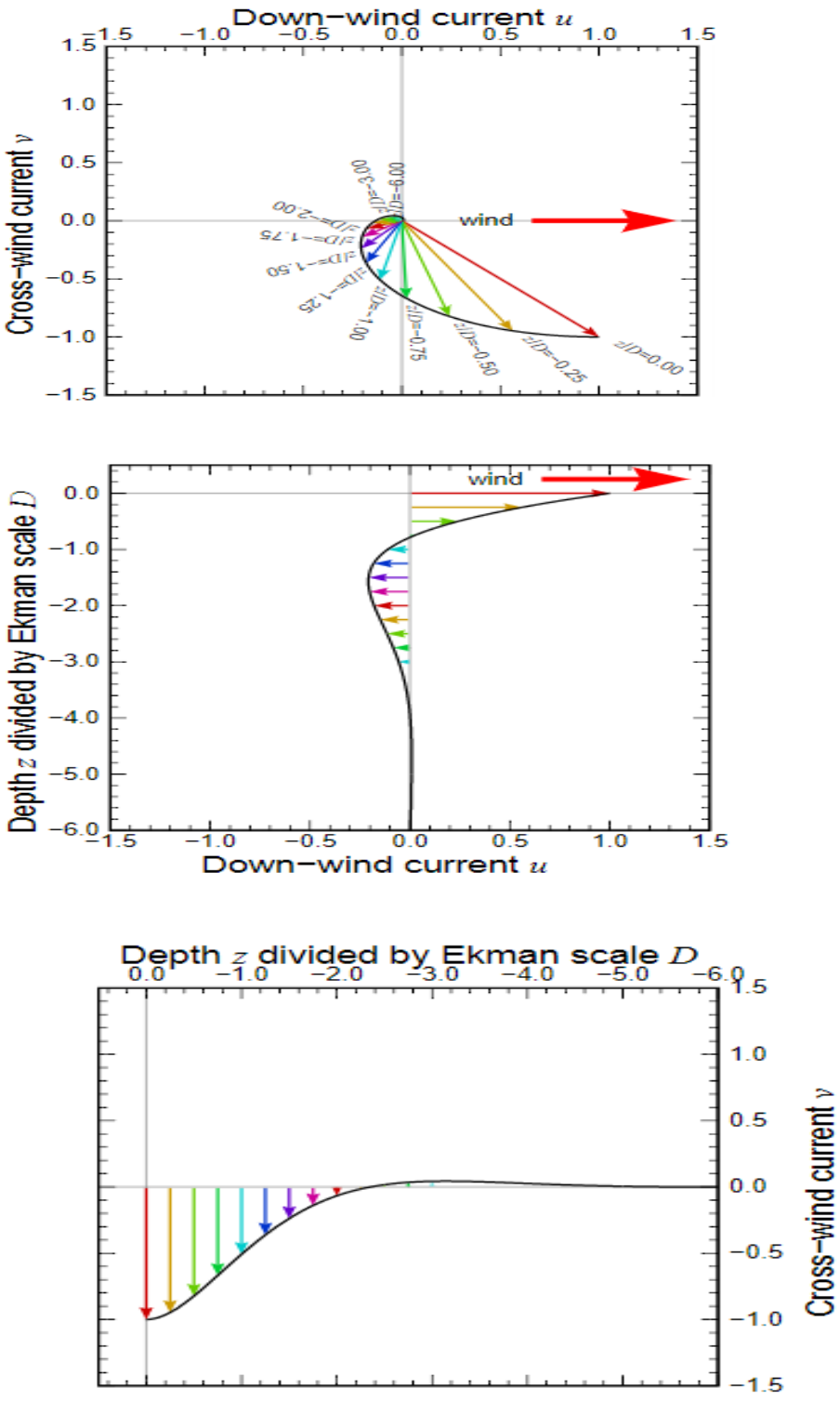

Figure B1: Three views of the wind-driven Ekman layer at the surface of the ocean in the Northern Hemisphere. The geostrophic velocity is zero, [(D= 2 ν / f) ^{½}, ν is eddy viscosity and f is the Coriolis parameter]. [Wikipedia, 2018]

APPENDIX C

Lambert Conformal Conic Grid

Conic projection normally based on two standard parallels, making it a secant projection. The latitude spacing increases beyond the standard parallels. This is the only common conic projection that represents the poles as a single point. (ArcGIS, 2008)

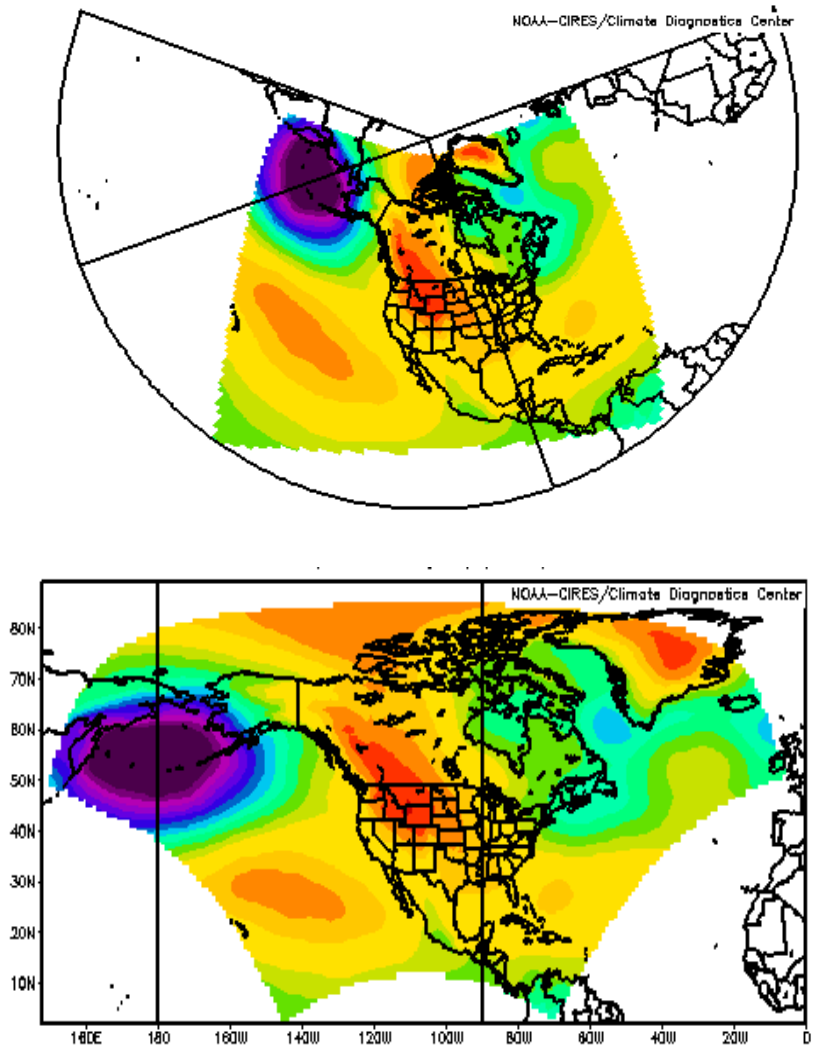

Figure C1: NARR model data Lambert Conformal Conic grid [NOAA, 2016]

APPENDIX D

LEEDCO Icebreaker project with six turbines simulation

As an additional run, a wind farm with six wind turbines at the same location and with the same layout of the LEEDCO Icebreaker project is simulated. The monthly-averaged plots (May to October, 2005) of the water surface temperature difference between a case when there is no wind farm and a case when there is a wind farm with 6 wind turbines are illustrated in Figures D1 to D6. The location of the wind farm is shown as a small blue rectangle. Due to the much smaller wind farm size and fewer number of the wind turbines compared to the case when there are 432 wind turbines the surface temperature difference barely reaches to 0.3 °C. In this case, the maximum temperature difference is in September. The 6-turbine simulation shows a maximum wind speed reduction in the wake of 30 percent, an average of 7 percent over an area of 260 km^2 within the wind farm downwind of the wind farm.

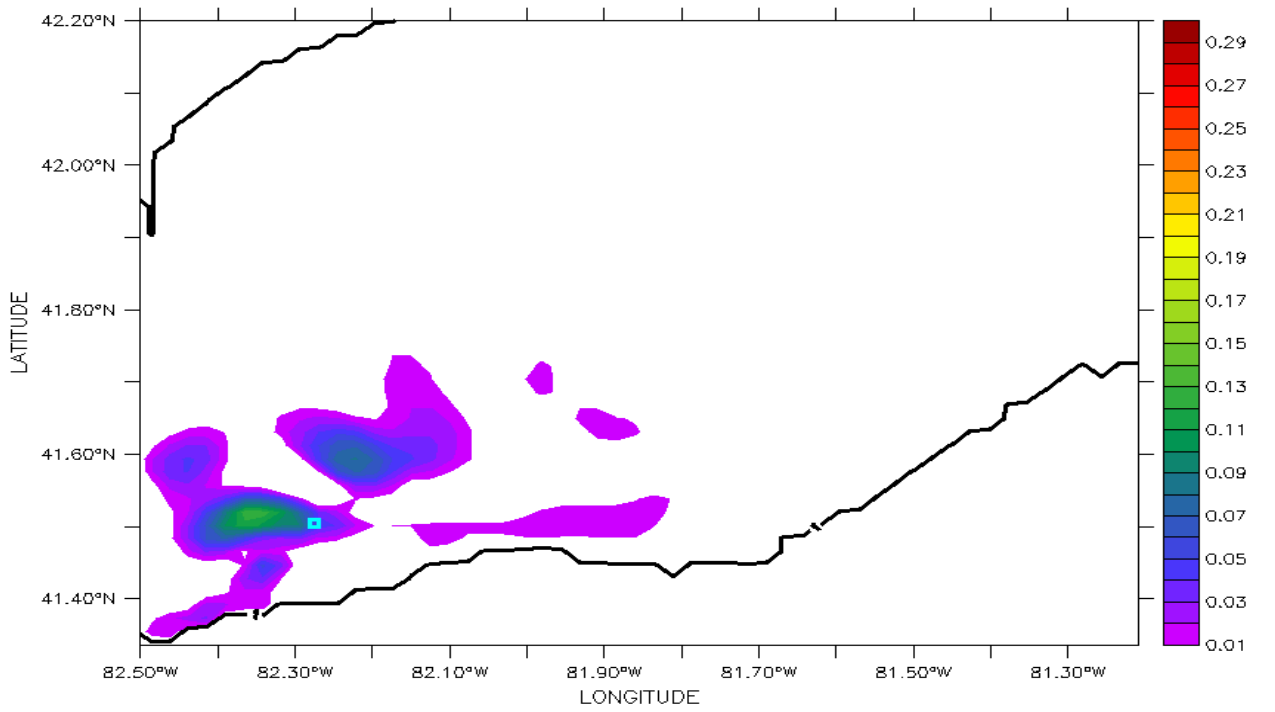

Figure D1: May-averaged surface water temperature difference of the presence and absence of a six wind turbines (deg C), 2005.

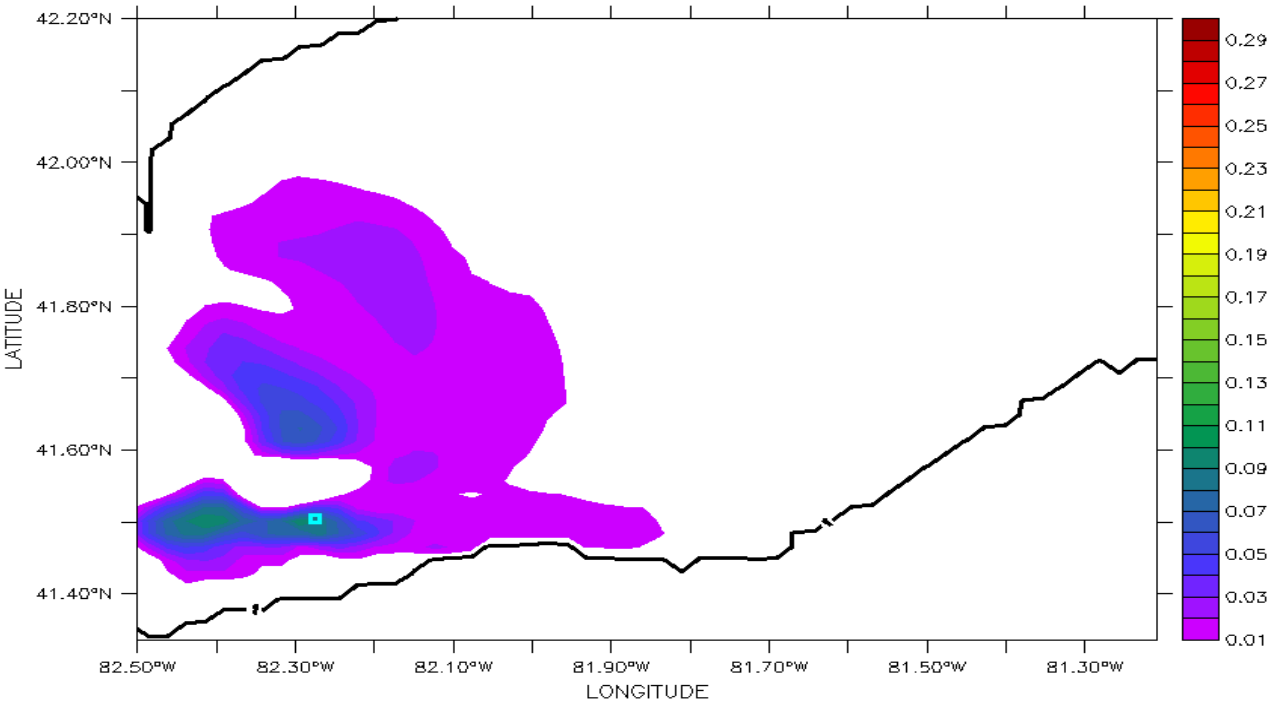

Figure D2: June-averaged surface water temperature difference of the presence and absence of a six wind turbines (deg C), 2005.

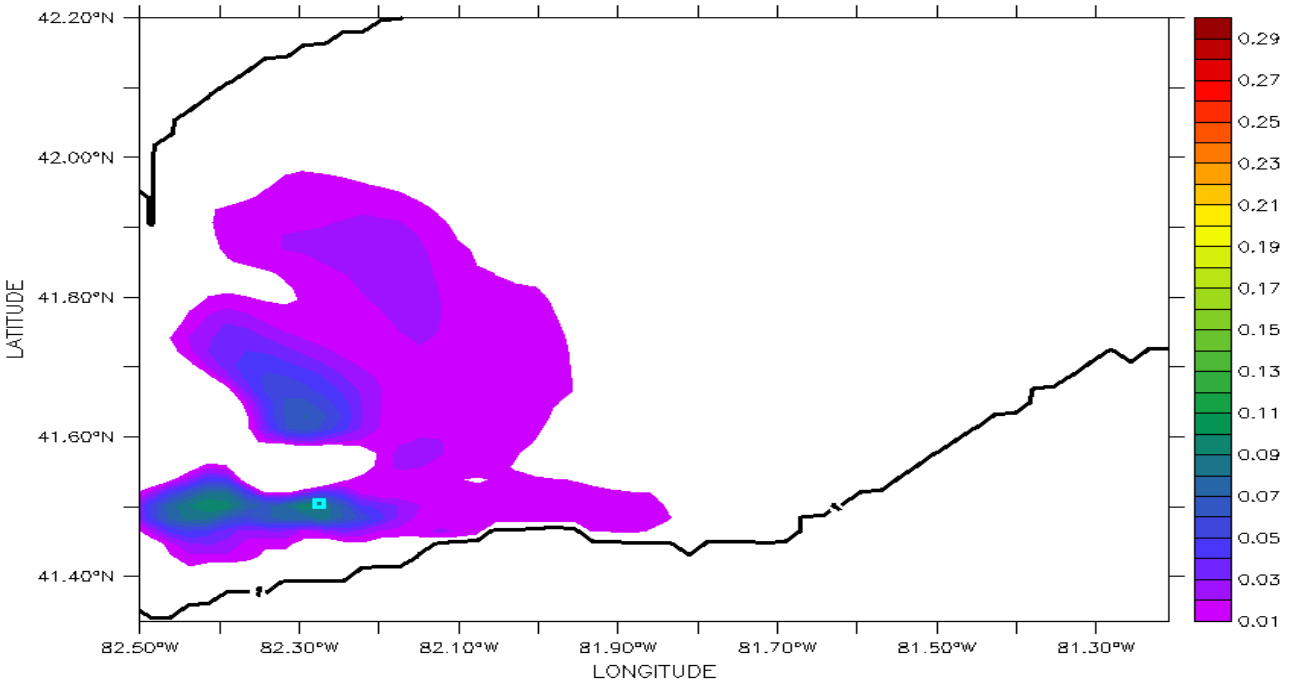

Figure D3: July-averaged surface water temperature difference of the presence and absence of a six wind turbines (deg C), 2005.

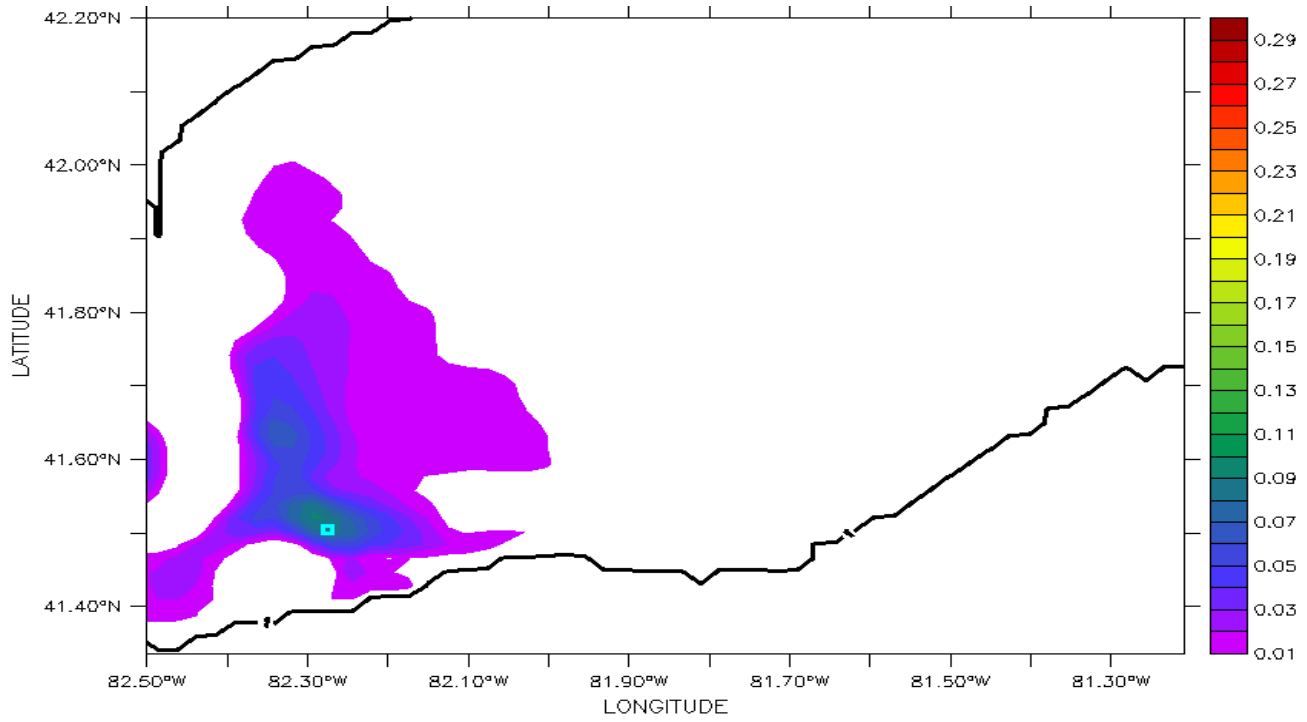

Figure D4: August-averaged surface water temperature difference of the presence and absence of a six wind turbines (deg C), 2005.

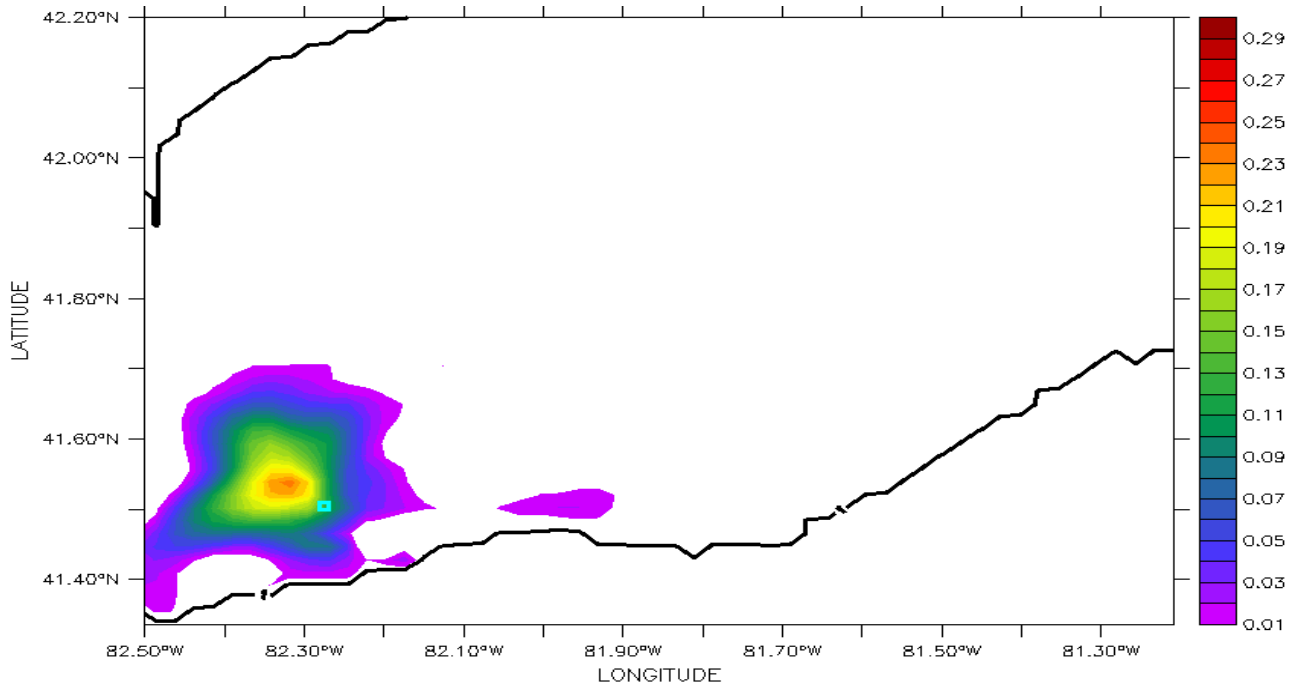

Figure D5: September-averaged surface water temperature difference of the presence and absence of a six wind turbines (deg C), 2005.

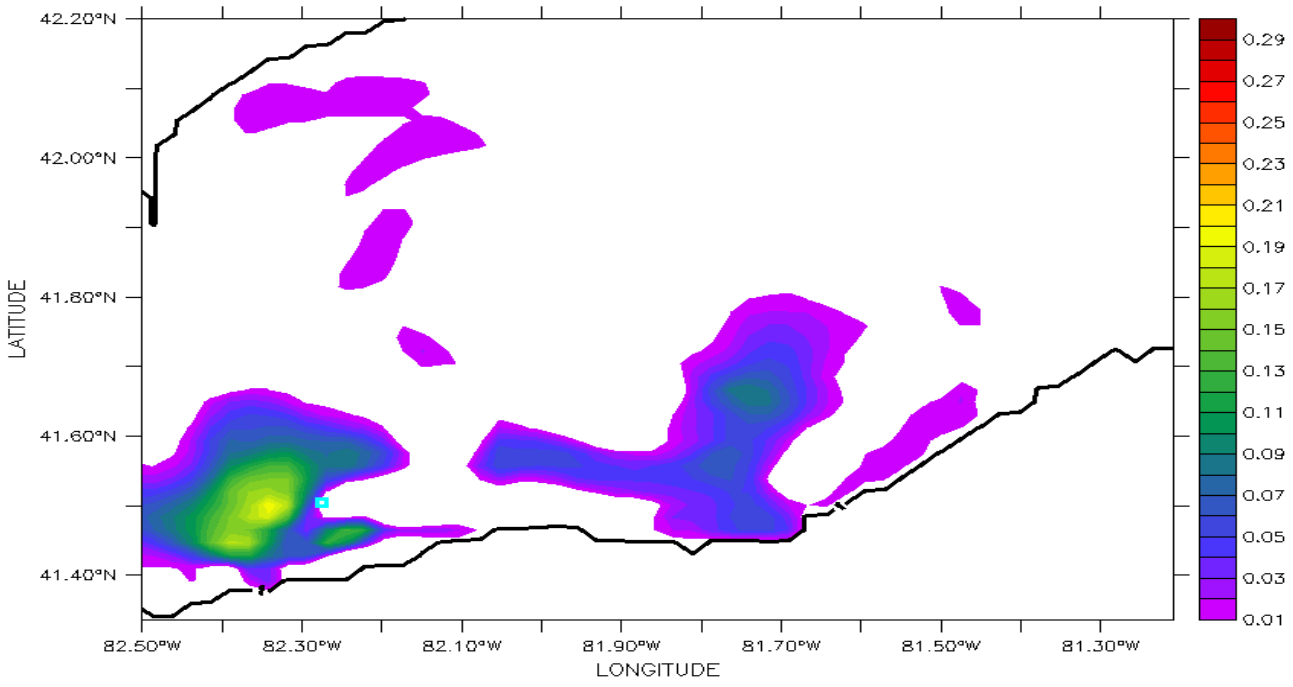

Figure D6: October-averaged surface water temperature difference of the presence and absence of a six wind turbines (deg C), 2005.